MODIS BRDF/Albedo Product: Algorithm Theoretical Basis Document Version 4.0

Principal Investigators:
A. H. Strahler, J.-P. Muller, MODIS Science Team Members

Document Prepared by

Alan H. Strahler[1], Wolfgang Wanner[1], Crystal Barker Schaaf[1],
Xiaowen Li[1,3], Baoxin Hu[1,3],
Jan-Peter Muller[2], Philip Lewis[2], Michael J. Barnsley[4]

[1] Boston University
[2] University College London
[3] Institute of Remote Sensing Application, Chinese Academy of Sciences
[4] University of Wales, Swansea


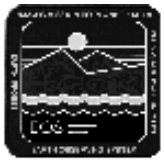


MODIS Product ID: MOD43
Version 4.0 – November 1996

Abstract

The BRDF/Albedo algorithm combines registered, multidate, multiband surface reflectance data from the EOS MODIS and MISR instruments to fit a Bidirectional Reflectance Distribution Function (BRDF) in seven spectral bands at 1-km resolution on a 16-day cycle. Then from this BRDF, the algorithm derives two albedo-like measures for each spectral band as well as for three broad bands covering the solar spectrum.

The BRDF of a surface describes the scattering of incident light from one direction in the hemisphere into another direction in the hemisphere. Because this function varies, the radiance of a surface changes with illumination and view position. In the BRDF/Albedo product, the BRDF is characterized by semiempirical trigonometric functions that describe the angular shape of the scattering function (the Ambrals BRDF model) based on simplifications of more complex physical models.

Obtaining the surface BRDF is useful because it (1) allows the "correction" of reflectance for BRDF effects, for example by standardizing the view angle in multidate images; (2) is required for accurate retrieval of surface reflectance in the presence of an atmosphere; (3) quantifies the directional information in the remotely- sensed signal, which is related to surface structure and scattering behavior and therefore ground cover type; and (4) provides a surface radiation-scattering model for boundary layer parameterization of surface-atmosphere radiation transfer for use in regional and global climate modeling.

The albedo of a surface is a dimensionless ratio of the radiant energy scattered away by a surface to that received, regardless of direction. It is often restricted to a particular wave-band or wavelength, in which case it is a spectral albedo. The spectral albedo of a surface depends on both the BRDF of the surface and the scattering behavior of the atmosphere above it. The MODIS/MISR BRDF/Albedo product provides two albedo measures: a "black-sky" albedo (directional–hemispherical reflectance) that integrates the BRDF over the exitance hemisphere for a single irradiance direction, and a "white-sky" albedo (bihemispherical reflectance) that integrates the BRDF over all viewing and irradiance directions. Because these albedo measures are purely properties of the surface, and do not depend on the state of the atmosphere, they can be used with any atmospheric specification to provide true surface albedo as an input to regional and global climate models. Albedo is a fundamental parameter for climate modeling, since it is a property that drives much of the energy flux at the land boundary layer. Maps of land surface albedo, which can be provided at fine to coarse scales using the BRDF/Albedo Product, will be extremely useful to global and regional climate modelers.

Contents

MODIS BRDF/Albedo Product:

Algorithm Theoretical Basis Document Version 4.0 – MOD43

1 INTRODUCTION

1.1 ALGORITHM AND DATA PRODUCT IDENTIFICATION

At-Launch:

- MOD43, Surface Reflectance; Parameter 3669, Bidirectional Reflectance
- MOD43, Surface Reflectance; Parameter 4332, Albedo

Post-Launch:

- MOD43, Surface Reflectance, Parameter 3665, Bidirectional Reflectance, with Topographic Correction
- MOD43, Surface Reflectance, Parameter 4333, Albedo, with Topographic Correction

1.2 INTRODUCTION

The earth's surface scatters radiation anisotropically in many wavelength regimes. The Bidirectional Reflectance Distribution Function (BRDF) specifies the behavior of surface scattering as a function of illumination and view angles at a particular wavelength. The albedo of a surface describes the ratio of radiant energy scattered upward and away from the surface in all directions to the downwelling irradiance incident upon the surface. Like the BRDF, albedo is spectrally dependent. If the BRDF is known, the albedo can be derived given knowledge of the atmospheric state. Note that the albedo is often integrated over all wavelengths of the downwelling solar spectrum for applications involving surface energy balance, and the general use of the term "albedo" implies this integration. However, in this document the term will also include spectral albedo, depending on the context.

The anisotropic reflectance behavior of earth surfaces presents an important problem for the interpretation of remotely-sensed images. Because of this behavior, a reflectance value observed from a single angular position cannot simply be multiplied by a constant to provide an albedo. Furthermore, since radiance measurements of the same surface cover will vary with viewing position, incorrect scene inference can occur when the same cover type is viewed under different geometries or at different times of day or season. On the other hand, the anisotropic reflectance provides an opportunity to infer information about the physical parameters of the surface cover that produce the anisotropic effect. Such inference will obviously require a

suite of reflectance measurements obtained from different viewing positions, rather than merely relying on data from a single image.

The angular reflectance of the land surface changes not only with viewing position, but also with the position of the source of irradiance in the hemisphere. Thus, both the radiance in a specific direction and the albedo of a surface are dependent on the sun's position in the sky. The angular pattern of downwelling diffuse radiance, which depends largely on the state of the atmosphere, will also influence both the albedo and the specific surface radiance observed in a given direction. This means that the atmospheric state (*e.g.*, turbidity) must be taken into account when BRDFs and the surface albedo measures derived from them are extracted from a series of directional observations.

The purpose of the BRDF/Albedo product is (1) to describe the anisotropic reflectance of the earth's surface at a fine spatial and temporal scale by fitting models of bidirectional reflectance distribution to angular observations, and (2) to provide two surface albedo measures ("black-sky" and "white-sky" albedos) that allow quantification, also at fine spatial and temporal scales, of the balance in upwelling and downwelling surface energy fluxes. The BRDF functions and albedo measures are provided for seven spectral bands spaced throughout the solar shortwave spectrum (0.4–3.0 μm), and in the case of albedo measures, for three additional, broad bands (0.4–0.7, 0.7–3.0, 0.4–3.0 μm). All outputs are surface descriptors that are independent of atmospheric characteristics. The BRDF/Albedo output product is described more completely in the following section.

Obtaining the surface BRDF is useful because it (1) allows the "correction" of reflectance for BRDF effects, for example by standardizing the view angle in multidate images; (2) is required for accurate retrieval of surface reflectance in the presence of an atmosphere; (3) quantifies the directional information in the remotely-sensed signal, which is related to surface structure and scattering behavior and therefore ground cover type; and (4) provides a surface-radiation scattering model for boundary layer parameterization of surface vegetation atmospheric transfer schemes for use in regional and global climate modeling.

Albedo is a fundamental parameter for global climate modeling, since it is a function that drives much of the energy flux at the land boundary layer. Black- and white-sky albedos, as pure surface properties, can be used with any atmospheric specification to provide true surface albedo as an input to regional and global climate models. Fine-grained global maps of land surface albedo will be extremely useful to regional climate modelers, and, given the way that our algorithm specifies BRDF and albedo, such maps can be easily collapsed to the coarser resolutions that global climate models can ingest directly.

1.3 DATA PRODUCT DESCRIPTION

The BRDF/Albedo algorithm combines registered, multidate, multiband surface reflectance data from the EOS MODIS and MISR instruments to fit two kernel-driven models of the Bidirectional Reflectance Distribution Function (BRDF) in seven spectral bands at 1-km resolution on a 16-day cycle. Then from this BRDF, the algorithm derives two albedo-like measures for each spectral band as well as for three broad

bands covering the solar spectrum. The gridded data are inverted using the kernel-driven semiempirical Ambrals (Algorithm for MODIS bidirectional reflectance anisotropy of the land surface) BRDF model (using Ross-kernels, Li-kernels, and a specular kernel; see Wanner *et al.*, 1995, 1997) and the empirical modified Walthall BRDF model (Walthall *et al.*, 1995; Nilson and Kuusk, 1989), where the first consists of a weighted sum of a volume-scattering (radiative transfer-based) kernel, a surface-scattering (geometric optics-based) kernel, and a constant (isotropic contribution), the latter of a set of empirical kernels.

When sufficient and appropriate observations are available, the directional reflectance pattern of the land surface element associated with each 1-km grid cell can be described by the kernels of the Ambrals BRDF model used and corresponding kernel weights (parameters) that best represent the scattering involved. Thus, the kernels producing the lowest root-mean-square (RMS) error in inversion of the observations are chosen to describe the BRDF and derive the bihemispherical integral ("white-sky" albedo) and the directional-hemispherical integral ("black-sky" albedo) of the BRDF. In addition, results from the empirical modified Walthall model are stored to allow global comparisons based on a single consistent model. The product will be generated for all seven MODIS land bands; broadband albedos (0.4–0.7, 0.7–3.0, 0.4–3.0 μm) will also be provided. The product will be derived over land only. Table 1 gives an overview of product contents.

Users of this product will be found among the global climate change community, most notably radiation budget investigators, and among regional and mesoscale modelers. Further users include other AM-platform teams, for example the MODIS atmospheric correction team or the CERES team, who will use surface BRDF in cloud detection. The product will also be used in land cover classification for the MODIS Land Cover Product.

1.4 DOCUMENT SCOPE

In the remainder of this document, overview and background information will be provided first; this includes the intended use of the BRDF products, and the history of the BRDF models. A detailed description of the algorithm follows in Section 3. It is presented from both a theoretical and practical viewpoint and consists of physical descriptions, mathematical formulations, uncertainty estimates, and discussions of various issues arising in the actual numerical implementations. A brief discussion of the assumptions used in this algorithm and various constraints is given in the final section.

Note that the development of the BRDF/Albedo algorithm is ongoing, and it will continue to be revised and refined in both pre- and postlaunch phases. This document provides a snapshot of the algorithm valid at the time of preparation of the document. Subsequent revisions will document the ongoing evolution of the algorithm and supporting studies.

Table 1: Outline of Contents of the MODIS BRDF/Albedo Product (Status: Version 1, 1996).

Param. Name	**Data Type**	**Dimensions**	**Comments**
BRDF Model Identifier	uint8	1: data rows 2: data columns 3: number of output models (2)	Identifies Ambrals BRDF model kernel combination and secondary global model used
BRDF Model Parameter	int16	1: data rows 2: data columns 3: number of output models (2) 4: number of land bands (7) 5: number of model parameters (4)	BRDF model parameters will allow reconstructing BRDF shape, white-sky albedo, and black-sky albedo at any solar zenith angle
Albedo	int16	1: data rows 2: data columns 3: number of output models (2) 4: number of land bands + 3 (10) 5: albedo type (2)	Albedo type 1 is white-sky albedo, albedo type 2 black-sky albedo at the mean sun angle of observation; 3 extra bands contain broadband albedos for 0.4–0.7, 0.7–3.0 and 0.4–3.0 μm.
Quality Control Flags	uint8	1: data rows 2: data columns 3: number of QC words (4)	Flag information on overall quality (3 bits), data base of inversion (5 bits), solar and viewing angle range available (7 bits), extra QC data (7 bits)
Inversion Information	uint16	1: data rows 2: data columns 3: number of words (6)	Lists: RMSE for the Ambrals model, RMSE of the secondary uniform model, sensitivity parameter, scattering type indicator, BRDF type indicator, TBD; the latter to be used for inferences.

1.5 LIST OF APPLICABLE DOCUMENTS AND PUBLICATIONS

The following recent publications of the BRDF/Albedo team are especially relevant to the BRDF/Albedo Product:

Abuelgasim, A. A. and A. H. Strahler, 1994, Modeling bidirectional radiance measurements collected by the Advanced Solid-State Array Spectroradiometer (ASAS) over Oregon Transect conifer forests, Remote Sens. Environ. 47:261-275.

Abuelgasim, A.A., Gopal, S. and Strahler, A.H., 1996, Retrieval of canopy structural parameters from multiangle observations using an artificial neural network, Proc. 1996 Internat. Geosci. Remote Sens. Symp., Lincoln, Neb., vol. 3, pp. 1426-1428.

Barnsley, M., Allison, D., and Lewis, P., 1995, On the Statistical Information Content of Multiple View Angle (MVA) Images. Proc. RSS 95, "Remote Sensing in Action", Southampton, UK, 11-14 Sept, 1298-1305.

Barnsley, M., Disney, M., Lewis, P., Hesley, Z., and Muller, J-P. 1996, On the intrinsic dimensionality of the BRDF: Implications for the retrieval of land surface biophysical properties. Proc. RSS 96, Durham, UK. 69-70

Barnsley, M. J., and J.-P. Muller, 1991, Measurement, simulation and analysis of bidirectional reflectance properties of earth surface material, Proc. Int. Conf. Spectral Signatures in Remote Sens., Courchevel, France, January 14-18 1991, pp. 375-382.

Barnsley, M. J., A. H. Strahler, K. P. Morris, and J.-P. Muller, 1994, Sampling the surface bidirectional reflectance distribution function (BRDF): Evaluation of current and future satellite sensors, Remote Sens. Rev. 8:271-311.

Burgess, D. W., Lewis, P., and Muller, J-P. 1995, Topographic Effects in AVHRR NDVI Data. Remote Sens. Environ, 54, 223-232.

Boissard, P., Akkal, N., Lewis, P., 1996, 3D Plant Modelling in Agronomy. Association of Applied Biologists: Modelling in Applied Biology: Spatial Aspects, 24/27 June 1996, Brunel, U.K.

Boissard, P., Akkal, N., Lewis, P., Valery, P., and Meynard, J-M., 1995, Linking a 3D Plant Model Database of Crop Structure to Models of Canopy Development. Int. Colloq. Photosynthesis and Remote Sensing, 28-31 Aug. 1995, Montpellier, Fr.

d'Entremont, R.P., Schaaf, C.B., and Strahler, A., 1996, Cloud detection and land-surface albedos using visible and near-infrared bidirectional reflectance distribution models, Proc. Amer. Met. Soc. Satellite. Met. Conf., January, 1996, Atlanta, GA, pp. 334-338.

d'Entremont, R.P., Schaaf, C.B., and Strahler, A.H., 1995, Cloud detection using visible and near-infrared bidirectional reflectance distribution models, Proc. CIDOS-95, (Cloud Impact on DOD Operations and Systems), October 24-26, 1995, Hanscom AFB, MA, pp. 87-91.

Hesley, Z., Barnsley, M., and Lewis, P., 1996, The significance of angular sampling errors of the MODIS and MISR sensors on the retrieval of surface biophysical parameters from BRDF models. Proc. RSS 96, Durham, UK. 537-542

Hesley, Z., Barnsley, M., and Lewis, P., 1995, Effect of Angular Sampling Regimes on the Retrieval of Biophysical Parameters from BRDF Models. Proc. RSS 95, "Remote Sensing in Action", Southampton, UK, 11-14 Sept, 342-349.

Hu, B., Li, X., and Strahler, A. H., 1996, Deriving the anisotropic point spread function of ASAS off-nadir images and removal of the adjacency effect, Proc. 1996 Internat. Geosci. Remote Sens. Symp., Lincoln, Neb., May 27-31, vol. 3, pp. 1587-1589.

Hu, B., Wanner, W., Li, X., and Strahler, A.H., 1996, Validation of kernel-driven semiempirical models for application to MODIS/MISR data, Proc. 1996 Internat. Geosci. Remote Sens. Symp., Lincoln, Neb., May 27-31, vol. 3, pp. 1669-1671.

Lewis, P., 1995, On the Implementation of Linear Kernel-Driven BRDF Models. Proc. RSS 95, "Remote Sensing in Action", Southampton, UK, 11-14 Sept, 333-340.

Lewis, P., 1995, The Utility of Linear Kernel-Driven BRDF Models in Global BRDF and Albedo Studies. Proc. 1995 Internat. Geosci. Remote Sens. Symp., Firenze, Italy, 1186–1188.

Lewis, P., and J.-P. Muller, 1992, The Advanced Radiometric Ray-Tracer: ARARAT for plant canopy reflectance simulation, Proc. 29th Cong. Int. Soc. Photogramm. Remote. Sens., Washington DC, pp. 26-34.

Lewis, P. and M. J. Barnsley, 1994, Influence of the sky radiance distribution on various formulations of the earth surface albedo, Proc. Sixth Int. Symp. on Physical Measurements and Signatures in Remote Sens., Val d'Isere, France, January 17-21 1994, pp. 707-715.

Lewis, P., Barnsley, M., Muller, J-P., and Sutherland, M., 1995, Deriving Spectral Albedo Maps for HAPEX-Sahel using Linear BRDF Models applied to ASAS and Landsat TM Data. Proc. 1995 Internat. Geosci. Remote Sens. Symp., Firenze, Italy, 2221–2223.

Lewis, P., and Boissard, P., 1995, A Botanical Plant Modelling System: a Model for Deriving and Describing Plant Form and Simulating the Canopy Shortwave Radiation Regime. Invited Paper (abstract only in proc.) RSS Meeting: "The Interaction of Vegetation Canopies with Radiation", Sheffield CEOS, May 24, 1995.

Li, X., and A. H. Strahler, 1986, Geometric-optical bidirectional reflectance modeling of a conifer forest canopy, IEEE Trans. Geosci. Remote Sens. 24:906-919.

Li, X. and A. H. Strahler, 1992, Geometric-optical bidirectional reflectance modeling of the discrete-crown vegetation canopy: Effect of crown shape and mutual shadowing, IEEE Trans. Geosci. Remote Sens. 30:276-292.

Li, X., A. H. Strahler, and C. E. Woodcock, 1995, A hybrid geometric optical-radiative transfer approach for modeling albedo and directional reflectance of discontinuous canopies, IEEE Trans. Geosci. Remote Sens. 33: 466-480.

Li, X., and Strahler, A., 1996, A knowledge-based inversion of physical BRDF model and three examples, Proc. 1996 Internat. Geosci. Remote Sens. Symp., Lincoln, Neb., May 27-31, vol. 4, pp. 2173-2176.

Li, X., Ni, W., Woodcock, C.E., and Strahler, A.H., 1996, A simplified hybrid model for radiation under discontinuous canopies, Proc. 1996 Internat. Geosci. Remote Sens. Symp., Lincoln, Neb., May 27-31, vol. 1, pp. 293-295.

Li, X., and, Wang, J., 1995, Canopy Reflectance Models, Inversion, and Characterization of Canopy Structure, Science Press, Beijing, 114 pp. (in Chinese).

Liang, S. and Lewis, P. 1996, A Parametric Radiative Transfer Model for Sky Radiance Distribution. J. Quant. Spectrosc. Radiat. Transfer, 55(2), 181-189.

Liang, S. and A. H. Strahler, 1993, An analytic BRDF model of canopy radiative transfer and its inversion, IEEE Trans. Geosci. Remote Sens. 31:1081-1092.

Liang, S. and A. H. Strahler, 1993, Calculation of the angular radiance distribution for a coupled system of atmosphere and canopy media using an improved Gauss-Seidel algorithm, IEEE Trans. Geosci. Remote Sens. 31:491-502.

Liang, S. and A. H. Strahler, 1994, Retrieval of surface BRDF from multiangle remotely sensed data, Remote Sens. Environ. 50:18-30.

Liang, S. and A. H. Strahler, 1995, An analytic radiative transfer model for a coupled atmosphere and leaf canopy, J. Geophys. Res. 100:5085-5094.

Liang, S., and A. H. Strahler, 1993, An analytic BRDF model of canopy radiative transfer and its inversion, IEEE Trans. Geosci. Remote Sens. 31:1081-1092.

Liang, S., and A. H. Strahler, 1993, Retrieval of surface BRDF from multiangle remotely sensed data, Remote Sens. Environ. 50:18-30.

Liang, S., and A. H. Strahler, 1994, A four-stream solution for atmospheric radiance transfer over a non-Lambertian surface, Appl. Optics 33:5745-5753.

Newton, A., J.-P. Muller, and J. C. Pearson, 1991, SPOT-DEM shading and its application to automated correction of topographic and atmospheric effects, Proc. Int. Geosci. Remote Sens. Symp., Espoo, Finland, June 3-6 1991, pp. 655- 659.

Ni, W., Li, X., Woodcock, C.E., Roujean, J.-L., Davis, R., and Strahler, A.H., 1996, Modeling solar radiation transmission in boreal conifer forests, Proc. 1996 Internat. Geosci. Remote Sens. Symp., Lincoln, Neb., May 27-31, vol. 1, pp. 591-593.

Running, S., C. Justice, D. Hall, A. Huete, Y. Kaufman, J-P. Muller, A. Strahler, V. Vanderbilt, Z-M. Wan, P. Teillet and D. Carnegie, 1994, Terrestrial remote sensing science and algorithms planned for EOS/MODIS, Int. J. Remote Sens. 15:3587-3620.

Schaaf, C. B. and A. H. Strahler, 1993, Solar zenith angle effects on forest canopy hemispherical reflectances calculated with a geometric-optical bidirectional reflectance model, IEEE Trans. Geosci. Remote Sens. 31:921- 927.

Schaaf, C. B. and A. H. Strahler, 1994, Validation of bidirectional and hemispherical reflectances from a geometric-optical model using ASAS imagery and pyranometer measurements of a spruce forest, Remote Sens. Environ. 49:138-144.

Schaaf, C. B., X. Li and A. H. Strahler, 1994, Topographic effects of bidirectional and hemispherical reflectances calculated with a geometric-optical canopy model, IEEE Trans. Geosci. Remote Sens. 32:1186-1193.

Soffer, R., Miller, J., Wanner, W., and Strahler, A.H., 1995, Winter boreal forest canopy BRF results: Comparisons between airborne data, laboratory simulations and geometrical-optical model data, Proc. 1995 Internat. Geosci. Remote Sens. Symp., Florence, Italy, July 10-14, 1995, vol 1., pp. 800-802.

Sutherland, M., Barnsley, M., Lewis, P., and Muller, J-P., 1995, Derivation of Surface Biophysical Parameters through Inversion of a BRDF Model for HAPEX-Sahel. Proc. RSS 95, "Remote Sensing in Action", Southampton, UK, 11-14 Sept, 325-332.

Strahler, A.H., Wanner, W., Zhu, Q., and Jin. X., 1995, Bidirectional reflectance modeling of data from vegetation obtained in the Changchun solar simulation laboratory, Proc. 1995 Internat. Geosci. Remote Sens. Symp., Florence, Italy, July 10-14, 1995, vol. 3, pp. 1965-1967.

Strahler, A.H., 1996, An overview of MODIS products for land applications, Proc. 8th Australasian Remote Sens. Conf., Canberra, Australia, March 25-29, CD-ROM, 8 pp.

Strahler, A.H., 1996, AVHRR applications in support of MODIS product development, Proc. 8th Australasian Remote Sens. Conf., Canberra, Australia, March 25-29, CD-ROM, 4 pp.

Wang, J., Li, X., Strahler, A., 1995, Tree tomography-an indirect method for measuring crown structure, Proc. of GeoInfomatics'95, Hongkong, vol. 1, pp. 371-378.

Wanner, W., Li, X. Strahler, A.H., 1995, A new class of geometric-optical semiempirical kernels for global BRDF and albedo modeling, Proc. 1995 Internat. Geosci. Remote Sens. Symp., Florence, Italy, July 10-14, 1995, vol. 1, pp. 15-17.

Wanner, W., Strahler, A.H., Muller, J.P., Barnsley, M., Lewis, P., Li, X., and Schaaf, C.B., 1995, Global mapping of bidirectional reflectance and albedo for the EOS MODIS project: The algorithm and the product, Proc. 1995 Internat. Geosci. Remote Sens. Symp., Florence, Italy, July 10-14, 1995, vol. 1, pp. 525-529.

Wanner, W., Strahler, A., Zhang, B., and Lewis, P., 1996, Kilometer-scale global albedo from MODIS, Proc. 1996 Internat. Geosci. Remote Sens. Symp., Lincoln, Neb., May 27-31, vol. 3, pp. 1405-1407.

Wanner, W., X. Li and Strahler, A., 1995, On the derivation of kernels for kernel-driven models of bidirectional reflectance, J. Geophys. Res., vol. 100, pp. 21077-21089.

Wanner, W., J.-L., Lewis, P., and Roujean, J.-L., 1996, The influence of directional sampling on bidirectional reflectance and albedo retrieval using kernel-driven models, Proc. 1996 Internat. Geosci. Remote Sens. Symp., Lincoln, Neb., May 27-31, vol. 3, pp. 1408-1410.

White, H.P., Miller, J.R., Soffer, R., and Wanner, W., 1996, Semiempirical modelling of bidirectional reflectance utilizing the MODIS BRDF/Albedo models, Proc. 1996 Internat. Geosci. Remote Sens. Symp., Lincoln, Neb., May 27-31, vol. 3, pp. 1411-1413.

2 OVERVIEW AND BACKGROUND INFORMATION

2.1 INTRODUCTION

The BRDF of a surface describes the scattering of incident light from one direction in the hemisphere into another direction in the hemisphere. It will generally vary as a function of wavelength. That is,

$$f_r(\theta_i, \phi_i; \theta_v, \phi_v; \Lambda) = \frac{dL_v(\theta_i, \phi_i; \theta_v, \phi_v; E_i; \Lambda)}{dE(\theta_i, \phi_i; \Lambda)}, \quad (1)$$

where $f_r(\theta_i, \phi_i; \theta_v, \phi_v; \Lambda)$ in units of sr^{-1} is the BRDF in waveband Λ; $\theta_i, \phi_i; \theta_v, \phi_v$ are zenith and azimuth angles of the direction of irradiance and viewing, respectively; $E(\theta_i, \phi_i; \Lambda)$ is the parallel-beam irradiance from the illumination direction in waveband Λ; and $L_v(\theta_i, \phi_i; \theta_v, \phi_v; E_i; \Lambda)$ is the radiance in the view direction in waveband Λ under the conditions of illumination (Nicodemus *et al.*, 1977).

In this document, we will define the BRDF as $\rho = \pi f_r$, so that the BRDF is directly comparable with the bidirectional surface reflectance values and hemispherical-directional reflectance factors that the BRDF/Albedo algorithm receives as inputs from other MODIS and MISR products. We will further use the notation ρ to refer to true, parametric values of the BRDF; R to refer to modeled values of ρ; and ρ' to refer to observations of BRDF, normally obtained from top-of-atmosphere radiances as corrected for atmospheric effects and surface BRDF. We will also assume the BRDF to be symmetric with respect to the principal plane of the illumination direction, and thus expressed as a function of θ_i, θ_v, ϕ, where ϕ is the relative azimuth between illumination and view directions, *i.e.* $\phi = |\phi_v - \phi_i|$,

The BRDFs of land covers are known to show peaks in the function in the backward–scattering direction of the principal plane, due to shadow hiding (*e.g.*, Li and Strahler, 1986). This position in the viewing hemisphere is known as the hotspot (Gerstl and Zardecki, 1985a, b), and its shape is characteristic of the shape and density of surface projections (*e.g.*, plant crowns) or scattering elements (*e.g.*, leaves) of the cover type (Jupp and Strahler, 1993). For some covers, notably water or wetlands, there will also be a forward-scattering specular peak in the function.

The spectral albedo of a surface is a dimensionless ratio of the radiant energy scattered away from the surface to that received by the surface at a particular waveband. That is,

$$\alpha(\Lambda) = \frac{E_\uparrow(\Lambda)}{E_\downarrow(\Lambda)} = \frac{\int_0^{2\pi}\int_0^{\pi/2} L_\uparrow(\theta_v, \phi_v; \Lambda)\sin\theta_v\cos\theta_v\, d\theta_v\, d\phi_v}{\int_0^{2\pi}\int_0^{\pi/2} L_\downarrow(\theta_i, \phi_i; \Lambda)\sin\theta_i\cos\theta_i\, d\theta_i\, d\phi_i}, \quad (2)$$

where $\alpha(\Lambda)$ is the spectral albedo in waveband Λ; $E_\uparrow(\Lambda)$ is the upwelling radiant energy flux from the surface in waveband Λ; $E_\downarrow(\Lambda)$ is the downwelling radiant energy flux in waveband Λ; $L_\uparrow(\theta_v, \phi_v; \Lambda)$ is the upwelling radiance in direction θ_v, ϕ_v in waveband Λ; and $L_\downarrow(\theta_i, \phi_i; \Lambda)$ is the downwelling radiance in direction θ_i, ϕ_i in waveband Λ. Note that the downwelling energy flux includes both the solar beam and the diffuse irradiance that is scattered downward by the atmosphere. Albedo is normally measured by paired instruments with hemispherical fields of view that integrate upwelling and downwelling radiance.

Because upwelling radiance depends on both the angular distribution of downwelling irradiance as well as the surface BRDF, surface albedo is dependent on the atmospheric state. It can change within minutes

as clouds come and go, or within hours as an air mass with different optical properties invades the region. Albedo will further change over the course of the day with the sun's path in the sky, even for constant atmospheric and surface conditions.

Rather than depending in this way on the state of the atmosphere, the albedo measures provided by the MODIS/MISR BRDF/Albedo product are purely properties of the surface. Two measures are provided. The first is directional–hemispherical reflectance ρ_b, a measure that integrates the BRDF over the exitance hemisphere for a single irradiance direction, which is normally the position of the sun in the sky at a time of interest. That is,

$$\rho_b(\theta_i;\Lambda) = \frac{2}{\pi}\int_0^{\pi}\int_0^{\pi/2} \rho(\theta_i,\theta_v,\phi;\Lambda)\sin\theta_v\cos\theta_v\, d\theta_v\, d\phi, \tag{3}$$

where $\rho(\theta_i,\theta_v,\phi;\Lambda)$ is the BRDF in waveband Λ. Because the measure is not integrated over the sky hemisphere for illumination directions, we refer to it as the "black-sky" albedo.

The second albedo measure is bihemispherical reflectance ρ_w, which is the double integral in waveband Λ of the BRDF over all viewing and irradiance positions. That is,

$$\rho_w(\Lambda) = 2\int_0^{\pi/2} \rho_b(\theta_i;\Lambda)\,\sin\theta_i\cos\theta_i\, d\theta_i. \tag{4}$$

Since this integral weights all irradiance positions equally, it provides the albedo under conditions of perfectly diffuse illumination. Thus, we term it the "white-sky" albedo. Black-sky and white-sky albedos are provided for each of the MODIS land bands as well as three broad bands covering the wavelength intervals 0.4–0.7 μm, 0.7–3.0 μm, and 0.4–3.0 μm. Broadband values are obtained by combining narrow-band measurements weighted by standardized solar spectral irradiance functions.

2.2 MODELING OVERVIEW

In modeling the BRDF of a surface, two contrasting approaches are possible — physical and empirical. In the empirical approach, a function (*e.g.*, a set of spherical harmonics) is fitted that describes the shape of the BRDF based on the observations at hand. That is, the BRDF is modeled as an empirical function of viewing and illumination angles and azimuths in the hemisphere. For accurate fitting, this approach requires many observations at numerous combinations of viewing and illumination positions. Although simple and direct, the method is not very practical for remote-sensing applications because the number of angular observations of a surface typically acquired by a single remote sensing instrument will usually be small. Furthermore, the coefficients that fit empirical models cannot be readily interpreted in terms of scene or surface properties. Instead, relationships must be obtained by further empirical studies, such as through correlation analyses.

In the physical approach, a scattering model is constructed that explains anisotropic surface scattering using physical principles. By inversion, reflectance observations are used to infer the physical parameters that drive the model. Once these are known, the BRDF may be determined for any view or illumination position without recourse to further measurements. Moreover, the parameters typically have physical interpretations in their own right that are of intrinsic interest beyond simply generating the BRDF. Note that

these parameters may vary among different physical models. A disadvantage of the physical approach is that a large number of parameters (perhaps 6 to 12) may be required to drive the model. Further, numerical inversion is normally required, which is computationally very intensive and not always robust.

A third approach, which we may term "semiempirical," combines physical and empirical approaches. Here, the BRDF is modeled as a weighted sum of a few (typically two or three) trigonometric functions of view zenith, illumination zenith, and relative azimuth angles that describe the shape of the BRDF. However, these functions are derived from physical approximations, and so have some physical meaning. The weight given to each function is determined empirically by fit to the observations. Thus, it is the weights of the physically-based functions that are retrieved, not a set of physical parameters governing the surface scattering.

The MODIS/MISR BRDF/Albedo product utilizes this hybrid approach, fitting a suite of semiempirical models to each set of angular observations. Each model typically consists of three components: a volume-scattering function, a geometric surface-scattering function, and a constant (*i.e.*, an isotropically-scattering function). The functions are referred to as "kernels" — hence, the corresponding semiempirical models may be called "kernel-driven." For the current work we employ two choices of volume-scattering kernels and two choices of geometric surface-scattering kernels developed for this project. We also exercise the modified Walthall model (Walthall *et al.*, 1985; Nilson and Kuusk, 1989) which supplies a purely empirical fit for each pixel on the globe. Although this model rarely provides the best fit, it is a simple and consistent expression and has been widely applied. (Further details are provided in Section 3.1) Semiempirical models also have the advantage of being very rapidly invertible, due to their linear nature. Furthermore, albedo calculations are greatly simplified since the kernels need to be integrated only once, before operational processing begins. Section 2.5 summarizes the historical development of physical, empirical, and semiempirical models in the literature.

In the fitting of surface BRDF models using top-of-atmosphere observations, a problem arises from the interaction between the anisotropic surface scattering and atmospheric scattering. In general, the effect of atmospheric scattering on surface BRDF retrieval will tend to damp the BRDF, making it appear more isotropic. Surface reflectance, when retrieved assuming an isotropic surface, will be underestimated in the bright parts of the BRDF and overestimated in the dark parts. Thus, surface BRDF is required to estimate bidirectional surface reflectance accurately, while BRDF fitting requires accurate surface bidirectional reflectances. In other words, some form of surface-atmosphere coupling is needed. To provide this coupling in deriving the BRDF/Albedo Product, atmospheric parameters are archived with each surface reflectance measurement, and a looping iteration is carried out in which (1) a surface BRDF is fitted to initial estimates of surface reflectances; (2) surface reflectances are rederived using this BRDF and the atmospheric parameters associated with each initial reflectance; and (3) a new and final BRDF is then fitted. More details are provided in Section 3.2.4.

2.3 EOS CONTEXT

The algorithm we describe in this document is targeted specifically to the remote sensing scenario presented by the EOS-AM and -PM platforms, which will place three instruments in polar orbits that can be used for BRDF/Albedo retrieval. Two of these will be MODIS instruments. A MODIS will orbit on each of the AM and PM platforms, with nominal equatorial crossing times of 10:30 and 13:30, respectively. By virtue of its wide scan ($\pm 55°$), MODIS images the earth on a two-day repeat cycle, with a one-day or more frequent repeat at higher latitudes greater than 30° due to orbital convergence. Thus, the same point on the ground will be potentially visible to MODIS from a number of different illumination and viewing positions in the hemisphere during the span of a few days. The third instrument, MISR (Multiangle Imaging SpectroRadiometer), will fly on the EOS-AM platform. MISR has a unique design that allows it to image the same point on the ground from nine along-track angles (Diner *et al.*, 1989). However, its across-track field of view is more restricted than that of MODIS, providing a 9-day one-look repeat cycle for global coverage as well as a 16-day two-look cycle. Relevant characteristics of the MODIS and MISR instruments for the inference of BRDF and albedo measures are discussed more fully in Section 2.6.

For calibration and validation of the BRDF/Albedo product in the post-launch time frame, CERES data will also prove useful. This instrument measures top-of-atmosphere and surface radiation flux in short- and longwave regions. It has a much larger field of view than either MODIS or MISR — 21 km at nadir — so that albedo can be validated only for broad regions. However, CERES will be very helpful in developing and maintaining the narrow-to-broadband spectral calibration that we will use to generalize short- and longwave albedos from MODIS and MISR sensors. Geostationary data from the GOES-NEXT and METEOSAT series of instruments may also prove useful for validating BRDF, in that multiangle measurements of radiance from a single point are acquired in the course of a single day. Postlaunch validation is discussed more fully in Section 3.3.4.3.

Another satellite instrument that will prove useful is POLDER (Polarization and Directionality of the Earth's Reflectances), a push–broom, wide–field, multiband imaging radiometer/polarimeter. Relying on an area detector array and a rotating filter wheel, POLDER is much like a framing camera that acquires overlapping images along the satellite ground track. Data are acquired in eight bands, of which three are designed for land imaging, centered at 443, 665, and 865 nm. The ADEOS satellite on which POLDER is mounted was successfully launched at 10.53 a.m. (JST) / 01:53 a.m. (UT) on August 17, 1996 from the Tanegashima Space Centre in Japan. ADEOS orbits the Earth in a height of about 800 km with an inclination of 98.6° in 100.8 minutes; it has a 10:41 a.m. local time descending node and a recurrence cycle of 41 days.

The initial check-out for POLDER was performed on September 16th and 26th, 1996 and indicated that POLDER was functioning normally. As a result, POLDER began routine observation of the Earth at the beginning of October 1996. Although the ground resolution cell size of 7km by 6km is considerably coarser than those of MODIS and MISR, POLDER data will be invaluable in testing the BRDF/Albedo algorithm.

Of our BRDF/Albedo team, two researchers are also members of the POLDER Science Team: M. J. Barnsley and X. Li. Acquisition of POLDER data in direct support of our MODIS effort is an objective of both of their work plans, and thus POLDER data will be available for the validation of the BRDF/Albedo algorithm shortly after launch (See Section 3.3.4).

2.4 EXPERIMENTAL OBJECTIVE

There are several applications envisioned for the BRDF products. First is an internal application in the MODIS Surface Reflectance Product. Accurate retrieval of Level 2 surface reflectance (MOD09, Parameter 2015) is dependent on knowledge of the surface BRDF. At launch, this parameter will initially assume an isotropic lower bound in reflectance retrieval, but will utilize the most recent BRDF as soon as possible in the postlaunch period (Vermote *et al.*, 1997).

The error in extracting surface reflectance assuming an isotropic lower boundary is significant, ranging from 5–15 percent or beyond, depending on the waveband and atmospheric turbidity (see Section 3.2.4).

Secondly, BRDF products are useful to normalize image pixels with respect to variations in solar illumination directions and viewing direction. Pixel values from different parts of a scan from wide field-of-view remote sensors, such as MODIS, will vary significantly depending on viewing position. For imagery obtained on different dates and/or at different times, and even within different parts of a single scan at high latitudes, solar illumination angles will change. Thus, multitemporal images or even pixels in the same image are not directly comparable without correction of angular effects. Detailed knowledge of surface BRDF, as well as the state of the atmosphere, is a prerequisite for such corrections. Within the MODIS processing sequence, the MODIS land cover product (MOD13) will utilize surface reflectance data adjusted for BRDF effects.

Thirdly, the BRDF/Albedo product will be directly and immediately useful for global climatic modeling. Land surface albedo is a key parameter for climate and ecosystem studies because of its role in the surface energy balance. More accurate and reliable estimates of earth surface albedo can only be obtained through algorithms that utilize the BRDF. Furthermore, future global climate modeling will need to turn to distributed-parameter BRDF databases for accurate modeling of surface–atmosphere boundary layer energy interactions. The semiempirical models and associated parameters of the BRDF product are directly ingestible for climate modeling work. Note that at present, global climate models are typically exercised at much coarser resolutions than 1-km. However, the linear semiempirical models used in the BRDF/Albedo product can be aggregated simply and easily to coarser resolutions as desired.

Fourthly, because the semiempirical models have a physical basis in their included kernels, the inference of physical parameters may be possible from the weights they receive in fitting to a particular ground reflectance pattern. For example, the weights of the volume scattering kernels include parameters of leaf area index (LAI), leaf reflectance–transmittance, and ground reflectance. (See Section 3.1.2, Table 4.) With some educated guesses about the leaf reflectance-transmittance and ground reflectance, the LAI is potentially retrievable from the directional signal alone. Note also that a structural parameter like LAI remains constant

across wavebands, providing an additional constraint that bridges the wavelength domain. Model selection may also provide a mechanism for physical inference. For example, consistent selection of the Li-sparse kernel for tall, prolate crowns could indicate sparse forest and provide for an inference of surface roughness. These options will be explored in post-launch research phases.

Lastly, BRDF parameters may be displayed over large areas as a way of mapping surface attributes (see Section 3.1.4.2 and Appendix J). Maps of kernel weights could be related to plant community composition on the broad scale, as in shrubland-woodland-savanna-forest gradients. In this situation, the mapping of these parameters would be analogous to the mapping of the Normalized Difference Vegetation Index (NDVI), which is an empirical measure with a strong intrinsic physical meaning that has proven very useful for global biophysical studies. Moreover, human activity is one of the primary influences affecting surface albedo. In fact, land-surface spectral albedo is one of the strongest signals of change to the land surface caused by human activity. Global albedo maps thus could be important inputs to global studies of human impact on the environment.

2.5 HISTORICAL PERSPECTIVE

The development of models describing bidirectional surface reflectance has been an active field within remote sensing in recent years. Physically-based BRDF models include radiative-transfer models, geometric-optical models, hybrid models and computer-simulation models (Goel, 1987, 1989; Strahler, 1994). Radiative transfer models normally treat the terrestrial surface as a plane-parallel layer in which soil or canopy elements are assumed to be small absorbing and scattering particles. Radiative transfer theory is then used to account for the angular characteristics of the radiation field. Geometric-optical models typically assume that the scattering surface consists of a set of geometric objects or protrusions of prescribed shapes and dimensions (cylinders, cones, spheres, spheroids, etc.) placed on the ground in a defined manner. They are driven by shadowing effects, which are a function of both the surface and the positions of viewing and illumination in the hemisphere. Hybrid models combine elements of both geometric-optical and radiative transfer models. These may range from the simple (Verstraete *et al.*, 1990; Iaquinta and Pinty, 1994) to the complex (Li *et al.*, 1994). Computer-simulation models predict radiation field characteristics by simulating photon trajectories and histories. Typically, these make use of Monte Carlo ray-tracing or radiosity techniques (Goel and Rozehnal, 1992; Borel *et al.*, 1991;. Lewis and Muller, 1992; Boissard *et al.*, 1996). For more thorough reviews of BRDF models, see Goel (1987) or Myneni *et al.* (1990). Note that the physical models developed thus far are each specific to a limited range of land surface types (*e.g.*, soil, sparse or dense vegetation, complex terrain). There is no universal physical model for all surface types. Empirical models are less well developed. The Walthall model (Walthall *et al.*, 1985) as modified by Nilson and Kuusk (1989) has been applied fairly widely. It is a four-parameter, second-order polynomial of view zenith, illumination zenith and relative azimuth. In shape, it lacks a hotspot. Barnsley and Muller (1991) fitted spherical harmonics to directional reflectances, and noted that the most important harmonics also appear in the Walthall model.

Semiempirical models are a recent development. The model of Roujean *et al.* (1992) provided the pattern for the semiempirical models used in the BRDF/Albedo algorithm — weighted sum of a volume-scattering kernel and a surface-scattering kernel, with a constant (see Section 3.1.2). It was successfully exercised in an AVHRR application (Leroy and Roujean, 1994) as a way of removing BRDF effects from NDVI. Wu, Li and Cihlar of the Canada Centre for Remote Sensing have also applied the Roujean model successfully to describe the anisotropy of top-of-the-atmosphere radiances in an AVHRR application (1995). However, the Roujean model does not fit all surface BRDFs well. The complex shadowing of a forest, for example, causes difficulties (Roujean *et al.*, 1992).

A semiempirical model of a different type was recently provided by Rahman *et al.* (1993a,b). This model calculates surface reflectance as a product of three functions: a modified Minnaert function (1941); a one-parameter Henyey-Greenstein function (1941); and a hotspot function based on the model of Pinty *et al.* (1990). Three parameters are used to drive the functions. Although none of the functions are derived directly from physical theory, they are known to fit directional scattering well in a number of real applications. In a form modified by Martonchik (Engelsen *et al.*, 1996) this model is being used to generate the BRDF for the MISR Surface Product(Diner *et al.*, 1996; Martonchik, 1997).

The semiempirical Ambrals model that we apply here (see Section 3.1.1) overcome the limitations of these predecessors. The Li-kernels are used for geometric surface scattering and therefore the complex shadowing of forest canopies are fit well. The Ross-kernels are used to fit the volume scattering cases. Furthermore, our combination of models are easily invertible by inversion of 3-by-3 or 4-by-4 matrices.

2.6 INSTRUMENT CHARACTERISTICS OF MODIS AND MISR

2.6.1 Spectral Characteristics

MODIS will provide comprehensive and frequent global earth imaging in 36 spectral wavebands and at several different spatial resolutions (nominally 250 m, 500 m and 1 km, dependent on the waveband). The swath width of MODIS is 2300 km, subtending an angle of 110° across-track field-of-view (*i.e.* ±55°, or about ±61° at the surface). Consequently, it will be capable of acquiring multiangle measurements of angular reflectance for a fixed field site by virtue of overlap between images obtained on separate orbital overpasses. MISR is the only EOS instrument designed to provide multiangle, continuous coverage of the earth with high spatial resolution. It uses nine separate charged-coupled device (CCD) pushbroom cameras to observe the earth at nine discrete view angles in four spectral bands. Note that MISR images along-track, while MODIS images in the cross-track direction. The approach in the BRDF/Albedo algorithm is to combine the views of these two instruments during a fixed time period to provide the best product.

Nominal spectral characteristics of the two instruments are shown in the Table 2 below. Both instruments utilize narrow bandwidths, ranging from 15–35 nm for MISR and 10–50 nm for MODIS. For MODIS, only bands 1–7 (land bands) are shown. Note that MODIS bands 4 and 2 substantially overlap MISR bands 2 and 4, respectively; for the purposes of the BRDF/Albedo product, we will regard these band pairs as identical.

Table 2: MODIS and MISR spectral bands (nominal), arranged by wavelength, in nm (Band numbers shown in parentheses).

Instrument	Spectral Band						
MODIS	(3)	(4)	(1)	(2)	(5)	(6)	(7)
	459–479	545–565	620–670	841–876	1230–1250	1628–1652	2105–2155
MISR	(1)	(2)	(3)	(4)			
	423–458	543–558	663–678	853–878			

MODIS band 1 and MISR band 3 overlap less substantially, but we will also consider them equivalent. MODIS band 3 and MISR band 1 are more problematic. They are 20 and 35 nm wide respectively, are separated by 1 nm, and span a range of 56 nm. In this wavelength range, the vegetation spectrum is fairly flat (Deering, 1989); however, mineral soil spectra show a slow increase across the region. This could provide a source of error when, by chance, significantly more measurements were available from one instrument than the other. Quantitative estimates of the spectral reflectance of typical vegetation-soil mixtures within these two nearby bands will be the topic of further study. However, until such studies are completed, we will regard the two bands as spectrally identical.

A further consideration is that MISR data are not available for wavelengths longer than near-infrared. Thus, BRDF/Albedo inference in MODIS bands 5–7 will of necessity be based only on MODIS measurements. However, the BRDF/Albedo algorithm performs model selection based on the goodness-of-fit of measurements to Bands 1–4 only. This means that the BRDF is constrained in Bands 5–7 to follow the general shape of the BRDF that best fits Bands 1–4. Since the models identify physical scattering mechanisms that are largely dependent on surface structural characteristics, which are in turn largely independent of wavelength, we do not anticipate overly large errors in fitting BRDF and albedo measures in these wavebands (see also Section 3.2.1.4).

2.6.2 Directional Sampling

Taken together, MISR and MODIS have the potential to sample the viewing hemisphere at any location quite well. MISR's nine cameras image with an operational swath width of 364 km, providing a repeat cycle of nine days at the equator, converging to two days near the poles. Due to the nature of the EOS-AM platform orbit, the global repeat time for double MISR coverage is 16 days. In contrast, the MODIS ground swath of 2300 km provides a two-day global repeat cycle, with a one-day cycle beginning at latitudes greater than about 30°.

Angular imaging characteristics of MISR are provided in Table 3. Cameras are lettered A to D in order of increasing focal length and view zenith angle, and further distinguished by the notation "n" for nadir, "a" for aft-pointing, and "f" for forward-pointing.

Table 3: Characteristics of MISR directional imaging.

	MISR Camera				
Instrument characteristic	An	Af, Aa	Bf, Ba	Cf, Ca	Df, Da
Platform view angle	±0.0°	±23.3°	±40.0°	±51.2°	±58.0°
Earth view angle	±0.0°	±26.1°	±45.6°	±60.0°	±70.5°
Crosstrack IFOV and sample spacing	250 m	275 m	275 m	275 m	275 m
Downtrack sample spacing	275 m	275 m	275 m	275 m	275 m
Downtrack IFOV length	214 m	*	*	*	707 m
Footprint area ratio to Af/Aa cameras in 1.1-km resolution mode	*	1.00	1.06	1.11	1.17

*: Data not available

For the production frequency of the BRDF/Albedo product, we have chosen the MISR two-look cycle repeat time of 16 days. During the sixteen days, the maximum number of looks possible with both MODIS and MISR on the AM platform will range from 31 at the equator to about 65 at 60° latitude (using equinox values), and even increasing beyond. Figure 1 provides plots showing the angular coverage of MODIS and MISR at a range of latitudes during a 16-day period centered around the equinox. By and large, the viewing hemisphere is sampled in two directions that are roughly orthogonal, corresponding to across-track sampling by MODIS and along-track sampling by MISR. These sampling axes rotate with latitude. Note also that orbital convergence with increasing latitude increases the sampling frequency and the range of solar zenith and relative azimuth angles for which data are acquired.

Both the hotspot peak, which can occur in the backward-scattering direction of the BRDF, and the specular peak, which can occur in the forward scattering direction, lie in the principal plane of the sun (shown in Figure 1 as the 0°–180° axis). The EOS-AM platform's sun-synchronous orbit constrains the relative azimuth of MODIS and MISR observations as a function of latitude, and it is not possible to sample close to the principal plane at all locations. Good principal-plane coverage will be obtained by MISR in southern latitudes in the range of 40°–60°. Beyond these latitudes, rotation of the along-track sensing plane with respect to the sun moves the sensing plane as much as 30° away from the principal plane. Note that although these conditions are not ideal for sensing forward- and backward-scattering peaks, the physically-derived kernels of the semiempirical Ambrals model constrain BRDF shapes to include these features. Thus, the BRDF/Albedo algorithm tends to mitigate this problem. Consider also that atmospheric scattering typically contributes significantly to top-of-atmosphere forward- and backward-scattering peaks (Gerstl and Zardecki, 1985a, 1985b), making derivation of surface reflectance at these geometries problematic. The sensitivity of BRDF fitting and albedo extraction as influenced by sampling constraints is described in more detail in Section 3.3.2.1.

Cloud cover will also restrict angular sampling for the BRDF/Albedo product during the 16-day com-

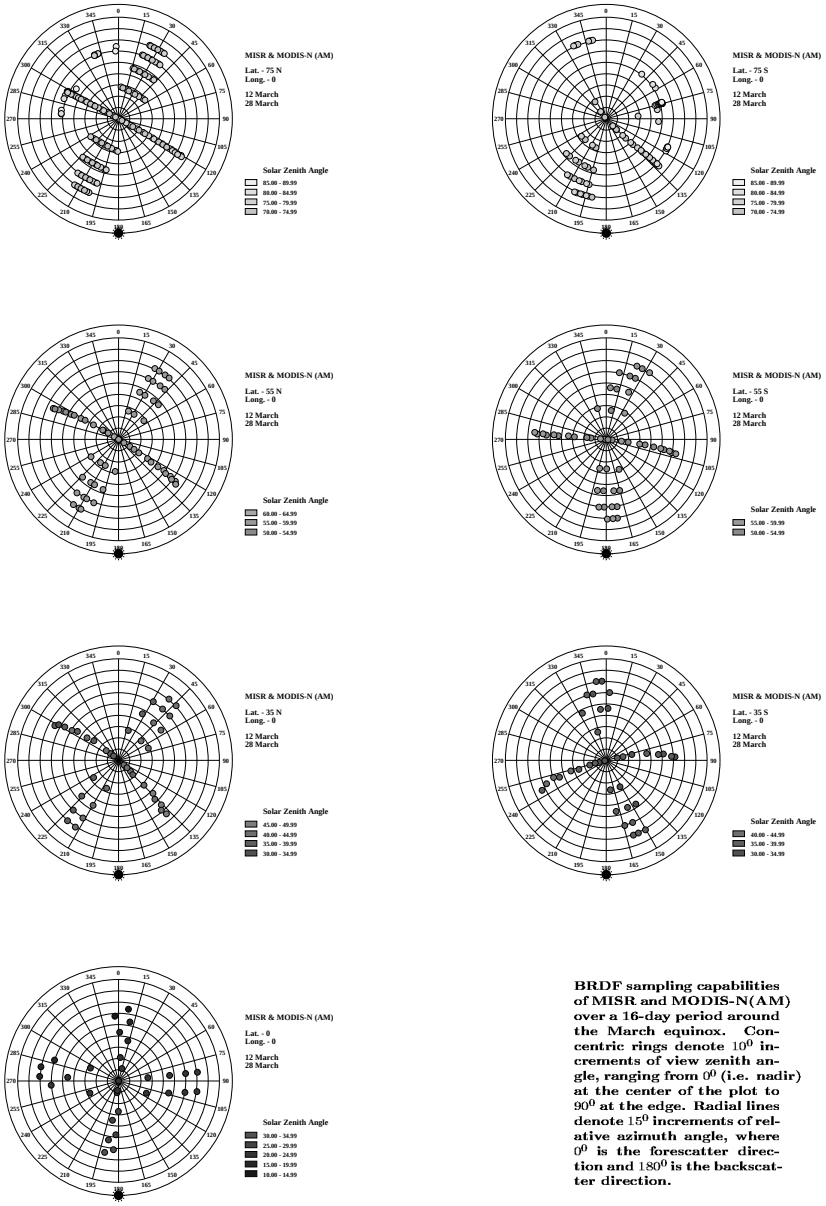

Figure 1: Sampling of the viewing hemisphere by MODIS and MISR during a 16-day period. Seven latitudes are shown for equinox conditions.

positing period. Cloud cover is discussed further in Section 3.3.2.1 and Appendix B. The minimum number of looks required for fitting a semiempirical model will depend on the exact distribution of view and azimuth angles with respect to the principal plane, but can be taken roughly as 8. If a sufficient number of looks is not available, information from supporting ancillary databases (previous BRDF/albedo product, land cover type, and an ancillary global BRDF database that will be built as our knowledge grows) will be used to limit or, if unavoidable, replace the inversion. Note that for some areas of the earth's land surface where cloud cover is persistent, BRDF/Albedo retrieval may be infrequent.

2.6.3 Spatial Resolution

MODIS and MISR data have differing spatial resolutions. MISR provides a switchable resolution that includes 275 m, 550 m, 1.1 km, and 2.2 km (250 m, 500 m, 1 km, 2 km for nadir camera), by combining outputs of detectors in its linear arrays. However, since each of MISRs nine cameras image the ground separately, their images must be registered after acquisition. Also, the individual bands acquired by each camera require registration. Considering these factors, the MISR team plans to produce its global land products at 1.1 km resolution in Space Oblique Mercator (SOM) projection. The resampling will also include terrain relief correction for those areas with gentle slopes. Input to the BRDF/Albedo algorithm will be Level 2 surface reflectance values produced at 1.1 km on the SOM grid.

The spatial resolution of the MODIS land bands varies by band. Red and infrared bands (1 and 2) are sensed at 250-m resolution, while the remaining five bands (3–7) are acquired at 500 meters. These spatial resolutions are nominal values at nadir. At off-nadir angles, the ground projection of the detector's field of view increases by a factor of about 2 in the along-track direction and 5 in the across-track direction to the scan limit of $\pm 55°$. From the viewpoint of BRDF retrieval, the far off-nadir looks are most useful even though they are imaged at a larger effective pixel size. A further complicating factor is that the instrument's across-track 10-pixel scanning swath width increases with angle so that successive scans overlap (the "bow-tie effect"). In fact, each ground location will be imaged twice at the far edge of the scan, appearing in two successive scans.

The change in footprint with scan angle for MODIS will have the effect of smoothing the fitted BRDF spatially, inducing an amount of spatial autocorrelation in the product. However, the MISR footprint, by virtue of the separate focal length of each camera, the readout rate, and averaging method used for 1.1 km resolution, increases only by 17 percent from nadir to D-camera imaging at 70° earth view zenith angle (see Table 3). Thus, relatively few of the actual MODIS and MISR observations assembled in a 16-day period will suffer from excessive pixel size.

Because the BRDF/Albedo is obtained from a set of measurements accumulated over a 16-day period, Level 2 MODIS/MISR data must be gridded to Level 2G (based on the ISSCP sinusoidal grid) and binned together before the Level 3 BRDF/Albedo product can be made.

3 ALGORITHM DESCRIPTION

3.1 THEORETICAL DESCRIPTION

Kernel-driven models for the bidirectional reflectance distribution function of vegetated land surfaces attempt to describe the BRDF as a linear superposition of a set of kernels that describe basic BRDF shapes, with the coefficients or weights chosen to adapt the sum of the kernels to the given case. Typically, semiempirical kernels are based either on one of several possible approximations to a radiative transfer scenario of light scattering in a horizontally homogeneous plant canopy (*e.g.*, a crop canopy), or on one of several approximations feasible in a geometric-optical model of light scattering from a surface covered with vertical projections that cast shadows (*e.g.*, a forest canopy). Deriving a kernel of this nature requires simplifying and manipulating a physical model for the BRDF until it reaches the form

$$R = c_1 k + c_2, \tag{5}$$

in which k is a function only of view and illumination geometry, c_1 and c_2 are constants containing physical parameters, and R is the modeled value of the true BRDF, ρ.

The following discussion presents each of the kernels used in the BRDF/Albedo algorithm. The algorithm that was developed for MODIS BRDF/Albedo Product is now known as "Ambrals" (Algorithm for MODIS bidirectional reflectance anisotropies of the land surface), and the kernels applied jointly as the Ambrals BRDF model. For more complete information on the theory and derivation of the kernels encompassed in this algorithm, see Wanner *et al.* (1995, 1997).

3.1.1 Kernels

The Ross kernels are derived from a formula presented by Ross (1981) for the directional reflectance above a horizontally homogeneous plant canopy calculated from radiative transfer theory in a single scattering approximation. The Ross-thick kernel was derived and described by Roujean *et al.* (1992). It is based on an approximation for large LAI values:

$$k_{thick} = \frac{(\pi/2 - \xi)\cos\xi + \sin\xi}{\cos\theta_i + \cos\theta_v} - \frac{\pi}{4}, \tag{6}$$

$$c_1 = \frac{4s}{3\pi}\left(1 - e^{-LAI\,B}\right), \tag{7}$$

$$c_2 = \frac{s}{3} + e^{-LAI\,B}\left(\rho_s - \frac{s}{3}\right). \tag{8}$$

In the kernel, θ_i and θ_v are zenith angles for illumination and view, respectively; ϕ is the relative azimuth of illumination and view directions; and ξ is the phase angle of scattering, $\cos\xi = \cos\theta_i\cos\theta_v + \sin\theta_i\sin\theta_v\cos\phi$. In the constants, s is leaf reflectance (= leaf transmittance); ρ_s is the (assumed isotropic) surface reflectance of the soil or understory; LAI is the leaf area index; and B is the average of secants of possible view and illumination zenith angles. For this formulation, a spherical leaf angle distribution is assumed. The Ross-thin

kernel simplifies Ross's equation based on an approximation for small LAI values:

$$k_{thin} = \frac{(\pi/2 - \xi)\cos\xi + \sin\xi}{\cos\theta_i \cos\theta_v} - \frac{\pi}{2}, \tag{9}$$

$$c_1 = \frac{2sLAI}{3\pi}, \tag{10}$$

$$c_2 = \frac{sLAI}{3} + \rho_s. \tag{11}$$

Although this kernel applies primarily to the case of a thin canopy of scatterers over a uniform background, it can also be appropriate for a very dense, uniform canopy of high leaf area, since in that case the leaf layers below the uppermost can act like a uniform background (Strahler *et al.*, 1995).

The Li kernels are derived from the modeling approach of Li and Strahler (1986, 1992). In this approach, the surface is taken as covered by randomly-placed projections (*e.g.*, tree crowns) that are taken to be spheroidal in shape and centered randomly within a layer above the surface. The BRDF is modeled as a function of the relative areas of sunlit and shaded, crown and background that are visible from the viewing position in the hemisphere. For the Li-sparse kernel, it is assumed that shaded crown and shaded background are black, and that sunlit crown and background are equally bright. Under these circumstances, and with some further approximations in the way that view and illumination shadows overlap, the Li-sparse kernel is:

$$k_{sparse} = O(\theta_i, \theta_v, \phi) - \sec\theta_i' - \sec\theta_v' + \frac{1}{2}(1 + \cos\xi')\sec\theta_v', \tag{12}$$

where

$$O = \frac{1}{\pi}(t - \sin t\cos t)(\sec\theta_i' + \sec\theta_v'), \tag{13}$$

$$\cos t = \frac{h}{b}\frac{\sqrt{D^2 + (\tan\theta_i' \tan\theta_v' \sin\phi)^2}}{\sec\theta_i' + \sec\theta_v'}, \tag{14}$$

$$D = \sqrt{\tan^2\theta_i' + \tan^2\theta_v' - 2\tan\theta_i' \tan\theta_v' \cos\phi}, \tag{15}$$

$$\cos\xi' = \cos\theta_i' \cos\theta_v' + \sin\theta_i' \sin\theta_v' \cos\phi, \tag{16}$$

$$\theta' = \tan^{-1}\left(\frac{b}{r}\tan\theta\right), \tag{17}$$

In these expressions, b is the vertical radius of the spheroid; h is the horizontal radius of the spheroid; and is the height of the center of the spheroid. For this model, and

$$c_1 = C\,\lambda\pi r^2, \tag{18}$$

$$c_2 = C. \tag{19}$$

Here, C is the brightness of sunlit surface, and λ is the count density of spheroids (number of spheroids per unit area). The sun zenith angle dependence of C may be approximated as $C/\cos\theta_i$ (Schaaf, Li and Strahler, 1994).

The Li-dense kernel differs from the Li-sparse kernel in that it accommodates mutual shadowing. It assumes a random distribution of crown heights to maximize the geometric-optical effect in a dense ensemble of canopies.

$$k_{dense} = \frac{(1+\cos\xi')\sec\theta'_v}{\sec\theta'_v + \sec\theta'_i - O(\theta'_i,\theta'_v)} - 2, \tag{20}$$

$$c_1 = \frac{C}{2}(1-\chi), \tag{21}$$

$$c_2 = C + (G-C)\chi. \tag{22}$$

These kernels are not yet linear in that they still contain two parameters, namely the ratios and , describing crown shape and relative height. For the present, we fix each parameter using a spherical shape close to the ground for the Li-sparse kernel ($b/r = 1$, $h/b = 2$) and a higher prolate shape for the Li-dense kernel ($b/r = 2.5$, $h/b = 2$). The fixed parameters for the Li-sparse kernel are intended for sparser vegetation covers exhibiting geometric-optical shadowing effects, such as shrublands or woodlands. It also fits some rough surfaces, such as plowed fields. The Li-dense kernel is intended to capture the three-dimensional mutual shadowing effects that occur in conifer forests and other vegetation covers with tall plant crowns.

As do most available BRDF models, all of these kernels assume that the BRDF depends only on the relative azimuth between the solar and the viewing direction. This symmetry may not be realized in some natural situations, for example for row effects or other preferential orientation of plants for ecological reasons. However, at this point we think that introducing another degree of freedom into the modeling is not warranted in view of the additional retrieval uncertainties this would introduce and our lack of knowledge concerning the relative importance of such effects. In a post-launch periods extensions of the modeling to non-symmetric BRDFs are possible.

In anticipation of situations in which forward scattering by water surfaces, as for example in rice paddies or flood zones, produce some specular reflection form water surface facets, we have provisionally added a kernel based on the Cox-Munk model (1954) for sea-surface scattering. With some assumptions, the Cox-Munk model can be made to fit the form $R = c1k + c2$, in which the kernel k_{spec}, is

$$k_{spec} = \frac{1}{\cos\theta_i}\left(1 - \frac{\tan^2\theta_n}{\sigma^2}\right) - 1 \qquad \text{if} \frac{\tan^2\theta_n}{\sigma^2} \leq 1,$$

$$k_{spec} = -1 \qquad \text{else.} \tag{23}$$

In this expression, σ^2 is the slope variance, given as $\sigma^2 = 0.003 + 0.00512w$, with w as the wind speed, in m/sec. The parameter θ_n is defined by

$$\cos^2\theta_n = \frac{1}{2}\left(\frac{(\cos\theta_i + \cos\theta_v)^2}{1+\cos\phi}\right). \tag{24}$$

The constants c_1 and c_2 for this model are

$$c_1 = c_2 = \frac{,(0,\epsilon)}{4\pi\sigma^2}, \tag{25}$$

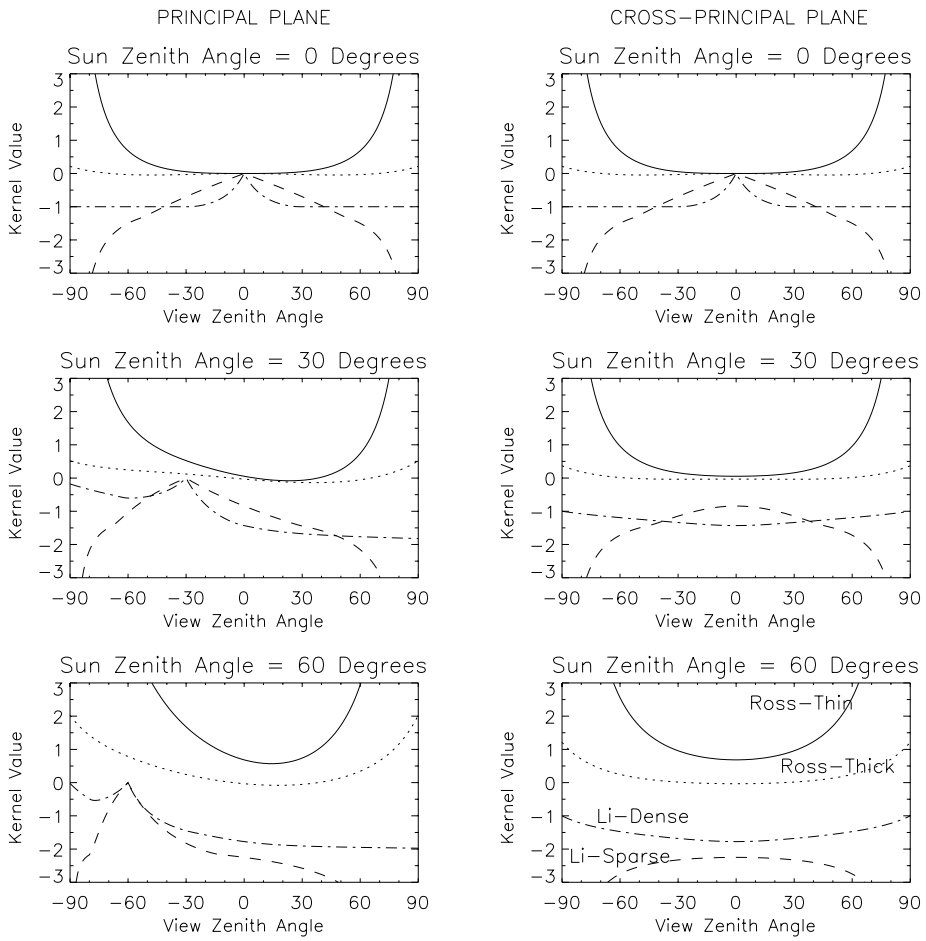

Figure 2: Kernel values (arbitrary units) on the principal and on the cross-principal planes for three different sun zenith angles.

where , (ζ, ϵ) is the Fresnel reflection coefficient of water with ζ set to a constant 0., and ϵ is the refractive index between water and air. For the application of in the BRDF/Albedo product, we have selected w = 5m/sec, which provides a fixed value of σ^2 =0.0286.

This kernel is included in the algorithm on a provisional basis. Final acceptance will be based on a more complete theoretical analysis and validation of the kernel by fit to forward-scattering observations.

Figure 2 provides plots of the kernel types given above for three sun angles as a function of view zenith along the principal plane and cross–principal plane. The kernel shapes are clearly well–differentiated.

These particular kernels have been selected as the most likely to capture the wide range of land cover anisotropy on a global basis. However, this scheme is flexible enough that other kernels can be easily adopted should any become available and should they be shown to be superior for a particular landtype.

3.1.2 Kernel-Driven Models

A complete kernel-driven semiempirical model is formulated as a linear combination of kernels. Most suitably it has the form

$$R = f_{iso} + f_{geo}k_{geo} + f_{vol}k_{vol}, \tag{26}$$

which is derived from adding appropriate choices of geometric-optical surface-scattering and radiative-transfer volume-scattering kernels, each multiplied by a proportion α or $(1-\alpha)$ that weights the contribution of each model. These proportions may be regarded as the areal proportions of land cover types exhibiting each type of scattering (neglecting multiple scattering between the two components), or as mixing proportions for land cover types that display both a volume–scattering and a geometric–optical contribution to the BRDF. The quantities and are the respective kernels; the factors f_{geo} and f_{vol} are their respective weights; and the term f_{iso} is the isotropic contribution. The formulae for f_{iso}, f_{geo}, and f_{vol} are shown in Table 4.

In the inversion and fitting of a semiempirical model to data, estimates of the weights f are retrieved from bidirectional reflectances and specification of viewing and illumination positions. Although this objective satisfies many of the goals of the BRDF/Albedo product, the existence of formulae for the weights f in terms of physical parameters could provide for direct inference of physical parameters from the weight values fitted (see Section 2.4). This possibility will be explored in the postlaunch phase as a research topic.

The kernel-driven semiempirical BRDF model using either the Ross-thin or the Ross-thick model for volume scattering and either the Li-sparse or the Li-dense kernel (using the crown height and shape parameters given above) are known and will be referred to as the Ambrals BRDF model (Wanner *et al.*, 1997).

3.1.3 The Modified Walthall Model

Empirical models can be understood as being of the kernel-driven model type as well, where the kernels are empirical functions. An example is the modified Walthall model, derived by Walthall *et al.* (1985) and improved by Nilson and Kuusk (1989). It has the form

$$R = p_0\left(\theta_i^2 + \theta_v^2\right) + p_1\theta_i^2\theta_v^2 + p_2\theta_i\theta_v\cos\phi + p_3. \tag{27}$$

Note that this is the same form as the semiempirical models discussed above — it is comprised of a weighted superposition of functions of angles, and the weights p are the parameters of the model. As a consequence, models like the modified Walthall model can be processed along with linear semiempirical models by the same linear inversion scheme.

3.1.4 Advantages of Linear Models

Linear models have a number of advantages in the context of global data processing. Linearity in BRDF models is comprehensively discussed by Lewis (1995) and demonstrated with the modified Walthall model. A first and foremost advantage is that any linear model can be inverted analytically through matrix inversion for the system of equations obtained by setting the derivative of the error function to zero (see Section 3.2.1).

Table 4: Semiempirical weight formulas

Model			Weight Formulae
Ross-thin plus Li-sparse:	f_{iso}	=	$\alpha C + (1-\alpha)\left(\frac{sLAI}{3} + \rho_s\right)$,
	f_{geo}	=	$\alpha C\ \lambda\pi r^2$,
	f_{vol}	=	$(1-\alpha)\frac{2sLAI}{3\pi}$.
Ross-thick plus Li-sparse:	f_{iso}	=	$\alpha C + (1-\alpha)\left(\frac{s}{3} + e^{-LAI\,B}\,(\rho_0 - \frac{s}{3})\right)$,
	f_{geo}	=	$\alpha C\ \lambda\pi r^2$,
	f_{vol}	=	$(1-\alpha)\frac{4s}{3\pi}\left(1 - e^{-LAI\,B}\right)$.
Ross-thin plus Li-dense:	f_{iso}	=	$\alpha C + (1-\alpha)\left(\frac{sLAI}{3} + \rho_s\right)$,
	f_{geo}	=	$\alpha\frac{C}{2}$,
	f_{vol}	=	$(1-\alpha)\frac{2sLAI}{3\pi}$.
Ross-thick plus Li-dense:	f_{iso}	=	$\alpha C + (1-\alpha)\left(\frac{s}{3} + e^{-LAI\,B}\,(\rho_0 - \frac{s}{3})\right)$,
	f_{geo}	=	$\alpha\frac{C}{2}$,
	f_{vol}	=	$(1-\alpha)\frac{4s}{3\pi}\left(1 - e^{-LAI\,B}\right)$.

This provides direct estimates of the parameters f_{iso}, f_{geo}, f_{vol} and while avoiding numerical inversion problems.

Second, both the directional-hemispherical and bihemispherical integrals of the BRDF (black-sky and white-sky albedos) may be precalculated for each kernel individually. The albedo of a model then is simply the sum of the kernel albedos, weighted by f values. By using a look-up table, numerical integration of the models can thus be avoided.

Third, linear BRDF models scale linearly in space if adjacency effects are assumed to be small. This allows for mixed pixel cases, as indicated by the areal proportion parameter in the model factors listed above. This feature also allows for the scaling of BRDF and albedo from one spatial resolution up to a coarser one, *e.g.*, to a particular resolution needed for a climate model. Finally, since some of the parameters driving the models are dependent on wavelength while others are not (*e.g.*, structural parameters), it may be possible to extract all or some of them from multiband analysis, making assumptions about the others.

3.1.5 Validation of Semiempirical Models

3.1.5.1 Fit of Semiempirical Models to Ground Data

Note: A full detailed report on the validation of the kernel-driven Ambrals semiempirical BRDF model is given in Appendix A. Please refer to this appendix for data sources, tables, figures and an in-depth discussion.

The ability of the Ambrals semiempirical BRDF model to describe naturally occurring BRDF shapes was tested using 27 different data sets measured on the ground or from airborne instruments. These data

sets include a wide variety of land cover types as will be encountered in global remote sensing. Among these are barren types (soils of different roughnesses), sparsely vegetated types (both patchy and uniformly sparse), dense vegetation (both broadleaf crops, and grasses and cereal crops), and forests (both needleleaf and broadleaf). When using such data sets to validate a BRDF model to be used in remote sensing at a spatial resolution of one kilometer, a scaling problem clearly exists. However, currently no good data sets over a variety of different land cover types exists that has both coarse spatial resolution and good angular sampling at several different solar zenith angles. Therefore, field-measured data sets are still indispensable for model validation. If the different BRDF shapes met in the field are fitted well by a BRDF model, it may be reasonably expected that the BRDFs observed for similar vegetation types at a scale of 1 km, which will probably be smoother, will also be fit well. In case of mixed land covers, the Ambrals BRDF model is expected to be better suited for modeling the mix than most other BRDF models (which were derived assuming homogeneous scenes) due to its linear superpositioning approach. Scaling issues are further discussed in Appendix F.

The 27 observed BRDF data sets were inverted for all available bands (mostly red and near-infrared) and all solar and view angles simultaneously. None of these data sets were fitted with an RMS absolute error of more than 0.046, the average RMSE being 0.034. Furthermore, the correlation coefficient between the modeled and the observed reflectances was determined for the red band and the near-infrared band. In the red band, 12 of the 27 data sets showed a correlation coefficient larger than 0.9; 18 of 27 one larger than 0.8; and 23 of 27 one larger than 0.75. Only one data set had a correlation coefficient smaller than 0.7, but this data set was found to have irregular features in the observed red band reflectances. In the near-infrared band, 13 of 27 data sets showed correlation coefficients larger than 0.9, 23 of 27 had ones larger than 0.8, and 26 of 27 had ones larger than 0.75. These values indicate a reasonable agreement between modeled and observed reflectances, validating the Ambrals BRDF model.

With respect to the kernel combinations found to best represent each land cover type, two results are mainly of interest. First, there is some correlation between the type of land cover being modeled and the kernel combinations producing the best fit. In shadow-casting cases like a plowed field or a sparse forest, the Li-sparse kernel was dominant. In cases of a dense forest, the Li-dense kernel produced the lowest RMSE. In the case of dense crops, kernel combinations including the Ross-thick kernel produced best fits. The second finding is that even though different kernel combinations may produce small values of the RMSE for a particular case, visual inspection of fits reveals that the model with the lowest RMSE indeed fits the observed data better than a model with a slightly higher RMSE, demonstrating the benefit of allowing multiple kernel combinations.

Validation of the Ambrals BRDF model was carried out in parallel to an evaluation of the modified RPV model (Rahman *et al.*, 1993b; Engelsen *et al.*, 1996). The comparison shows that the Ambrals model results are very similar, perhaps even slightly better, than those for the modified RPV model.

Please refer to Appendix A for a full report of these validation results, including tables, figures and more detailed analysis.

3.1.5.2 Inversion and Fitting of Semiempirical Models to ASAS Data Researchers at University College London recently applied two semiempirical models to directional image data obtained for a semiarid region of West Africa near Niamay, Niger (Barnsley *et al.*, 1996; Lewis *et al.*, 1995; see Appendix J). In this study, NASA's Advanced Solid-state Array Spectrometer (ASAS) (Irons *et al.*, 1991) acquired image data from an aircraft platform over the HAPEX-Sahel west central, east central and southern super-sites on various dates during September 3–17, 1992. The ASAS acquires images at ten sensor view angles during a single overpass — one at nadir and nine others at 15° increments between 75° forward and 60° aft of the aircraft platform on which it is mounted. These images are recorded in 64 continuous narrow spectral wavebands in wavelengths ranging from the visible to the near-infrared. Spatial resolution is about 4 m. Data processing involved manipulating the multiple–view–angle and multiple flight–line ASAS image data in four steps: (i) geometric registration; (ii) radiometric correction; (iii) atmospheric correction; and (iv) estimation of the surface (spectral) BRDF and albedo through BRDF model inversion.

Geometric registration of the multiple-view-angle and multiple flight-line data was perhaps the most problematic task. Standard polynomial warping techniques are generally unable to cope with the very high frequency, localized geometric distortions present in most airborne scanner images. Consequently, Barnsley *et al.* (1996) used an automated image registration procedure based on "interest point" extraction and area-based matching of small patches of image around each interest point (Allison *et al.* 1991, Allison and Muller 1992) to define an initial polynomial mapping followed by pixel patch-by-pixel patch (typically 15 x 15 pixels) matching using adaptive least-squares image correlation (Otto and Chau, 1989). These techniques are capable of registering multiple view-angle ASAS images to subpixel accuracy (<0.4 pixels) globally throughout the scene (Allison *et al.* 1994). In this case, each of the off-nadir images was registered to the nadir view. Radiometric correction was effected using gain values provided by NASA to convert the instrument's raw DN values to spectral radiances. Atmospheric correction was applied by use of the 6S atmospheric correction code (Vermote *et al.* 1994) with atmospheric parameters derived from sun photometer data (Brown de Colstoun *et al.*, 1996).

With registered and corrected data at hand, the Walthall and Roujean models were inverted and fitted to the data on a pixel-by-pixel basis (Barnsley *et al.*, 1996; see Appendix J). This allowed the construction of images of the weights associated with each term of each model. The nadir reflectance images in the blue and near-infrared bands have low contrast and appear noisy. In these bands, the models seem to be fitting noise rather than signal. In contrast, the green and red bands show a coherent scene structure. The first parameters from both Walthall and Roujean models are strongly related to overall brightness and thus mimic the nadir reflectance. The second and third parameters of the Walthall model show little spatial structure, although some bright and dark spots seem to correlate well with particular patches in the nadir image. In contrast, the Roujean model shows strong spatial structure in both the first and second parameters. The second parameter is the weight of the geometric kernel, which seems to vary inversely with the first parameter. This indicates that the BRDF becomes more isotropic with increasing brightness, which is not unexpected if multiple scattering increases with brightness. The fine texture in the images of the third

parameter may be related to fine errors in registration, rather than real changes in BRDF within the scene. Overall, the weight of the third parameter is quite low, indicating that volume scattering is not important for these surfaces. Since vegetation is quite sparse over most of the target area, this is not unreasonable. These results demonstrate that a pixel-by-pixel inversion of empirical/semiempirical models is possible, and that the model parameters vary systematically in a meaningful spatial pattern.

More recently, (Muller and Disney, 1997; Muller *et al.*, 1997a, b) have processed all of the ASAS data into surface directional reflectance for all three study sites. Preliminary results are presented in Appendix F of two applications of these spectral directional reflectance fields. In the first application, a study was performed (results shown here for Southern Super Site and West Central Super Site) of the impact of spatial resolution on the type of models which are retrieved. The results indicate that at 3m resolution, the modified Walthall model is chosen consistently over two different cover types (millet and savannah) whereas at 30m, 90m and 240m the RossThick–LiDense is primarily chosen for the same regions. This indicates that we may have difficulties using field spectro-radiometric data acquired at around a couple of meters to validate MODIS/MISR derived BRDF/albedo over sparse canopies.

In the second application (Muller *et al.*, 1997a), the ASAS modified Walthall results were used to generate training statistics for a TM supervised maximum likelihood classification after registration and resampling of the ASAS directional reflectance values. This has allowed a spectral albedo map to be produced for the whole of the Southern Supersite area at 30m for use in simulation and testing of the MODIS/BRDF inversion algorithm. In addition, broadband albedo data are available for validating these ASA/TM-derived spectral albedos to assess how accurate the inverted albedos will be (see Appendix G).

In the final application, a Monte Carlo ray-tracing system (Lewis and Muller, 1992) was used together with geometrical-optical models of millet plants to simulate the radiance at the ASAS sensor, and these values were compared with those extracted from ASAS after atmospheric correction (Muller *et al.*, 1997b). The MCRT allows studies to be made of the significance of the biophysical parameters included within the semiempirical models as well as the impact of different sampling scenarios (MODIS only, MISR only, MODIS+MISR, cloud-cover impacts) on the accuracy of the derived BRDF parameters and spectral as well as broadband albedo values (see Appendix H for more details).

3.1.5.3 Inversion and Fitting of Semiempirical Models to AVHRR Data As part of an European Union consortium investigating land cover change in the Sahel, researchers at UCL have also been investigating the application of the Ambrals model to AVHRR data (see Appendix J). Six months (May–October 1992) of LAC derived surface reflectance data of the HAPEX-Sahel grid square have been processed using the model and aspects of model fit and model selection investigated (Lewis and Ruiz de Lope, 1996).

The results indicate that the Ambrals kernels are able to describe the shape of the BRDF (processed on a 16-day window, 1-day step, moving window) well over the period of study. Relatively large errors in model fit can, however, occur during the rainy season, due to variations in the surface reflectance on a sub-16-day timescale. In spite of this, the trends in normalized reflectance, albedo and BRDF model

parameters are generally well-maintained. The temporal trajectory of these model parameters is currently being investigated with a view to providing information on variations in the surface cover.

The main kernel selection criterion in Ambrals, the RMSE in model fit, is found in many cases not to provide very consistent results (either temporally and spatially). It is understood that Ambrals will have to make use of additional information in aiding kernel selection, and so the team at UCL have been investigating the issues involved. Currently, an approach that considers temporal consistency in the main selection criterion, weighted by the RMSE is being tested. Early results indicate that this is indeed promising, and that it can be implemented efficiently within Ambrals.

In addition to this research, work is currently underway testing the application of Ambrals to the AVHRR Pathfinder (PAL) dataset for Africa north of the Equator. Two years of data have been processed so far (1989 and 1992) and the 1992 results compared with the LAC data over HAPEX-Sahel described above. While many of the trends observed appear to be similar in the two datasets, the magnitude of the trends are very different, probably mainly due to the poor atmospheric correction of the data (PAL corrects for only Rayleigh scattering and ozone absorption).

3.2 THE MODIS BRDF/ALBEDO ALGORITHM

3.2.1 Model Inversion and Retrieval of BRDF and Albedo

3.2.1.1 Theoretical Background: Inversion A kernel-driven model has the form

$$R(\theta_i, \theta_v, \phi, \Lambda, I_1, I_2) = \sum_{k=1}^{n} f_k(I_1(\Lambda))\, k_k(\theta_i, \theta_v, \phi, \Lambda, I_2(\Lambda)), \tag{28}$$

or, for a set of discrete values of the BRDF,

$$R_l(\Lambda) = \sum_{k=1}^{n} f_k(I_1(\Lambda)) k_{kl}(I_2(\Lambda)), \tag{29}$$

where R is the reflectance; θ_i and θ_v are the zeniths of view and illumination, respectively; and ϕ is the relative azimuth; Λ is the waveband; I_1 and I_2 are lists of parameters describing light scattering in the scene, with the kernel-internal parameters; the parameters of the BRDF model; and k_k the kernels, where the index stands for a particular viewing and illumination geometry, $(\theta_i, \theta_v, \phi)_l$. This formula expresses that kernel-driven BRDF models for a waveband are formulated as a superposition of basic BRDF shapes, where the kernel shapes k are functions of viewing and illumination geometry only (provided that the parameters I_2 have been fixed); and the respective contribution of each kernel value k_{kl} to the resulting reflectance is given by the corresponding parameter or weight f_k, depending on the internal parameters as a function of wavelength. The number of kernels to be superimposed is n. Usually three kernels are chosen — the first is the constant unity, representing isotropic scattering, the second represents volume scattering, the third surface scattering.

An observation consists of N directional measurements $\rho'_l(\Lambda)$ where l runs from 1 to N. The difference between the modeled and the observed reflectances is measured by an error function E, which generally is

defined in the following way:

$$E^2(\Lambda) = \frac{1}{d}\sum_{l=1}^{N}\frac{(\rho_l'(\Lambda) - R_l(\Lambda))^2}{w_l(\Lambda)}, \tag{30}$$

where w_l are the weights attributed to the respective observations. Choices for error weights include $w_l(\Lambda) = 1$, $w_l(\Lambda) = \rho_l'(\Lambda)$, $w_l(\Lambda) = R_l(\Lambda)$, or $w_l(\Lambda) = \rho_l'^2(\Lambda)$. The quantity d is the degrees of freedom, *i.e.*, $d = N - n$. E is taken as the root-mean-square error, or RMSE.

Inversion of the BRDF model aims at determining the parameters k of the model. The parameters wanted are those for which E attains a minimum. In other words, those k for which (dropping explicit mention of waveband dependencies)

$$\frac{\partial E^2}{\partial f_j} = \frac{1}{d}\sum_{l=1}^{N}\frac{2}{w_l}(\rho_l' - R_l)\left(\frac{\partial \rho_l'}{\partial f_j} - \frac{\partial R_l}{\partial f_j}\right) = 0, \tag{31}$$

provided that the solution to this equation is a minimum and not a maximum or a saddle point. The derivative of the observed reflectances with respect to the parameters is zero, of course, but for modeled reflectances $\partial R_l/\partial f_j$ we have

$$\frac{\partial R_l}{\partial f_j} = \frac{\partial}{\partial f_j}\left(\sum_{k=1}^{n} f_k k_{kl}\right) = \sum_{k=1}^{n}\left(\frac{\partial f_k}{\partial f_j}k_{kl} + f_k\frac{\partial k_{kl}}{\partial f_j}\right) = \sum_{k=1}^{n}\delta_{kj}k_{kl} = k_{jl}, \tag{32}$$

where $\delta_{kj} = 1$ if $k = j$, otherwise 0.

Thus,

$$\frac{\partial E^2}{\partial f_j} = \frac{1}{d}\sum_{l=1}^{N}\frac{2}{w_l}(\rho_l' - R_l)k_{jl} = 0, \tag{33}$$

or

$$\sum_{l=1}^{N}\frac{\rho_l' k_{jl}}{w_l} = \sum_{l=1}^{N}\frac{R_l k_{jl}}{w_l} = \sum_{l=1}^{N}\sum_{k=1}^{N}\frac{f_k k_{kl} k_{jl}}{w_l}. \tag{34}$$

Introducing the vector V and the Matrix M as

$$V_j = \sum_{l=1}^{N}\frac{\rho_l' f_{jl}}{w_l}, \tag{35}$$

$$M_{jk} = \sum_{l=1}^{N}\frac{k_{jl}k_{kl}}{w_l}, \tag{36}$$

we can write the equation for the parameters delivering the best fit as

$$V_j = \sum_{k=1}^{n} M_{jk} f_k \tag{37}$$

and arrive at the solution

$$f_k = \sum_{j=1}^{n} M_{jk}^{-1} V_j \tag{38}$$

for the parameters. Thus, the BRDF model has been analytically inverted via an analytical solution to the single stationary point of the error function. From physical arguments, we can show that this is the global minimum (Lewis, 1995).

However, the values f_k that are obtained by this procedure are not constrained to lie within proper physical bounds. For example, if the kernels in a particular semiempirical model are inappropriate for the surface type, the best fit might require a negative weight on one of the kernels, which is not physically possible given the physical derivation of the weight functions. Although not yet implemented, it is a simple matter to constrain the solution such that the f_k lie within reasonable bounds via Lagrange multipliers (Lewis, 1995). In the event that the model with the constrained solution actually presents the lowest error among all semiempirical models, a flag will carry forward the information that the fit was constrained and thus is of lower confidence.

3.2.1.2 Advantages of the Kernel-Based Approach The algorithm that was developed for MODIS BRDF inversion and albedo computing, (known as "Ambrals", the Algorithm for MODIS bidirectional reflectance anisotropies of the land surface) was programmed in a kernel-oriented, rather than model-oriented, fashion so that it would be both flexible and efficient. Values of all kernels occurring at the viewing and illumination angles at hand are computed and tabulated so that the functions have to be processed only once for each geometric situation and each kernel . After that, each kernel value k_{kl} is referred to via a look-up table. This allows rapid computing, for example, of the matrix M as a function of the model chosen, or of the reflectances resulting from the parameters found (needed, for example, for calculating the RMSE). Since the suite of models to be inverted share kernels, this makes the code efficient by avoiding duplication of computations. Trigonometric expressions that are shared by several kernels are also computed only once.

The algorithm's kernel-based approach has the additional advantage of easily allowing an increase in the number of kernels and of formulating new models by allowing the free combination of any number of kernels. This feature is also essential in the spatial degrading of the BRDF/albedo product (see Section 3.3.2 and Appendix F).

3.2.1.3 Matrix Inversion and Error Function Used Inversion of the matrix $M_{jk} = \sum_l k_{jl} k_{kl}/w_l$ is performed by a standard LU decomposition algorithm. In the general case, is dependent on wavelength and the inverse needs to be calculated for each band separately. However, if the weights w_i are chosen to be independent of the wavelength, M is independent as well, assuming that if the kernels contain internal physical variables I_2 these have been set to fixed values. Then for each set of observations sampling a given BRDF, M needs to be inverted only once for all bands observed.

This is the case with the error function chosen for the current BRDF inversion problem, which was selected to measure the mean squared absolute deviation of modeled and observed reflectances,

$$E^2(\Lambda) = \frac{1}{d} \sum_{l=1}^{N} (\rho'_l - R_l)^2 \tag{39}$$

i.e., w_l was chosen to be 1. The RMSE of a given model is defined as the root of the average of E^2 over all bands, although for selection of the best-fitting model, only bands 1–4 are considered. The weighting function w_l was chosen in this way because it allows most accurate modeling of the commonly found upturning of the BRDF for large zenith angles, which is of importance in deriving albedo; the cost is a reduced relative accuracy of reflectances with a low value. Studies on penalty functions and more complex forms of will be conducted in the near future.

3.2.1.4 Model Selection In the MODIS processing scenario, level-2 reflectances that have been cloud cleared and atmospherically corrected are binned into the MODIS level-2G grid over a period of 16 days and combined with all MISR observations acquired during that same time. The data from each image are interpolated to a spatial resolution of one kilometer, where each observation is weighted by the respective overlap between the grid cell and the observation footprint. Quality information associated with the data is translated to quality coefficients that are used to weight individual observations in the subsequent BRDF inversion. This allows special consideration of data where, for example, atmospheric correction was difficult or aerosol information was taken from standard tables because no aerosol retrievals were available.

The directional observations thus assembled are then analyzed by inverting the five model variants as decribed above to find the Ambrals kernel combination that fits the observations best. The four bands common to MODIS and MISR are inverted first. The model chosen as best from this analysis is then applied to the three remaining bands, in which only MODIS data are available. The model parameters found are written to output along with extensive quality control data and other information necessary for an assessment of the product. Integration of the BRDF is carried out to provide black-sky and white-sky albedos.

In general, the kernel combination which provides the fit with the smallest root band-averaged mean squared error (RMSE) as described above is selected. The two cases where an exception is made are if the RMSE found is large, or angular sampling coverage is bad enough to mistrust the inversion, either because observations span only a small angle range or their number is too small. In these cases information from the supporting ancillary databases is used to limit the inversion.

If angular sampling is good but the RMSE found is high, the kernel combination suggested by the ancillary data (previous BRDF, the historical accumulated BRDF database, land cover type, and topography) is used instead (if the resulting RMSE is not much worse). The model parameters are still derived from a full inversion of the reflectances.

If angular sampling is bad or the number of reflectances available is too small, a full inversion cannot be trusted and gaps in the product would result. In this case, the BRDF kernel combination and model parameters suggested by the ancillary databases will be used, but the magnitude of the BRDF (the isotropic constant of the model) will be adjusted to the observed reflectances. Through this the shape but not the magnitude of the BRDF will be fixed. This procedure also guarantees that the reflectance information available in cases not permitting a full BRDF inversion will not be simply lost but used to the extent

possible.

In each case, the source of the resulting BRDF information will be recorded so that users can filter the output according to their needs. The ancillary database accumulating BRDF knowledge over time, keyed by season, and the relationships between land cover type and BRDF used will be established post-launch from the data observed and updated at intervals.

The flexibility of the Ambrals model means that the mathematical expressions used on adjacent pixels may be slightly different. While this is expected to provide the best BRDF and albedo information on a per-pixel basis, it may introduce too much complexity in applications where a much simpler uniform approach is desired. As a consequence, the MODIS BRDF/albedo product will always also provide the full inversion results for the modified Walthall BRDF model [Walthall *et al.*, 1985; Nilson and Kuusk, 1989]. This model is purely empirical and is expected to produce results of reduced accuracy, particularly under conditions of sparse angular sampling. But the simplicity of the mathematical expression used and the fact that it will be the same for all pixels make it attractive for applications where such a reduced accuracy is acceptable.

3.2.1.5 Albedo Calculation Deriving the directional-hemispherical and bihemispherical integrals from the BRDF requires, in the general case, a numerical integration of the BRDF, which is computationally very costly if it is to be performed routinely for a global product at the 1-kilometer scale. The linearity of kernel-driven models with respect to their parameters allows a handy way out of this dilemma. Since the integration is with respect to the occurring angles and only the kernels depend on these angles, and since these are known in advance, the integral of the BRDF may be written as a weighted sum of the integrals of the kernels, where the weights are the same as those in the BRDF model. The integrals of the kernels may, then, be computed numerically in advance (once) and the results stored in a table. Albedo calculations are then reduced to forming a simple linear combination of these tabulated values. This applies to both black-sky and white-sky albedo. The black-sky albedo of the individual kernels is tabulated as a function of solar zenith, where the zenith is incremented by a small amount (*e.g.*, 0.25° — although the table is not large in any case) and interpolated for intermediate values. Therefore, black-sky albedo at any solar zenith angle and white-sky albedo for both models (the "best fit" model and the Walthall model) can be constructed with almost no computational effort directly from the model parameters using these small look-up tables of precomputed kernel integrals which will be provided to users with the product. Broadband albedos will be given in a similarly parameterized form.

In addition, the product will provide a single set of black-sky albedo values for the median sun angle for the suite of observations that were inverted to fit the BRDF. (Note that the black- and white-sky albedos are provided in each of seven spectral bands, two aggregated bands and one broad band.)

3.2.1.6 Algorithm Flow and Execution Figure 3 demonstrates data flow in connection with the BRDF/Albedo algorithm. Surface reflectances produced by the MODIS and MISR atmospheric correction algorithms are passed into a BRDF subsetting and database compilation process along with selected infor-

mation on atmospheric state. These data are referenced to the Level 3 grid through a process producing data pointers referred to as Level 2G. A compilation process builds from this Level 2G data a multiangular reflectance database with a common spatial resolution of 1 km for ingest into the BRDF/Albedo algorithm. Decisions about observations to be discarded based on the atmospheric correction quality and weights to be attributed to individual reflectances are made at this stage, and a binning process is carried out using footprint location information provided by the 2G pointer processing. This process also produces texture information for the land cover classification process.

The main BRDF/Albedo product generation process will be executed at the EDC DAAC. This process additionally reads various Level 3 ancillary data, a kernel albedo look-up table (static, calculated prelaunch, size less than 10 KByte), an albedo value look-up table giving albedos taking into account diffuse skylight as a function of atmospheric state (static, calculated prelaunch by Eric Vermote and also used by MOD09:L2/Surface Reflectance, size less than 1 GByte). If the BRDF/atmosphere coupling terms used in atmospheric correction, which are based on the previous BRDF/Albedo product or other sources remain unchanged, the new BRDFs obtained are regarded as final; otherwise new coupling terms are derived utilizing the data describing atmospheric state, the surface reflectances are updated, and an improved BRDF is derived (see Section 3.2.4).

This process will also write an intermediate file that contains BRDF-corrected reflectances for input to the Land Cover Product Database. These are bidirectional reflectances for nadir view at the nominal sun angle of the compositing period. The nominal sun angle is taken as the solar zenith angle at the time of nominal overpass (about 10:30 AM) for the pixel on the eighth day of the 16-day compositing period. It will vary with latitude and day of the year.

3.2.1.7 Quarter Degree Climate Model Grid In addition to the one-kilometer BRDF/Albedo product, a product spatially degraded to a quarter-degree resolution will be produced for direct use in climate models. This spatial degradation procedure is not simply an averaging exercise, since different pixels are described by potentially different models with different parameters. However, the Ambrals algorithm allows for the free formulation of models with any number of kernels, and if adjacency effects are neglected, the linearity of the modeling approach allows for the description of the BRDF of several pixels as a linear combination of the individual BRDFs that are weighted by the respective areal proportion of each type. Since the total number of kernels that may occur is limited, the number of kernels that need to be added to form a BRDF model of the superpixel is limited to a reasonable number as well. Most importantly, the white-sky and black-sky albedos of the superpixel may be directly computed without further assumptions. Thus, the quarter-degree product can be directly formulated by descaling the one-kilometer product to meet the coarser GCM scale requirements. This product will also retain some information on the subgrid variability of albedo. Refer to Appendix F for a preliminary discussion of model behavior with respect to scaling.

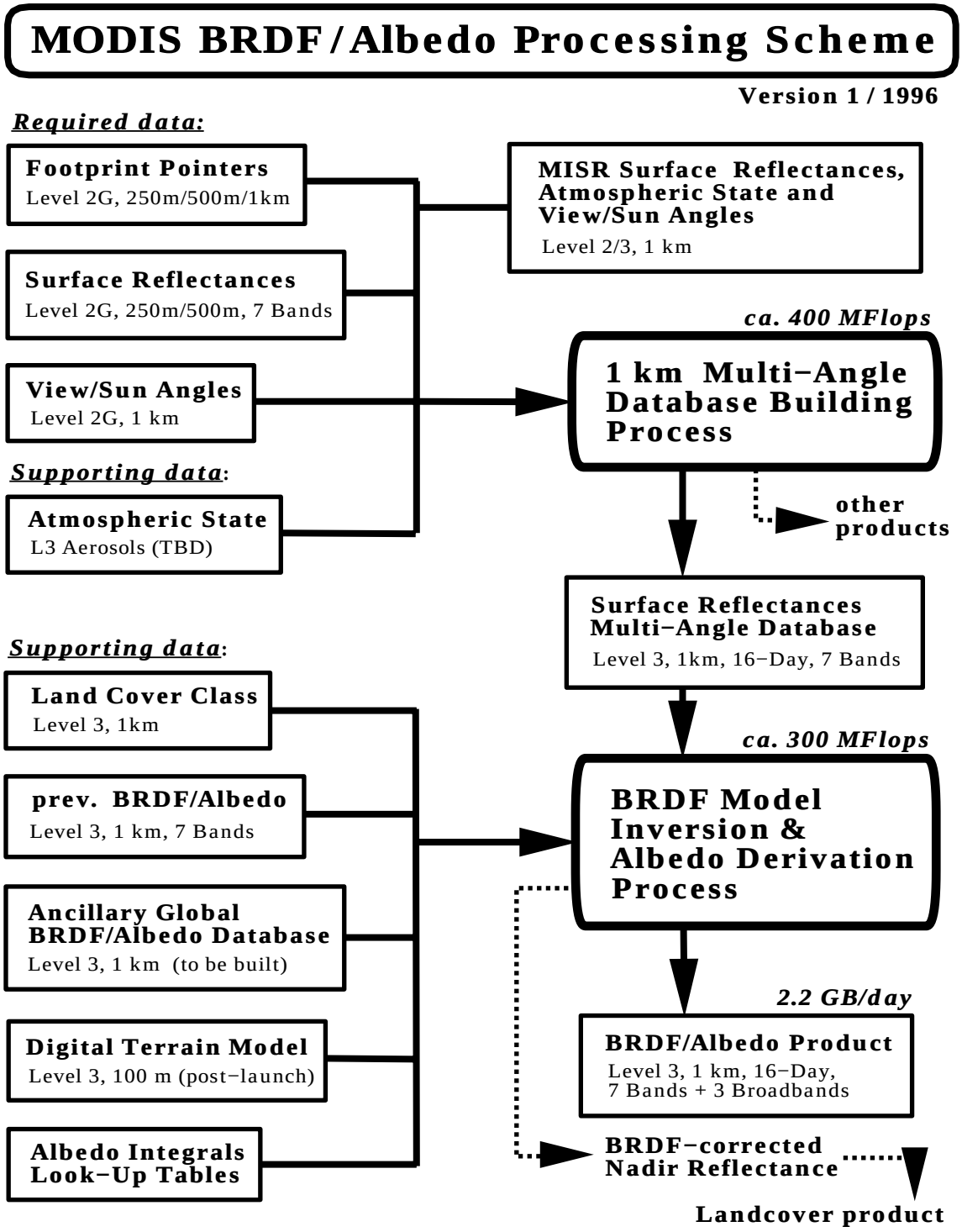

Figure 3: Flow chart for data processing by the BRDF/Albedo algorithm. Processes are shown as circles; boxes are files and/or data products.

3.2.2 The Algorithm for BRDF Retrieval by the Product User

The BRDF/albedo product gives an identifier of the best-fit Ambrals model kernel combinations and the corresponding parameters found from inversion of the observations. A user of this product who wants to standardize given observations to common viewing and illumination geometries or wants to extrapolate observations to angles not observed, or wishes to reconstruct the BRDF for any other purpose will require an algorithm that contains the code for all the kernels and allows easy accomplishment of the tasks required. For this reason, the Ambrals code used for BRDF inversion to generate the product was programmed to not only serve inversion, but also to serve forward modeling, *i.e.*, reconstruction of the complete BRDF from the parameters given by the product.

The code is written with the end-user of the product in mind. It is highly adaptable to specific situations; an extensive user-guide has been written to guide the user in operating the algorithm (this includes instructions on how to alter, expand and adapt the code); it provides various options concerning details of the forward modeling process, and it allows numerical integration of the BRDF if needed. This code is also useful for theoretical studies as it allows free combinations of kernels to be investigated and adding of new expressions. It may be used to create artificial data for testing algorithms depending on the BRDF product. The code will be archived and distributed by the appropriate DAAC. It is presently available from the authors upon request.

3.2.3 Narrowband to Broadband Albedo Conversion

Black-sky and white-sky albedos are provided for the land bands of MODIS and MISR. To provide a more useful albedo product for global climate models (Dickinson, 1983), we also provide these albedos in three broad bands. Two of these, 0.4–0.7 μm and 0.7–3.0 μm, are separated at 0.7 μm. This wavelength divides the downwelling solar spectrum into two portions — one in which vegetation dominantly absorbs radiation and another in which vegetation dominantly scatters radiation. The two are weighted and summed in a third broadband albedo that covers the range 0.4–3.0 μm.

This narrowband-to-broadband albedo conversion will be achieved by weighting the narrowband albedos by the associated proportion of downwelling solar irradiance they encompass. This method has been used with nadir Landsat measurements (Brest and Goward, 1987) and was shown to be satisfactory by Ranson *et al.* (1991), although Starks *et al.* (1991) report a case where a significant bias occurred. Since the downwelling solar irradiance depends on the atmospheric state during observation, there is an undesirable dependence of the broadband albedos on that state. We currently are considering resolving this situation by using the irradiance found from applying molecular scattering alone (clean-sky case). Note that the spectral albedos will be provided by the MODIS BRDF/albedo product as well, so individual researchers will always be able to carry out their own conversions.

Table 5 shows sample results illustrating the potential accuracy achievable in narrowband-to-broadband albedo conversion using the seven MODIS land bands for three different land cover types. The broadband

Table 5: Spectral-to-Broadband Albedo Conversion: Accuracy of Results Based on 7-Band Splines as Compared to Exact Results.

	Exact Results			Band-Based, Deviations		
Cover	total	vis	IR	total	vis	IR
Type	0.4–2.2 μm	0.4–0.7 μm	0.7–2.2 μm	0.4–2.2 μm	0.4–0.7 μm	0.7–2.2 μm
grass	0.22	0.058	0.34	-0.9%	+0.5%	-1.2%
soil	0.18	0.10	0.24	-0.4%	-3.2%	+0.4%
snow	0.84	0.99	0.72	-2.1%	-0.2%	-4.0%

albedos derived from splines applied to the spectral values are within 1 or 2 percent of the true values.

3.2.4 The BRDF-Atmospheric Correction Loop

A problem arises in the fitting of models of surface bidirectional reflectance from satellite observations. Because surface-leaving radiance is multiply scattered between the surface and atmosphere and within the atmosphere, the atmosphere and surface are coupled together in a complex fashion by radiative transfer. This means that even with perfect knowledge of atmospheric properties, it is not possible to correct a top-of-atmosphere radiance measurement to produce surface radiance or reflectance without prior knowledge of the surface BRDF. However, for our application, the surface BRDF is unknown and is to be retrieved from atmospherically-corrected surface reflectances.

To overcome this problem, the MODIS BRDF/Albedo algorithm couples atmospheric correction and BRDF inversion in a one-iteration loop procedure. In short, atmospheric correction is performed on MODIS observations under the assumption of an isotropic surface BRDF or BRDF derived from a prior product; the reflectances are then used to fit a new BRDF; the reflectances are then recalculated using the new BRDF; and if they have changed significantly, a final BRDF is then fitted to the recalculated values. At present, we plan only a single correction loop. Simulation studies show that a second loop changes the retrieved parameters by only a few percent, except in cases of high turbidity (*e.g.*, t=0.5). By the third or fourth loop, change is only a few hundredths of a percent.

We have tested the one-iteration coupled process and have been exploring the impact of assuming an anisotropic surface rather than an isotropic one in atmospheric correction (See Appendix D) by using the radiative transfer code 6S (Vermote *et al.*, 1994) and an implementation of the MODIS atmospheric correction scheme (Vermote *et al.*, 1995). In its forward mode, 6S can calculate the reflectance at the top of the atmosphere for a given viewing and illumination geometry. In its inverse mode, 6S can perform atmospheric

correction of top of atmosphere values to obtain surface reflectances.

The atmospheric correction procedure describes the top of atmosphere reflectance as

$$\begin{aligned}\rho_{toa}(\mu_s,\mu_v,\phi) &= \rho_0 + e^{-\tau/\mu_v}e^{-\tau/\mu_s}\rho_s(\mu_s,\mu_v,\phi) + e^{-\tau/\mu_v}t_d(\mu_s)\bar{\rho} + e^{-\tau/\mu_s}t_d(\mu_v)\bar{\rho'} \\ &\quad + t_d(\mu_s)t_d(\mu_v)\bar{\bar{\rho}} + \frac{(e^{-\tau/\mu_s}+t_d(\mu_s))(e^{-\tau/\mu_v}+t_d(\mu_v))S(\bar{\bar{\rho}})^2}{1-S\bar{\bar{\rho}}} \qquad (40)\end{aligned}$$

where ρ_{toa} is the reflectance at the top of the atmosphere; ρ_0 is the atmospheric reflectance due to path radiance; ρ_s is the directional surface reflectance; S is the reflectance of the atmosphere for isotropic light entering the base of the atmosphere; μ_s is the cosine of the solar zenith angle, and μ_v is the cosine of the view zenith angle; ϕ is the azimuthal difference between the sun and view zenith angle; $e^{-\tau/\mu_s}$ and $t_d(\mu_s)$ are the downward direct and diffuse transmittance of the atmosphere along the path of the incoming solar beam, respectively; $e^{-\tau/\mu_v}$ and $t_d(\mu_v)$ are the upward direct and diffuse transmittance of the atmosphere in the viewing direction, respectively; τ is the atmospheric optical depth; $\bar{\rho}$, $\bar{\rho'}$, and $\bar{\bar{\rho}}$ are the surface hemispherical-directional (black-sky albedo associated with the illumination angles), the directional-hemispherical (black-sky albedo associated with the viewing angle), and the bihemispherical reflectance (white-sky albedo) respectively, and couple the atmospheric optical parameters and the surface reflectance properties.

Of these parameters, ρ_0, τ, $t_d(\mu_s)$, $t_d(\mu_v)$, and S are functions only of the atmospheric state. They are calculated by the surface reflectance product algorithm as derived from MODIS aerosol product inputs. These parameters are stored with the Level 2 surface reflectance of each pixel in an internal product read by the BRDF/Albedo algorithm.

Note that operationally, there will be a difference in the input data that are obtained from MODIS and MISR. The MODIS surface reflectance is a bidirectional reflectance — that is, an instantaneous value of the BRDF at the view and illumination positions associated with the observation. The MISR data, however, are hemispherical-directional reflectance factors for nonisotropic incident radiation. They include the effects of anisotropic diffuse irradiance scattered into the view direction. To equate the two measures, we will approximate the MISR measurement by using the proportion of diffuse skylight to total irradiance to adjust the value. This proportion is easily retrieved from the atmospheric correction procedure.

As demonstrated by Hu *et al.* (see Appendix D), the behavior of the atmospheric correction process can vary significantly depending on whether a Lambertian or anisotropic surface boundary is assumed. In this study, the forward mode of 6S was first used to calculate top of atmosphere simulated MODIS and MISR data in the red and near-infrared bands for four typical land cover types (Kimes *et al.*, 1983, 1985, and 1986). An angular sampling typical of MODIS and MISR for latitudes between 60°N and 60°S during a 16-day period in March was used, while atmospheric conditions were simulated for a continental aerosol model with a variety of aerosol optical depths.

First, an atmospheric correction using a Lambertian surface boundary was performed on the simulated top-of-atmosphere values. The hemispherical-directional, the directional-hemispherical, and the bihemispherical reflectances are all assumed to be one. The figures (Figures 1 and 2) and the RMSE tables

(Table 3) in Appendix D demonstrate the significant departure from the reality the Lambertian surface assumption causes in the shape of the BRDF.

Next, the Ambrals BRDF model is used to fit a surface BRDF to the values corrected with the Lambertian assumption and in combination with the atmospheric optical parameters, to generate new black-sky and white-sky albedos. These in turn are used to correct the top of atmosphere values. The figures (Figures 1 and 2) and tables (Table 4) in Appendix D show how closely the shape of the BRDFs derived from these newly corrected values matches that of the original BRDF.

The results of this work clearly show that a coupling of the surface reflectance retrieval with the BRDF will be required for accurate inference of both surface reflectance values and surface BRDF/albedo. The results also point out the danger of assuming isotropic surface reflectance.

3.2.5 Water Surfaces and Snow-Covered Surfaces

In certain regions or at certain times of year, there may be standing water on the land surface that will create a forward-scattering reflectance. Often such surfaces, such as rice paddies or flood zones, will be partly vegetation-covered. We have provisionally added a new kernel based on the Cox-Munk model (1954) for sea-surface scattering. (Note that we will not fit BRDF/Albedo functions where the land/water mask of Menzel (MOD35), carried by MOD09, indicates deep water bodies.)

Preliminary research has indicated that snow-covered vegetation will be adequately handled by the Ross kernels, although further research is need to validate these kernel models against field measurements and data. Flooding and snow cover conditions can occur abruptly and only exist for a short time. Work is currently underway to correctly accommodate such fleeting signals in the 16-day processing cycle of the product.

3.2.6 Topographic Correction

In addition to pixel shifts caused by topography, which should be corrected using level 1B navigation, there are a number of radiometric effects induced by topography. Holben and Justice (1980) defined one of these as the variation in radiance from an inclined surface compared with radiance from a horizontal surface, taken as a function of the orientation of the surface relative to the light source and the sensor position. However, this definition excludes any neighborhood effects that may be present, particularly at 1-km resolution. The most obvious neighborhood effect is shadowing, including both mutual and self-shadowing of surface projections. A less obvious topographic effect is the variation in path length within regions of complex terrain, which has been studied in some detail by Teillet and Staenz (1993) for vegetation indices.

Proy *et al.* (1989) looked at topographic effects produced by diffuse illumination variations that are caused by sky hemisphere obscuration and mutual illumination in rugged terrain. Although these radiometric effects are very small in sunlit areas, they can contribute up to one-third of the detected radiance in shadowed areas. Burgess *et al.* (1995) used Monte Carlo ray-tracing (Lewis and Muller, 1992; Muller and Dalton,

1988) to demonstrate that at the 1 km scale, even in rugged areas, residual topographic effects in NDVI can be swamped by surface (facet) BRDF effects, and suggest that it is typically more important to account for the latter than the former in NDVI products. However, the impact on individual wavebands, and hence on BRDF modelling, albedo etc., will tend to be larger. Muller and Eales (1990) performed a quantitative assessment of topography requirements and concluded that a global 100-m Digital Elevation Model (DEM) was needed to account for radiometric effects in 1-km resolution imagery.

Since the primary effects of topography are manifest through mutual and self-shadowing, the Li-kernels, which are based on physical models of mutual and self-shadowing of surface projections, may be expected to accommodate much of the effect of within-pixel topographic variation.

(Liang et al., 1996) has performed some initial simulation experiments using both radiosity and Monte Carlo ray-tracing on Gaussian elevation fields to assess the accuracy of simulated radiance fields which showed large differences between the radiosity and Monte Carlo ray-traced simulations. Simulation experiments are planned to be performed using 100-m DEMs, particularly for the coterminous U.S., to assess whether the semiempirical BRDFs can account for most, if not all, of the radiometric effects due to topography. In addition, this study will yield information on whether topographic radiometric corrections need to be made prior to BRDF calculations and if so, how these will be made (see, for example, Newton et al., 1991, for an example of the applications of Monte Carlo ray-traced reflectance fields and their application to the georadiometric correction of Landsat-TM data).

3.3 PRACTICAL CONSIDERATIONS

3.3.1 Cloud Cover

The MODIS BRDF/Albedo product depends on the retrieval of a sufficient number of cloud-free, atmospherically corrected bidirectional reflectances so that the BRDF of a surface pixel can be reconstructed with one of a selection of semiempirical models. However, the span of time over which these reflectances can be obtained from MODIS and MISR is constrained by the natural temporal variability of land surfaces. In transitional seasons (*e.g.*, spring and fall), a BRDF may remain constant for only ten days to two weeks, while at other times (summer or snow-free periods of winter) a BRDF may be applicable for a month or more. Therefore, the repeat schedule of the MODIS BRDF/Albedo product must balance the requirement to capture the natural temporal variability against the very real difficulty of obtaining sufficient cloud-free looks to reconstruct the BRDF adequately.

The MODIS cloud masks will be based on heritage algorithms from the International Satellite Cloud Climatology Project-ISCCP (Rossow and Gardner, 1993), the CLouds from AVhRr (CLAVR) approach (Stowe *et al.*, 1991), the Support of Environmental Requirements for Cloud Analysis and Archive (SERCAA) project (Gustafson *et al.*, 1994, Neu *et al.*, 1994), CO_2 slicing research underway at the University of Wisconsin (Wylie *et al.*, 1994) and spatial coherence techniques developed by Coakley and Bretherton (1982). The ISCCP algorithms depend on only two bands (0.6 and 11 μm) from both AVHRR and geostationary

satellites. Cloud/nocloud decisions are made at a 30-km resolution and the final global cloud amounts are provided every 3 hours on a 280-km grid. The CLAVR multispectral algorithms use only AVHRR data (bands 0.63, 0.86, 3.7, 10.7, 11.8 μm) and cloud/nocloud decisions are performed on groups of 4 GAC pixels. SERCAA algorithms make use of both polar orbiting (AVHRR and DMSP) and geostationary satellites and perform cloud/nocloud decisions at sensor resolution. Final results are provided on a 24-km resolution grid (although the sensor resolution cloud analyses can be retained if required). The CO_2 slicing techniques depend on High-resolution InfraRed Sounder (HIRS) polar orbiting data and use the 15 μm CO2 absorption band to detect clouds at various atmospheric levels. These algorithms are useful in detecting thin cirrus. The IR spatial coherence method is best used to discriminate between completely cloudy and clear pixels when the surface is homogeneous (such as water) and when both cloudy and clear fields stretch over large regions. The MODIS cloud masks can use the many spectral channels (and spatial resolutions) available on MODIS to incorporate aspects of all of these heritage algorithms. The 1.38 μm channel will be particularly useful in detecting thin cirrus. There will also be an attempt to use a mulispectral approach to flag areas of cloud shadowing although further research is needed on this issue. Neural nets and hierarchical decision trees are being explored to handle the difficult cloud detection cases posed by smoke, aerosols, and ice clouds over snow. The MODIS Cloud Mask will provide cloud/no-cloud analyses at 1-km and 250-m resolutions.

Those observations identified as cloud-free will be atmospherically corrected and then passed to the MODIS BRDF/Albedo algorithm. Additional pixels associated with optically thin clouds may also be corrected and incorporated into the database. After an appropriate amount of time, a sufficient number of colocated cloud-free, atmospherically corrected radiances should be available to reconstruct the BRDF associated with each 1 km grid cell.

However, some discussion was necessary to determine this appropriate amount of time. Several researchers involved in BRDF or albedo reconstructions have encountered problems in accumulating sufficient directional data. Meyer (1994), using some of the CLAVR cloud/nocloud algorithms on AVHRR data from the American midwest, had difficulty in obtaining the five or more cloud-free data points necessary to initialize a 4-parameter BRDF model (Pinty *et al.*, 1989). Meyer found that even after expanding his time constraint to 30 days, he was only able to obtain sufficient clear- sky radiances 60 percent of the time. Wu *et al.* (1994) used a semiempirical model (Roujean *et al.*, 1992) to compute top-of-atmosphere BRDFs from 1-km AVHRR data of 19 homogeneous land cover types in North America. They used CLAVR and spatial coherence cloud detection algorithms to isolate cloud-free data from the 1990-1992 growing seasons over each of the 20 km^2 sites. Even monthly accumulations of data revealed that only 30 percent of the data were cloud-free and therefore usable in reconstructing the various BRDFs.

These researchers' concerns in obtaining sufficient cloud-free data are also supported by some cloud analyses performed over a large region of east Asia with the SERCAA algorithms by the Geophysics Directorate, USAF Phillips Laboratory and Atmospheric and Environmental Research, Inc. (AER) in an informal collaboration with BU. AVHRR HRPT data of the east coast of North America were accumulated over the 18-day period September 3-20, 1994, and were carefully coregistered. SERCAA cloud algorithms were applied to

Table 6: Number of Cloud-Free Looks Obtained From the NOAA-12 AVHRR Over New England September 3–20, 1994

Clear looks:	0	1	2	3	4	5	6	7	8	9	10	11	12–18
Proportion, %:	10	1	2	4	6	11	14	10	11	15	12	4	0

a 402-by-400 km region on images from the NOAA-12 AVHRR, which has a morning local crossing time between 7:45 and 9:30 AM. Cloud cover statistics were generated on a 1-km basis (Table 6) Ten percent of all pixels were continuously obscured, and no pixel had more than 11 cloud-free looks. The median number of cloud-free looks was 7. Note that for the BRDF/Albedo Product, high, thin cirrus will be atmospherically corrected, thus increasing the number of cloud-free looks.

The experience of these researchers in accumulating cloud-free data for BRDF research led to the adoption of a 16-day MODIS BRDF/Albedo repeat cycle. Sixteen days will allow the acquisition of at least two MISR looks, and should greatly increase the chance that sufficient directional data will be available for use with the semiempirical BRDF models that make up the MODIS BRDF/Albedo Product. In the absence of clouds, 16 days would lead to between 30 multiangular observations available at the equator, and about 55 observations at 60 degrees latitude, subject to variation with season. Using a coarse statistic of mean global cloud cover probability (Wylie and Menzel, 1989; Wylie *et al.*, 1994) as a function of latitude, one may predict that generally about 15 to 20 multiangular observations will be available at all latitudes (except at the equator, where an abundance of cloudy conditions is likely to create problems).

3.3.2 Errors and Sensitivity

A number of problems may affect the accuracy with which BRDF and albedo are retrieved. These include random noise in the observed reflectances; systematic bias; angular sampling range and density; and change in the BRDF during the compositing period.

A systematic bias may be introduced into the observations from problems with atmospheric correction at large zenith angles and adjacency effects. A bias might also occur as a result of problems arising from combining the data of the MODIS and the MISR sensor, as they will differ in atmospheric correction, in the registration and resampling schemes applied, and in their slightly different spectral characteristics (see Section 2.6.1). We plan post-launch studies comparing simultaneous acquisitions of near-nadir center-swath pixels for MODIS and MISR to test for such biases and develop any needed correction algorithms.

Angular sampling patterns as a function of latitude and time of year will also have an influence on the accuracy of BRDFs and albedos retrieved. Although we may expect good angular coverage of the viewing hemisphere from MODIS and MISR, the range of sun angles will be restricted by the sun-synchronous orbit of the platform. Since the BRDF is inferred from a limited number of samples, the effect is to extrapolate

Table 7: Estimate of Average Number of MODIS and MISR Observations Available given Cloud Cover: Xsatview Orbital Simulation (Barnsley et al., 1994) and Cloudiness Probabilities From Wylie and Menzel (1989) and Wylie et al. (1994).

Latitude	Number of Clear-Sky Observations		Land Cloud	Number of Remaining Observations	
	Winter	Summer	Prob.	Winter	Summer
–80	166	0	0.33	111	0
–60	54	0	0.42	31	0
–50	47	42	0.54	22	19
–40	40	36	0.63	15	13
–30	34	31	0.33	23	21
0	31	34	0.90	3	3
30	36	40	0.45	20	22
40	42	47	0.60	17	19
60	0	54	0.57	0	23
80	0	166	0.33	0	111

the BRDF to solar zenith angles where no samples were acquired. This will affect the accuracy of black-sky albedo and carry over into the white-sky albedo, since the latter is the integral of black-sky albedo over all solar zenith angles. Thus, the angular ranges sampled as well as the density of samples in that range need to be taken into account when assessing the results of inverting the observations. The quality flags described in Section 3.3.5 and Table 1 will give some indication of the accuracy to be expected. Note that when data from the MODIS on the PM platform are introduced into the algorithm in the post- launch period, the range of sun angles and azimuths will be significantly expanded, thus mitigating this problem. Data from geostationary satellites, which observe with constant view angle but changing sun angle, will be used in the validation phase and could be incorporated into later versions of the product.

A sampling problem also arises in MODIS bands 5–7, as noted earlier in Sections 2.6.1 and 3.2.1.4. Since MISR does not record data in these wavelengths, BRDF/Albedo inference must be based entirely on MODIS measurements, a situation that restricts the range of available view zenith and azimuth angles. However, model selection is based on RMS error as measured only across bands 1–4. In this way, we ensure that the selected kernels are appropriate to the physical scattering mechanism of the cover type and are not simply chosen by accidents of noise in bands 5–7. Since the selection of a model specifies a type of scattering behavior, it constrains the shape of the BRDF, and thus we expect that fitting BRDFs in these bands will not be subject to large errors.

Yet another concern is that the BRDF and albedo of the land surface is not constant, but may be expected to vary with time. Vegetation growth and senescence will be a major cause of BRDF/Albedo change, since much of the scattering behavior of land surfaces is determined by the vegetation cover. Generally, vegetation processes vary slowly and may be regarded as constant during a 16-day period. However, rapid change may be expected at some times, as when a crop cover is harvested, or when a soil is wetted by rainfall just prior to an observation. Another possibility is that wind effects on vegetation canopies will change leaf angles sufficiently to influence the BRDF. Rapid changes of this nature may influence the BRDF and albedo retrieved during a cycle, especially if one of the MISR overpasses records a surface condition different from that seen by MODIS on other days in the cycle. In such a case, we may expect that the RMSE of the model fit will be larger, and the BRDF/Albedo value will be flagged with that characteristic. It may also be possible to detect and flag such major changes directly by such strategies as analyzing the time sequence of near-nadir measurements from both instruments. Also, a pre-inversion outlier analysis may be used to filter out extreme cases.

Landscape variability, convolved with the sensor's footprint as it changes with acquisition angle, will also add error. Although the surface cover may be quite varied at MODIS/MISR spatial resolutions of 250-m to 1.1-km, this does not present a problem for the BRDF/Albedo algorithm, since the semiempirical models are linear BRDF combinations. That is, the BRDF of the mixed pixel will be equal to the sum of the BRDFs of the different cover types within it as weighted by their relative areas, provided that adjacency effects may be ignored. This property is also important for degrading BRDF and albedo to spatial resolutions of less than 1.1 km when required, as for example for global climate modeling at 0.5° resolution.

However, scene heterogeneity is partly a function of resolution cell size. Given the larger projected IFOV of MODIS at extreme off-nadir angles, the effect will vary in magnitude across the instrument scan line. As a result, spatial autocorrelation will increase and we may also expect that angular samples obtained at extreme view angles will also be more highly correlated. One possible impact of this may be to smooth the apparent BRDF at extreme view angles by reducing the spatial variance in detected radiance (Barnsley and Kay, 1990). However, the product will be derived from MODIS bands with 250- and 500-m spatial resolution that are gridded 1-km; similarly, the MISR product will be derived from collapsing 275-m spatial resolution data to 1.1 km. These data characteristics will reduce the effect to an important degree. Some aspects of spatial scaling a briefly discussed in Appendix F.

A related effect is misregistration noise, in which the geolocation of an observation contains errors. If the errors are random and unbiased, then the effect will be to enlarge the effective footprint of the detector and smooth the BRDF. Note that extensive efforts will be made by both MODIS and MISR teams to reduce biases in geolocation using postlaunch characterization of instrument performance. Other than reducing the spatial resolution of the product, there is little that can be done to correct for the effects of errors in registration.

In order to accommodate noise, bias and sampling effects, we note that the inversion algorithm attributes individual weights to each observation. This allows us to lessen the impact of problematic data points by reducing their weight, rather than simply eliminating them. We may want to use some of the information in problematic points, especially if they were acquired in an angular range that is otherwise not well sampled.

Another factor influencing the quality of the product is data availability. The MISR Level 2 surface product will be phased in during the first five quarters following launch, so that in the immediate post-launch period, the BRDF/Albedo product will be derived only from MODIS data for many parts of the world. As the sixth quarter approaches, successively more area will be covered by the MISR product until land and tropical ocean coverage is complete. Quality flags will indicate when the BRDF/Albedo product is made for a grid cell without MISR data (see Table 1).

The issues of noise, bias and sampling need to be addressed systematically as part of the development of the product. The following two sections, as well as Appendices B and C which give greater detail, discuss the two most important of these effects: the influence of noise-like effects in the reflectances and the effect of changing and limited angular sampling on BRDF and albedo retrievals.

3.3.2.1 Retrieval Accuracies of BRDF and Albedo from MODIS and MISR Angular Sampling

Note: A full detailed report on the retrieval accuracies from MODIS and MISR angular sampling using the kernel-driven Ambrals semiempirical BRDF model is given in Appendix B. Please refer to this appendix for tables, figures and an in-depth discussion.

A study was carried out to determine the effects of the particular angular sampling available from MODIS and MISR on BRDF and albedo retrievals, and the effects of seasonal and latitudinal changes in

Table 8: Summary of Median Predicted Retrieval Accuracies at the Mean Sun Zenith Angle of Observation: All Latitudes, Times of Year, Biome Types.

Model	Albedo		Nadir Reflectance	
Ambrals	3.1	(0.5–9.6)	3.3	(0.7–8.1)
mod. RPV	3.2	(0.4–8.3)	2.7	(0.9–8.8)
mod. Walthall	5.0	(1.1–11.8)	14.5	(2.3–35.8)

that sampling on these parameters. Since the exact distribution of angular sampling is important for a study as this, and observed BRDFs are not sampled in a corresponding manner nor are available in conjunction with ground truth, the only way to conduct such a study is to use a complex numerical forward model to simulate observations and then use a simpler inversion BRDF model to invert them and derive quantities of interest. A comparison of this sort, model against model, clearly has its drawbacks, as problems found could be due to either model. For example, if the inversion model has problems fitting the BRDF at large zenith angles, the problem could be due to unrealistic behavior at large zenith angles in either model. Still, in the absence of real MODIS and MISR data this method is the best available to reach some understanding of the accuracy to be expected from MODIS and MISR BRDF and albedo retrievals given their specific angular sampling geometries.

The study was conducted as follows. The orbital simulation tool Xsatview (Barnsley *et al.*, 1994) was used to generate simulated MODIS and MISR viewing and illumination geometries for geographic latitudes of observation between 80 degrees south and 80 degrees north, and for 8 different 16-day time periods throughout days of the year. For each of the observation geometries generated, a discrete ordinates method radiative transfer code (Myneni *et al.*, 1992) was used to compute simulated observations of the bidirectional surface reflectance for six distinct BRDF types resembling six different land cover types in the red and the near-infrared (NIR) wavebands. These types were grasslands, semi-arid shrublands, broadleaf crops, savanna, broadleaf and needleleaf forests.

The resulting reflectances were then inverted using the Ambrals kernel-driven BRDF model. For comparison, the modified RPV BRDF model (Rahman *et al.*, 1993b; Engelsen *et al.*, 1996) and the empirical modified Walthall model (Walthall *et al.*, 1985; Nilson and Kuusk, 1989) were also inverted.

The accuracy and variation with which the following parameters were derived was investigated: nadir-view reflectance and black-ksy albedo at the mean sun angle of observation ("interpolation"); nadir-view (actually, 10 degree zenith angle to avoid the hotspot) reflectance and black-sky albedo at nadir sun angle; and white-sky albedo.

Table 9: Summary of Predicted Retrieval Accuracies: All Latitudes, Times of Year, Biome Types and Solar Zenith Angles, Irrespective of the Solar Zenith Angle of Observation. Median and Two-Thirds of Cases Range, the Ranges Being With Respect to Solar Zenith Angle.

Model	Albedo		Nadir Reflectance	
Ambrals	2.0–8.1	(0.5–16.0)	3.2–7.9	(0.7–28.7)
mod. RPV	2.5–7.9	(0.4–15.4)	2.3–10.3	(0.9–28.2)
mod. Walthall	3.5–26.5	(1.1–48.6)	8.7–19.0	(2.0–55.6)

Table 10: Summary of Predicted Retrieval Accuracies as a Function of Cloud Probability: All Latitudes, Biome Types and Solar Zenith Angles for a 16-Day Time Period Beginning Day of Year 96. Median and Two-Thirds of Cases Range, the Ranges Being With Respect to Solar Zenith Angle.

Prob. of Cloud	Albedo		Nadir Reflectance	
0 %	2.0–7.8	(0.7–18.4)	3.2–9.2	(0.4–31.4)
25%	1.9–8.0	(0.8–17.9)	3.2–9.0	(0.5–30.8)
50 %	2.3–8.1	(0.7–18.6)	3.1–9.2	(0.7–31.2)
75 %	3.1–9.0	(0.7–18.7)	2.6–9.3	(0.7–29.6)

In a first step, accuracies possible if no observations are lost to clouds were derived. These are the bottom-line accuracies that allow studying how additional effects lead to an increase of error. Table 8 summarizes error across band for retrievals at the mean sun angle of observation. The numbers given refer to the median (typical) relative error made and the range of relative errors typically found between good and bad retrievals. The Ambrals and the modified RPV BRDF models perform similarly well, with median accuracies of albedo and reflectance retrievals of only a few percent (less than 10 percent even in typical bad cases); but the modified Walthall model shows larger errors due to its empirical nature. This shows that the semiempirical models retain some of their physical properties despite the severe approximations made in deriving them. The modified Walthall model is attractive only because of its great mathematical simplicity, which is attractive to some applications where accuracy requirements are less strict.

Table 9 shows results for a more severe test. It gives median expected errors for retrievals not only at the mean sun angle of observation but at other sun angles (0, 30 and 60 degrees) as well, testing extrapolation of the derived parameters away from the angles of observation. The numbers given refer to the median (typical) relative error made, the range being with respect to variations in the sun zenith angle of prediction, and the range of relative errors typically found between good and bad retrievals. Despite the severity of the test, one may see that both nadir-view reflectance are retrieved to within 10 percent at all sun zenith angles, irrespective of the angle of observation. Again results for the modified RPV model are very similar, but those for the modified Walthall model are clearly inferior, with median errors of up to 25 percent found at some sun angles.

Table 10 determines whether these accuracies are expected to strongly deteriorate as observations are lost to cloud cover. It shows that this is not the case even if 75 percent of observations are (randomly) lost. This is true if loss is such that the angular sampling patterns gets sparser, but good angle coverage is retained. Retrievals are expected to still be approximately accurate in line with Tables 8 and 9 in the presence of clouds.

Please refer to Appendix B for a full report of this retrieval accuracy study, including tables, figures and more detailed analysis.

3.3.2.2 Sensitivity of MODIS and MISR BRDF and Albedo Retrieval to Noisy Data

Note: A full detailed report on the noise sensitivity of the kernel-driven Ambrals semiempirical BRDF model for MODIS and MISR angular sampling is given in Appendix C. Please refer to this appendix for tables, figures and an in-depth discussion.

Actual measurements of surface reflectance will always include a certain amount of noise, which may be random, systematic, or a combination of both. Such noise will result in error in retrievals of BRDF parameters and albedo. A key criterion to assess the validity of the retrieval process is to verify that it does not amplify the noise-like errors associated with individual measurements of surface reflectance. In order to investigate this problem, a full noise sensitivity study was conducted for the Ambrals BRDF model.

The behavior of kernel-driven BRDF models under the conditions of varying angular sampling and noisy

data can be studied analytically due to the mathematical form of these models. It is given by the the so-called "weights of determination", calculated using theory that originates with Gauss (Whittaker and Robinson, 1960). Kernel-driven models give the reflectance R in form of a sum, $R = \sum f_i k_i$, where f_i are the model parameters and k_i are mathematical functions ("kernels") giving basic BRDF shapes depending only on sampling geometry. The expected error in a term u given by a linear combination of model parameters, $u = \sum f_i U_i$ (e.g., R itself at a given combination of angles, or integrals of the BRDF such as directional and diffuse albedo), is given by $\epsilon_u = e/\sqrt{w_u}$, where e is the estimate of standard error in the observed data (approximated by the RMSE in model fitting), and $1/w_u$ is the weight of determination of term u under the sampling considered. This weight is given through $1/w_u = [U]^T[M^{-1}][U]$, where U is a vector composed of the terms U_i and M^{-1} is the inverse matrix providing the analytical solution to the problem of inverting a set of reflectances R_i for model parameters f_i minimizing a given error function. Note that this analysis is independent of any specific BRDF function.

In our investigation, we have studied the sensitivity to random noise of all kernel combinations that comprise the Ambrals BRDF model using sampling for a variety of combinations of the MODIS and MISR sensors, and for different periods of data accumulation. From these, we here report selected findings on 16-day sampling only for 3 different sensor combinations. Both interpolating and extrapolating the BRDF were tested in that nadir reflectance and directional-hemispherical ("black-sky") albedo were derived both at the mean sun angle of the observation and for nadir sun. Additionally, bihemispherical ("white-sky") albedo and the model parameters themselves were investigated.

Table 11 summarizes findings. The base case studied was 16-day sampling for combined MODIS and MISR data, as for the MODIS BRDF/albedo product. We further investigate whether using MODIS data alone is an option, and whether a second MODIS sensor to be launched on the EOS-PM-1 platform is a potential substitute for MISR in view of the three additional bands that MODIS has over MISR. Table 11 lists first the median weights of determination found for sampling throughout the year and at all latitudes. Given are the values found for the BRDF model with the smallest and with the largest median weight. Second, it gives the worst-case range of values. Range here is defined as the central two thirds of values occurring.

Results show that the MODIS-AM/MISR sensor combination will allow retrieval of the BRDF with an accuracy that is smaller than the RMSE of the inversions (weights if determination smaller than one). Retrieval of nadir reflectance and black-sky albedo at the mean prevailing sun zenith angle is very stable and more reliable than deriving these quantities for a nadir sun. But even the latter, requiring extrapolation of the BRDF to angles where typically no observations were made, is possible with an accuracy of less than the value of the RMSE. The same is true for the white-sky albedo. The expected error of the model parameters themselves is larger than that of derived quantities. Naturally, cloud cover will increase these error estimates. Assuming that the angular distribution of samples is not affected by loss of observations due to clouds, the weights of determination can be shown to increase as $1/\sqrt{N}$, where N is the number of observations.

Table 11: Median Weights of Determination (left) and Worst-Case Ranges of Weights of Determination (right).
Left: smallest and largest median error of models; Right: smallest and largest worst case model error.
Rnad = reflectance at nadir view angle; bsa = black-sky albedo; wsa = white-sky albedo; f_{vol} = volume scattering kernel coefficient; f_{geo} = surface scattering kernel coefficient.

		Median Error Weights			Worst-Case Ranges of Error Weights		
16–day sampling		MODIS–AM + MISR	MODIS–AM	MODIS–AM+PM	MODIS–AM	MODIS–AM	MODIS–AM+PM
Interpolation	Rnad	0.18–0.23	0.30–0.40	0.17–0.23	0.18–0.28	0.29–0.44	0.17–0.25
$\theta_s = \langle\theta_s\rangle$	bsa	0.16–0.18	0.25–0.55	0.15–0.29	0.15–0.20	0.40–0.72	0.23–0.41
Extrapolation	Rnad	0.17–0.93	0.28–3.45	0.16–1.94	0.73–1.08	1.47–5.72	0.86–3.18
$\theta_s = 0$	bsa	0.18–0.28	0.29–0.82	0.17–0.45	0.19–0.49	0.30–2.54	0.17–1.47
Global, $\int \theta_s d\theta_s$	wsa	0.17–0.42	0.31–1.60	0.18–0.95	0.21–0.82	0.66–2.42	0.40–1.41
Parameters	f_{vol}	0.15–0.89	0.39–2.01	0.23–1.19	0.33–1.76	1.21–3.52	0.72–1.97
	f_{geo}	0.27–0.60	0.68–2.32	0.39–1.28	0.45–0.69	0.99–3.73	0.58–1.99

Using the MODIS-AM sensor alone yields a worse product quality, notably for nadir-view nadir-sun totally angle corrected reflectance, and nadir-sun albedos. This emphasizes the importance of combining MISR data with MODIS data for a sound retrieval. The MODIS-AM/MODIS-PM sensor combination will allow a better retrieval than when using MODIS-AM alone, but is not as good as using MODIS-AM/MISR. This suggests that MISR should also be used in retrievals after the launch of MODIS-PM in the four bands concerned.

In summary, these results show that BRDF and albedo can be retrieved from noisy reflectance data both at the prevailing mean sun angle of observations and at other angles to within a fraction of the noise RMSE under conditions of angular sampling as obtained from the combined MODIS and MISR sensors, using the kernel-driven Ambrals BRDF model. The noise sensitivities reported will increase as cloud cover leads to a loss of observations, but since the numbers reported are mostly rather small, this will not constitute a major problem.

For comparison, an equivalent analysis was also conducted for the modified RPV BRDF model, showing that it is similarly stable with respect to albedo and reflectance retrievals (two of its three parameters seem to be rather susceptible to noise, though). Where one model has an increased susceptibility to noise, the other does, too, demonstrating that the problem lies in the angular distribution of samples available, not in the models themselves.

Please refer to Appendix C for a full report of these noise sensitivity results, including tables, figures

and more detailed analysis.

3.3.3 Numerical Computation Considerations

On the computational side, the two issues of interest are requirements in computing power and storage size of the output product. No special requirement is foreseen for the memory required for execution of the algorithm.

Timing was conducted on the version 1 software delivered in the summer of 1996 at SDST. There are two processes currently being delivered for the BRDF/Albedo product. One is the multiangular 1-km reflectances database building process (MOD43B1) which serves several other products besides BRDF/Albedo and is in itself not strictly related to BRDF and albedo retrieval. Running on the SDST-supplied synthetic data set, scaled for latitudinal variations in the number of observations occurring, and including a 4/7 share of processing for MISR data, this process is currently estimated to require 400 MFlop/s of computing power.

The actual BRDF and albedo process (MOD43B2) was timed not using the synthetic data set but a more realistic SCF-produced data set. This set was more realistic in that it contained a BRDF (which the SDST-provided synthetic data set does not) and it was scaled to reflect typical average numbers of observations. The process is currently estimated to require 300 MFlops/s of computing power.

These numbers were derived using SDST-provided assumptions and following SDST's computing outline.

Increases in speed are possible for the version 2 code but hard to quantify at present.

The size of the BRDF/Albedo Product is found to be 33.1 GByte in 16 days or 2.1 GByte per day, each subdivided into sets of 355 tiles, for land only.

3.3.4 Calibration and Validation

The prelaunch efforts to validate the BRDF/Albedo Product emphasize: (1) a validation of the ability of the semiempirical models to fit observed measurements of bidirectional reflectance, and by integration, albedos; and (2) a validation of the ability of the algorithm to process data acquired over large regions in an appropriate and efficient fashion. In the postlaunch era, validation efforts will focus on a comparison of the BRDFs and albedos produced by the operating algorithm with the actual measurements acquired during the initial period of product compilation.

All of these efforts rely on the availability of diverse, well characterized test sites with sufficient ground instrumentation to accumulate comprehensive validation data sets. The MODLAND products teams are embracing the EOS test site five-tiered hierarchy of (1) Intensive Field Campaigns (such as Boreas and LBA); (2) Fully Instrumented Long Term Super Sites (such as the ARM/CART sites); (3) Biome Tower Sites (networks of long term instrumented sites such as LTER); (4) Globally Distributed Test Sites (minimally instrumented permanent sites widely distributed over the globe such as SURFRAD or the NOAA CMDL Flask Network); and (5) Instrument Calibration Sites (such as White Sands). While individual team scientists are involved in all the recent and planned Intensive Field Campaigns, and at the ARM/CART

sites, White Sands or Railroad Playa, the MODLAND team is specially focusing on the development, characterization and instrumentation of the Tier 3 and 4 sites. The current plan is to have 10 Tower Sites in place prelaunch and add 10 more soon after launch with as many as 60 operating worldwide eventually. Quantities to be observed for radiometric validation are the following: (1) atmospheric properties (aerosol optical thickness and properties, water vapor, ozone); (2) irradiance characteristics (downwelling irradiance total and angular distribution); (3) reflectance characteristics (land surface BRDF, directional-hemispherical reflectance and bihemispherical reflectance); (4) land surface properties (land surface/canopy type and major structural characteristics, current seasonal state, LAI, leaf reflectance, soil brightness and type). The instrument package (CIMEL multi-directional sunphotometer, pyranometer, pyrgeometer, gas flux instrumentation, and basic meteorological instrumentation) and temporal and spatial sampling plans will be prototyped at two existing research sites (the SALSA site and the Oak Ridge site) in the summer of 1997.

In addition to ground measurements from these Tier 3 Tower Sites or from Tier 2 Intensive Field Campaigns, the BRDF/ALbedo Product validation effort will rely extensively on laboratory measurements, modeling exercises, and data from multidirectional aircraft and space based sensors.

3.3.4.1 Validation of Model Fit. Future validation of the ability of semiempirical models to fit observed data involves laboratory, field, and aircraft measurements. In the laboratory, data from two ongoing research programs are of particular interest. The first program involves a collaboration between Boston University and the Chinese Academy of Science. As a part of this program, data were acquired under our direction at a unique Chinese facility-the Solar Simulation Laboratory of the Jingyuetan Remote Sensing Test Site, Changchun, China (Strahler and Liang, 1994). In this laboratory, we illuminated several target plant canopies of 1 m2 extent with a parallel beam from an arc lamp providing near-solar illumination conditions. A semicircular framework, moving in a circular target around the track, supported radiometers acquiring measurements at 10° increments of view zenith and azimuth in Thematic Mapper Bands 1–4. Solar zenith angle was variable between 0° and 45°. Data acquired in 1994 and 1995 included canopies of soybean, nasturtium, and other plants as well as bare soil. Because these data were acquired without significant diffuse illumination, they do not require atmospheric correction. The data are currently in the analysis phase, and early indications are that the semiempirical models fit the observations very closely (Strahler *et al.*, 1996). More data acquisitions are planned for 1997.

A second set of laboratory data that is being used to test the fit of the semiempirical models to reflectance measurements has been acquired by J. Miller at York University – multiband, multiangular measurements of reflectance of an artificial conifer canopy acquired by the Compact Airborne Spectrographic Imager (CASI) instrument (Babey and Soffer, 1992). The canopy consists of model trees designed to simulate the physical shape and structure of individual conifer crowns (Soffer and Miller, 1995). They are sprayed with cellulose material that emulates the spectral response of leaf tissue, and are arranged according to field measurements of real conifer stands. This laboratory setup allows a systematic exploration of the influence of background

brightness, tree density, and solar zenith angle on the BRDF in a way that is not possible in a field campaign. In tests involving a random spatial distribution of trees and a spatial pattern resembling the BOREAS Jack Pine site, the semiempirical models have fit the data quite well.

In addition to these direct laboratory measurements, numerical simulation studies using the Monte Carlo ray-tracing system (Lewis and Muller, 1992) and Botanical Plant Modelling System (Lewis, 1990; Lewis *et al.*, 1991) will be used at UCL to simulate directional reflectance measured by instruments with an equivalent pixel IFoV of 3m at the vegetation canopy level. (see section 3.1.4.2 for more details as well as Appendix H).

This effort is providing a full simulation of all the characteristics affecting the BRDF and albedo under controlled conditions. In particular, the influence of the BRDF of plant components (such as leaves) and the soil on the canopy-level BRDF can be studied. This effort will also aid in understanding how semiempirical BRDF parameters may be interpreted in a physical sense and whether any of the parameters, such as LAI, have any physical significance. Simulation of datasets for HAPEX-Sahel are the primary focus of the work at present.

Another source of model validation data exists in ground measurements of surface radiance as a function of view and illumination positions. Such data are usually expressed as bidirectional reflectance factors (BRFs) and include the effects of diffuse (sky) irradiance of the target. However, there is no barrier to fitting these data to semiempirical models as long as it is noted that the functions describe BRF observations rather than true BRDFs. In such cases, the presence of skylight will smooth the BRDF shape to some degree. Thus far, we have fit semiempirical models to over 27 sets of observations with very good results (see Section 3.1.4.1 and Appendix A). These include the classic datasets of Ranson *et al.* (1985), Kriebel (1978) among others. In addition, a considerable archive of angular surface reflectance data acquired by D. Deering with the PARABOLA instrument was been tested. There are also plans to collocate PAROBOLA with the CIMEL directional sun photometer during the Tier 3 Tower Site prototype exercise in the summer of 1997. It is hoped that a downward pointing scanning CIMEL photometer will adequately characterize the BRDF in the vicinity of the tower in an automated fashion and provide a valuable source of pre and post launch validation data.

As part of the ongoing collaboration between the Boston University Center for Remote Sensing and the Chinese Academy of Science (CAS) Institute of Remote Sensing Application (IRSA), we will also acquire field data from an agricultural experiment station located at Yucheng, Shandong Province, China. Instead of multiangle measurements made during a short time period, we will observe crop reflectance from a fixed position on a nearby tower as sun angle changes during the day. In this way, we will observe the day-to-day variability of directional reflectance as environmental and crop conditions change.

Aircraft acquisitions are a further source of directional reflectance data. The principal source of such data is the ASAS (Advanced Silicon Array Spectrometer) instrument (Irons *et al.*, 1991), which acquires fine spatial resolution multispectral measurements at view zenith angles from $+75°$ (forward) to $-60°$ (aft) in the flight direction. Typically, observations are made along the principal plane, across the principal plane, and at an azimuth angle of $45°$ to the principal plane. Most ASAS data are of homogeneous targets and

are accompanied by measurements characterizing aerosol properties and optical depth, allowing testing of the BRDF-atmospheric correction loop (see Section 3.2.4). Among the investigators on the BRDF/Albedo team, we already have about a dozen ASAS datasets that may be used for validation.

ASAS data from the Hapex-Sahel has been processed at UCL to remove geometric distortions due to aircraft motion (Allison et al., 1991; Allison and Muller, 1992; Allison et al., 1994). Unfortunately, the C-130 aerial photographs taken at the same time as the ASAS imagery were not taken with sufficient stereo overlap to create detailed DEMs and orthoimages and no GPS-based control has been able to be acquired from HSIS for geocoding of the aerial photographs using a 30m DEM created using ERS tandem SAR interferometry. However, using the 6S simulation system (Vermote et al., 1994) and in situ atmospheric optical depth measurements from Halthore (Brown de Coulstoun et al., 1996) , it was possible to atmospherically correct the data (see Section 3.1.5.2). Barnsley et al. (1996) describe how multiple flight-lines of ASAS processed data over the HAPEX- Sahel southern super-site were used to retrieve empirical (Walthall) BRDF distributions at 3m resolution using the aforementioned methods (see Appendix J). Work has been completed at UCL to process the entire HAPEX-Sahel dataset (18 flight-lines over 3 sites) into "at surface" reflectance". These registered reflectance maps have been used to invert "ambrals" and for two models (modified Walthall and RossThick-LiSparse) have been used to derive spectral BRDFs and spectral albedos for a complete LANDSAT-TM scene (see section 3.1.5.2 and Appendix G). The derived albedos, once integrated over the shortwave region, will be compared with in situ measurements acquired by solarimeters (Allen et al., 1994). Work is also underway at UCL to extend these studies to other ASAS flight-lines, where the other necessary datasets (e.g., atmospheric optical depth measurements, aerial photographs, DEMs) are available.

In addition to this work, similar inversions will also be made at UCL with atmospherically-corrected airborne POLDER data over HAPEX-SAHEL (Roujean et al., 1996) and BOREAS (Bicheron et al., 1996; Breon et al., 1996) and results compared with those from ASAS (see Section 2.6 for more detail on the POLDER instrument). POLDER simulator data are also available for the La Crau test site in southern and for BOREAS (V. Vanderbilt, personal communication). At present, the La Crau data are being fitted to semiempirical models at CAS-IRSA under the direction of X. Li, a member of the POLDER Science Team who is also a member of the BRDF/Albedo product team.

A similar airborne instrument belonging to the Chinese Academy of Science acquired data from the Changping region, near Beijing, in the fall of 1995. These data sets are currently being analyzed.

J. Miller of York University has also indicated interest in fitting the semiempirical models to airborne CASI data acquired during BOREAS from stands of old jack pine, with and without a ground cover of snow (J. Miller, personal communication).

An excellent source of future airborne measurements will be provided by the AirMISR which will begin acquiring data early in 1997. Several of the sites initially scheduled for overflights will also supply PARABOLA data thereby generating very interesting BRDF validation data sets. Coordination is underway between MODLAND and MISR to schedule several overflights of the intitial Tier 3 MODIS Biome Tower sites early in 1998.

3.3.4.2 Large-Area Application In addition to validation of the ability of the semiempirical models to describe BRDFs and infer albedos, there is a need to apply the BRDF/Albedo algorithm to MODIS-like data from large areas to validate the operational aspects of the algorithm. The most suitable data for this purpose are AVHRR LAC data, since the AVHRR has a view geometry and pixel size in LAC mode similar to that of MODIS, although the orbital crossing times are somewhat different.

As described in Section 3.3.1, AVHRR LAC data from the east coast of North America are currently being accumulated by the Geophysics Directorate of the USAF Phillips Laboratory and Atmospheric and Environmental Research, Inc., in an informal collaboration with Boston University. The primary objective is to characterize the BRDF of the surface as an aid to cloud detection for use in cloud characterization algorithms. In addition to providing information on the availability of cloud-free surface observations, the study will exercise the BRDF/Albedo algorithm over a large region through time. Although there are no supporting ground truth data for BRDF or albedo for direct validation, we can nonetheless check for reasonable results. The study will help us both to understand better operational problems and constraints, and to estimate processing times more accurately.

A similar AVHRR LAC dataset is also being accumulated in China for a 54,000 km2 region incorporating the area expected to be flooded following the completion of the Three Gorges Dam on the Yangtse River. Data acquisition, which started in early 1995, is supported by the National Science Foundation of China and the CAS Institute of Remote Sensing Applications under a grant with X. Li as Principal Investigator. As part of the project, ground truth measurements will be acquired that can be used to test BRDF/Albedo retrievals directly. Dr. Li is also a member of the SPOT-VEGETATION team, with an approved proposal to use SPOT-VEGETATION data for environmental surveillance of the Three Gorges Dam region. Thus, we may be able to use SPOT-VEGETATION data in validation as well (see Section 3.3.4.3).

In yet another AVHRR application, D. Meyer at the EROS Data Center is applying semiempirical models to AVHRR LAC data for a transitional region in the northern midwest that exhibits a range of vegetation covers. The study will focus on albedo retrieval and model selection for the various cover types. Some ground validation data will also be acquired (D. Meyer, personal communication).

GAC data from the AVHRR Pathfinder dataset can also serve as a source for testing large-scale application of the BRDF/Albedo algorithm. However, this application is limited by the subsampling pattern of the instrument in GAC mode, as well as by problems of geometric accuracy and atmospheric correction.

Data from the ADEOS borne POLDER instrument is also very useful in validating the BRDF/Albedo algorithm. Since it acquires successive overlapping images of the ground along the orbital path, it is closer to MISR in its imaging characteristics than to MODIS. The instrument is discussed in more detail in Section 2.6. It provides the opportunity to apply the BRDF/Albedo algorithm in an operational context and also allow some measure of validation with ground truth. This effort is supported by X. Li and M. Barnsley, members of the POLDER Science Team who are also a members of the MODIS BRDF/Albedo team, as well as M. Leroy, who is heading the POLDER surface reflectance-BRDF effort. Test sites for acquisition of POLDER data range from La Crau, FIFE and BOREAS sites to the previously mentioned Changping and Yucheng

sites in China.

3.3.4.3 Postlaunch Validation During the postlaunch validation phase, emphasis will be placed on comparing the BRDF/Albedo Product with (1) ground data at the Tier 3 and 4 EOS Test Sites; (2) ground data from Tier 2 sites-of-opportunity in connection with future multidisciplinary field experiments (*e.g.*, FIFE, BOREAS, LBA); (3) MISR surface reflectance, BRDF and albedo products; (4) POLDER surface reflectance, BRDF and albedo products; and (5) possible BRDF/Albedo products from AVHRR Pathfinder.

The MISR instrument is colocated with MODIS on the AM platform and, although the MISR surface reflectance data are used in the MODIS BRDF/Albedo Product, the single instrument products can also serve as a source of validation. The MISR Surface Product depends on the Rahman–Pinty–Verstraete model (RPV) (Rahman *et al.*,1993) in a form modified by Martonchik (Englesen *et al.*, 1996) to supply BRDF and albedo parameters (Diner *et al.*, 1996; Maronchik, 1997). As shown by Wanner (see Appendix B), either the RPV or the Ambrals models retrieve these parameters with reasonable accuracy. Postlaunch validation will therefore include a component of comparison to highlight the similarities and differences between these products and address the effects of difference atmospheric correction schemes, temporal variation and spectral coverage.

Other satellite-based postlaunch validation opportunities concern the SPOT–VEGETATION instrument and the meteorological satellites. SPOT–VEGETATION, due for launch several months after the AM platform, is a wide-field, three-band (blue, red, near-infrared) pushbroom instrument with a 1-km spatial resolution. It differs from the AVHRR primarily in its blue band and in the fact that its spatial resolution, by virtue of the pushbroom design, will be constant in the across-track direction. At this time, the SPOT–VEGETATION science plan is still under development, and we are not certain which products will be most useful for validation.

Current and future GOES US geostationary meteorological satellites have improved, onboard, visible radiometric calibration (not available before GOES-8) and finer 10-bit (vs. older 8-bit for pre-GOES-8) radiometric resolution at a nominal 1-km spatial resolution. With these characteristics, spatially coincident geostationary and polar orbiting data may be helpful in validation of the BRDF/Albedo product. In contrast to MODIS/MISR, in which view angle and azimuth vary freely while sun position is constrained by latitude and the platform crossing time, geostationary satellites hold view position constant through the day, while sun position changes throughout the full diurnal cycle. Given auxiliary data on the atmospheric state throughout the day covering the MODIS swath, it will be possible to compare the exoatmospheric radiance directional reflectance for any given area based on the MODIS/MISR BRDF at a variety of different solar angles with the exoatmospheric radiance available from GOES. Eventually with MODIS-PM data it may be possible to improve the accuracy of the BRDF extrapolation to other solar angles (van Leeuwen et al., 1996). In addition, it may eventually be possible to integrate GOES-derived "at-surface" directional reflectance to provide for diurnal cycles of albedo which are required by hydrologists.

Arino *et al.* (1991, 1992) and Dedieu (1992) provide an approach to validation for AVHRR with ME-

TEOSAT that may be useful for the BRDF/Albedo product in the postlaunch period. In this method, geostationary satellite exoatmospheric radiance is predicted using the surface BRDF and the derived atmospheric parameters, assuming a constant atmosphere for the time interval under study. The GOES-Next series of satellites will be particularly relevant for this purpose, although their spectral bands are much broader than MODIS. At-satellite radiance is predicted using atmospheric codes such as 6S (Vermote *et al.*, 1994). If the terrain is suitably rugged (see discussion in Section 3.2.6), the simulation may also need to take into account mutual illumination effects. Monte Carlo ray-tracing (Lewis and Muller, 1992; Muller and Dalton, 1988) can then be used to represent these multiple scattering events. However, the large computational requirements of ray tracing will probably restrict its use to a few well-defined EOS test sites.

Polar orbiting instruments, such as SCARAB and CERES, which will be on multiple platforms, will also provide the opportunity to validate BRDF/Albedo in the context of the global radiation budget. CERES will provide shortwave albedo from the same platform as MODIS. However, the coarser resolution of CERES and the greater likelihood that partial fields-of-view will be cloud-covered pose some obstacles to direct comparisons with the CERES albedos with the BRDF/Albedo product.

In addition to these directly sensed measurements, the BRDF/Albedo product can be validated by comparisons with existing coarse-resolution global albedo databases. These range from static parameterizations based on land cover (such as the ISLSCP Initiative I and II products for albedo) to satellite-based observations in broad and narrow bands by METEOSAT and, in the past, by ERBE (Earth Radiation Budget Experiment). Li and Garand (1994) enumerate these datasets more fully. For BRDF, the scene- dependent top-of-atmosphere angular reflectance models of ERBE (Barkstrom and Smith, 1986; Taylor and Stowe, 1984) are an obvious point of comparison, although the footprint of ERBE radiometers is about 40 km at nadir. A comparison with these coarse resolution databases will be facilitated by the use of linear semiempirical models of BRDF/Albedo, which can be easily aggregated to coarse resolutions for quantitative overlays to alternative datasets.

3.3.5 Quality Control and Diagnostics

MODIS standard data products are comprised of science data sets and metadata. The EOSDIS Core System (ECS) architecture provides for the storage of QA results in both the metadata and in the science data sets. Mandatory ECS QA flags are stored in the core metadata. These mandatory flags include QA statistics and text that summarize the application of runtime or post run time QA procedures. Additional QA information can be stored by the science team members in the product metadata.

Spatially explicit QA results are stored in the science data sets. MODLAND has developed a QA plan for these spatially explicit QA results (Roy, 1996). This specifies two QA science data sets (a mandatory and an optional) for each distinct data product and at each spatial resolution. The mandatory QA science data set will include information on cloud state (bits 0-2), overall quality information (bit 3) and crucial product specific QA (bits 4-7). A synopsis of the QA definitions will be stored in a text based field in the product metadata. The science team members will determine the content of the crucial QA results. Additional

product specific and spatially explicit QA results can be stored in the optional QA science data set (which can have any number of bits and any structure and content).

The BRDF/Albedo product envisions a number of quality and consistency flags to allow assessment of the reliability of the data produced (Table 12). Since different applications may require different levels of accuracy, our approach is to be rather generous in supplying a result and then to indicate by a flag whether a result is less reliable. In this way, each user can decide which data of which quality will be used and which discarded, instead of this decision being made at the production level.

At present 4 words worth of QA are defined for the BRDF/Albedo product. That encompasses one word of QA for the best BRDF model (lowest RMSE), one for the globally applied BRDF model (modified Walthall), and two for generally applicable information. Identification of the 4 bits worth of QA information deemed most crucial (and therefore stored in the mandatory QA science data set) is still being explored at this time. The remainder of the QA results will be stored in the optional science data set.

Currently part of the first two words will include a general quality flag for the BRDF model with eight possible settings summarizing the more detailed quality flags that follow. Flags from input products signaling problematic input may lead to a deterioration of the value of this flag. Further flags in the first two words indicate whether the BRDF given is newly computed from data, computed with a predetermined model, computed with a predetermined shape or from a default (probably landcover based) source. Another flag indicates whether the fit was equally good in all wave bands or whether a particular range of bands produced worse fits.

Flags in the third word indicate coverage and density of sampling in viewing and illumination hemispheres, allowing the user to roughly assess the zenith angle range utilized and the density and relative orientation of samples in azimuth. A flag indicating whether an atmospheric correction loop was performed is also included in this word.

Finally, in the last word, information on the effects of topography, the compositing period, possible reasons product might not have been produced, and availability of MISR data is stored.

In summary, the quality of the data delivered will be assessed by analyzing the input data (and its associated quality flags if applicable), by checking the consistency of the result with respect to previous findings for that pixel, and by understanding the sensitivity of particular results to various influences.

3.3.6 Exception Handling

Pixels associated with line dropouts, detector failures and the like problem will be eliminated from the accumulation of data to be gridded and inverted in the production of the BRDF/Albedo product. Pixels associated with clouds, cloud shadows, cloud adjacency, and water surfaces will also be eliminated. In most cases these pixels have been flagged by the surface reflectance product (MOD09). Regions where insufficient values exist to invert the Ambrals models will be supplied or adjusted by a model or shape predetermined from either the previous product or an ancillary generic BRDF. Information about these decisions will be conveyed in the QA flags.

Table 12: Version 1 BRDF/Albedo Product Quality Assurance Flags.

Word 1 (Best Fit BRDF) and Word 2 (Globally Applied BRDF)			
Bit	Flag	Key	
00–02	Overall Quality	0=not processed	4=acceptable
		1=bad	5=fair
		2=problematic	6=good
		3=unsatisfactory	7=very good
03	Land cover use	0=not used	1=used
04–05	Inversion status	0=new	2=shape predetermined
		1=model predetermined	3=default estimate
06–07	Fit over bands	0=even across bands	2=poor in bands 5–7
		1=poor in bands 1 or 2	3=others

Word 3 Angular Information			
Bit	Flag	Key	
00–01	View Angle Coverage	0=parameter problematic	2=parameter moderate
		1=parameter weak	3=parameter good
02–03	Sun Angle Coverage	0=range 0–10°	2=range 20–30°
		1=range 10–20°	3=range 30–90°
04–06	Median Sun Angle	0=range 0–10°	4=range 40–50°
		1=range 10–20°	5=range 50–60°
		2=range 20–30°	6=range 60–70°
		3=range 30–40°	7=range 70–90°
07	Atmospheric Correction	0=not iterated	1=iterated

Word 4 General Information			
Bit	Flag	Key	
00–01	Topographic Effects	0=no topographic effects	2=some effect from varied topography
		1=uniform slope	3=strong effect from varied topography
02–03	Nonproduction Reason	0=not enough looks	2=ocean
		1=inland water	3=bad data or code problem
04	Period Used	0=16 days	1=32 days
05	MISR Availability	0=not used	1=used
06–07	spare		

3.3.7 Data Dependencies

The input data include:

Required data

• Gridded MODIS surface reflectance data (product MOD09) in the seven MODIS land bands (1–7), including information on atmospheric state passed to the BRDF/Albedo algorithm as an internal product

• Gridded MISR surface reflectance and atmospheric parameters (MISR Level 2 Aerosol/Surface Product)

• Level 2G Footprint Pointers

• Angular Information

Supporting Data

• The MODIS Land Cover Product (MOD12)

• The BRDF/Albedo product from the prior time period

• An ancillary generic BRDF/Albedo database

• Topographic information on within-pixel slope facet angles and orientations from a 100-m resolution DEM for topographic correction (postlaunch)

• Atmospheric state

3.3.8 Output Products

Table 1 provides a complete description of the BRDF/Albedo product output . The principal features are:

• Best-fitting BRDF model identifier, with parameter values, RMS error, black-sky albedo function coefficients and white-sky albedo for the model

• Parameters and RMS error for the modified Walthall model

• A comprehensive set of flags describing overall quality, band-wise quality, sun and view angle coverage, and consistency for the best- fitting model.

4 CONSTRAINTS, LIMITATIONS, ASSUMPTIONS

Constraints, limitations and assumptions are largely discussed *ad seriatim* in the body of this document. A brief itemization is provided below.

4.0.9 ASSUMPTIONS AND CONSTRAINTS

• MISR/MODIS data are georegistered with sufficient accuracy that BRDF/Albedo calculations are not significantly affected by misregistration

. • The resampling inherent in georegistration of MISR radiances does not significantly affect BRDF/Albedo retrievals.

• The derivation of atmospheric parameters from MISR and MODIS is sufficiently accurate that BRDF/Albedo calculations are not significantly affected by their errors.
• The physical parameters controlling BRDF/Albedo remain constant during the production cycle, although we plan to screen for obvious changes.
• Topographic effects on BRDF can be described within the semiempirical model fitted to the pixel (at launch) or separated from surface cover (postlaunch)
• The Ambrals semiempirical BRDF model kernel are sufficiently complete to describe well the range of BRDFs and albedos encountered on the earth's land surface.

4.0.10 LIMITATIONS

The BRDF/Albedo product will be made every 16 days for every land pixel. If the set of surface reflectance measurements within that period is insufficient to provide new BRDF and albedo values, a value from an earlier period or a value based on the ancillary generic data set will be output.

Acknowledgments

We would like to thank Baojin Zhang for work on model inversion accuracy under varying angular sampling, Jordan Borak for investigating spectral-to-broadband albedo conversion, Matt Disney and Encarna Vives Ruiz de Lope for excellent work applying the Ambrals model to data at UCL, Zoltan Hesley for work done at the University of Wales, Robert P. d'Entremont at Atmospheric and Environmental Research for investigations into the effects of cloud cover, and Jim Tallent for taking the beta-version of the Ambrals code to version 1. This work was supported by NASA under NAS5-31369; in the UK, work was supported partially by NERC under the TIGER-SVATS programme, and by the European Union under the 3rd Famework Human Capital and Mobility Programme.

5 LITERATURE CITED

Allen, S. J., J. H. C. Gash, M. V. K. Sivakumar, and J. S. Wallace, 1994, Measurements of albedo variation over natural vegetation in the Sahel.: Int. J. Climatology, v. 14, p. 625-636.

Allison, D.A., and J-P. Muller, 1992, An automated system for sub-pixel correction and geocoding of multispectral and multi-look aerial imagery, Proc. 17th Cong. Int. Soc. Photogramm. Remote Sens., Washington DC, August 2-14 1992, 29(B2), pp. 275-285.

Allison, D.A., M. J. Barnsley, P. Lewis, N. Dyble, and J-P. Muller, 1994, Precise geometric registration of ASAS airborne data for land surface BRDF studies, Proc. Int. Geosci. Remote Sens. Symp., Pasadena, California, USA, August 8-12 1994, pp. 1655-1657.

Allison, D., M. J. Zemerly and J.-P. Muller, 1991, Automatic seed-point generation for stereo matching and multi-image registration, Proc. Int. Geosci. Remote Sens. Symp., Espoo, Finland, 3-6 June 1991, pp. 2417-2421.

Arino, O., G. Dedieu and P. Y. Deschamps, 1991, Accuracy of satellite land surface reflectance determination, J. Appl. Met. 30:960-972.

Arino, O., G. Dedieu and P. Y. Deschamps, 1992, Determination of land surface spectral reflectances using METEOSAT and NOAA/AVHRR shortwave channel data, Int. J. Remote Sens. 13:2263-2287.

Babey, S. K. and R. J. Soffer, 1992, Radiometric calibration of the Compact Airborne Spectrographic Imager, Can. J. Remote Sens. 18:233-242.

Barkstrom, B. R., and G. L. Smith, 1986, The Earth radiation budget experiment: Science and implementation, Rev. Geophys. 24: 379-390.

Barnsley, M. J., P. Lewis, J.-P. Muller, and M. Sutherland, 1996, Deriving Improved Estimates of Land Surface Albedo through inversion of BRDF models using NASA-ASAS images of HAPEX- SAHEL Southern Supersite.: J. Hydrology (submitted 4/95, accepted 12/95).

Barnsley, M. J. and S. A. W. Kay, 1990, The relationship between sensor geometry, vegetation-canopy geometry and image variance, Int. J. Remote Sens. 11:1075-1084.

Barnsley, M. J., and J.-P. Muller, 1991, Measurement, simulation and analysis of bidirectional reflectance properties of earth surface material, Proc. Int. Conf. Spectral Signatures in Remote Sens., Courchevel, France, January 14-18 1991, pp. 375-382.

Barnsley, M. J., A. H. Strahler, K. P. Morris, and J.-P. Muller, 1994, Sampling the surface bidirectional reflectance distribution function (BRDF): Evaluation of current and future satellite sensors, Remote Sens. Rev. 8:271-311.

Bicheron, P., M. Leroy, and O. Hautecoeur, 1996, Analysis of airborne POLDER data on boreal forest covers.: IGARSS'96, p. 1901-1903.

Boissard, P., Akkal, N., Lewis, P., 1996, 3D Plant Modelling in Agronomy. Association of Applied Biologists: Modelling in Applied Biology: Spatial Aspects, 24/27 June 1996, Brunel, U.K.

Borel, C. C., S. A. W. Gerstl and B. Powers, 1991, The radiosity method in optical remote sensing of structured 3- D surfaces, Remote Sens. Environ. 36:13-44.

Breon, F.-M., V. Vanderbilt, M. Leroy, P. Bicheron, C. L. Walthall, and J. E. Kalshoven, 1996, Evidence of hot spot directional signature from airborne PODLER measurements: IEEE Trans. Geosci. Rem. Sens., v. in press.

Brest, C. L., and S. N. Goward, 1987, Deriving Surface Albedo Measurements from Narrow-band Satellite data: Int. J. Remote Sensing, v. 8, p. 351-367.

Brown de Coulstoun, E. C., C. L. Walthall, A. T. Cialella, E. R. Vermote, R. N. Halthore, and J. R. Irons, 1996, Variability of BRDF with land cover type for the West Central HAPEX-Sahel Super Site.: IGARSS'96, p. 1904-1907.

Burgess, D., P. Lewis, and J.-P. Muller, 1995, On topographic effects in AVHRR NDVI data: Remote Sensing Environment, v. 54, p. 223- 232.

Choudhury, B. J. and A. T. C. Chang, 1981, On the angular variation of solar reflectance of snow, J. Geophys. Res. 86:465-472.

Coakley, J .A., and F. P. Bretherton, 1982, Cloud cover from high resolution scanner data: Detection and allowing for partially filled fields of view, J. Geophys. Res. 87:4917- 4932.

Dedieu, G.,1992, Surface radiation budget in the shortwaves using the METEOSAT ISCCP B2 data-set, Proc. 9th METEOSAT Scientific Users' Meeting, Locarno, Switzerland, September 14-18 1992, EUMETSAT, Darmstadt, pp. 69-76.

Deering, D. F., 1989, Field measurements of bidirectional reflectance, in Theory and Applications of Optical Remote Sensing, G. Asrar, ed., John Wiley & Sons, New York, pp. 14-65.

Dickinson, R. E., 1983, Land surface processes and climate- surface albedos and energy, Adv. Geophys. 25:305-353.

Diner, D., J. V. Martonchik, C. Borel, S. A. W. Gerstl, H. R. Gordon, R. Myneni, B. Pinty, and M. M. Verstraete, 1996 MISR LEvel 2 Surface Retrieval Algorithm Theoretical Basis, NASA EOS-MISR Document, JPL D-22401, Rev. B, 78 pp.

Diner, J. D., C. J. Bruegge, J. V. Martonchik, T. P. Ackerman, R. Davies, S. A. W. Gerstl, K. P. Klaasen, G. W. Lilienthal, D. I. Nakamoto, R. J. Pagano, and T. H. Reilly, 1989, MISR: A Multiangle Imaging Spectroradiometer for Geophysical and Climatological Research for EOS, IEEE Trans. Geocsci. Remote Sens. 27:200-210.

Disney, M., J.-P. Muller, P. Lewis, and M. J. Barnsley, 1997, Production and validation of BRDF/albedo maps over HAPEX- SAHEL.: Int. Coll. on Spectral signatures of objects in Remote Sensing.

Engelsen, O., B. Pinty, M. M. Verstraete, and J. V. Martonchik, 1996,Parametric bidirectional reflectance factor models: evaluation, improvements and applications, Report, Joint Research Centre of the European Commission, EU 16426,, 114 pp.

Gerstl, S. A. W. and A. A. Zardecki, 1985a, Discrete- ordinates finite-element method for atmospheric radiative transfer and remote sensing, Appl. Optics 24:81-93.

Gerstl, S. A. W. and A. A. Zardecki, 1985b, Coupled atmosphere/canopy model for remote sensing of plant reflectance features, Appl. Optics 24:94-103.

Goel, N. S., 1987, Models of vegetation canopy reflectance and their use in estimation of biophysical parameters from reflectance data, Remote Sens. Rev. 3:1-212.

Goel, N. S., 1989, Inversion of canopy reflectance models for estimation of biophysical parameters from reflectance data, in Theory and Applications of Optical Remote Sensing, G. Asrar, ed., John Wiley & Sons, New York, pp. 205-251.

Goel, N. S. and I. Rozehnal, 1992, An architecturally realistic model for radiation regime in vegetation canopies, Proc. Int. Geosci. and Remote Sens. Symp., Houston TX, May 26-29 1992, 1:48-50.

Gustafson, G. B., R. G. Isaacs, R. P. d'Entremont, J. M. Sparrow, T. M. Hamill, C. Grassotti, D. W. Johnson, C. P. Sarkasian, D. C. Peduzzi, B. T. Pearson, V. D. Jakabhazy, J. S. Belfiore, A. S. Lisa, 1994, Support of Environmental Requirements for Cloud Analysis and Archive (SERCAA): Algorithm Descriptions, Technical Report PL-TR-94-2114, Phillips Lab, Hanscom AFB MA 01731, 100 pp.

Gutman, G., 1992, Anisotropy of visible and near-IR reflectances over land as observed from NOAA AVHRR, Proc. Int. Radiation Symposium, Tallinn, Estonia, pp. 436-439.

Gutman, G., 1994, Normalization of multi-annual global AVHRR reflectance data over land surfaces to common sun-target- sensor geometry, Adv. Space Res. 14:121-124.

Henyey, L. G. and T. L. Greenstein, 1941, Diffuse radiation in the galaxy, Astrophys. J. 93:70-83.

Holben, B. N., and C. O. Justice, 1980, The topographic effect on spectral response from nadir-pointing sensors, Photogramm. Engr Remote Sens. 46(9):1191-1200.

Hu, B., W. Wanner, X. Li, and A. H. Strahler, The sensitivity of atmospheric correction of reflectances to the surface BRDF, 1996, Proc. 1st Int. Workshop Multiang. Remote Sens., Beijing, China, in press.

Hu, B., W. Wanner, X. Li, and A. Strahler, Validation of kernel-driven semiempirical BRDF models for application to MODIS-MISR data, 1996, Proc. Int. Geosci. Rem. Sens. Symp. 96, Lincoln, Nebraska, 1669–1671.

Iaquinta, J. and B. Pinty, 1994, Adaptation of a bidirectional reflectance model including the hot-spot to an optically thin canopy, Proc. Sixth Int. Symp. on Physical Measurements and Signatures in Remote Sens., Val d'Isere, France, January 17-21 1994, pp. 683-690

Irons, J. R., K. J. Ranson, D. L. Williams, R. R. Irish and F. G. Huegel, 1991, An off-nadir pointing imaging spectroradiometer for terrestrial ecosystem studies, IEEE Trans. Geosci. Remote Sens. 29:66-74.

Jupp, D. L. B. and A. H. Strahler, 1991, A hotspot model for leaf canopies, Remote Sens. Environ. 38:193-210. Kimes, D. S., 1983, Dynamics of directional reflectance factor distribution for vegetation canopies, Appl. Optics 22:1364-1372.

Kimes, D. S., W. W. Newcomb, C. J. Tucker, I. S. Zonneveld, W. van Wijngaarden, J. de Leeuw, and G. F. Epema, 1985, Directional reflectance factor distributions for cover types of Northern Africa, Remote Sens. Environ. 18:1-19.

Kimes, D. S., W. W. Newcomb, R. F. Nelson, and J. B. Schutt, 1986, Directional reflectance distributions of a hardwood and a pine forest canopy, IEEE Trans. Geosci. Remote Sens. GE-24:281-293.

Kimes, D. S., A. G. Kerber and P, J, Sellers, 1993, Spatial averaging errors in creating hemispherical reflectance (albedo) maps from directional reflectance data, Remote Sens. Environ. 45:85-94.

Kriebel, K. T., 1978, Measured spectral bidirectional reflection properties of four vegetated surfaces, Int. J. Remote Sens. 17:253-259.

Lee, T. Y. and Y. J. Kaufman, 1986, Non-Lambertian effects on remote sensing of surface reflectance and vegetation index, IEEE Trans. Geosci. Remote Sens. GE-24:699-708.

Leroy, M. and J.-L. Roujean, 1994, Sun and view angle corrections on reflectances derived from NOAA/AVHRR data, IEEE Trans. Geocsci. Remote Sens. 32:684-697.

Lewis, P., and J.-P. Muller, 1990, Botanical Plant Modelling for Remote Sensing Simulation Studies: International Geoscience and Remote Sensing, p. 1739-1742.

Lewis, P., and E. Vives Ruiz de Lope, 1996, An Application of kernel-driven BRDF Models and AVHRR data to monitoring Land Surface Dynamics in the Sahel, First Internat. Workshop Multiangular Remote sens., Bejing, China, Sept 1995.

Lewis, P., 1995, On the Implementation of Linear Kernel-Driven BRDF Models. Proc. RSS 95, "Remote Sensing in Action", Southampton, UK, 11-14 Sept, 333-340.

Lewis, P. and M. J. Barnsley, 1994, Influence of the sky radiance distribution on various formulations of the earth surface albedo, Proc. Sixth Int. Symp. on Physical Measurements and Signatures in Remote Sens., Val d'Isere, France, January 17-21 1994, pp. 707-715.

Lewis, P., M. J. Barnsley, M. Sutherland and J.-P. Muller, 1995, Estimating land surface albedo in the HAPEX-Sahel experiment: Model-based inversions using ASAS data, Proc. Int. Geosci. Remote Sens. Symp., Florence, Italy, July 10- 14, 2221–2223.

Lewis, P., and J.-P. Muller, 1992, The Advanced Radiometric Ray-Tracer: ARARAT for plant canopy reflectance simulation, Proc. 29th Cong. Int. Soc. Photogramm. Remote. Sens., Washington DC, pp. 26-34.

Lewis, P., J.-P. Muller, and K. Morris, 1991, Quality assessment of a botanical plant modelling system for remote sensing simulation studies, Proc. Int. Geosci. Remote Sens. Symp., Espoo, Finland, June 3-6 1991, pp. 1917-1920

Li, X. and A. H. Strahler, 1986, Geometric-optical bidirectional reflectance modeling of a conifer forest canopy, IEEE Trans. Geosci. Remote Sens. GE-24:906-919.

Li, X. and A. H. Strahler, 1992, Geometric-optical bidirectional reflectance modeling of the discrete-crown vegetation canopy: Effect of crown shape and mutual shadowing: IEEE Trans. Geosci. Remote Sens. 30:276-292.

Li, X., A. H. Strahler, and C. E. Woodcock, 1995, A hybrid geometric optical-radiative transfer approach for modeling albedo and directional reflectance of the discrete crown vegetation canopy, IEEE Trans. Geosci. Remote Sens. 33:466- 480.

Li, Z., and L. Garand, 1994, Estimation of surface albedo from space: A parameterization for global application, J. Geophys. Res. 99:8335-8350.

Li, Z. and H. G. Leighton, 1992, Narrowband to broadband conversion with spatially autocorrelated reflectance measurements, J. Appl. Met. 31:421-432.

Liang, S., P. Lewis, R. Dubayah, W. Qin, and D. Shirey, 1996, Topographic effects on surface Bidirectional Reflectance scaling.: Int. Workshop on "Multi-angular Remote Sensing: Measurements, Models and Applications", Beijing, Sept 13-18. 17pp.

Liang, S. and A. H. Strahler, 1993a, Calculation of the angular radiance distribution for a coupled system of atmosphere and canopy media using an improved Gauss-Seidel algorithm, IEEE Trans. Geosci. Remote Sens. 31:491-502.

Liang, S. and A. H. Strahler, 1993, An analytic BRDF model of canopy radiative transfer and its inversion, IEEE Trans. Geosci. Remote Sens. 31:1081-1092.

Liang, S., and A. H. Strahler, 1994a, A four-stream solution for atmospheric radiance transfer over a non-Lambertian surface, Appl. Optics 33:5745-5753.

Liang, S. and A. H. Strahler, 1994b, Retrieval of surface BRDF from multiangle remotely sensed data, Remote Sens. Environ. 50:18-30.

Martonchik, J. V., 1997, Determination of aerosol optical depth and land surface directional reflectances using multi-angle imagery, J. Geophys. Res., in press.

Meyer, D., 1994, The Estimation of Clear Sky Albedo over a Tallgrass Prairie using the Advanced Very High Resolution Radiometer. Ph.D Dissertation, U. of Michigan, Ann Arbor, MI, 145 pp.

Minnaert, M., 1941, The reciprocity principle in lunar photometry, Astrophys. J. 93:403-410.

Muller, J.-P., and M. Disney, 1997, The impact of spatial scale on BRDF/albedo retrieval over HAPEX-SAHEL using ASAS data.: Rem. Sens. Env., v. in preparation.

Muller, J.-P., M. Disney, and P. Lewis, 1997a, Monte Carlo ray- tracing of millet plants in HAPEX-SAHEL using stereo photogrammetry for assessing BRDF/albedo algorithms.: Rem. Sens. Env. (in preparation).

Muller, J.-P., M. Disney, P. Lewis, and M. J. Barnsley, 1997b, Spectral albedo maps of the HAPEX-SAHEL area using LANDSAT- TM and multi-flightline ASAS data.: Rem. Sens. Env., in preparation.

Muller, J.-P., and P. Eales, 1990, Global topography accuracy requirements for EOS, Proc. Int. Geosci. Remote Sens. Symp., Washington DC, May 21-24 1990, pp. 1411-1414.

Muller, J.-P., and M. Dalton, 1988, Application of ray- tracing to satellite image understanding, Proc. Int. Geosci. Remote Sens. Symp., Edinburgh, September 13-16 1988, pp. 1187-1190.

Myneni, R. B., G. Asrar and S. A. W. Gerstl, 1990, Radiative transfer in three dimensional leaf canopies, Transport Theory and Stat. Physics 19:205-250.

Myneni, R. B., G. Asrar, and F. G. Hall, 1993, A three-dimensional radiative transfer method for optical remote sensing of vegetated land surfaces, Remote Sens. Env., 41:105–121.

Nicodemus, F. E., J. C. Richmond, J. J. Hsia, I. W. Ginsberg and T. Limperis, 1977, Geometrical Considerations and Nomenclature for Reflectance, Nat. Bur. Stand. Rept. NBS MN-160, 52 pp.

Nilson, T. and A. Kuusk, 1989, A reflectance model for the homogeneous plant canopy and its inversion, Remote Sens. Environ. 27:157-167.

Neu, T. J., R. G. Isaacs, G. B. Gustafson, and J. W. Snow, 1994, Improved cloud analysis for CDFSII through the SERCAA research and development program, Seventh Conf. Satellite Meteorol. Oceanog., Monterey, CA, June 6-10 1994, pp. 239- 242.

Newton, A., Muller, J.-P., & Pearson, J. C. (1991). SPOT-DEM shading and its application to automated correction of topographic and atmospheric effects, Proc. Int. Geosci. Remote Sens. Symp., Espoo, Finland, June 3-6 1991, pp. 655- 659.

Otto, G. P., and T. K. W. Chau, Region-Growing Algorithm For Matching Of Terrain Images, Image And Vision Computing, 7, 83 - 94, 1989.

Pinker, R. T. and J. A. Ewing, 1986, Effect of surface properties on the narrow to broadband spectral relationship in satellite observations, Remote Sens. Environ. 20:267-282.

Pinty, B., M. M. Verstraete, and R. E. Dickinson, 1989, A physical model for predicting bidirectional reflectance over bare soil, Remote Sens. Environ., 27:273-288.

Pinty, B., M. M. Verstraete and R. E. Dickinson, 1990, A physical model of the bidirectional reflectance of vegetation canopies, 2. Inversion and validation, J. Geophys. Res. 95:11,767-11,775.

Prince, S. D., Y. H. Kerr, J.-P. Goutorbe, T. Lebel, A. Tinga, P. Bessemoulin, J. Brouwer, A. J. Dolman, E. T. Engman, J. H. C. Gash, M. Hoepffner, P. Kabat, B. Monteny, F. Said, P. Sellers, and J. Wallace, 1995, Geographical, biological and remote sensing aspects of the Hydrologic Atmospheric Pilot Experiment in the Sahel (HAPEX-SAHEL): Rem. Sens. Env., v. 51, p. 215-234.

Proy, C., D. Tanr and P. Y. Deschamps, 1989, Evaluation of topographic effects in remotely-sensed data, Remote Sens. Environ. 30:21-32.

Rahman, H., M. M. Verstraete and B. Pinty, 1993a, Coupled surface-atmosphere reflectance (CSAR) model, 1. Model description and inversion on synthetic data, J. Geophys. Res. 98:20,779-20,789.

Rahman, H., B. Pinty and M. M. Verstraete, 1993b, Coupled surface-atmosphere reflectance (CSAR) model, 2. Semiempirical surface model usable with NOAA Advanced Very High Resolution Radiometer data, J. Geophys. Res. 98:20,791-20,801.

Ranson, K. J., L. L. Biehl and M. E. Bauer, 1985, Variation in spectral response of soybeans with respect to illumination, view and canopy geometry, Int. J. Remote Sens. 6:1827-1842.

Ranson, K. J., J. R. Irons, and C. S. T. Daughtry, 1991, Surface albedo from bidirectional reflectance, Remote. Sens. Environ. 35:201-211.

Ross, J. K., 1981, The Radiation Regime and Architecture of Plant Stands, Dr W. Junk, The Hague. Rossow, W. B., and L. C. Garder, 1993, Cloud detection using satellite measurements of infrared and visible radiances for ISCCP, J. Climate 6:2341-2369.

Roujean, J. L., D. Tanre, F. M. Breon, and J. L. Deuze, 1996, Retrieval of land surface parameters for GCM from POLDER bidirectional measurements during HAPEX-Sahel.: J. Geophys. Res., v. in press.

Roujean, J. L., Latoy, M., and Deschamps, P. Y., 1992, A bidirectional reflectance model of the earths surface for the correction of remote sensing data, J. Geophys. Res. 97:20455-20468.

Roy, D. P., 1996, The MODIS Land (MODLAND) Quality Assurance Plan, available from droy@kratmos.gsfc.nasa.gov.

Sancer, M. L., 1969, Shadow-corrected electromagnetic scattering from a randomly rough surface, IEEE Trans. Ant. Prop. AP-17:577-585.

Schaaf, C. B. and A. H. Strahler, 1993, Solar zenith angle effects of forest canopy albedos calculated with a geometric-optical bidirectional reflectance model, IEEE Trans. Geosci. Remote Sens. 31:921-927.

Soffer, R. J. and J. R. Miller, 1995, Bidirectional reflectance factors (BRF) of an open tree canopy by laboratory simulation, Proc. 17th Can. Remote Sens. Symp., Saskatoon, Canada, June 1995.

Soffer, R., Miller, J., Wanner, W., and Strahler, A.H., 1995, Winter boreal forest canopy BRF results: Comparisons between airborne data, laboratory simulations and geometrical-optical model data, Proc. 1995 Internat. Geosci. Remote Sens. Symp., Florence, Italy, July 10-14, 1995, vol 1., pp. 800-802.

Starks, P. J, J. M. Norman, B. L. Blad, E. A. Walter-Shea and C. L. Walthall, 1991, Estimation of shortwave hemispherical reflectance (albedo) from bidirectionally reflected radiance data, Remote Sens. Environ. 38:123-134.

Stowe, L. L., E. P. McClain, R. Carey, P. Pellegrino, G. G. Gutman, P. Davis, C. Long and S. Hart, 1991, Global distribution of cloud cover derived from NOAA/AVHRR operational satellite data, Adv. Space Res. 11:51-54.

Strahler, A. H., 1994, Vegetation canopy reflectance modelingrecent developments and remote sensing perspectives, Proc. Sixth Int. Symp. Physical Measurements Spectral Signatures, Val d'Isere, France, January 17-21 1994, pp. 593-600.

Strahler, A. H. and S. Liang, 1994, Comparisons of radiative transfer models of vegetation canopies with laboratory measurements, Proc. Int. Geosci. Remote Sens. Symp., Pasadena, California, USA, August 8-12 1994, 4:2345-2347.

Strahler, A. H., W. Wanner, Q. Zhu, and X. Jin, 1995, Bidirectional reflectance modeling of data for vegetation obtained in the Changchun Solar Simulation Laboratory, Proc. Int. Geosci. Remote Sens. Symp., Florence, Italy, July 10-14 1995, 1965–1967.

Taylor, V. R. and L. L. Stowe, 1984, Reflectance characteristics of uniform Earth and cloud surfaces derived from NIMBUS-7 ERB, J. Geophys. Res. D89:4987-4996. Teillet, P. M., and K. Staenz, 1993, Atmospheric effects due to topography on MODIS vegetation index data simulated from AVIRIS imagery over mountainous terrain, Can. J. Remote Sens. 18:283-292.

van Leeuwen, W. J. D., A. R. Huete, S. Jia, and C. L. Walthall, 1996, Comparison of Vegetation Index compositing scenarios: BRDF vs. Maximum VI approaches.: IGARSS'96, p. 1423-1425.

Vermote, E., D. Tanr, J. L. Deuze, M. Herman, and J. J. Morcrette, 1994, Second Simulation of the Satellite Signal in the Solar Spectrum (6S), User Guide, available from E. Vermote, GSFC.

Vermote, E. F., N. El Saleous, C. O. Justice, Y. J. Kaufman, J. L. Privette, L. Remer, J. C. Roger, and D. Tanre, 1997, Atmospheric correction of visible to middle infrared EOS-MODIS data over land surface: background, operational algorithm and validation, J. Geophys. Res., in press.

Verstraete, M. M., B. Pinty and R. E. Dickinson, 1990, A physical model of the bidirectional reflectance of vegetation canopies, 1. Theory, J. Geophys. Res. 95-755- 765.

Walthall, C. L., J. M. Norman, J. M. Welles, G. Campbell and B. L. Blad, 1985, Simple equation to approximate the bidirectional reflectance from vegetation canopies and bare soil surfaces, Appl. Optics 24:383-387.

Wanner, W., X. Li, and A. H. Strahler, 1995, On the derivation of kernels for kernel-driven models of bidirectional reflectance, J. Geophys. Res., 100: 21077–21090.

Wanner, W., A. Strahler, J.-P. Muller, M. Barnsley, P. Lewis, X. Li and C. Barker Schaaf, 1995, Global mapping of bidirectional reflectance and albedo for the EOS MODIS project: The algorithm and the product, Proc. Int. Geosci. Remote Sens. Symp., Florence, Italy, July 10-14 1995, 525–529.

Wanner, W., A. H. Strahler, B. Hu, P. Lewis, X. Li, J.-P. Muller, and M. J. Barnsley, 1996, Global BRDF and albedo from the EOS MODIS and MISR sensors, Proc. 1st Int. Workshop Multiang. Remote Sens., Beijing, China, in press.

Wanner, W., A. H. Strahler, B. Zhang, and P. Lewis, Kilometer-scale global albedo from MODIS, 1996. Proc. Int. Geosci. Rem. Sens. Symp. 96, Lincoln, Nebraska, 1405–1407.

Wanner, W., P. Lewis, and J.-L. Roujean, The influence of directional sampling on bidirectional reflectance and albedo retrieval using kernel-driven models, 1996, Proc. Int. Geosci. Rem. Sens. Symp. 96, Lincoln, Nebraska, 1408–1410.

Wanner, W., A. H. Strahler, B. Hu, X. Li, C. L. Barker Schaaf, P. Lewis, J.-P. Muller, and M. J. Barnsley, 1997, Global retrieval of bidirectional reflectance and albedo over land from EOS MODIS and MISR data: theory and algorithm, *J. Geophys. Res.*, accepted.

Whittaker, E., and G. Robinson, 1960, The Calculus of Observations, Blachie and Son, Glasgow, 397 pp.

Wu, A., Z. Li and J. Cihlar, 1995, Effects of land cover type and greenness on advanced very high resolution radiometer bidirectional reflectances: analysis and removal, J. Geophys. Res., 100: 9179–9192.

Wylie, D. P., W. P. Menzel, H. M. Woolf and K. I. Strabala, 1994, Four years of global cirrus cloud statistics using HIRS, J. Climate, vol 7, pp. 1972-1986.

Wylie, D. P., and W. P. Menzel, Two years of cloud cover statistics using VAS, J. Climate, 2, 380–392, 1989.

6 RESPONSE TO ATBD REVIEWS

6.1 1994 REVIEW: Comments and Response

6.1.1 Comments from the Reviewers (June, 1994)

A numerical assessment was made in six categories for each of the individual ATBDs:

1. Degree to which product meets EOS priorities
2. Soundness (feasibility/practicality) of approach
3. Appropriateness of algorithm input
   (a) Intermediate Products
   (b) Dependence on other AM products
   (c) Ancillary data (nonplatform data)
4. Completeness of sensitivity and error budget
5. Soundness of validation strategy
6. Release of useful products at launch
7. Other comments

Each category was given a numerical grade as follows:

Grade 9 — High or strongly agree
Grade 5 — Neutral
Grade 1 — Low
Grade 0 — Insufficient Information

The BRDF/Albedo product was rated as follows:

1. (Grade 9) Two products wil result from this algorithm (i) the BRDF and (ii) surface albedo. The latter is obtained by angular and spectral integration of the BRDF. Both products are relevant to the MTPE programs.

2. (Grade 6) The proposed approach could be enormously complex to implement. It has never been tried over as large a region as even a single satellite pixel, and therefore is high risk for producing reliable global products by launch.

3. (Grade 8) (a) With dependence on the AM products as an additional complication, the developers propose to invert a coupled atmosphere-surface model, obtaining simultaneously the atmospheric and canopy properties. This renders the problem even more complex and spectral region dependent. Land cover maps will also be needed. The land cover classes needed to do this will likely be more complex and finer spatial resolution than those required by the ecosystem process models. Who will produce these maps? The problem

would be much less complex were the developers to use atmospherically corrected data. The algorithm will also need cloud-screened data. (b) As to the appropriateness of intermediate products, it is not clear that there will be any EOS algorithms that utilize the BRDF data directly without further synthesis into products such as albedo. There is no question however, that BRDF data would be enormously useful for many computations and investigations. (c) As for the need for ancillary data, topographic data will be critical to the model inversion problem as well as meteorological data to analyze canopy status to initialize the BRDF inversions. Other data such as soils maps, global land cover maps etc. would be needed.

4. (Grade 0) No error modeling or sensitivity analysis is presented.

5. (Grade 0) No validation strategy is presented.

6. (Grade 1–5) Given the immaturity of the this algorithm, the probability of BRDF data generated at 1km globally is very unlikely. Even with an algorithm, it is not clear how many orbits will be required to build up the requisite cloud–free views to develop a reliable BRDF. Thus, the BRDF product will likely be one where the holes are slowly filled in.

7. (Comments) It is not obvious how the complete BRDF can be constructed from MISR. Much of the variability and asymmetry occurs near the principal plane for which even the scan–plane of MODIS will not come close in certain seasons. It is also not clear given cloud cover probabilities in most vegetated regions, how long it will take to acquire enough data to build the BRDF. Multiple acquisitions at several different relative azimuths may be required for some vegetation types. In addition, the implementation of the approach has not been thought out in detail and will present many practical problems when attempting to implement it on a global scale. The largest practical problem is that no universal canopy reflectance model exists that can handle the range of canopies to be encountered on a global scale. To circumvent this problem, the developers propose several different models, to be selected to address the complexity of different ecosystems. Thus a logic will need to be worked out, with objective criteria specified, for selecting which model to use for what pixel. This selection criteria might also need to select different models for different MODIS bands since models for bands where multiple scattering is not important might not work for bands for which multiple scattering dominates. This will require a front end to the algorithm to generate the input parameters to the criteria.

It is not made clear how the MODIS and MISR data will be combined to produce the BRDF since different bands and spatial resolutions are involved. The developers propose to produce a BRDF for each 1 km. This will potentially present a large processing load, and in fact may be unnecessary where large portions of an ecosystem might be rather homogeneous over several kilometers. The approach does not rely on direct observation of BRDF, rather it infers it from inversion of reflectance models to obtain surface parameters, but very little, if any work has been done using the extracted parameters to construct a BRDF for the purpose of computing surface albedo.

6.1.2 Algorithm Changes in Response to the 1994 Review

Here is a summary of the major changes in the algorithm:

G1. Use of semiempirical models.

BRDF is now fitted using a suite of simple, linear, semiempirical models. In effect, these models fit the angular pattern of observed bidirectional reflectance measurements using a mixture of simple, contrasting BRDF shapes that are derived by simplifying more complex physical BRDF models. That is,

$$R = f_{iso} + f_{geo}k_{geo} + f_{vol}k_{vol} \tag{41}$$

where R is the BRDF as a function of illumination zenith, view zenith, and relative azimuth; k_{geo} and k_{vol} are two shape functions that depend only on illumination zenith, view zenith, and relative azimuth; f_{geo} and f_{vol} are weights that mix the two BRDF shapes; and f_{iso} is a constant, corresponding to isotropic (Lambertian) BRDF shape.

The shape function k_{geo} is derived from BRDF theory for surfaces dominated by geometric-optical shadowing effects. There are currently three choices for this function, derived from the theory of (1) rectangular projections on a plane; (2) sparse spheroidal projections on a plane; and (3) dense spheroidal projections on a plane. The shape function k_{vol} is derived from theory describing the volume scattering of leaves in a homogeneous layer. Two choices are currently available for this shape function, derived from theory for (1) thin, and (2) thick, leaf layers. A third volume-scattering shape function, derived from the theory of volume scattering of snow, is under development. We also fit the Walthall model for BRDF, which is of a mathematical form similar to that above, but relies on empirical functions rather than BRDF shapes derived from physical models.

G2. Inversion speed.

The algorithm now runs very quickly. Fitting a single semiempirical model requires only inversion of a 3 by 3 matrix. This allows us to fit multiple combinations of models and choose the one with the best fit. Realistic timings of the algorithm in execution now fall easily within instrument and product resource allocations.

G3. 16-day cycle instead of 9-day.

Following preliminary studies of cloud cover, we now plan to provide the product on a 16-day cycle, instead of a 9-day cycle. (Sixteen days is the repeat cycle for double MISR coverage – that is, the 16-day cycle provides at least two possible MISR acquisitions at all latitudes.)

G4. Atmospheric coupling.

The coupling between the atmosphere and surface is accomplished by an iterative loop in which a prior

(or Lambertian) BRDF is used to extract surface bidirectional reflectances given their atmospheric state; a provisional BRDF is fitted; surface bidirectional reflectances are reextracted; and the next BRDF is calculated. Only one or two loops are needed in nearly all cases to convergence within a few percent. The atmospheric correction logic is that of the MODIS surface reflectance product (Vermote), similar to that used in the 6S program. The looping logic follows MISR=D5s approach.

G5. Spatial resolution.

The product is still produced at 1-km resolution (now 1.1 km resolution on the ISSCP Level 3 grid). This fine resolution is needed for input to the surface reflectance product, which produces output at (nominal) 250- and 500-m resolutions and requires the BRDF for accurate calculation. However, the linear nature of the semiempirical models allows easy extrapolation of both BRDF and albedo measures to coarse resolutions. In this way, the needs of both global climate modelers and regional climate-surface energy balance modelers for albedo and BRDF data can easily be accommodated.

6.1.3 Specific Responses to the Panel's Comments

P1. Complexity.

The panel notes that the approach described in the old ATBD could be enormously complex to implement and has never been tried over a region of any size. However, the revised algorithm using semiempirical models is enormously simpler. Computational tests show that it can be applied globally at reasonable levels of processing power. We have also applied several semiempirical models (although not the full suite yet) to ASAS imagery on a pixel-by-pixel basis. We will shortly apply the full algorithm to a registered LAC dataset of New England. Both of these applications are discussed in more detail in the new ATBD.

P2. Atmospheric Correction.

The panel noted that inverting a coupled atmosphere-surface model produces an added complication. The new algorithm couples surface and atmosphere in a simple loop that requires one or two iterations. (See G4. above.)

P3. Error modeling and sensitivity analysis.

The panel notes that no error modeling or sensitivity analysis is presented. The new ATBD provides such analyses.

P4. Validation.

The panel observes that no validation strategy is presented. The new ATBD provides an extensive discussion of validation.

P5. Scan geometry for MODIS and MISR.

The panel expressed the concern that between MODIS and MISR, insufficient observations may be acquired along the principal plane, where much variability and asymmetry in the BRDF occurs. The acquisition of observations along the principal plane is a complex function of orbit, sensor geometry, latitude, and time of the year. Because MISR acquires data in the along-track direction and MODIS in the across-track direction, there is normally good coverage of the view hemisphere, with observations from one or the other instrument near the principal plane. The subject is treated in more detail in our recently published paper (Barnsley et al., 1994) and in the new ATBD. Note that the use of semiempirical models, in which the BRDF shapes are physically-based, mitigates this problem. Since the BRDF shape is restricted by the physics and is not allowed to vary freely, principal plane measurements are less important.

P6. Cloud cover.

The panel pointed out that, given cloud cover, it is not clear how long it will take to acquire enough observations to fit a BRDF. We are investigating the cloud cover problem, and as a result of studies described in the new ATBD, we have changed the product cycle from 9-day to 16-day. (See G3. above.)

P7. Model selection.

The prior algorithm relied on a selection process to choose an appropriate physical BRDF model to invert on a pixel-by-pixel basis. The panel was concerned that this process was not sufficiently well thought- out or specified. The new algorithm eliminates this selection process.

P8. Data combination.

The panel pointed out that the issue of combining MISR and MODIS data with varying spatial and spectral resolutions was not well specified in the ATBD. This has been remedied in the new document.

P9. 1-km resolution.

The panel was concerned that the 1-km spatial resolution presented a large processing load, and that for at least some regions, large portions of an ecosystem might be rather homogeneous over several kilometers. With the speed of the new algorithm, the processing load is no longer a problem. Although there may be some large, homogeneous regions with unchanging BRDF, there will certainly be other regions where fine-grained land surface variation will require fine resolution of the BRDF and albedo. Note also that for accurate results, the surface reflectance algorithm (Vermote) requires BRDF at as fine a resolution as practical.

P10. Albedo from BRDF.

The panel comments that little, if any, work has been done on the construction of a BRDF for the purpose of computing a surface albedo. Actually, there is long history of this for TOA BRDFs in the asymmetry

factors of Taylor and Stowe (1984) for ERB and follow-on work (e.g., Baldwin and Coakley, 1991; Green and Smith, 1991). For surface measurement, a number of recent papers have used BRDF functions in relating directional measurements to albedo (e.g., Ranson et al., 1991; Starks et al., 1991). So some work of this nature has been done, and more is likely to be on the way. Combining bidirectional measurements through the mechanism of a BRDF is really the only way to measure the albedo of a small patch of land surface directly from space. Other approaches (e.g., Sellers et al., 1994) require even more modeling.

P11. Land cover information.

The panel notes that fine-grained land cover information is needed for the model-selection procedure (see 3. above) and that appropriate data might not be available. Land cover information is not used for model selection operationally in the new algorithm, although it may be used to "prime the pump" at time zero. Land cover information will be available at launch, probably as the IGBP 1-km Land Cover Database derived from the global 1-km AVHRR NDVI composite now being processed at EDC (see Land Cover Product ATBD).

P12. Use by other EOS algorithms.

The panel remarks that it is not clear that there are any EOS algorithms that utilize the BRDF data directly. However, MODIS surface reflectance uses BRDF directly. This is because the errors induced by assuming isotropic surface reflectance can be as large as 15 percent for turbid cases (discussed in new version of ATBD). Calculations by Lee and Kaufman documented this back in 1986. We are presently working with Eric Vermote to integrate the BRDF and surface reflectance algorithms together into a single processing chain.

P13. Ancillary data.

The panel remarks that extensive ancillary data (topographic, soils, meteorological) are needed. However, these were for the model selection procedure that is now eliminated.

6.1.4 Specific Responses to the Mail Reviewers' Comments

For the mail reviewers, many specific comments are obviated by the changes in the both the algorithm and document. Thus, the responses below are directed to the more general concerns that they express.

Ross-Nilson-Kuusk

R1. Choice of reflectance models is problematic.

This review commented that other physical models should be explored. However, our product no longer uses physical models–just semiempirical models. The review also expressed some concern about the validation of the Liang-Strahler model against radiative transfer calculations. Again, this model is no longer

used. The model selection issue, commented on in P7. above, was also raised. Use of semiempirical models obviates the problem.

R2. Atmospheric coupling.

These reviewers suggest that atmospheric coupling is important and needed to be developed in more detail in the document. This has been done.

R3. Albedo calculation.

The review requested better development of the procedure for calculating albedo from integrating the BRDF, noting problems with atmospheric effects and pixel sizes at large view zenith angles. Both of these issues are now addressed in the new ATBD.

R4. Multisensor, multichannel data needed.

The review noted that retrieval of physical parameters from inversion of physical models can be problemmatic and that additional multisensor, multichannel data may be required to provide good accuracy. However, the algorithm no longer inverts physical models to infer physical parameters.

Borel-Gerstl

B1. Mixed pixels.

These reviewers point out that MODIS-sized pixels will contain mixtures of cover types, and individual physical models may not fit them well. Further, there were cover types that were not fitted well by any of the physical models we had selected, such as snow, standing water, etc. In the new algorithm, the semiempirical models handle mixtures easily and should be able to accommodate these other cover types without difficulty.

B2. Inversion issues.

The reviewers express concerns about numerical inversion procedures (no longer required); the processing power needed for global calculations (not a problem for the semiempirical models, see G2. above); effects of noise on inversion (new sensitivity studies in ATBD show good results); computational costs of numerical integration of BRDFs to give albedo measures (now trivial due to fixed kernels with variable weights and a linear model); and that maps of BRDF parameters from multiangular data have never been produced (now included in the new ATBD).

B3. Global use of Walthall model.

The reviewers suggest we consider use of a few simpler models, and suggest the Walthall et al. (1985) model as a candidate. We have, in effect, taken their advice by using the semiempirical models.

B4. MODIS-MISR data combination issues.

The reviewers note that the issues of merging MISR and MODIS data are not well addressed in the document. The issues include not only geometry but also the fact that sun angle and atmospheric condition will vary with each MODIS image. A new section in the revised ATBD handles the data merging issue, and the atmospheric correction procedure accepts the fact that the atmosphere is different for each MODIS observation. See also P5. above.

B5. Research issues.

The reviewers list several issues that require more study: (1) the number of observations needed to derive the BRDF of a pixel (10 is our cutoff, but sensitivity studies have not been done yet); (2) the sensitivity of the retrieved parameters to errors introduced by noise and errors in atmospheric correction (some noise studies are complete and in the new ATBD, others are planned); (3) the effects of registration errors on BRDF parameter extraction for heterogeneous surfaces (studies are planned); and (4) the allowable interval in which can we consider the BRDF of a vegetation cover to be constant (16 days, we hope, with studies planned for spring/fall AVHRR data to see how quickly BRDF/Albedo changes).

Meyer Review

M1. Land cover dependence.

This reviewer notes that in our prior algorithm, land cover information was used in model selection, raising issues of updating of land cover information in the face of land cover change on a three-month time scale, while BRDF/Albedo was observed much more frequently. However, model selection is no longer necessary, obviating the need for land cover for this purpose.

M2. Sensitivity to atmospheric influences.

More sensitivity studies detailing the effect of atmospheric correction errors on model parameter retrieval need to be done, according to the reviewer. We agree, and plan such studies.

M3. Sensitivity to geometric and radiometric errors.

Angular, geolocational and spectroradiometric errors need to be investigated systematically in the context of merging MODIS and MISR data. We agree, and plan such studies.

Verstraete Review

Note that this review is exceedingly lengthy (14.5 pages of 10-point type), and that most of the detailed comments related to the specific text by page and paragraph. Since the text has been entirely rewritten, these no longer apply. The response here is directed toward the overall evaluation paragraphs that begin

the review.

V1. Algorithms are not suitable for operational products.

The reviewer is concerned that the proposed algorithms are under development and mostly suitable for academic research. However, with the new semiempirical model approach, we believe we have now developed algorithms suitable for operational products. (See G2 above.)

V2. Per-pixel BRDF is unrealistic and of low interest.

The reviewer expresses the concern that the computer resources needed for per-pixel determination are large and that there is not much scientific interest in the results. However, the semiempirical model algorithm now runs well within the resources available for the MODIS instrument and AM platform. (Timings are documented in the new ATBD.) As for scientific interest, the panel review states, "There is no question... that BRDF data would be enormously useful for many computations and investigations." Note also that to deliver surface reflectance accurately from MODIS, BRDF is required.

V3. Albedo needs a clearer definition.

The new ATBD clearly specifies the albedo measures we provide in definitions traceable from Nicodemus' classic NBS monograph.

V4. Deficiencies in science, numerical analysis.

The reviewer offers the opinion that various parts of the algorithm suffer from deficiencies in science and numerical analysis. However, the semiempirical approach we have now selected for the product is fully grounded in the science of BRDF modeling as it has developed over the past decade or so. Numerical inversion is no longer necessary, thus obviating this concern.

V5. Prerequisite datasets.

The reviewer notes that the algorithm was dependent on collateral datasets for model selection that were not well specified. As noted before, the new algorithm operates independently and these datasets are no longer required.

V6. Relative contributions of MODIS and MISR to the data pool.

The reviewer expresses the concern that since the product will only be produced when MISR data are available, the contribution of MODIS to the data pool will be minor. (1) The new algorithm will not be limited to pixels for which MISR data are available, and will provide a product for every pixel every 16 days. If there are insufficient observations to update the BRDF and albedo, we will reach back to the prior product or use a stock BRDF/Albedo based on prior experience and past history with the pixel. Flags will inform the user in these cases. (2) For accurate BRDF retrieval, both MISR and MODIS data are needed,

because the two instruments sample the viewing hemisphere from different directions. The contribution of MODIS is no less important than that of MISR. See P5. above. The exact mixture of MODIS and MISR observations for a pixel during a time period will be a function of cloud cover during the period.

V7. More detail is needed on issues of scale, spectral bands, accuracy, coregistration, the effect of clouds on data availability, and computations of albedo in SWIR bands.

We agree that these topics all need more work. Of these issues, we have concentrated on accuracy and cloud impacts, and our results are provided in the revised document. Future studies are planned to address all of these areas more fully.

V8. Albedo and BRDF are part of the same product, even though the user communities may be different.

The reviewer observes that the user communities and requirements for albedo may be quite different from those of BRDF, and that alternative strategies for global albedo products should be considered and discussed. Albedo is a product that is consumed on a number of scales. Needs can range from coarse resolution (e.g., 1-degree) values that change in the spring and fall for global climate modeling to fine- resolution data that is directly ingestible by regional climate and surface energy balance models operating at finer time scales. At coarse resolution, there are a number of approaches, well summarized by Li and Garand (1994), ranging from table lookup based on land cover to derivation of TOA albedo from such data sources as ERBE sensors and correction of that TOA albedo to surface albedo through empirical corrections derived from radiative transfer simulations. Whatever the approach, all satellite applications must overcome problems of clear scene identification, spectral and angular corrections, and the removal of atmospheric effects. MODIS and MISR, by virtue of their fine resolution yet global coverage, are more suited to provide fine resolution albedo products. At the fine resolution, we see no viable alternative to extracting albedos through the mechanism of the BRDF (see P10. above), given the spatial and temporal variability of the earth's surface at the 1-km, biweekly time scale. Had the reviewer been more specific, we might be able to respond more specifically.

V9. Physical models are home-grown.

The reviewer notes that the physical BRDF models selected rely largely on the work of authors, and a more open policy of model selection is desirable. Although the set of physical models in the prior algorithm focused largely on those developed with MODIS support for the MODIS/MISR application, the semiempirical models draw more broadly on the work of the BRDF community. Models of Roujean (1992), Ross (1981), and Walthall et al. (1985) as modified by Nilson and Kuusk (1989) are integrated into the algorithm, and the forward-scattering kernel of Sancer (1969) as used by Choudhury and Chang (1981) will soon be added. The suite of semiempirical models we have developed has been requested by, and provided to, a number of key researchers in the field, including Roujean, Meyer, Ross, and J. Miller, who are assessing its application. It is also being tested by colleagues C. Zhu and Q. Zhu in China.

6.1.5 Literature Cited

Baldwin, D. G. and J. A. Coakley, Jr., 1991, Consistency of Earth Radiation Budget Experiment bidirectional models and the observed anisotropy of reflected sunlight, J. Geophys. Res. 96:5195-5207.

Barnsley, M. J., A. H. Strahler, K. P. Morris, and J.-P. Muller, 1994, Sampling the surface bidirectional reflectance distribution function (BRDF): Evaluation of current and future satellite sensors, Remote Sens. Rev. 8:271-311.

Choudhury, B. J. and A. T. C. Chang, 1981, On the angular variation of solar reflectance of snow, J. Geophys. Res. 86:465-472.

Green, R. N. and G. L. Smith, 1991, Shortwave shape factor inversion of Earth Radiation Budget observations, J. Atmos. Sci. 48:390-402.

Lee, T., and Y. J. Kaufman, 1986, The effect of surface nonlambertianity on remote sensing, IEEE Trans. Geosci. Remote Sens., GE24:699-708.

Li, Z., and L. Garand, 1994, Estimation of surface albedo from space: A parameterization for global application, J. Geophys. Res. 99:8335-8350.

Nilson, T. and A. Kuusk, 1989, A reflectance model for the homogeneous plant canopy and its inversion, Remote Sens. Environ., 27:157-167.

Ranson, K. J., J. R. Irons and C. S. T. Daughtry, 1991, Surface albedo from bidirectional reflectance, Remote Sens. Environ. 35:201-211.

Ross, J. K., 1981, The Radiation Regime and Architecture of Plant Stands, The Hague: Dr W. Junk.

Roujean, J. L., Latoy, M., and Deschamps, P. Y., 1992, A bidirectional reflectance model of the earth's surface for the correction of remote sensing data, J. Geophys. Res. 97:20455-20468.

Sancer, M. L., 1969, Shadow-corrected electromagnetic scattering from a randomly rough surface, IEEE Trans. Ant. Prop. AP-17:577-585.

Sellers, P. J., C. J. Tucker, G. J. Collatz, S. O. Los, C. O. Justice, D. A. Dazlich and D. A. Randall, 1994, A global 1-degree by 1-degree NDVI data set for climate studies. Part 2: The generation of global fields of terrestrial biophysical parameters from the NDVI, Int. J. Remote Sens., in press.

Starks, P. J., J. M. Norman, B. L. Blad, E. A. Walter-Shea, and C. L. Walthall, 1991, Estimation of shortwave hemispherical reflectance (albedo) from bidirectionally reflected radiance data, Remote Sens. Environ. 38-123-134.

Taylor, V. R. and L. L. Stowe, 1984, Reflectance characteristics of uniform Earth and could surfaces serived from NIMBUS-7 ERB, J. Geophys. Res. 89:4987-4996.

Walthall, C. L., J. M. Norman, J. M. Welles, G. Campbell and B. L. Blad, 1985, Simple equation to approximate the bidirectional reflectance from vegetation canopies and bare soil surfaces, Appl. Optics 24:383-387.

6.2 1996 EOS LAND REVIEW: Comments and Response

6.2.1 Comments from the Reviewers (Sept, 1996)

A numerical assessment was made in four categories of evaluation criteria and near– and long–term recommendations were prepared for each of the individual land products:

1. Technical/soundness of algorithm/approach
2. Value of data product to the Land science community
3. Soundness of the validation strategy
4. Extent to which the 1994 ATBD Review issues have been addressed
5. Near–term recommendations for improvements to the data product
6. Long–term recommendations for improvements or additions to the data product

In addition, the reviewers were asked to evaluate the balance of AM-1 Land Data Products and decide whether they met the needs of the Land science community.

1. Extent to which the ATBD addressed the compatibility of this data product with other instruments data products and the needs of the community
2. Assessment of plans for the comparison or enhancement of similar data products from other instruments.
3. Recommendations to improve the balance of land data products

Each category was given a numerical grade as follows:

Grade 9 — Excellent, strongly agree or high

Grade 5 — Average, neutral, medium

Grade 1 — Poor/needs work, disagree, or low

N/A — Not applicable

The BRDF/Albedo product was rated as follows:

Product

a. (Grade 5) The basic approach chosen by the team reduces to a sophisticated non–linear regression analysis — fitting a non–linear function to 6-10 points. They chose this simple approach to make it only observation–based, robust, rapid and scaleable. There are a few concerns/questions that arise based on the ATBD documentation provided:

1. The kernels assume that BRDF depends only on the relative azimuth angle between sun and view directions. This assumes azimuthally isotropic vegetation, an assumption not applicable to row crops or orchards; a caveat that should be noted in the ATBD.

2. The fit and the values of weights will depend upon the data points, especially if the scene is heterogeneous. For example, if one deletes a few of the observations,(*e. g.*, hot spot direction, viewing parallel to the row direction etc.) the fit may be better. Likewise, addition of some observations may make the fit worse. In other works, the calculated surface reflectance for a given scene/target may depend on what data points are chosen, not a desirable situation.

3. RMS error is not the most desirable measure. For example, a calculated reflectance of 0.60 vs. measured reflectance of 0.55 will contribute 0.0025 to RMS error, same as calculated reflectance of 0.08 and measured reflectance of 0.03, although in the latter case the fit is extremely poor. The team should consider using percentage (or fractional) RMS error or another alternative measure. (It is noted that the team has been investigating the fitting stability as a function of different scenarios of data sampling with MISR or MODIS, as has been reported at the IGARSS'96 meeting. These results shold be very helpful in addressing the above concerns and need to be documented in the ATBD).

4. If the derived BRDF is used to estimate biophysical parameters, it is likely that the estimation of the structural parameters will be inaccurate because of the smoothing effect of the fitting procedure. Consideration might be given to giving more weight to near–nadir observations in biophysical retrievals.

5. Is there a linear relationship between the weights as calculated for say 256 1km by 1km pixels and one 16km by 16km pixel: If not, the whole approach (which combines MODIS and MISR data at different resolution levels) is flawed. Scaleability needs to be studied.

6. A 16 day product was chosen to ensure enough cloud–free reflectance data for fitting. For certain cases, vegetation will significantly change in such a period. Another big concern (based on some work with AVHRR) is that there will not be enough good observations to fit a function. This will almost certainly be true at latitudes north of 45° over land in summer. What will the algorithm do then? With a rapid seasonal change it may not be feasible to extend the permissible period.

7. The surface reflectance calculated used a particular atmospheric scattering mode. Will the calculated BRDF represent the right boundary condition for another atmospheric scattering model?

8. MISR data are not available for wavelengths used in MODIS bands 5–7. The model selection is done using MODIS/MISR data in Bands 1–4. Thus it is assumed that BRDF shape in Bands 5-7 follows the general shape in Bands 1–4. Is this a justifiable assumption?

b. (Grade 5) BRDF and albedo are useful for biophysical and climate modeling, angle correction of land surface reflectances, a lower boundary condition for atmospheric radiative transfer, and surface energy balance calculations. For example, the landcover product needs equivalent nadir reflectances, and the hydrological (climate) modeling community needs monthly albedo data at 10 (50) km spacing . Many of the atmospheric correction models assume a Lambertian earth to get surface reflectance and radiance and knowledge of the earth BRDF will improve corrections.

However, the quality of the product, especially BRDF, may not be good for certain purposes. See comments under technical/scientific soundness.

c. (Grade 5) The validation approach consists of fitting the semi–empirical model to a wide range of field–measured BRDF sets (from literature), aircraft–measured data (ASAS, POLDER, CASI), laboratory data and simulated data. The team also plans to do large scalestudies.

Since the general model has many parameters, one would expect that the model will fit to the observed data (PARABOLA or ASAS). What is important is what happens to the fitted parametres if the data poinst are changed and some of the points have measurement erros. If the fitting approach is not "stable", the validity of the whole approach is questionable. However, see the comments above regarding the fitting tests being reported by the team at the recent IGARSS'96 meeting.

d. (Grade 7) Before the 1994 ATBD review, the team were planning to use physical BRDF modeling and the reviewers raised several concerns about the physical approach, included the operational feasibility, need of ancillary data, adequacy of the angular data. In response to the comments, the team has completely changed the approach to the present semiemipirical approach. The physical approach has its attractive features. The panel urges a longer–term EOS strahtegy that adopts the semi–empirical approach for an at-launch product but is open to a new initiative for an advanced post-launch product based on physical–modeling research program.

e. Near–term recommendations.

- Systematically evaluate the fitting process as a function of number of observations and the solar/viewing directions of the observations. These "observations" could be generated by a canopy reflectance model or from an instrument (*e. g.* PARABOLA). This study should be carried out for heterogeneous canopies.
- Determine how sensitive the product is to the choice of a different atmospheric scattering model, such

as those used by the ASTER or MISR teams. A collaboration with the atmospheric scattering modeler(s) who may use the product whould be mutually beneficial.

• Determine the usefulness of the product in biophysical parameter estimation by carrying out the inversions for known vegetation canopies.

f. Long–term recommendations.

• Investigate the possibility of developing an approach which has a proper balance between physical and empirical modeling, which uses vegetation classification to minimize the complexity.

Balance

a. (Grade 5) BRDF and albedo are very useful for biophysical and climate modeling, angle correction of land surfaces, and surface energy balance calculations. A knowledge of earth BRDF will improve the accuracy of ASTER based atmospheric correction to get surface properties. BRDF is also the basis for higher level biophysical products. Consequently, the quality of the BRDF product is especially important.

b. (Grade 5) On the basis of oral comments, it appears that the team will work with team members from other instruments, especially MISR. It also appears that the team will use simulated data from MISR and vice-versa to improve on the product and enhance the data–formate compatibility and explore the complementarity of MODIS in a synergistic way to improve the accuracy of various surface reflectance products.

c. (Recommendations for change) See comments above.

6.2.2 Specific Responses to the Land Review Panel's Comments (Section 5.2.6a of the EOS-AM-1 Land Data Product Review Report)

Prepared by Alan Strahler, Wolfgang Wanner and Crystal Barker Schaaf

We would like to thank the SWAMP Review Panel for a very thorough and constructive review. The members of the panel not only brought a great deal of their own understanding and experience to the review, but also clearly spent a lot of time in a careful examination of our specific algorithm. We very much appreciate their efforts.

The purpose of this document is to respond specifically to queries and concerns called out in the review report, keying them especially to version 4.0 of the BRDF/Albedo ATBD.

Product

(a) Technical/Scientific Soundness

1. The panel notes that the BRDF models used depend only on relative, not absolute, azimuth. This implies an azimuthally isotropic surface, an assumption that would not be true for row crops or orchards. The panel requests that this caveat be noted in the ATBD.

   We acknowledge that the semiempirical and empirical models that we use make this assumption. However, our opinion is that the differences between a 3-angle BRDF and a 4-angle one fitted to the same surface are probably not large for most practical cases. Clearly the regular shadowing pattern of row canopies will show some differences from random ones that are implied in most models, but the differences are likely to be significant only for a few view and illumination angles. Some further studies using row crop reflectance models (*e.g.*, those of Goel *et al.*), might be useful to confirm these opinions. In any event, we have noted this caveat in the revised ATBD.

2. The panel expresses the concern that the calculated surface reflectance function for a given scene or target may be overly dependent on the specific data points chosen, noting that removal of points could lead to better fits, and addition of points could lead to worse fits.

   A great deal of effort has gone in to exploring the dependencies of retrieved BRDF and albedo on noise and variation in angular sampling with latitude and time of year. Our Appendixes B and C address these topics in some detail; section 3.3.2 summarizes these results. In short, we have good evidence that we will retrieve albedos with accuracies around 5 percent and bidirectional reflectances in the 5–10 percent range.

3. The panel brings up the problem of relative versus absolute error in measuring the RMSE of a particular model fit, suggesting that relative error be considered.

   This topic has been the subject of much debate within our research group and within others faced with the same problem. (Verstraete, Pinty and Martonchik for MISR, and Roujean for POLDER, for example.) The issue is valid at within-band and across-band levels.

   Within a single spectral band, minimizing absolute error will constrain the BRDF to follow the larger values more closely. This strategy is particularly suited to reducing the error in albedo estimation, where integration of the BRDF is required. On the other hand, minimizing relative error will cause the function to fit smaller observed values more closely, thereby following the BRDF shape more closely. We use absolute error to favor the accuracy of albedo, since we believe the albedo will be used more often and more directly, at least at first, by EOS investigators. Absolute error is also used in the MISR and POLDER algorithms for the same reason. Note, however, that Appendix A, Figures 2 and 3, and Appendix B, Figure 3, show that fits using absolute error still match data (Appendix A) and alternative models (Appendix) quite well.

At the across-band level, our algorithm chooses among the possible kernel models by selecting that model that fits best across the four VNIR bands of MODIS and MISR. That is, each band votes for each structural model, with its vote proportional to the absolute RMSE associated with the model in that band. The winning model is then used for all bands, with different f-values calculated for each band.

An alternative would be to weight the vote of each band by the proportion of shortwave downwelling solar irradiance associated with the band. This would again favor albedo. However, since it is the structural scattering mechanism that is being selected, we allow each band to be equally weighted. That could change in the postlaunch era if albedo retrievals are to be further emphasized. Note that all BRDF models are capable of producing a full BRDF with the usual features — *e.g.*, bowl-shape and hotspot — depending on the f-values associated with each kernel.

In short, the issue of relative versus absolute error is not easy to resolve. Our choice is to favor albedo, while making sure that BRDF fits are still reasonable.

4. We are puzzled by comment (4), which states, "If the derived BRDF is used to estimate biophysical parameters, it is very likely that the estimation of the structural parameters will be inaccurate because of the smoothing effect of the fitting procedure. Consideration might be given to giving more weight to near-nadir observations in biophysical retrievals." We are not sure to which structural parameters the panel is referring, but it is well-established in the literature that the primary source of structural information is directional, and thus near-nadir observations are not any more important a priori than off-nadir observations. In fact, they may be less important.

   If this comment applies to the idea that a real nadir-view image may have more information than a nadir-view image reconstructed from the BRDF, perhaps this is true. However, Appendix A, Figure 6, provides a comparison of real and reconstructed nadir images, and it is obvious that they are very similar.

5. The panel draws attention to the scalability and linear relationship of model weights with coarsening resolution, remarking that if the relationship is not linear, then our approach is flawed.

   The semiempirical models we use in Ambrals stem directly from Roujean's original model, which was developed specifically to address the scalability problem using a top-down approach. Theory shows that as long as a mixed pixel is composed of a number of discrete patches of different surface types, then the BRDF of the mixed pixel will be a linear function of the individual BRDFs weighted by their proportional areas. However, when the surface types are more intimately intermixed, they will interact by multiple scattering. At the finest scale of mixing, we have a surface type that is modeled as a composite of intermixed scattering elements, such as the plant crowns of the Li kernels. Thus, the problem would seem to be only for finer (but not finest) scales of mixing, on the order of patches of changing vegetation covers on the size of perhaps 5–10 meters.

Appendix F provides some preliminary results of scaling studies for HAPEX-Sahel, in which Ambrals models are fitted to ASAS data at increasingly coarse resolutions. These results show that model selection is variable at resolutions of 3 to 30 meters. If significant nonlinearities are present, we would expect the model choice to continue to be unstable as BRDF shape changes with aggregation. However, the data show that beyond 30 meters, the choice of model is quite stable, indicating a linear scaling behavior.

The problem of scaling is also an important one for validation. We will need to scale up BRDF measurements from individual plots with field instruments to kilometer-sized pixels from spaceborne instruments by bridging the gap with aircraft data, such as that acquired by AirMISR. These studies will also validate the scalability of the semiempirical model approach. Section 3.3.4 addresses validation issues and plans in more detail.

6. The panel notes that cloud cover may restrict the number of available observations in a 16-day period sufficiently that a BRDF cannot be fitted and wonders what provision is made for that case.

   Cloud cover is discussed in more detail in Section 3.3.1. The effect of loss of data due to random clouds is simulated in Appendix B, Table 3, which shows the errors in estimation of albedo and nadir reflectance with data points randomly removed to simulate the effect of cloud cover on retrievals. The data summarize all latitudes, all biome types, and all solar zenith angles for a 16-day period at the equinox. Even with 75 percent of the observations removed, median retrieval accuracies remain about the same. Even the variance in accuracies holds constant.

   At present, the algorithm requires 8 looks for an inversion. Section 3.2.1.4 describes the procedure used when fewer than eight observations are available. In such cases, a model and kernel weights are selected from a database of accumulated knowledge about the grid cell and its general land cover type. In the fitting, the shape of the BRDF is preserved, but the overall height is adjusted to fit the available data. (This amounts to fitting only the isotropic weight f_0.) If no data at all are available, the prior or database-indexed BRDF is supplied. In either case, flags are set to indicate the procedure and the quality of the retrival is downgraded.

7. The panel raises the question of the interaction between the scattering model used in atmospheric correction and the BRDF retrieval, noting that among MODIS, MISR and ASTER, three different aerosol scattering models and codes are employed. They ask if our BRDF will represent the right boundary condition for another atmospheric scattering model.

   The BRDF we retrieve is the true BRDF, ρ, independent of the atmosphere (see section 3.2.4 and equation (40)). This parameter is a pure surface property and does not vary with scattering model, so it is certainly the right boundary condition. Appendix D shows that BRDF and albedo can be retrieved within a mean error of less than one percent by the simple iterative coupling we use in our algorithm provided that the atmospheric properties are known.

8. The panel questions the assumption that model selection, which is based on VNIR bands 1–4, is extensible to SWIR band 5–7.

   Model selection is based on the structure of the surface rather than on its spectral characteristics. Ross-thin and Ross-thick kernels are differentiated by leaf area index; Li-sparse and Li-dense kernels are differentiated by the size and spacing of individual plant crowns. It is the weights on the kernels that reflect the scattering mechanisms, which are wavelength-dependent. Thus an open forest or shrubland may be appropriately characterized by the Ross-thick/Li-sparse model, but for the red band, where volume scattering is small and geometric effects are dominant, and the Li-sparse kernel will carry the weight. In the near-infrared, the Ross-thick kernel will dominate, since leaf scattering will reduce or outweigh geometric effects. Thus, theory suggests that the model selection is, indeed, extensible to the SWIR bands.

   However, it would be nice to confirm this with observations. Of the sources of bidirectional reflectance data commonly available, only one instrument, PARABOLA, acquires data beyond silicon wavelengths, and that is for the wavelength region of MODIS band 6 (TM band 5) only (1.62—1.69 μm). Data are entirely lacking for MODIS Bands 5 and 7. Although our efforts have focused heretofore on red and NIR bands almost exclusively, we will reanalyze our PARABOLA datasets to examine this question.

(e) Near-term Recommendations for Improvements to the Data Product

1. The panel specifically requests that we evaluate the fitting process as a function of number of observations and the solar/viewing directions of the observation, and that this also be accomplished for heterogeneous canopies.

   As noted in our response to (a).1. above, evaluating the accuracy of the fitting of BRDF and retrieval of albedo to noise, angular sampling, and data limitations has been a major thrust of our work of late. Appendices B and C and Section 3.3.2 summarize these results. However, our work has not examined heterogeneous canopies thus far, and we will endeavor to do so as model development and validation proceed in the prelaunch time frame. Note that this may not be an easy task, as few if any bidirectional reflectance models of heterogeneous canopies (beyond savannas) exist, and most measurement campaigns are directed at homogeneous cover types! AirMISR will help considerably, since its 10-km swath width is wide enough to acquire directional imagery from complex heterogeneous targets.

2. The panel suggests that we systematically evaluate the linearity of the scaling for the models.

   As noted in our response to (a).5. above, we will endeavor to do so.

3. We are charged with exploring how sensitive the product is to alternative atmospheric scattering models and to help explore its use with atmospheric scattering modelers.

In response to the SWAMP review panel's concerns about alternative atmospheric correction algorithms, a working group of atmospheric correctors from MODIS, MISR, and ASTER has been formed under the lead of Eric Vermote. We will work with this group on these issues.

4. The panel requests that we determine the usefulness of the product in biophysical parameter estimation by carrying out the inversion for known vegetation canopies.

   We already have some early indications that such biophysical parameters as land cover type can be retrieved from the product. Appendix A, Figure 1 documents how patterns of RMSEs to the various models can indicate cover type from the inference of the dominant scattering mechanisms. Appendices I and J document the mapping of kernel weights for the modified Walthall and Roujean models and illustrate that the spatial context of the weights contains information about the land cover type.

   We wish to reassure the panel that we are just as interested in retrieving biophysical parameters from our models as they are! Originally our plan was for structured inversion of physical models, but in response to early reviews, we have concentrated on developing a practical, data-driven, robust algorithm for the purposes of albedo retrieval and characterizing the shape of the BRDF for view angle correction. We view biophysical retrievals as the next important step for this algorithm and line of research, and will pursue it vigorously in the future.

APPENDIX TO:

MODIS BRDF/Albedo Product: Algorithm Theoretical Basis Document Version 4.0

Principal Investigators:
A. H. Strahler, J.-P. Muller, MODIS Science Team Members

Document Prepared by
Alan H. Strahler[1], Wolfgang Wanner[1], Crystal Barker Schaaf[1],
Xiaowen Li[1,3], Baoxin Hu[1,3],
Jan-Peter Muller[2], Philip Lewis[2], Michael J. Barnsley[4]

[1] Boston University
[2] University College London
[3] Institute of Remote Sensing Application, Chinese Academy of Sciences
[4] University of Wales, Swansea


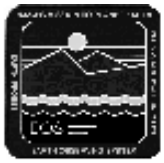


MODIS Product ID: MOD43
Version 4.0 – November 1996

APPENDIX A:
VALIDATION OF KERNEL-DRIVEN SEMIEMPIRICAL MODELS FOR GLOBAL MODELING OF BIDIRECTIONAL REFLECTANCE (PAPER BY HU ET AL.)

Draft – November 1996 to be submitted in revised form to Remote Sens. Environ.

Validation of Kernel-Driven Semiempirical Models for Global Modeling of Bidirectional Reflectance

Baoxin Hu, Wolfgang Wanner, Xiaowen Li, and Alan H. Strahler

The semiempirical, kernel-driven Ambrals BRDF model (Wanner et al., 1995) was developed for correcting and studying view and illumination angle effects of a wide variety of land covers in remote sensing applications. This model, also scheduled for use in producing a global bidirectional reflectance distribution function and albedo data product from EOS-MODIS and MISR data, is validated in this paper by demonstrating its ability to model 27 different multiangular data sets well, representing major types of land cover. The selection of the kernels used in the model is shown to relate to land cover type, and the inversion accuracy to be good in nearly all cases: the correlation coefficient between modeled and observed reflectances is larger than 0.9 for about half of the data sets and larger than 0.75 in all but one case where the observations are irregular. The average root mean squared error of the inversions is 0.034. A new kernel modeling the sun zenith angle dependence of multiple scattering is introduced and shown to improve fits for dense vegetation. Operation of the Ambrals model is demonstrated by applying it to an ASAS image on a per-pixel basis.

INTRODUCTION

With the increasing use of coarse and medium-resolution off-nadir viewing sensors producing reflectance data for global monitoring, analysis of the BRDF (Bidirectional Reflectance Distribution Function) of each pixel is becoming more and more important. The BRDF can not only be used to compare observations obtained at different angles or standardize observations to a common geometry but also to provide surface physical parameters and the boundary condition for radiative transport in the coupled atmosphere-earth system.

At the same time, global change research introduces new requirements into the modeling of the bidirectional reflectance of vegetation. Studies of the BRDF properties of vegetation have for the most part been carried out over thematically homogeneous surfaces and for a limited variety of land covers. The BRDF models developed also usually assume homogeneity of the land cover. However, to allow frequent global coverage the satellite sensors used in global change research typically do not possess high spatial resolution. For example, the U.S. National Oceanographic and Atmospheric Administration (NOAA) Advanced Very High Resolution Radiometer (AVHRR), commonly used in land surface monitoring, has a spatial resolution of 1.1 km at nadir. The Moderate Resolution Imaging Spectroradiometer (MODIS) to be launched in mid-1998 on the EOS-AM-1 platform, which will be the primary Earth Observing System (EOS) sensor for observations of terrestrial dynamics (Running et al., 1994), is a 36-channel radiometer covering 0.415–14.235 μm in wavelength with a spatial resolution ranging from 250 m to 1 km at nadir, depending on the band. For sensors of this kind, a given pixel will frequently contain a heterogeneous mixture of bare soil and vegetation canopies, or a mixture of spatially distinct types of vegetation with different structural and optical properties. Because of the global coverage provided, a very large number of different surface types will be viewed. Therefore, it is necessary to develop BRDF models of a type that can readily be applied to a variety of inhomogeneous land covers, that is flexible enough to respond to changing scenarios, and that is up to the demands of global data processing by being very rapidly invertible.

One type of BRDF model that fulfills these re-

[1]Center for Remote Sensing and Department of Geography, Boston University

Address correspondence to Baoxin Hu, Center for Remote Sensing, Boston University, 725 Commonwealth Avenue, Boston, MA 02215, USA.

Received 1 January 1999; revised 1 January 1999.

quirements very well is the semiempirical kernel-driven type originally suggested by Roujean et al. (1992) and later developed further by Wanner et al. (1995a) in form of the Ambrals BRDF model (Wanner et al., 1997). This model type has been successfully applied to a variety of remotely sensed data sets including AVHRR data (Leroy and Roujean, 1994; Li et al., 1996; Ruiz de Lope and Lewis, 1997) to correct for surface BRDF effects, for example in the vegetation index. The Ambrals model will also be used in generating the global MODIS BRDF and albedo standard data product (Strahler et al., 1996; Wanner et al., 1997).

Previously, only limited validation of the mathematical expressions used in the Ambrals model has been published (Strahler et al., 1995; Wanner et al., 1995b; Hu et al., 1996; Wanner et al., 1997). In this paper, we now present more extensive validation of the Ambrals BRDF model using various bidirectional reflectance data collected over a wide variety of surface types. Since currently almost no BRDF data sets for heterogeneously mixed land surfaces are available, validation is restricted to homogeneous cover types even though it is expected that the models will display their strength more obviously for mixed pixels. Data for mixed scenes will be more readily available in a few years.

MODELING BIDIRECTIONAL REFLECTANCE WITH KERNEL-DRIVEN MODELS

Kernel-Driven BRDF Models

In operational processing, the physical approach to BRDF modeling is problematic since it still is neither flexible enough nor computationally simple enough to allow global rapid inversions on a regular basis. It has therefore been the strategy for the three largest planned operational BRDF and albedo products, those from MODIS, the EOS Multi-Angle Imaging Spectroradiometer (MISR) (Diner et al., 1991), and the POlarization and Directionality of the Earth's Radiation instrument (POLDER) (Deschamps et al., 1994; Leroy et al., 1997) to use linear or semilinear semiempirical BRDF models. These models retain some physical interpretation while being highly capable of adapting to many BRDF shapes and being very rapidly invertible. Their number of parameters is small, usually three. MISR will be using the semiempirical RPV BRDF model developed by Rahman et al. (1993) in a form modified by Martonchik (Engelsen et al., 1996), POLDER will use the Roujean kernel-driven model (Roujean et al., 1992), and MODIS will rely on the kernel-driven semiempirical Ambrals BRDF model (Wanner et al., 1995a, 1997) that will here be validated, and will also run the empirical modified Walthall model (Walthall et al., 1985; Nilson and Kuusk, 1989) in parallel. Ambrals stands for: Algorithm for MODIS bidirectional reflectance anisotropy of the land surface.

In the kernel-driven semiempirical approach, the BRDF is modeled as a weighted sum of a volume scattering function and a surface scattering function (called kernels), and a constant (Roujean et al., 1992). These kernels are derived from approximations to physical BRDF models, so they retain a physical meaning. In model inversion, the weight given to each kernel is determined empirically by fitting to the multiangular observations made. Thus, it is the weights of the semiempirical kernels that are retrieved, characterizing the balance between volume and geometric scattering in the possibly mixed scene viewed.

Volume and surface scattering kernels are derived from physical radiative transfer models and geometric optical models by simplifying them to the following format by reasonable approximations:

$$R(\theta_i, \theta_v, \phi; \lambda) = c_1(\lambda)k(\theta_i, \theta_v, \phi) + c_2(\lambda), \quad (1)$$

where c_1 and c_2 are constants containing physical parameters, R is the modeled value of the bidirectional reflectance of surface objects, and k is the kernel function dependent only on viewing and illumination geometry; θ_i and θ_v are illumination and viewing zenith angles, ϕ the relative azimuth, and λ the wavelength. If after approximations the kernel k still contains parameters, they are set to a typical value that may vary from one kernel to the next.

A complete kernel-driven semiempirical model has the form

$$\begin{aligned} R(\theta_i, \theta_v, \phi; \lambda) &= f_{iso}(\lambda) + f_{geo}(\lambda)k_{geo}(\theta_i, \theta_v, \phi) \\ &\quad + f_{vol}(\lambda)k_{vol}(\theta_i, \theta_v, \phi), \end{aligned} \quad (2)$$

where the quantities k_{geo} and k_{vol} are the geometric-optical surface-scattering kernel and the radiative-transfer volume-scattering kernel, and the factors f_{geo}

and f_{vol} are their respective weights. The term f_{iso} is the contribution of isotropic scattering.

The Ambrals BRDF Model

The original Roujean model used a kernel derived from a single-scattering radiative transfer theory by Ross (1981), called the Ross-thick kernel, and a geometric-optical kernel for rectangular protrusions (Roujean et al., 1992). The latter kernel was found not to fit some cover types well, especially dense forest canopies (Roujean et al., 1992). The Ambrals BRDF model makes use of an improved set of kernels. The Ross-thick kernel, derived for large values of the effective scattering leaf area index, is also used, but alternately an approximation for low effective values of the leaf area index, called the Ross-thin kernel, is available (Wanner et al., 1995a). Which of the two kernels to use for a given inversion is decided a priori, is based on previous experience, or is decided such that the kernel chosen produces the least root mean squared error (RMSE) in inversion. Similarly, the Ambrals model allows for two alternate choices for the geometric-optical kernel, derived for different types of scenes (Wanner et al., 1995a). One, called the Li-sparse kernel, is an approximation to the geometric-optical mutual shadowing model by Li and Strahler (1992) for sparse ground objects, where the BRDF is mainly governed by shadow casting. The second geometric kernel, the Li-dense kernel, is determined by the bright sunlit object faces mainly visible due to mutual shadowing effects in dense ensembles of ground objects, for example dense forests.

The Ambrals model, as it is to be used for generating the MODIS BRDF/albedo data product, thus occurs in four variants that are used to optimize the inversion. These are the Ross-thin/Li-sparse, the Ross-thick/Li-sparse, the Ross-thin/Li-dense, and the Ross-thick/Li-dense modes of the model. The Li-sparse kernel is formulated for round crowns, the Li-dense kernel has prolate crowns with a diameters ratio of 2.5. Both kernels model crowns where the mean distance from the ground to the lower edge of the crown is half of the crown height.

Error Functions Used

Like all linear models, the Ambrals BRDF model can be inverted analytically through matrix inversion (Lewis, 1995), avoiding costly numerical inversion problems. In each wave band, a set of model parameters is determined through minimization of an error function,

$$e^2 = \frac{1}{N - n_p} \sum_{j=1}^{N} \frac{\left(R_j^{obs} - R_j^{model}\right)^2}{W_j}. \qquad (3)$$

Here, N is the number of observations, n_p the number of parameters of the model, R^{obs} and R^{model} are observed and modeled reflectances, respectively, and W_j is a weighting factor that may be chosen to give different weights to different observations if desired. In the absence of qualifying knowledge, W_j is commonly specified as unity. For a relative error measure, $W_j = R_j$. An absolute error measure generally ensures best accuracy for large values of the reflectance, which dominate albedo, but does not put a strong emphasis on small reflectances that may be of particular interest for some applications. A relative measure of error does not show this latter problem, but since larger absolute deviations are allowed for large values of the reflectance, albedo derived from the BRDF is likely to possess a larger absolute error as well.

A similar problem exists when attempting to find a function for minimizing the error in several wave bands simultaneously. The weight given to the error made in each band may be determined either to be equal, to favor bands with small albedos by introducing a weight in each band proportional to the size of the albedo, or by weighting according to the proportion of radiation present in each band. In this study, the RMSE determined for a specific data set and model is given by

$$RMSE = \sqrt{\frac{1}{n_b} \sum_{i=1}^{N_{band}} \frac{e^2}{w_i}}, \qquad (4)$$

with both W_j and w_i presently set to unity, the latter determining the contribution of each band to the selection of the best-fitting kernel combination of the Ambrals model; n_b is the number of wave bands.

DATA SETS USED

As mentioned earlier, kernel-driven BRDF models have been developed for applications at the global scale. They are designed to describe the bidirectional reflectance of mixed land cover types. But before more measurements for heterogeneous scenes are available, it is necessary and useful to validate the model using field-measured data over a single land cover type. A number of such data sets are available as detailed below, covering a large variety of land cover types with variations, for example, in canopy coverage and differences in leaf area index (LAI). All of these data sets are available for several different sun zenith angles. Some studies (e.g., Engelsen et al., 1996) have also used numerical BRDF forward modeling to explore model properties, but due to possible similarities in the mathematical expressions used in the modeling of both the forward and the inverse model their use for validation is limited. Table 1 summarizes basic properties of the data sets that were used.

1) BRDF data sets by Kimes

Kimes (1983) collected a series of multiangular data sets of a plowed field, a corn field, orchard grass and a grass lawn with 0, 25, 50 and 97 percent of vegetation cover, measured near Beltsville, Maryland. In situ measurements made in Northern Africa of three land covers with low and two land covers with high vegetation coverage were reported by Kimes et al. (1985). They are annual grassland, hard wheat, steppe grass, irrigated wheat, and soybean. Their corresponding coverage is 4, 11, 5, 70 and 90 percent, respectively. Helicopter measurements were performed on two kinds of high coverage forest (70 and 79 percent) dominated by pine trees in one case and hardwood trees in the other, both situated in Virginia (Kimes et al., 1986). Data collected in the red (580–680 nm) and the near-infrared (730–1100 nm) bands were used in this work, available for either three or four sun zenith angles depending on the case. The view zenith angles range from 0° to 75° in increments of 15°. Relative azimuth angles varied from 0° to 345° in increments of 45°.

2) Soybean data by Ranson

Three bidirectional reflectance data sets were collected by Ranson et al. (1985) over a commercial soybean field in West Lafayette, Indiana, on three dates during the summer of 1980 with an Exotech model 100 radiometer in four spectral bands (500–600, 600–700, 700–800, and 800–1100 nm). The view zenith angles observed at were 0°, 7°, 22°, 30°, 45° and 60°. View azimuth angles ranged from 0° to 315° in steps of 45°. On the three dates (July 18, July 25, and August 27), Vegetation coverage was 72, 83 and 99 percent.

3) Boreal forest data by Deering

Deering et al. (1995) measured the bidirectional reflectance of Old Jack Pine, Old Black Spruce and Aspen at the BOREAS forest in Canada on dates May 31, June 7 and July 21. The instrument used was PARABOLA, which allows to acquire radiance data for nearly the complete sky- and ground-looking hemispheres. Data are post-processed and binned to intervals of 15° in zenith angle and 30° in azimuth angle. In this study, data for the red (0.650–0.670 nm) and the near-infrared (810–840 nm) bands were used.

4) Soil data by Irons

Three data sets of a bare soil multiangular reflectance were collected by Irons et al. (1992) in 1989 using the MMR instrument on the ground and for several different sun zenith angles. The three data sets differ in the surface roughness of the soil, which was produced by working the soil with different agricultural machines. Surface roughnesses were 1.2, 2.6, and 3.9. The view zenith angle ranged from 0° to 70° in intervals of 10° and the view azimuth angle from 0° to 180° in intervals of 45°.

5) Grassland data from FIFE

The reflectance of a grassland at the FIFE study site located south of Manhattan in the Konza Prairie of northeastern Kansas was measured on July 11 and October 9, 1987 using MMR (cf. Walthall and Middleton, 1992). Vegetation was primarily a mixed grass including several species. View zenith angles observed were 0°, 20°, 35°, and 50°, the solar zenith angle was around 20° for one data set and around 55° for the other.

6) Airborne POLDER data

An airborne version of the POLDER instrument was used to collect multiangular reflectance data in the area of La Crau, France, in June, 1991 (Leroy et al., 1996). The area is covered by a wide variety of vegetation types, such as sorghum, sunflower, vegetable, vine and grass. After registration of several POLDER images, data with various view and illumi-

nation angles were obtained for the red (630–670 nm) and near-infrared (830–870 nm) wave bands.

EVALUATION OF MODEL PERFORMANCE

RMSEs of Inversion and Kernel Selection

To evaluate the four available kernel combinations for the Ambrals model, each was fitted to each of the multiangular data sets and the RMSEs and correlation coefficients between the predicted and observed reflectances were computed. Inversions were carried out simultaneously for all available bands, i.e., each kernel combination was required to not only fit the reflectances in each band well, but also to minimize the error across bands (mostly two, red and near-infrared) according to equation (4) at the same time. The results show that nearly all data sets are fit well by at least one of the model variants.

This may be seen in Figure 1, which shows the RMSE for each model variant for selected different land cover types. As expected, different kernel combinations produce the best fit (the lowest RMSE) for different types of land cover.

Cases with bare soil or sparse vegetation, such as the barren plowed field, the bare soil (Irons), the annual grass (coverage 4 percent), or the hard wheat (coverage 11 percent) are fitted better by the Ambrals variants with the Li-sparse kernel than those with the Li-dense kernel. For these land cover types, shadow-casting of clumps of soil and vegetation mainly affects the bidirectional reflectance. Thus surface scattering dominates the scattering of solar radiation. Due to the smallness of the contribution due to volume scattering, the selection of volume scattering kernel has little influence. Of the two surface scattering kernels, the Li-sparse kernel is chosen over the Li-dense kernel because it is the one that most strongly derives its shape from effects of shadow-casting.

For horizontally uniform vegetation canopies with many leaves, the type most different from bare soil and sparse vegetation, results are appropriately different. Examples shown in Figure 1 are the orchard grass (LAI is 1.0) and the irrigated wheat (LAI is 4.0). Their canopies tend to be continuous and thus volume scattering is dominant. Whether the Li-sparse or the Li-dense kernel is selected does not make much difference in these cases. But the model variants containing the Ross-thick kernel fit the bidirectional reflectances better than those using the Ross-thin kernel.

A third type of canopy is represented by dense vegetation composed of individual crowns, where mutual shadowing in viewing and illumination direction is the dominant process. In such cases, only illuminated tops of crowns are visible at large view zenith angles. Shadows cast by the crowns are mostly invisible due to mutual overlapping in the view direction, and no background is visible, which makes this case different from the case of sparse vegetation, where the shadows remain visible. As expected, model variants using the the Li-dense kernel are found to provide the best fit to the dense forest canopy, such as the hardwood forest data set.

But for the sparser old black spruce stand, shown in Figure 1 in contrast to the hardwood forest, both mutual shadowing of crowns and shadow casting play a role. Thus the model variants with the Li-sparse kernel fit this data set a little better than those with the Li-dense kernel, although all four fit it well.

For some land cover types, all four model variants fit at almost the same level. Examples are the soybeans (data from Kimes and Ranson), the grassland (FIFE) and the sunflowers (POLDER). This may be because the respective canopies do not display strong bidirectional reflectance properties for the given angular samplings.

From this analysis it is obvious that the BRDFs of different land cover types are best represented by different kernels in the Ambrals model. No data set is fitted with an RMSE of more than 0.046. The pattern given by which kernels fit well and which do not in a particular case can indicate basic characteristics of the observed surface, information that is potentially useful in land cover classification since it is different from the spectral information (for example the sparse/dense distinction for forests). What is retrieved is not merely the parameters required for a reasonable fit, but the kernel choice also reveals whether one particular approximation made or the other is more suitable for describing the BRDF. Such information would not be obtained in this way from a single BRDF model variant, especially since all Ambrals kernel combinations produce fits RMSEs in a seemingly reasonable range.

Principal Plane and Principal Cone Fits

This leads to an important question regarding the RMSEs of the four Ambrals kernel combinations plotted for each data set in Figure 1. Do the relatively moderate differences seen in the value of the RMSE between the four model variants signify relevant differences in the modeled reflectances? To answer this question, Figure 2 shows principal plane and principal cone plots of the modeled reflectance for the best-fitting and the worst-fitting kernel combinations, and the observed data, for a few cases and in the red and near-infrared wave bands. These cases were selected to have similar solar zenith angles of observation and to represent major types of vegetation, bare, sparse, dense and forest.

The bare soil and very sparse annual grass data sets were best represented by models containing the Li-sparse kernel. Figure 2 shows this fit and, for comparison, that obtained when using the Li-dense kernel instead. Obviously, employing the Li-sparse kernel provides a better fit in the hotspot region. For the annual grass, the azimuthal dependence of reflectance on the principal cone is not modeled too well by the model variants containing the Li-dense kernel.

The plots for the dense irrigated wheat show that the model variant based on the Ross-thick kernel fit the azimuthal change of reflectance on the principal cone much better than those containing the Ross-thin kernel, use of which leads to a clear underestimation of the reflectance.

Finally, the plots for the hardwood forest show that while both the best-fitting model variant, Ross-thick/Li-dense, and the worst-fitting model, Ross-thin/Li-sparse, have some problems with this data set, the fits provided by the former are better than those of the latter, especially on the principal plane in the near-infrared.

Figure 2 serves to demonstrate that not only do different types of land cover respond to different kernel combinations used in the Ambrals model, but the combinations producing the smaller RMSE also fit the data better to an extent that justifies, we believe, using different kernel combinations depending on the case. Even though the RMSEs of the bad-fitting kernel combinations are not much higher than those of the best-fitting combinations, the fits produced are not of similar quality. Since cases may be found where one or the other kernel combination works best, all should be retained in modeling.

Consequently, the best-fitting model variant in terms of the RMSE is chosen for the subsequent analysis. Table 1 identifies the best kernel combination and the band-averaged RMSE for each data set found from the inversion. In two cases, the best fit was obtained when the observations were modeled purely from volume scattering.

Correlation Between Modeled and Observed Data

For each data set the correlation coefficient between modeled and observed reflectances is calculated in the red and the near-infrared. The results are also shown in Table 1. In the red band, nearly half of all data sets, 12 of 27, had correlation coefficients larger than 0.9; 18 of 27 had coefficients larger than 0.8; and 23 of 27 sets had coefficients larger than 0.75. Only one set had a correlation coefficient less than 0.7, which will be explained later. In the near-infrared, the fits are even better. Half of all sets, 13 of 27, have correlation coefficients larger than 0.9. 23 of 27 have coefficients larger than 0.8, and 26 of 27 have coefficients larger than 0.75. These values indicate a reasonable agreement between the modeled and observed values.

Scatter plots of modeled versus observed reflectance are shown in Figure 3. For each of four different land cover types, bare, forest, broadleaf crops, and grasses, the data with the best correlation coefficient and the data with the worst correlation coefficient are shown to demonstrate the range of results obtained. The bare soil is modeled quite well in both cases, with correlation coefficients over 0.9. For the other land cover types, the good fits are excellent while for the ones with lower correlation coefficients display some scatter of points away from the diagonal. In the case of the pine forest, it is probable that the insufficient handling of multiple scattering by the kernels, which approximate it as being isotropic, causes the problems. An isotropic approximation to multiple scattering may be reasonable for sparse canopy cases, but the pine forest has a coverage of 70% and the data were obtained at four sun zenith angles ranging from 26° to 74°. The effect of multiple scattering may be expected to be large. We will later show that an im-

provement of the multiple scattering treatment of the model will indeed improve this fit.

In the broadleaf crop class, the corn data produces the worst fit, with a correlation coefficient in the red of 0.47. However, these data are extremely noisy, either due to problems during the measurement or due to actual local peculiarities of the canopy viewed that are probably not relevant on the larger scale of satellite remote sensing. Figure 4 plots a part of these data in the red to illustrate the point; the results for this data cannot be taken as typical in any way, or as testing a model. The unsystematic change of reflectances observed in the red band is not present as strongly in the near-infrared band, which promptly produces a better fit, the correlation coefficient being 0.75. Roujean et al. (1992), testing their model on this data set, also found correlation coefficients of the same magnitude, 0.37 and 0.73. Consequently, instead of this data set, Figure 3 displays the next-worst fit for a broadleaf crop, that for soybean data (Kimes).

A similar situation is encountered with the worst example of a fit to grass-like vegetation, where the grass observed by POLDER has a correlation coefficient in the near-infrared that is singularly small. It is possible that registration errors cause noisiness in the data in this case. Here, as in the corn data case, the fit is greatly improved when in inversion different weights are given to individual observations, these weights having been chosen according to the distance each data point has from the local mean. The next-worst typical case, shown in Figure 3, is the lawn data set (Kimes).

The overall conclusion is that, with the exception of the two data sets mentioned that have other problems and should be treated with caution, all land cover types investigated may be reasonably well represented by the Ambrals BRDF model. From Figure 2 one may note that different shapes of the BRDF are represented, such as ones with a hotspot (field, annual grass) or a bowl shape (irrigated wheat, hardwood forest).

This paper is concerned only with the Ambrals model, but it is interesting to see how it compares with one other semiempirical model, the three-parameter RPV BRDF model developed by Rahman et al. (1993) and modified by Martonchik (Engelsen et al., 1996). The RMSEs and correlation coefficients given in Table 1 cannot be directly compared with values published for the RPV model, since the orginal publication (Rahman et al., 1993) is not based on the modified version, whereas the publication using the modified version (Engelsen et al., 1996) postprocessed the data sets used to correct for diffuse skylight, a method not employed in this study to avoid using a standard atmosphere for data sets collected under various conditions. Therefore, table 2 gives RMSEs and correlation coefficients for the datasets measured by Kimes and co-workers for the Ambrals and the RPV model in direct comparison. In terms of the band-averaged RMSE, the Ambrals model has a lower RMSE in 9 out of 11 cases, the other two being ties. The average RMSE from the Ambrals model is 0.034, that from the modified RPV model 0.041, or 20 percent more. In terms of the correlation coefficient, in the red band, the Ambrals model produces better correlation between measured and observed reflectances for 8 of 11 data sets, with one tie. In the near-infrared band, Ambrals produces better fits in 9 of 11 cases, also with one tie. Judged by this particular series of data sets, the Ambrals model seems to be somewhat better. In many cases, however, the differences are not large. The modified RPV model clearly is similarly capable of also generating good fits to the data.

IMPROVED TREATMENT OF MULTIPLE SCATTERING

In the kernel-driven semiempirical modeling approach, multiple scattering is generally assumed to be isotropic, covered by the isotropic constant of the model. In reality, however, multiple scattering is dependent on the sun zenith angle. In some applications, this dependence is weak enough to be ignored, but in others it is not. When fitting the models to data covering several different sun zenith angles, problems may occur.

We study this problem further by using a fourth kernel term in the models to describe the sun zenith angle dependence of multiple scattering more explicitly. This kernel, the Hapke kernel, is derived from theory put forward by Hapke (1981). Based on the fundamental principles of radiative transfer theory, Hapke derived an analytical equation for the bidirectional reflectance function of a semi-infinite medium.

The single-scattered radiance is derived exactly. A two-stream approximation is used to calculate the multiply scattered radiance of isotropic scatterers. From the resulting expression, a kernel is derived that has the following form:

$$R_H = \frac{1 - \sqrt{1-\omega}}{1 + 2\cos(\theta_i)\sqrt{1-\omega}}, \qquad (5)$$

where ω is the single-scattering albedo.

Since ω cannot be a free parameter if this term is to be used in a kernel-driven model adhering to the form given by equation (2), it is set to fixed values in each wave band, here chosen to be 0.08 in the red and 0.8 in the near-infrared.

This term is dissimilar to the other kernels and may therefore be used in a 4-parameter BRDF model. Figure 5 compares inversion results from the 3-parameter and the corresponding 4-parameter model for several different data sets using scatter plots. For sparse vegetation, here represented by hard wheat (coverage is only 11 percent) and steppe grass (coverage 5 percent), no difference is observed between modeling with and without the Hapke kernel. This is expected, since multiple scattering plays only a negligible role for sparse vegetation. For dense vegetation, however, the accuracy of the fits increases. Coefficients between modeled and observed reflectances increase in both the red and the near-infrared bands, for example from 0.775 to 0.880 in the red and from 0.715 to 0.804 in the near-infrared for the pine forest data set. For the lawn grass, the increase is from 0.724 to 0.787 in the red, and from 0.835 to 0.955 in the near-infrared. Similar results apply to the soybean data set. These results demonstrate that in cases of dense vegetation, adding one parameter related to multiple scattering can improve the fit quality of the model, whereas no change is achieved for sparse vegetation.

Caution should be used when applying the Hapke kernel to reflectance data remotely sensed from space. The Hapke kernel depends on a determination of the solar zenith angle dependence of the reflectance. However, in many remote sensing applications no range or just a rather small range of solar zenith angles is available in a particular period of time, for example for AVHRR, MODIS or MISR. As a consequence, the weight of this kernel will be ill determined for such applications. A 3-parameter model will allow more stable retrievals.

POSSIBLE IMPROVEMENTS TO THE INVERSION PROCESS

This paper has shown that all 27 data sets used were fitted well by at least one of the four kernel combinations that comprise the Ambrals BRDF model. This model may be used reliably for correcting angular effects in remote sensing applications. The capability of the model to describe bidirectional reflectance properties of surface objects can be further used to infer basic properties of the land covers viewed.

However, the inversions could perhaps be further improved in future work by considering the following factors. Firstly, the data used are field-measured. Radiation reaching the earth surface includes both direct and diffuse radiation owing to atmospheric scattering, which results in a partial smoothing of bidirectional reflectance. The data could be corrected for this effect where atmospheric characterization is available for the respective times and locations when the measurements were made. Using a standard atmospheric model could be considered in the absence of such data (Engelsen et al., 1996).

Secondly, the error function used in model inversion has an important influence on the resulting fits and the choice of kernels used. The weights W_j (see equation (3) qualify the contribution of every measurement to the error function. This may be used to improve the inversion, for example when a data set with nonuniform angular sampling displays a cluster of observations in a particular angle range. Most of the clustered observations do not contribute to establishing the shape of the BRDF but affect the error function unless they are given a smaller weight. Similarly, if a particular observation out of a set is considered to be noisy, the information it contributes to the inversion should be lessened by giving it a small weight. One possible way to approach this problem is to select a suitable weight for each observation based on an initial regression analysis. That is, the model is first inverted using the same weight for all observations, then weights are attributed to each observation according to a statistical criterion that identifies outliers, then the inversion is repeated. A different approach is to use error functions that are inherently more stable against noise and outliers (Tarantalo, 1987).

The problem of how to weigh the RMSEs achieved

in individual bands for deriving a band-averaged RMSE on which to base kernel selection has already been mentioned. Whether the difference in the magnitude of reflectances in the visible and in the infrared wavelength regions should enter the error function in form of a weighting term depends on whether a relative deviation (implying larger absolute errors in the infrared) or an absolute error (implying larger relative errors in the red) are preferable. Large relative errors are less favorable for deriving albedo from the BRDF, large absolute errors for deriving small reflectance values. In the present study, this problem is also visible in that the kernel combination best fitting both bands simultaneously is the combination fitting the near-infrared band for all 11 data sets by Kimes and co-workers, whereas it is also the best-fitting combination for the red band in only 7 of the 11 cases (and second-best fitting in 3 other cases). Thus for at least some types of vegetation, a suitable weight value should be added to the individual bands to avoid biasing the kernel selection towards the near-infrared reflectances.

Finally, the Li-kernels used contain two kernel-internal parameters describing crown shape and relative height that were each set to fixed values for sparse and dense canopies based on general considerations. If prior structural knowledge for specific land cover types is available, these parameters could be set to more appropriate values than the current ones. Wanner et al. (1995a) show that the crown shape in particular has an influence on BRDF shape.

MODELING BRDF EFFECTS IN AN ASAS IMAGE: A DEMONSTRATION

We demonstrate operation of the Ambrals model on a remotely sensed data set acquired by the airborne Advanced Solid-State Array Spectroradiometer (ASAS) (Irons et al., 1991) over the Walnut Gulch area in Arizona. Multiangular observations were acquired during overflights at a sun zenith angle of 38° and in the solar principal plane. The ASAS instrument was set up to acquire seven discrete images of the area at zenith angles 15°, 30° and 45° both forward-looking and aftward-looking, and at nadir. The ground spatial resolution at nadir was 2.01 m along the flight direction and 4.25 m across. All images were registered to the nadir image, and Ambrals model BRDF inversions were carried out on each pixel.

Figure 6a shows a spatial mosaic composited of three bands with center wavelengths of 549, 661, and 787 nm. The right half of the image is the data acquired at 45° zenith angle in the backscattering direction, where the sun is behind the sensor. The left half of the image is data acquired at 45° forward scattering zenith angle, where the sensor is facing the sun. For obvious reasons, more shadows are visible in the image showing the forward-scattering reflectances (left half) than in the image showing the backscattering reflectances (right half). A clearly visible seam runs through the image where the data from the two different viewing directions meet. This seam illustrates the magnitude of the BRDF effect present in a surface such as this one if not removed. Clearly, angular effects would have an impact on land cover classification and image interpretation if they were not corrected. Seams like this are known from AVHRR data in areas where data from different orbits, implying different viewing geometries, are mosaicked together (see Li et al. (1996) for an example and discussion), and will also occur for the similarly cross-track scanning MODIS instrument.

After fitting the Ambrals model to the string of 7 bidirectional reflectances available for each pixel, the model was used in forward mode to predict the reflectances for the left half of the image for the backscattering view zenith of 45°, corresponding to the angle at which the right half of the image was acquired. If the Ambrals model fails to correctly model the BRDF seen, the predicted reflectances and the resulting image will be noisy or the seam will be still visible. However, Figure 6b shows the composite, where the left half is the forward-modeled data and the right half is the same data as shown in Figure 6a. The seam is gone. Shadows vanish where they should as the model takes the reflectances into the hotspot. Instead of shaded backsides, illuminated front sides of objects and slopes are now visible. This demonstrates once more that the Ambrals model is indeed capable of modeling correctly the reflectances observed.

Figure 6c shows the nadir reflectance predicted for each pixel by the Ambrals model where the inversion is carried out using the 6 bidirectional reflectances excluding the nadir observation. Figure 6d shows for comparison the actually observed nadir image. The two are clearly very similar, illustrating that nadir

reflectance can be predicted from a string of observations at different angles similar to angles applicable to AVHRR and MODIS observations. Again, a failure of the Ambrals model to produce a reasonable fit for each pixel would have resulted in a noisy image.

CONCLUSIONS

In this paper, we have analyzed the capability of the kernel-driven semiempirical Ambrals BRDF model to provide adequate mathematical descriptions of the anisotropic reflectance of a variety of natural surfaces. Kernel-driven models combine advantages of physical models and empirical models in that they are highly adaptable to a large variety of occurring BRDF shapes, especially to BRDFs of different land cover types and of mixed pixels, but retain a basically-physical interpretation of the shapes produced. They can be inverted analytically through matrix inversion, they scale spatially and possess only three parameters, which is probably the maximal number that can reliably be inverted from the limited angular sampling available from most space-based instruments. The Ambrals model will thus be used in producing the global MODIS BRDF/albedo standard data product.

The mathematical expressions used in the Ambrals model introduced by Wanner et al. (1995a) are validated in this paper using 27 different measured BRDF data sets of a large variety of land covers. We find that the Ambrals model is fully capable of modeling these BRDFs with reasonable accuracy, the RMSEs being 0.034 on the average and correlation coefficients between modeled and observed data being larger than 0.8 or even 0.9 in a great majority of cases. Furthermore, the kernels selected may tentatively be related to vegetation structural characteristics, with differences observed between shadow-casting canopies and those where mutual obscuring of objects occurs, and between shadow-casting and strongly volume-scattering canopies. While several avenues for further improving the inversions have been discussed, the models in their current form are well-developed enough to be applied to remote sensing problems involving the extraction of the BRDF and the correction of multiangular imagery.

We would like to thank all investigators who allowed us to use BRDF data they collected, especially Jim Irons for making available the ASAS data of Walnut Gulch. We also thank the members of the MODIS BRDF/albedo team for their support and numerous discussions. This work was supported by NASA under NAS5-31369.

REFERENCES

Deering, D. W., S. P. Ahmad, T. F. Eck, and B. P. Banerjee, Temporal attributes of the bidirectional reflectance for three boreal forest canopies, *Proc. Int. Geosci. Remote Sens. Symp. 95*, 1239–1241, 1995.

Deschamps, P. Y., F. M. Breon, M. Leroy, A. Podaire, A. Bricaud, J. C. Buriez, and G. Seze, The POLDER mission: Instrument characteristics and scientific objectives, *IEEE Trans. Geosci. Remote Sens., 32*, 598–615, 1994.

Diner, D., C. J. Bruegge, J. V. Martonchik, G. W. Bothwell, E. D. Danielson, V. G. Ford, L. E. Hovland, K. L. Jones, and M. L. White, A multi-angle image spectroradiometer for terrestrial remote sensing with the Earth Observing System, *Int. J. Imag. Sys. Tech., 3*, 92–107, 1991.

Engelsen, O., B. Pinty, M. M. Verstraete, and J. V. Martonchik, Parametric bidirectional reflectance factor models: evaluation, improvements and applications, *Report, Joint Research Centre of the European Commission, EU 16426,*, 114 pp., 1996.

Hapke, B., Bidirectional Reflectance Spectroscopy, 1. Theory, *J. Geophys. Res., 86*, 3039–3054, 1981.

Hu, B., W. Wanner, X. Li, and A. Strahler, Validation of kernel-driven semiempirical BRDF models for application to MODIS-MISR data, *Proc. Int. Geosci. Remote Sens. Symp. 96*, 1669–1671, 1996.

Irons, J. R., K. J. Ranson, D. L. Williams, R. R. Irish, and F. G. Huegel, An off-nadir pointing imaging spectroradiometer for terrestrial ecosystem studies, *IEEE Trans. Geosci. Remote Sens., 29*, 66–74, 1991.

Irons, J. R., G. S. Campbell, J. M. Norman, D. W. Graham, and W. M. Kovalick, Prediction and measurement of soil bidirectional reflectance. *IEEE Trans. Geosci. Remote Sens., 30*, 249–260, 1992.

Kimes, D. S., Dynamics of directional reflectance factor distribution for vegetation canopies, *Appl. Opt., 22(9)*, 1364–1372, 1983.

Kimes, D. S., W. W. Newcomb, C. J. Tucker, I. S. Zonneveldt, W. van Wijngaarden, J. de Leeuw, and G. F. Epema, Directional reflectance factor distributions for cover types of Northern Africa, *Remote Sens. Env., 18*, 1–19, 1985.

Kimes, D. S., W. W. Newcomb, R. F. Nelson, and J. B. Schutt, Directional reflectance distributions of a hardwood and a pine forest canopy, *IEEE Trans. Geosci. Remote Sens., 24*, 281–293, 1986.

Leroy, M., and J.-L. Roujean, Sun and view angle corrections on reflectances derived from NOAA/AVHRR data, *IEEE Trans. Geosci. Remote Sens., 32*, 684–697, 1994.

Leroy, M., Surface reflectance angular signatures from airborne POLDER data, *Remote Sens. Environ., 57*, 97–107, 1996.

Leroy, M., J. L. Deuze, F. M. Breon, O. Hautecoeur, M. Herman, J. C. Buriez, D. Tanre, S. Bouffies, P. Chazette, and J.-L. Roujean, Retrieval of atmospheric properties and surface bidirectional reflectances over land from POLDER/ADEOS, *J. Geophys. Res., this issue*, 1997.

Lewis, P., The utility of kernel-driven BRDF models in global BRDF and albedo studies, *Proc. Int. Geosci. Remote Sens. Symp. 95*, 1186–1187, 1995.

Li, X., and A. H. Strahler, Geometric-optical bidirectional reflectance modeling of the discrete crown vegetation canopy: effect of crown shape and mutual shadowing, *IEEE Trans. Geosci. Remote Sens., 30*, 276–292, 1992.

Li, Z., J. Cihlar, X. Zheng, L. Moreau, and H. Ly, Detection and correction of the bidirectional effects in AVHRR measurements over northern regions, *IEEE Trans. Geosci. Remote Sens.*, in press, 1996.

Nilson, T., and A. Kuusk, A reflectance model for the homogeneous plant canopy and its inversion, *Remote Sens. Env., 27*, 157–167, 1989.

Rahman, H., B. Pinty, and M. M. Verstraete, Coupled surface-atmosphere reflectance (CSAR) model, 2, Semiempirical surface model usable with NOAA advanced very high resolution radiometer data, *J. Geophys. Res., 98*, 20,791–20,801, 1993.

Ranson, K. J., L. L. Biehl, and M. E. Bauter, Variation in spectral response of soybeans with respect to illumination, view and canopy geometry, *Int. J. Remote Sens., 6*, 1827–1842, 1985.

Ross, J. K., *The Radiation Regime and Architecture of Plant Stands*, 392 pp., Dr. W. Junk Publishers, The Hague, 1981.

Roujean, J. L., M. Leroy, and P. Y. Deschamps, A bidirectional reflectance model of the earth's surface for the correction of remote sensing data, *J. Geophys. Res., 97*, 20,455–20,468, 1992.

Ruiz de Lope, E. V., and P. Lewis, Monitoring land surface dynamics in the HAPEX Sahel area using kernel-driven BRDF models and AVHRR data, to be submitted to Remote Sens. Environ., 1997.

Running, S. W., C. O. Justice, V. Salomonson, D. Hall, J. Barker, Y. J. Kaufman, A. H. Strahler, A. R. Huete, J.-P. Muller, V. Vanderbilt, Z. M. Wan, P. Teillet, and D. Carneggie, Terrestrial remote sensing science and algorithms planned for EOS/MODIS, *Int. J. Remote Sens., 15*, 3587–3620, 1994.

Strahler, A. H., M. J. Barnsley, R. d'Entremont, B. Hu, P. Lewis, X. Li, J.-P. Muller, C. B. Schaaf, W. Wanner, and B. Zhang, MODIS BRDF/albedo product: Algorithm theoretical basis document, *NASA EOS-MODIS Doc. and update*, version 3.2, 65 pp., 1995.

Strahler, A. H., C. B. Schaaf, J.-P. Muller, W. Wanner, M. J. Barnsley, R. d'Entremont, B. Hu, P. Lewis, X. Li, and E. V. Ruiz de Lope, MODIS

BRDF/albedo product: Algorithm theoretical basis document, *NASA EOS-MODIS Doc.*, version 4.0, 1996.

Tarantola, A., *Inverse problem theory : methods for data fitting and model parameter estimation*, Elsevier Science Pub. Co., 1987.

Walthall, C. L., J. M. Norman, J. M. Welles, G. Campbell, and B. L. Blad, Simple equation to approximate the bidirectional reflectance from vegetation canopies and bare soil surfaces, *Appl. Opt., 24*, 383–387, 1985.

Walthall, C. L., E. M. and Middleton, Assessing spatial and seasonal variations in grasslands with spectral reflectances from a helicopter platform, *J. Geophys. Res., 97*, 18905–18912, 1992.

Wanner, W., X. Li, and A. H. Strahler, On the derivation of kernels for kernel-driven models of bidirectional reflectance, *J. Geophys. Res., 100*, 21077–21090, 1995a.

Wanner, W., A. H. Strahler, J.-P. Muller, M. Barnsley, P. Lewis, X. Li, and C. L. Barker Schaaf, Global mapping of bidirectional reflectance and albedo for the EOS MODIS project: the algorithm and the product, *Proc. Int. Geosci. Remote Sens. Symp. 95*, 525–529, 1995b.

Wanner, W., A. H. Strahler, B. Hu, X. Li, C. L. Barker Schaaf, P. Lewis, J.-P. Muller, and M. J. Barnsley, Global retrieval of bidirectional reflectance and albedo over land from EOS MODIS and MISR data: theory and algorithm, *J. Geophys. Res.*, in press, 1997.

Table 1: Summary of Data Sets, Kernel Selection, Inversion RMSEs and Correlation Coefficient (r) Between Modeled and Observed Reflectances

Data Source	Cover Type	Cov. %	LAI	θ_i, Range	Best-Fitting Kernel	RMSE	r (red)	r (NIR)
Kimes (1983),	Plowed Field	0	0	26-45	Ross-thick/Li-sparse	0.016	0.976	0.976
Kimes et al.	Corn	25	0.65	26-68	Ross-thin/Li-dense	0.028	0.467	0.750
(1985, 1986)	Lawn Grass	97	9.9	42-70	Ross-thin/Li-dense	0.046	0.724	0.835
	Soybeans	90	4.6	28-76	Ross-thick/Li-sparse	0.043	0.783	0.806
	Hardwheat	11		27-51	Ross-thick/Li-sparse	0.019	0.963	0.938
	Annual Grass	4		28-50	Ross-thick/Li-sparse	0.023	0.945	0.878
	Steppe Grass	5		35-63	Ross-thick/Li-sparse	0.024	0.887	0.922
	Irrigated Wheat	70	4.0	26-59	Ross-thick	0.037	0.911	0.917
	Orchard Grass	50	1.0	45-82	Ross-thick/Li-sparse	0.030	0.837	0.914
	Pine Forest	70		26-74	Ross-thin/Li-dense	0.041	0.775	0.715
	Hardwood Forest	79		25-79	Ross-thick/Li-dense	0.030	0.902	0.890
Ranson et al.	Soybeans	72	3.0	20-49	Ross-thick/Li-sparse	0.017	0.753	0.892
(1985)		83	3.9	21-38	Ross-thin/Li-dense	0.015	0.738	0.851
		99	2.9	31-61	Ross-thick	0.011	0.914	0.927
Deering	Aspen			45-59	Ross-thick/Li-sparse	0.025	0.922	0.883
et al.	Old Black Spruce			36-59	Ross-thick/Li-sparse	0.011	0.949	0.943
(1995)	Old Jack Pine			34-60	Ross-thin/Li-dense	0.010	0.899	0.947
Irons et al.	Soil I	0	0	16-68	Ross-thick/Li-sparse	0.027	0.920	0.915
(1992)	Soil II	0	0	34-53	Ross-thick/Li-sparse	0.016	0.971	0.970
	Soil III	0	0	28-54	Ross-thick/Li-sparse	0.027	0.931	0.933
FIFE (Walthall	Grass I		1.3	19-25	Ross-thin/Li-sparse	0.021	0.769	0.896
and Middleton, 1992)	Grass II		0.9	53-61	Ross-thin/Li-sparse	0.031	0.913	0.898
POLDER	Grass			37-47	Ross-thick/Li-sparse	0.042	0.706	0.560
	Sorghum			38-45	Ross-thin/Li-sparse	0.028	0.785	0.874
	Vineyard			38-45	Ross-thin/Li-sparse	0.024	0.809	0.934
	Vegetable			37-45	Ross-thin/Li-sparse	0.036	0.888	0.793
	Sunflower			38-47	Ross-thin/Li-sparse	0.023	0.869	0.910

Table 2: Comparison of Inversion RMSEs and Correlation Coefficients (r) Between Modeled and Observed Reflectances for the Ambrals Model and the Modified RPV Model

Data set	Ambrals			mod. RPV		
(Kimes)	RMSE	r (red)	r (NIR)	RMSE	r (red)	r (NIR)
Plowed Field	0.016	0.976	0.976	0.016	0.976	0.976
Corn	0.028	0.467	0.750	0.031	0.718	0.652
Lawn Grass	0.046	0.724	0.835	0.046	0.706	0.839
Soybeans	0.043	0.783	0.806	0.057	0.871	0.600
Hardwheat	0.019	0.963	0.938	0.025	0.941	0.897
Annual Grass	0.023	0.945	0.878	0.028	0.911	0.822
Steppe Grass	0.024	0.887	0.922	0.026	0.883	0.897
Irrigated Wheat	0.037	0.911	0.917	0.039	0.891	0.907
Orchard Grass	0.030	0.837	0.914	0.050	0.796	0.723
Pine Forest	0.041	0.775	0.715	0.049	0.659	0.560
Hardwood Forest	0.030	0.902	0.890	0.044	0.864	0.890

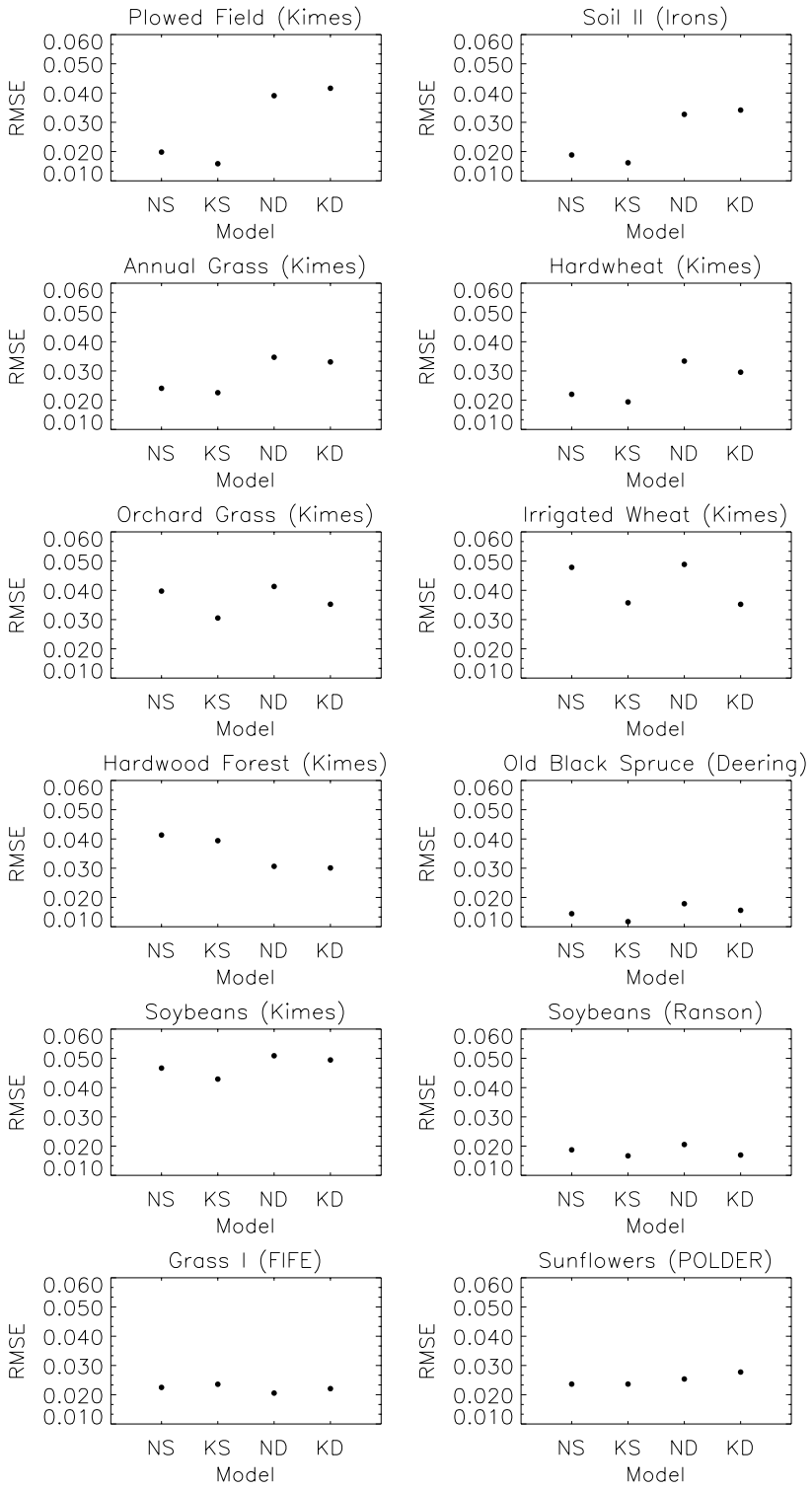

Figure 1: RMSEs of Ambrals model inversions for selected data sets representing different types of land covers (barren, sparsely vegetated, grass-like, forest, broadleaf crops; refer to Table 1 for coverages and LAIs). Kernel combinations are keyed as follows: NS, Ross-thin/Li-sparse; KS, Ross-thick/Li-sparse; ND, Ross-thin/Li-dense; KD, Ross-thick/Li-sparse.

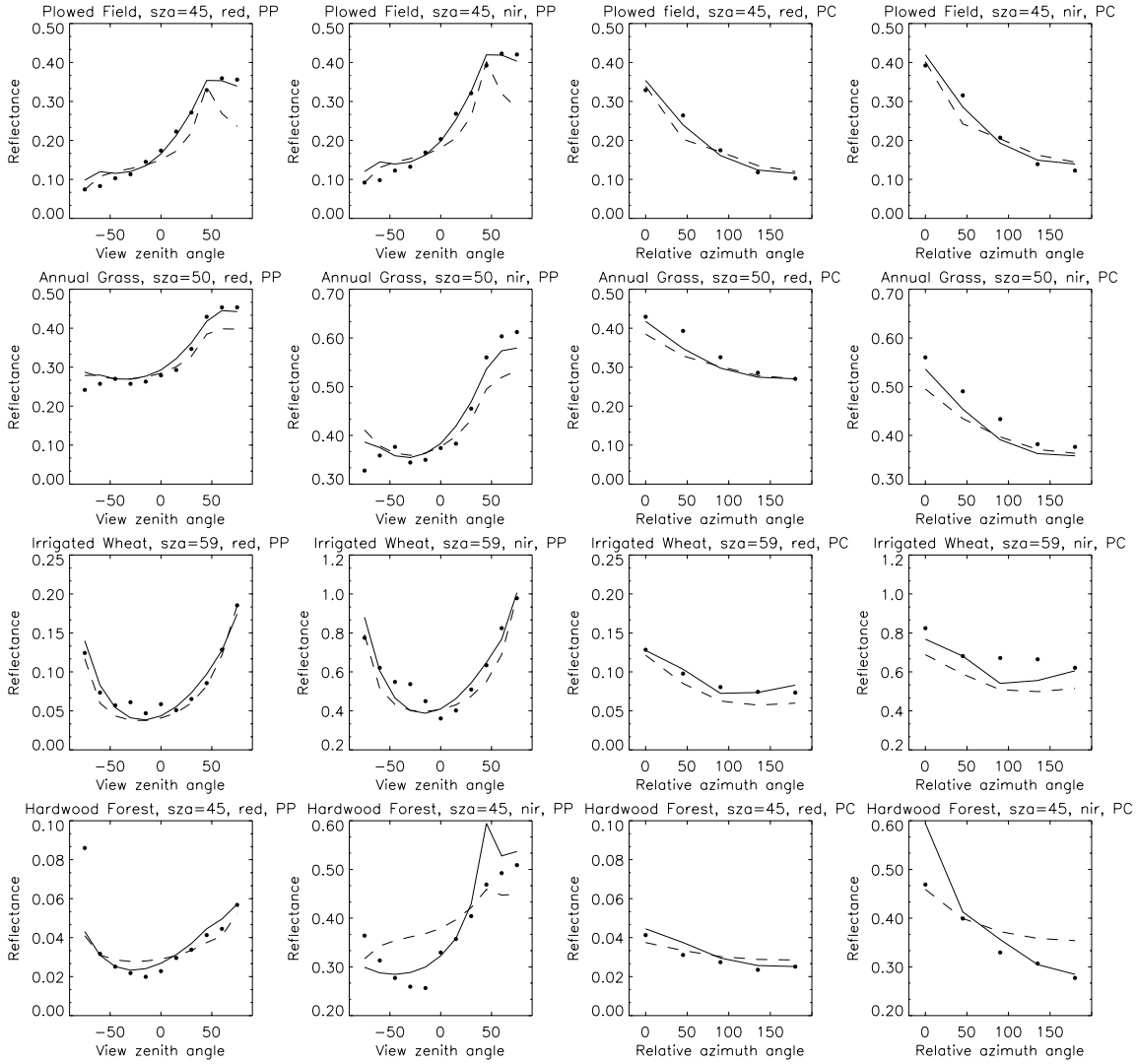

Figure 2: Comparisons of fits produced by good (solid lines) and bad (dashed lines) Ambrals kernel combinations on the principal plane and on the principal cone for selected data (dots) representing different types of land cover.

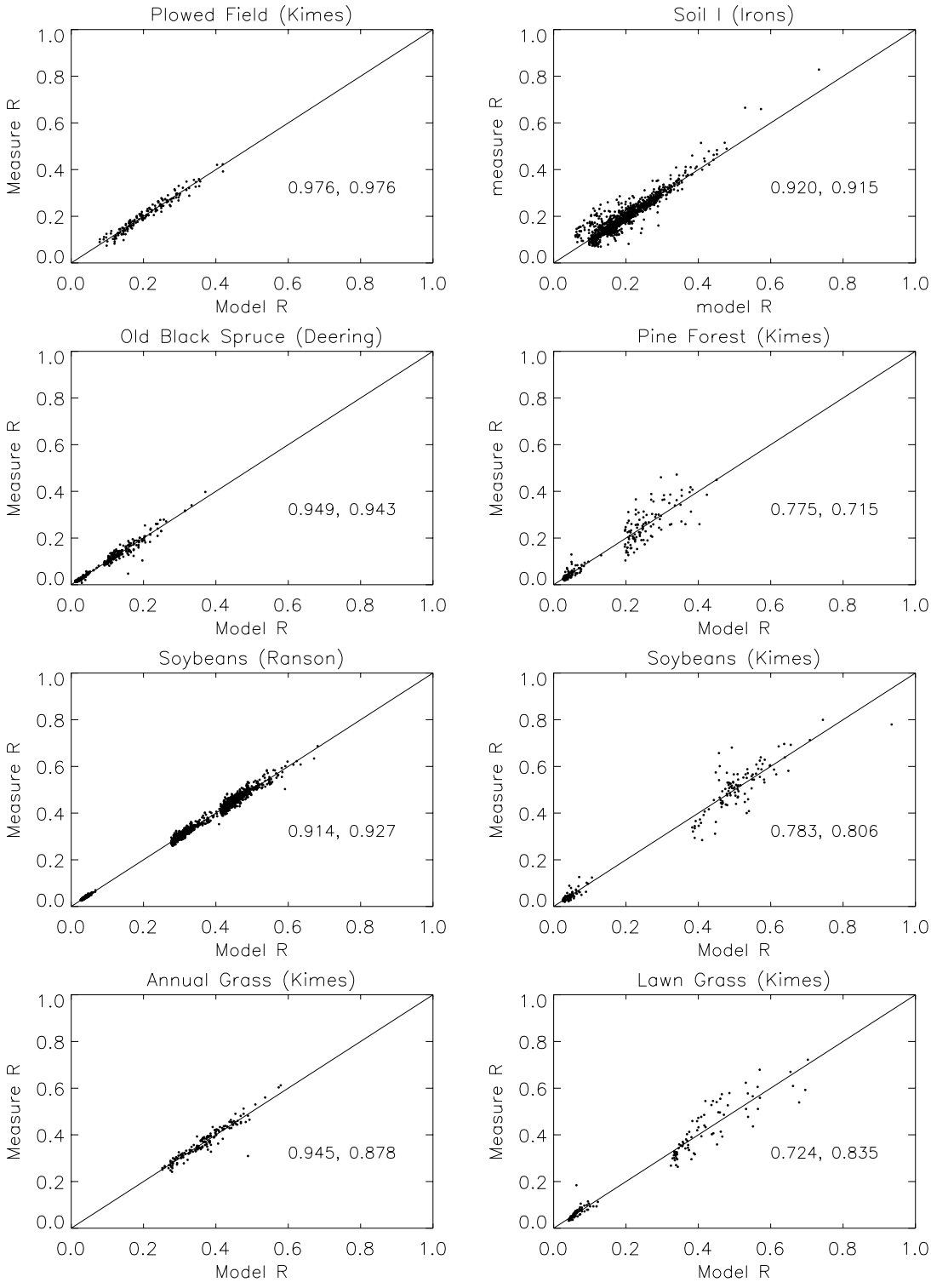

Figure 3: Modeled versus observed reflectances in the red and near-infrared for different types of land cover (barren, forest, broadleaf crops, grass-like). The numbers given in each panel are the correlation coefficient in the red and in the near-infrared bands, respectively.

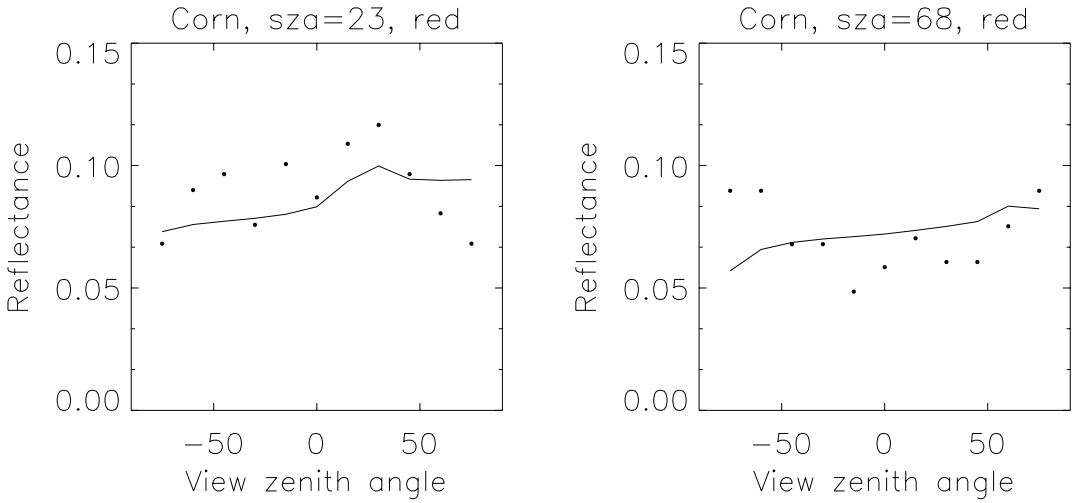

Figure 4: The corn data set shows irregular behavior of the observed reflectances (dots), leading to poor fits (solid lines). The situation is similar at other zenith angles in the red, and somewhat better in the near-infrared.

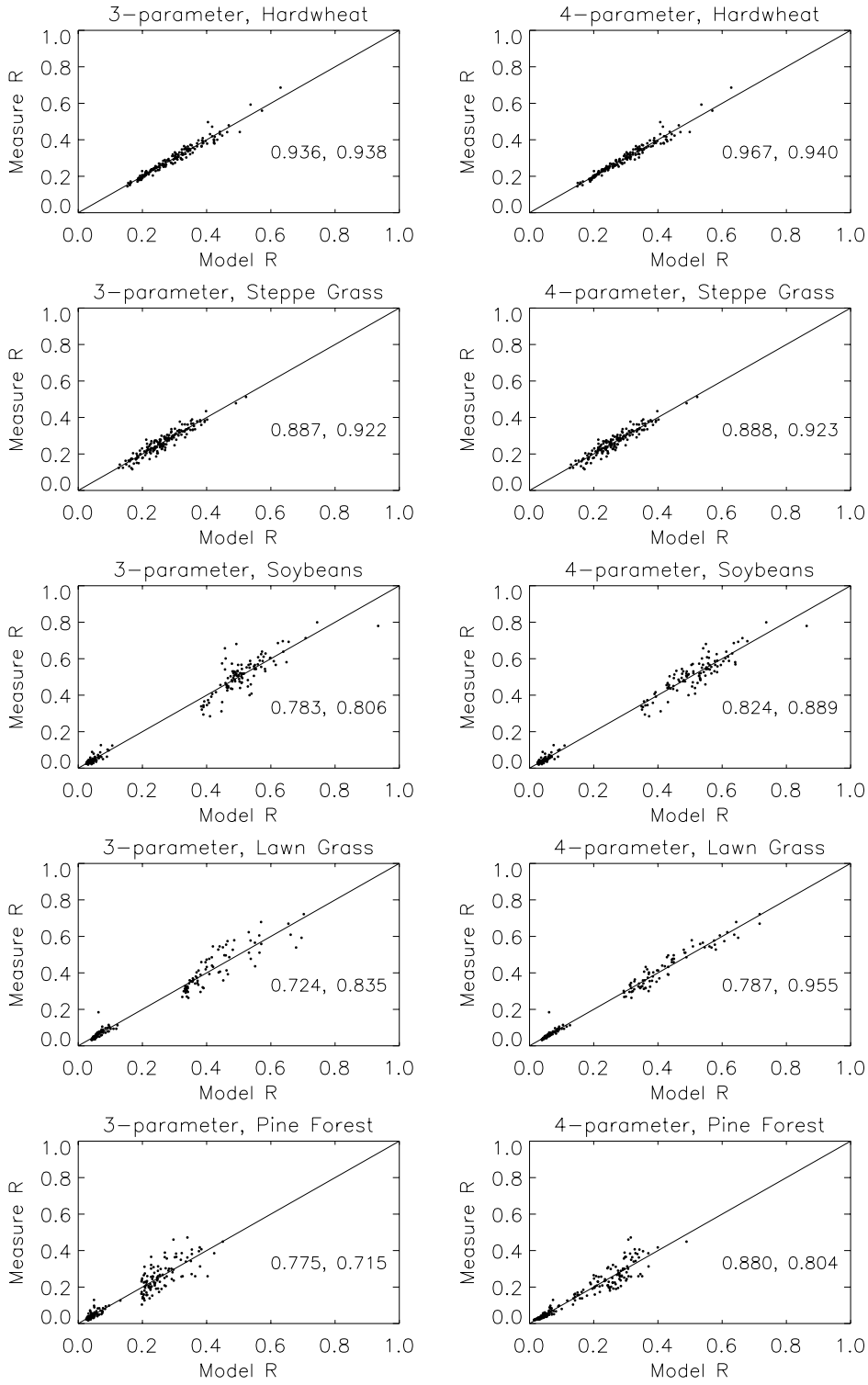

Figure 5: Modeled versus observed reflectances in the red and near-infrared for different types of land cover (top two rows: sparse vegetation; bottom three rows: dense vegetation) and for a 3-parameter model (left) and a 4-parameter model (right) where the Hapke-kernel for multiple scattering was added. The numbers given in each panel are the correlation coefficient in the red and in the near-infrared bands, respectively. Note that fits improve for the dense vegetation.

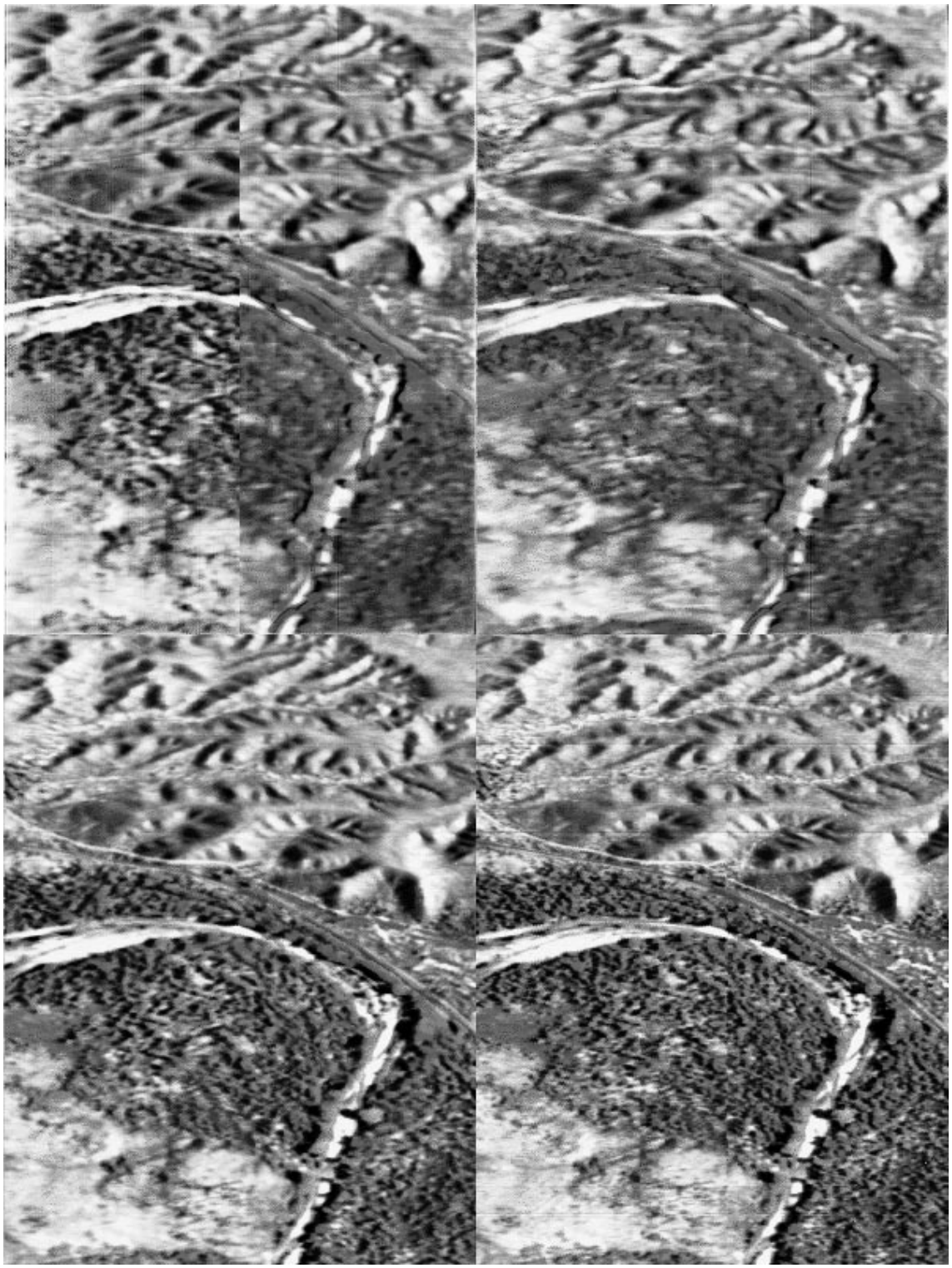

Figure 6: Grey-scale representation of a three-band composite image of ASAS data (wavebands centered at 549, 661, and 787 nm) over Walnut Gulch, Arizona. Sun zenith angle during data acquisition was 38°. Panel (a) (top left) shows in the right half data acquired at 45° zenith angle in the backscattering direction and in the left half data acquired at 45° zenith angle in the forward-scattering direction, where more shadows are visible. The second panel, (b) (top right), shows in its left half the same data as shown in the left half of panel (a), and in the right half data predicted for a backscattering view zenith angle of 45° using the Ambrals model on each pixel and inverting the seven reflectances observed by ASAS at 45°, 30°, 15°, and nadir in the forward and backscattering directions; i.e., the right half of this image is observed data, the left half BRDF-modeled reflectance predictions. Panel (c) (bottom left) is the nadir reflectance modeled from inverting the 6 off-nadir ASAS observations, panel (d) (bottom right) is the actual nadir-view observation.

APPENDIX B:
RETRIEVAL ACCURACIES OF BRDF AND ALBEDO FROM EOS-MODIS AND MISR ANGULAR SAMPLING (PAPER BY WANNER)

Draft Manuscript (Nov. 96): to be revised and submitted to JGR

Retrieval Accuracies of BRDF and Albedo from EOS-MODIS and MISR Angular Sampling

Wolfgang Wanner

Center for Remote Sensing and Department of Geography, Boston University, Boston, MA, USA

Abstract. This paper reports expected accuracies of bidirectional reflectance and albedo retrievals from the angular sampling provided by NASA's upcoming MODIS and MISR sensors on the EOS-AM-1 satellite platform. A numerical discrete ordinates method radiative transfer model by Myneni is used to simulate combined MODIS and MISR angular sampling as a function of latitude and time of year for six different BRDF types (land cover types) in the red and near-infrared wavebands. These simulated observations are then inverted using three different simple BRDF models scheduled for use in the future operational MODIS and MISR BRDF/Albedo Products:the reciprocal Ambrals, the modified RPV, and the modified Walthall BRDF models. Bidirectional reflectance and albedo retrievals are studied not only at the mean solar zenith angle of observation, but extrapolated to arbitrary other sun zenith angles as well. The influence of loss of observations to clouds is also examined. Results show that albedo may be retrieved with 2 to 8 percent median accuracy using either the Ambrals or the modified RPV model for any solar zenith angle for any MODIS/MISR sampling, and that the accuracy of predicted nadir-view reflectance is also mostly within a 10 percent error margin. The Ambrals model may be slightly more accurate with respect to the forward model used. The empirical modified Walthall model clearly performs worse than the two semiempirical models. These results also allow to establish error distribution histograms that may serve for assessing the overall accuracy to be expected from the planned MODIS BRDF/Albedo Product.

1. Introduction

While the elevated standpoint of a low-Earth orbit permits systematic global remote sensing observations of great value for monitoring continents and the Earth as a whole, it also brings with it restrictions given by orbital and instrumental mechanics and the limitations of operating an instrument remotely in space. It is of great interest for the assessment of remote sensing missions to determine the accuracy with which parameters of interest may be retrieved from space. This paper discusses the accuracy to be expected for bidirectional reflectance distribution function (BRDF) and albedo retrieval from the Moderate Resolution Imaging Spectroradiometer (MODIS) and the Multi-Angle Imaging Spectroradiometer (MISR), two instruments to be launched on the EOS-AM-1 platform in mid-1998 that are central to NASA's Earth Observing System (EOS) (Running et al., 1994; Diner et al., 1991).

In focusing on BRDF and albedo, this paper studies two parameters that quantify the directional reflectance characteristics of the Earth's surface, which is the lower boundary for atmospheric transfer of radiation. BRDF and albedo are consequently of relevance for precise determinations of the Earth's radiation budget, climate simulations and atmospheric correction. Other applications are in angular normalization of images, land cover classification and cloud detection. Besides shedding some light onto the more general question of how effectively BRDF and albedo may be derived from space-based remote sensing measurements, this study also is intended to provide much-needed accuracy predictions and error distribution histograms

for BRDF and albedo retrievals from MODIS and MISR observations. Such retrievals are to be performed for the operational BRDF/Albedo standard data product that will be produced routinely from EOS data by the MODIS project (Strahler et al., 1996; Wanner et al., 1997).

The following section 2 outlines the experimental plan and gives details on its components. Sample results for BRDF retrieval are presented in section 3, sample results for albedo retrieval in section 4. Overall BRDF and albedo retrieval accuracies are detailed statistically in section 5, which is followed by a discussion and conclusions in section 6.

2. The Experimental Plan

2.1. Outline of the experimental plan

The study was conducted as follows. The orbital simulation tool Xsatview (Barnsley et al., 1994) was used to generate simulated MODIS and MISR viewing and illumination geometries for different geographic latitudes of observation and days of the year. For each of the observation geometries generated, a discrete ordinates method radiative transfer code (Myneni et al., 1992) was used to compute simulated observations of the bidirectional surface reflectance for six distinct BRDF types resembling six different land cover types in the red and the near-infrared (NIR) wavebands. These were then inverted using three different semiempirical or empirical BRDF models that are slated for use in operational BRDF/albedo products. These are the Ambrals kernel-driven BRDF model (Wanner et al., 1995, 1997), the Rahman-Pinty-Verstraete model (RPV) (Rahman et al., 1993) in a form modified by Martonchik (Engelsen et al., 1996), and the empirical modified Walthall model (Walthall et al., 1985; Nilson and Kuusk, 1989). The first and last are to be used for the MODIS BRDF/Albedo Product (which also uses MISR data) (Strahler et al., 1996, Wanner et al., 1997), the second for the MISR Surface Product that includes BRDF and albedo parameters (Diner et al., 1996, Martonchik, 1997).

The BRDF model parameters resulting from the inversions conducted allow reconstruction of the full BRDF and calculating directional-hemispherical and bihemispherical albedo. The different sampling geometries studied represent inversions of the six different BRDF (landcover) types under changing sparse angular sampling, these changes being given by changes in the latitude and time of year of the satellite observations. Any variations in the reflectances and/or albedos found in these experiments for any of the land cover types are consequently due alone to changes in the angular distribution of samples, everything else having been kept constant. They reflect the capability of the different models to interpolate and extrapolate the BRDF observed, given the angular sampling available from observations from space. For example, sampling close to the principal plane may allow a more reliable reconstruction of the BRDF observed than sampling close to the cross-principal plane. Sampling at large solar zenith angles may lead to more problems in the inference than at small solar zenith angles since the approximations made in the BRDF models mostly become questionable at very large zenith angles. Additionally, one BRDF model may be superior to another in its ability to correctly infer realistic BRDFs from incomplete angular sampling.

The investigation of this problem consists of two parts. First, bottom-line accuracies of BRDF and albedo retrievals need to be determined, which are given by the accuracies achievable in the absence of any other confounding factors such as clouds, atmosphere and noise. Consequently, BRDF model inversion is studied in this paper assuming angular sampling from MODIS and MISR without loss of observations to cloud cover and assuming perfect atmospheric correction of observations (i.e., no atmosphere). Also, the observations are assumed not to be noisy, although some residual noise from the discreteness of the forward-modeling scheme used is present. In this way, the errors found will represent problems with angular sampling geometry only. Given the models used, retrievals can never be expected to be better than what is found under such conditions.

A second part of the overall investigation, currently in progress, is required to establish how these baseline

accuracies will change given uncertainties in the aerosol optical depth and atmospheric correction, loss of observations to cloud cover, and the presence of possibly noisy data. When judging the results of those studies, however, it will be essential to know what the accuracies achievable under optimal conditions are, if individual sources of error are to be separated. The needed baseline accuracies are reported here. However, some results on the impact of loss of observations to cloud cover are given in section 5. Indications are that with MODIS and MISR sampling, the accuracies remain about the same even in the presence of cloud cover, making the results derived in this study rather general.

The effect of noisy data on BRDF and albedo retrieval using MODIS and MISR angular sampling is being reported elsewhere (Wanner et al., 1996; Lewis and Wanner, 1997).

2.2. MODIS and MISR Angular Sampling

The EOS-AM-1 platform carrying MODIS and MISR will be placed into a polar orbit with a 10:30 a.m. equatorial crossing time. The orbital two-repeat cycle is 16 days, which is also the time resolution at which the global MODIS BRDF/Albedo Product will be routinely produced.

The viewing geometries of the two instruments used in generating this product complement each other. Whereas MISR is an along-track imager, MODIS scans across-track. In 16 days, MISR observations will have been made that cut across the viewing hemisphere at an approximately constant azimuth relative to the solar plane and are close to perpendicular to a similar cut provided by MODIS observations. The azimuth angles found depend on the latitude and the time of year. This setup ensures a good coverage of the viewing hemisphere when data from the two instruments are used jointly. This applies even to cases where some observations are lost due to cloud cover. Coverage of the solar hemisphere is more problematic, as the solar zenith angle for MODIS and MISR observations will vary only slightly in each 16-day period, but vary strongly between latitudes.

MODIS BRDF and albedo will be derived in seven spectral bands ranging from 0.47 μm to 2.13 μm, with MISR data being available between 0.43 μm and 0.87 μm. The spatial resolution of the product will be one kilometer, with good geolocation of each pixel ensured by a greater spatial resolution of the original data used in building a multiangular database. This slight degradation of the spatial resolution in producing the product is essential in regions with heterogeneous land covers.

MODIS and MISR viewing and illumination geometries were simulated using orbital simulation software called Xsatview (Barnsley et al., 1994). Observation geometries are represented approximately due to some simplifications made, but are sufficiently accurate for the purposes of this study. Observations were simulated at 9 different latitudes between 80 degrees northern and 80 degrees southern latitude, and for solar positions corresponding to every third 16-day time period throughout the year (8 periods). Of the 72 resulting sampling scenarios, 60 provide observations with the sun above the horizon. Observations with sun zenith angles larger than 75 degrees were discarded since this will also be the case in MODIS atmospheric correction processing.

2.3. BRDF Forward Modeling from DOM/RTCODE

Forward BRDF Modeling was carried out using a discrete ordinates code provided by Myneni (Myneni et al., 1992) that solves the radiative transfer equations of light scattering in structured vegetation canopies and also takes geometrical shadowing effects into account. This code, used in version available in early 1996 (here called DOM/RTCODE), is written to predict the BRDFs of six land cover types with distinct characteristics. These so-called biomes are: grasses and cereal crops (biome 1); semi-arid shrublands (biome 2); broadleaf crops (biome 3); savanna, which is a grassy understory with a sparse overstory of trees (biome 4); broadleaf forest (biome 5); and needleleaf forest (biome 6).

The parameters for each biome simulation, between 17 and 32 depending on the case, were set to realistic

values. For all biomes, the soil background was assumed to be Lambertian and have a red hemispherical reflectance of 0.1 and a near-infrared hemispherical reflectance of 0.2. The fraction of direct illuminating radiation was assumed to be 0.8, not so much to simulate diffuse skylight (which in remote sensing applications would have been corrected for in atmospheric correction) but to make the BRDFs less ideal in terms of the crispness of features produced by idealistic mathematical models but not found in a natural situation. Leaf optical properties were generally taken to be similar across biomes. Red hemispherical leaf reflectance was 0.076, leaf hemispherical transmittance 0.042. The corresponding values in the near-infrared were 0.52 and 0.41. Stem and branch optical properties were mostly similar to the leaf properties but sometimes chosen to be less transparent.

The grassland biome had a leaf area index (LAI) of 2.0 with a canopy height of 0.8 m. The leaf normal inclination was assumed erectophile. The shrubs in the semi-arid shrubland were simulated to have a LAI of 2.0 with a ground cover of 50 percent, that is the plot LAI was 1.0. The height of the shrubs was assumed to be 4 m, sitting on the ground, and the leaf angle distribution to be uniform. The broadleaf crop canopy was characterized as having a LAI of 3.0 with a stem and branch area index of 0.6. Ground cover was assumed to be 80 percent, resulting in a plot LAI of 2.4. Stand height was taken to be 1.25 m, the leaf angle distribution to be uniform and the stem normal orientation vertical.

The savanna biome type was characterized as having a 20 percent tree cover, the trees being 5 m high with crowns of 2 m length. The LAI was taken to be 4.0 with a uniform leaf angle distribution. The understory of grass was assumed to be 1.0 m high and erectophile with an LAI of 2.0, resulting in a plot LAI of 2.8. The broadleaf forest is characterized by a 90 percent ground cover consisting of trees 10 m high, with crowns measuring 4 m in height and 3m in diameter. The branch/stem orientation and the leaf angle distribution are uniform. LAI is 5.5. The understory is 1 m high, has a uniform leaf angle distribution and a LAI of 1.0. Total stand LAI is 5.95. The needleleaf forest, finally, has an 80 percent ground cover with a tree leaf area index of 2.5. The trees are 10 m high with crowns measuring 4 m in height and 2 m in diameter, the shoots having a uniform leaf angle distribution but the needles showing clumping. The angle between needle and shoot is 49 degrees. As before, the understory has a uniform leaf angle distribution and an LAI of 1.0 with a plant height of 1 m. Plot LAI is 3.0.

Bidirectional reflectances were generated from the DOM/RTCODE for MODIS and MISR viewing and illumination geometries, and the corresponding directional-hemispherical and bihemispherical albedos determined. Since two wave bands, red and near-infrared, were simulated, a total of 12 BRDFs was sampled in 60 different ways as a function of latitude and day of year, resulting in 720 observations of a BRDF from which to attempt a retrieval of BRDF and albedo.

Generally, the BRDFs produced by DOM/RTCODE were satisfactory in the angle ranges mainly of interest. Biomes 1 and 5 displayed no obvious problems. For biome 3, the discretization of the scheme was visible for close-to-nadir solar zenith angles. Biomes 2 and 5 displayed small residual irregularities at nadir view zenith for small solar zenith angles, mostly in the red band, but these were not deemed to be overly problematic for the current study. Biome 4 displayed some noise in the backscattering direction for large viewing and solar zenith angles, but again this was not deemed critical. Differences in BRDF shape between biomes consisted mainly of the steepness of the bowl, the properties of the hotspot region, and the magnitude of the reflectances. All in all, however, the BRDFs for the six biomes are somewhat similar in their overall appearance. This may either be due to similarities in the modeling used for the different biome types, or to the fact that natural BRDFs are more similar than expected when both shadowing and radiative transfer-type effects are both combined realistically in the same model.

2.4. Inverse Modeling Using Simple BRDF Models

Three different BRDF models were used for inverting the simulated MODIS and MISR multiangular observations, the Ambrals BRDF model (Wanner et al., 1995, 1997) in a slightly modified form, the modified

BRDF model by Rahman et al. (1993), commonly called RPV, and the modified Walthall model (Walthall et al., 1985; Nilson and Kuusk, 1989). These models were chosen because they will be used for generating BRDF and albedo from the MODIS and MISR instruments and probably are the only BRDF models currently feasible for large-scale operational applications. The latter is mainly due to their small number of parameters and the fact that they may be inverted without recourse to iterative numerical inversion schemes, which cannot be afforded in global kilometer-scale processing given currently achievable computer power. A model similar in approach to the Ambrals model is also used for BRDF and albedo modeling from data acquired by the polarization and directionality of the earth's radiation (POLDER) instrument (Deschamps et al., 1994; Leroy et al., 1997).

The Ambrals model and the RPV model are semiempirical models based on somewhat different philosophies. The Ambrals model is formulated as a sum of two expressions, one that characterizes the shadow casting of discrete ground objects as determined by inter-object gaps, and one that characterizes volume scattering from homogeneously distributed scattering elements as determined by intra-canopy gaps (Roujean et al., 1992). Expressions for these two components, geometric and volume scattering, are derived through a series of simplifying approximations from physical BRDF theories (Wanner et al., 1995), most notably a radiative transfer theory taken from Ross (1981) and the Li-Strahler geometric-optical mutual shadowing model (Li and Strahler, 1992). In inversion, the relative contributions of volume and geometric scattering, and an isotropic constant, are retrieved. These may be interpreted to reflect either the sub-resolution mixture of land cover types that are dominated by either volume or geometric scattering, or to quantify the respective scattering contributions from a single type of land cover.

For volume and geometric scattering, the Ambrals model provides a choice of two alternate mathematical expressions each, called kernels, representing different types of scattering due to different types of approximations made. For volume scattering, the two kernels available describe canopies with high or low effective leaf area index (Ross-thin, Ross-thick kernels), for geometric scattering they model sparse and dense canopies (Li-sparse, Li-dense kernels). In this study, the kernels to be used for each inversion were chosen such that a minimum root mean square absolute error between modeled and observed reflectances is achieved (Hu et al., 1996, 1997; Wanner et al., 1995, 1997). The crown structural parameters used in the Li kernels were: sparse kernel, crown height to width ratio 1.0, dense kernel 2.5; both kernels, height to the center of crown 2.0, resulting in a lower sparse canopy than dense canopy. These values were chosen because they are likely to also be used in operational BRDF processing for MODIS.

One change was made to the published version of the Ambrals model Li kernels (Wanner et al., 1995). The original Li-Strahler BRDF model was formulated for a fixed angle of illumination (Li and Strahler, 1992). The angle dependence of the scene component reflectances was not part of the modeling conducted. Schaaf and Strahler (1994) and Schaaf, Li and Strahler (1994), however, gave an expression for the most important of these component signatures, the reflectance of the sunlit crowns. This was modeled as following the ratio of actual to projected sunlit crown area. In deriving the geometric Li kernels for the Ambrals model, initially a constant sunlit crown component reflectance was assumed for simplicity. This, however, led to the kernels being not reciprocal with respect to an exchange of sun and viewing angle. The version of Ambrals used in this paper resolves this situation. The sunlit crown component reflectance C was modeled in approximation as $C/\cos(\theta_s)$, where $\cos(\theta_s)$ is the solar zenith angle. This also makes the Li kernels reciprocal.

The RPV BRDF model, on the other hand, is based on a somewhat more empirical approach that quantifies the qualitative features of BRDF shape. Three functions that each govern one distinct aspect of the BRDF shape are multiplied by each other to form the model (Rahman et al., 1993). These are a modified Minnaert term, used to describe the bowl-shape of the BRDF, a Henyey-Greenstein function describing the skew in the BRDF between forward and backscattering, and a hotspot term. Like the Ambrals model, the RPV model has three parameters, quantifying the overall intensity of the reflectance, the strength of the anisotropy, and the relative amount of forward and backward scattering. This provides for a wide variety of shapes as may typically be found for observed BRDFs (Engelsen et al., 1996). The model is nonlinear,

which is undesirable for reasons of computing resources in operational applications. Therefore, the model was modified by Martonchik (Engelsen et al., 1996) to be semi-linear, requiring only a few simple iterations for inversion. This modified form, slated for use in MISR data processing, was used in this study.

The modified Walthall model (Walthall et al., 1985; Nilson and Kuusk, 1989), finally, is a purely empirical model with four parameters based on very simple expressions containing the view and illumination angles. The attraction of this model is mainly that it manages to capture the main features of BRDF shape while being very simple (albedo, for example, can be calculated analytically). However, it is interesting to investigate whether the fact that the Ambrals and the RPV model are based on a more physical reasoning than the Walthall model leads to smaller errors for these models when extrapolating BRDF inversion results to angles where no observations were acquired, for example a different sun angle. As will be seen later, the empirical model is indeed found to be doing worse than the two semiempirical models in this respect despite the fact that it has one more free parameter.

In keeping with the stated goal of deriving bottom-line accuracies, models were inverted by minimizing the error function separately in the red and the near-infrared band, not simultaneously. There is an inherent problem with respect to coupled BRDF and albedo retrieval in the two principal ways in which error in the red and in the near-infrared band can be traded off. If the combined absolute error is to be minimized, the larger reflectances are modeled relatively more accurately than the smaller ones. This provides for a precise retrieval of albedo, which is dominated by the large reflectances, but is less desirable in the retrieval of red band BRDFs. A relative error measure, on the other hand, allows better modeling of small reflectances, e.g., a better BRDF retrieval in the red band, but by the same token allows larger deviations in large reflectances, which translate into undesired larger errors in albedo. This contradiction in the requirements for the error function with respect to BRDF and albedo retrieval is not basically resolvable. In this study, absolute error was minimized, but separately in each band, avoiding definition of a tradeoff between errors in the larger near-infrared reflectance values and the smaller ones in the red band, and allowing to establish the sought-for bottom-line accuracies.

3. Examples of BRDF Retrievals

Since albedo is derived through integration of the BRDF, the first concern is for accurate retrieval of the BRDF. Figure 1 shows MODIS and MISR sampling at different latitudes for a 16-day period starting day of the year 96, in April. Obviously, sampling of the viewing hemisphere is rather reasonable, and even loss of observations to clouds should not regularly impact the angle coverage in a decisive way. At some latitudes, though, the principal plane is not being sampled by either instrument. This could be a problem in some cases since BRDFs tend to be more dissimilar on the principal plane than on the cross-principal plane.

The main shortcoming of the angular sampling available, however, is in the solar angle hemisphere. At each latitude the range of solar zenith angles covered is only very small, usually not more than 10 degrees. But the main concern is that the mean solar zenith angle of observations varies strongly from one latitude to another, covering most of the full zenith angle range. In other words, the BRDF as a function of viewing angle will be well determined at solar angles that vary with latitude, and with time of year.

The main question with respect to BRDF retrieval consequently is whether the retrievals achievable at the solar angle of observation may safely be extrapolated to other solar zenith angles, allowing for example the standardization of surface reflectances not only to a common viewing geometry but also to a common solar geometry. The angles most preferred for such a standardization would be nadir viewing and illumination since under such conditions the understory will be most visible and no shadows will contaminate the scene. However, structural information to be derived from the BRDF is best obtained at off-nadir angles where shadow characteristic may be determined. Off-nadir angles also determine albedo.

Consequently, the following rather severe test is applied to BRDF retrieval. Inversion results are in-

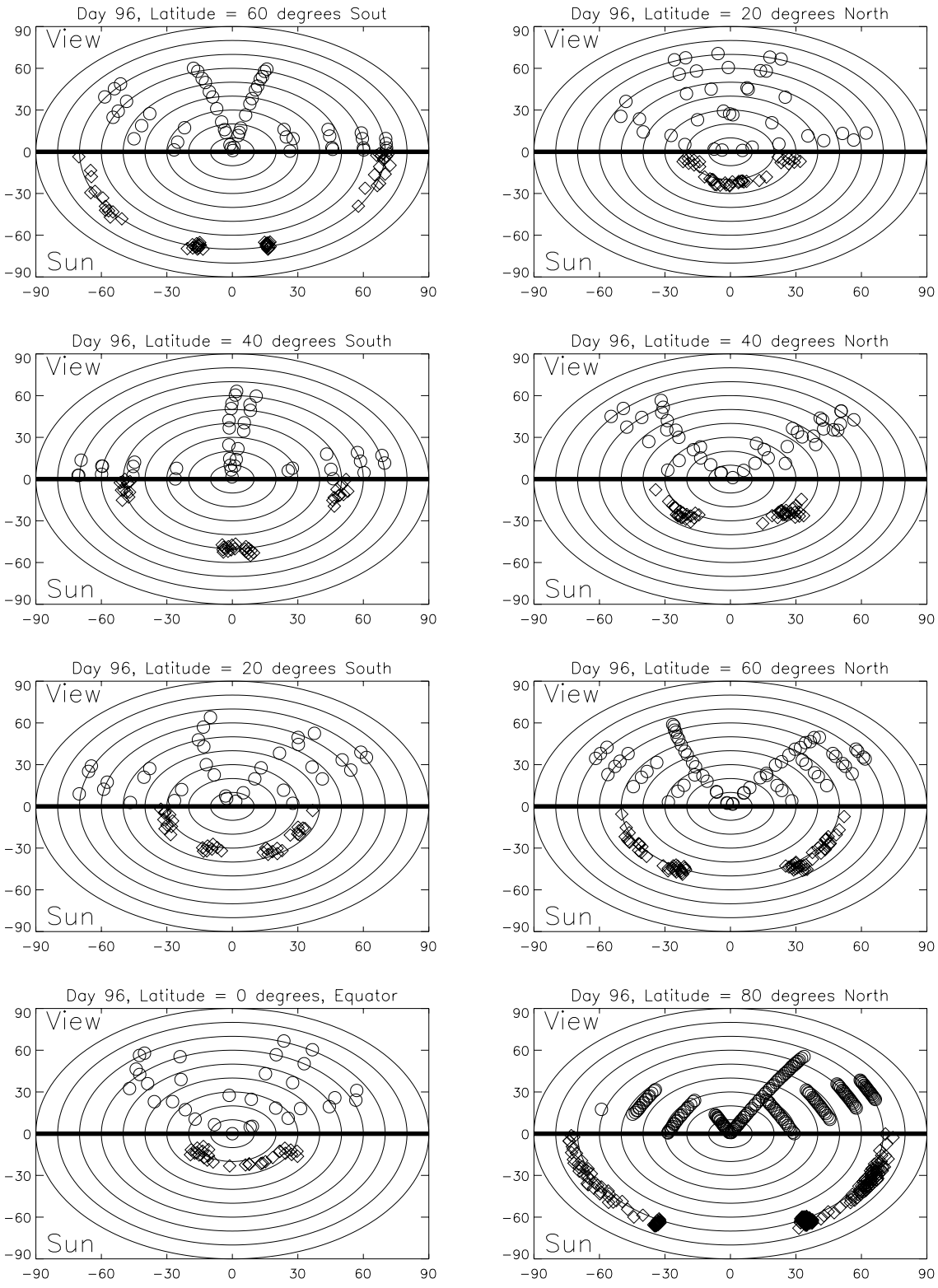

Figure 1: Angular sampling from MODIS and MISR as predicted by Xsatview (Barnsley et al., 1994) for different latitudes and days of the year 96 to 112 (in April). Shown are polar plots of view zenith (upper part of each plot, circles) and solar zenith (lower half, diamonds) and relative azimuth, the latter having been normalized to one semihemisphere because the BRDF models used are symmetric with respect to the principal plane. Zero azimuth is to the right.

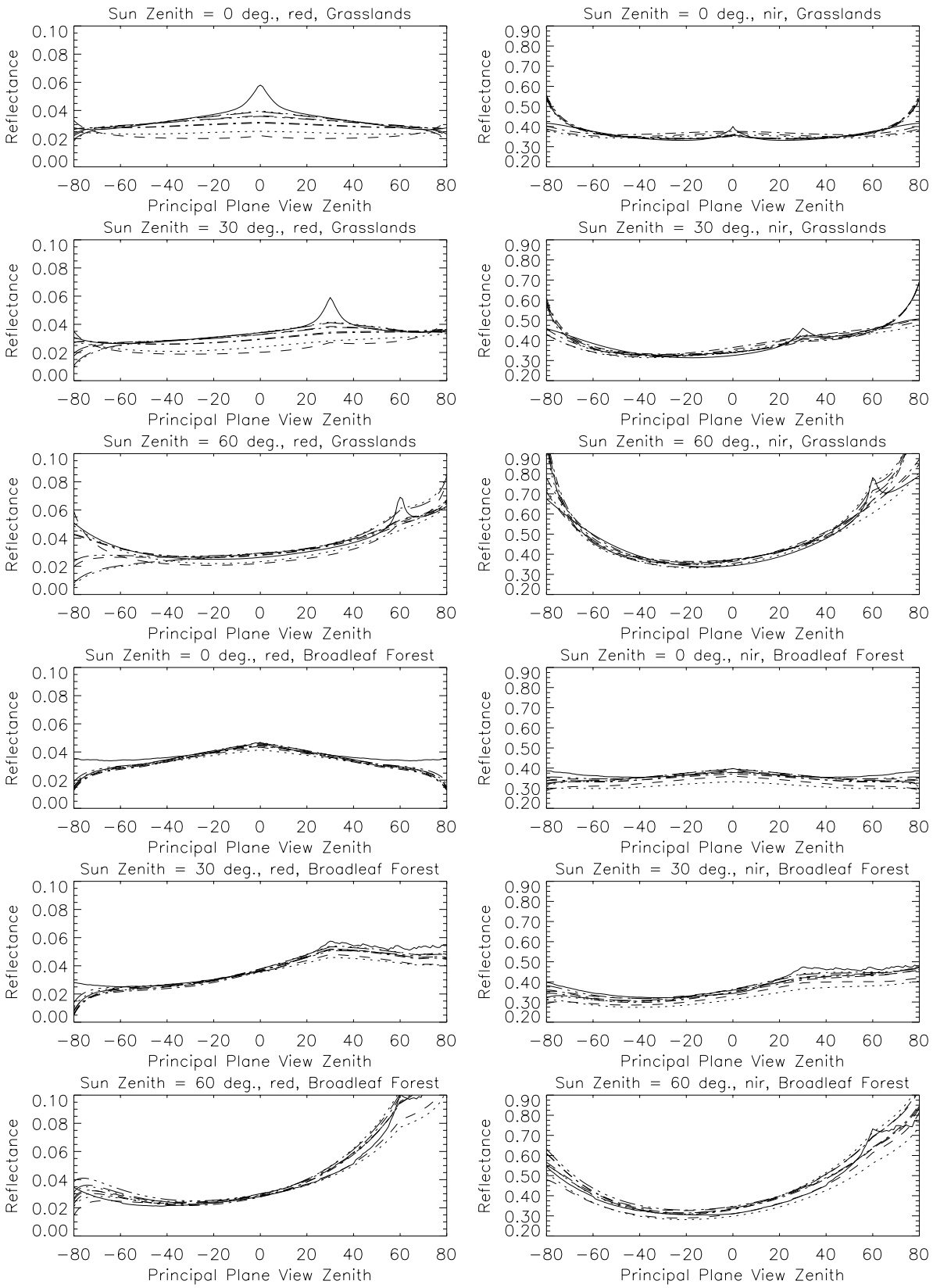

Figure 2: Principal-plane inversion results for a 16-day period starting day of year 96 using the Ambrals model. Land cover types are grasslands (top panels) and broadleaf forest (bottom panels) in the red (left column) and the near-infrared (right column). Solid lines are the result from DOM/RTCODE, all other lines the BRDFs retrieved at different latitudes ranging from 60 degrees south to 80 degrees north from the respective MODIS and MISR angular sampling. BRDF retrievals are shown for solar zenith angles of 0, 30 and 60 degrees, irrespective of the solar zenith angle of the observation.

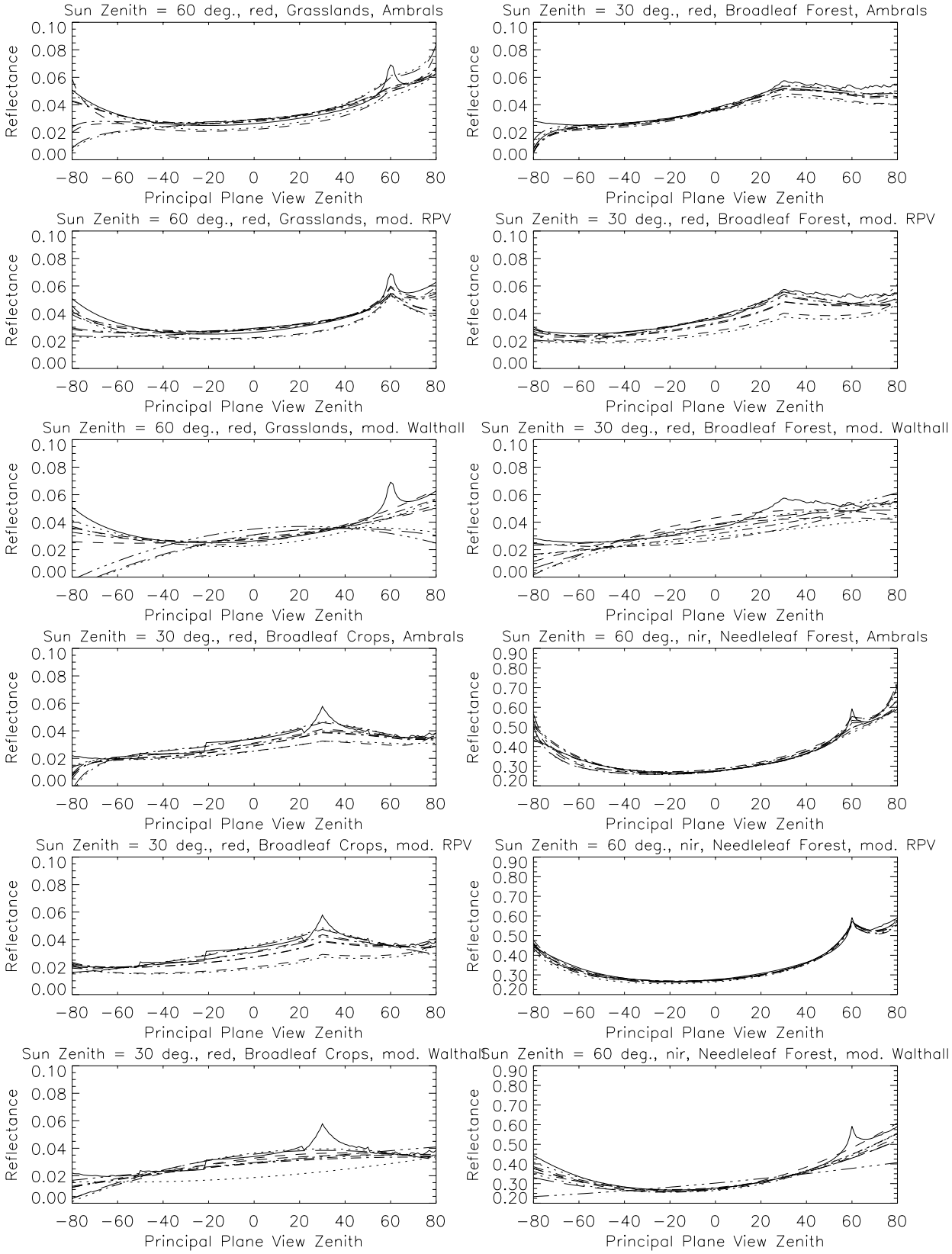

Figure 3: Selected principal-plane inversion results for a 16-day period starting day of year 96 using the Ambrals, modified RPV and modified Walthall models. Solid lines are the result from DOM/RTCODE, all other lines the BRDFs retrieved at different latitudes ranging from 80 degrees south to 60 degrees north from the respective MODIS and MISR angular sampling. BRDF retrievals are shown for the land cover types, bands and sun zenith angles indicated for each panel, where the latter are chosen irrespective of the solar zenith angle of observation.

vestigated at solar zenith angles of 0, 30 and 60 degrees regardless of the solar zenith angle at which the observations were acquired. Depending on what the angle of observation was, varying amounts of extrapolation are required to derive the BRDF at 0, 30 or 60 degrees in solar zenith angle. In some cases, extrapolation may be as much as 70 degrees (for example for day of the year 96, at latitude 60 degrees south, the solar zenith of observation is about 70 degrees, making an extrapolation of the retrieval to a nadir illumination angle a very severe test). However, if reciprocity holds for natural BRDFs, and if the BRDF models used correctly reflect the underlying physical process, the inversion for the viewing hemisphere should provide information on the solar zenith angle dependence of the BRDF at the same time.

Figure 2 shows examples of retrievals for two different land cover types, grasslands and a broadleaf forest, and for inversions using the Ambrals model. The forward-modeled BRDF from DOM/RTCODE is shown as solid lines for different solar zenith angles in the red and near-infrared wavebands. All other lines show retrievals for a 16-day period starting day of the year 96, chosen arbitrarily here as in other examples in this paper, and for MODIS/MISR angular sampling at different latitudes between 60 degrees south and 80 degrees north for the 3 solar zenith angles 0, 30 and 60 degrees.

Clearly, the retrieved BRDFs generally follow the forward-modeled original BRDF quite well. The Ambrals model is capable of producing the variation in shape from one solar angle to another, and properly adapts to the differences in shape between the red and the near-infrared wavebands in extrapolation of the solar zenith angle away from that of observation. Only the extrapolations for the grasslands in the red band seem to be running into some difficulties in cases with fairly large observation solar zenith angles, the predictions being somewhat low and lacking the hotspot (the exact shape of which is not explicitly modeled in Ambrals modeling since from space it rarely is sampled at all). The modified RPV model also shows this same problem, indicating that the problem is not necessarily related to the models used but that the respective sampling does not provide the required information on exact BRDF shape. The near-infrared retrievals and all retrievals for the broadleaf forest are good (but again, deviations seem to largest in the red for nadir illumination), not showing any clear variation with the solar zenith angle of observation, i.e., with the amount of extrapolation required. The average root mean squared absolute error of all Ambrals inversions for all cases was found to be very low, about 0.1 to 0.2 percent in the red and 0.5 to 1.6 percent in the near-infrared, depending on the biome modeled.

These results are typical for Ambrals retrievals. Actually, the grassland retrieval in the red is one of the worst found. Figure 3 shows four more examples for Ambrals BRDF retrieval, selected to show different typical BRDF shapes. The figure also shows the respective retrievals for the modified RPV and modified Walthall BRDF models, allowing comparisons of a few typical cases. The grasslands example shows how the modified Walthall model, being purely empirical, is sometimes not capable of producing the right BRDF shape in situations where the two semiempirical models still function properly. The example of broadleaf crops shows a case where the modified RPV model has greater difficulties than the Ambrals model, as is the case with the broadleaf forest (however, this is not generally the case). The behavior of the modified RPV model is better than that of the Ambrals model at zenith angles larger than about 75 degrees, where the Ambrals models begins to suffer from mathematical terms describing projections approaching mathematically correct but unrealistically large values. The modified Walthall model clearly provides the worst BRDF retrievals in all cases. The modified RPV model produces the hotspot best, especially in the case of the needleleaf forest. In the case of broadleaf crops, notice an example of remnants of the discretization in DOM/RTCODE in the forward-modeled result.

As illustrated by the examples given, the conclusion on BRDF retrieval is that given MODIS and MISR combined cloudfree sampling, retrievals are generally very good, with problems occurring only on occasion. Deviations of the retrieved from the true BRDF may be present particularly if the extrapolation in solar zenith angle is large, the zenith angle itself is large, or the hotspot is of particular interest.

A systematic statistical analysis of bidirectional reflectance retrieval errors across all biomes, bands and sun angles will follow in the discussion section of this paper.

4. Examples of Albedo Retrievals

Integration of the BRDF over the viewing hemisphere gives directional-hemispherical albedo, also called black-sky albedo because the BRDF describes the reflectance in the absence of diffuse skylight (Strahler et al., 1995; Wanner et al., 1997). Black-sky albedo is a function of solar zenith angle. The double integral over the viewing and illumination hemispheres produces bihemispherical or white-sky albedo, a constant describing total average reflectance under isotropic illumination (an approximation perhaps to overcast skies) (Strahler et al., 1995; Wanner et al., 1997). Black-sky and white-sky albedo are important parameters to be derived from remote sensing since they describe average reflectance properties of the surface under different angles of illumination, and represent the albedos of the extremes of a clean or clear and a strongly turbid atmospheric condition. Surface albedos directly enter atmospheric correction algorithms and energy budget calculations and are an important driver in climate and weather models. Their global derivation and mapping is one of the goals of NASA's Earth Observing System.

Figure 4 shows black-sky and white-sky albedo retrieval relative errors as a function of latitude for all six BRDF types (land cover types) studied for different solar zenith angles in the red and the near-infrared, and for a 16-day period beginning day of the year 96. Retrievals for the mean solar zenith angle of observation are shown in the top two panels, illustrating the relative error made under prevailing illumination conditions. The other panels show retrieval accuracies at solar zenith angles 0, 30 and 60 degrees irrespective of the solar angle of the observations. White-sky albedo retrieval errors are shown in the bottom panels. The shaded band marks the plus/minus 10 percent region, within which retrievals ideally should be contained. It is important to note that all variations displayed in this figure are due to changes in sampling geometry alone. Clearly, a trend of error with latitude is seen, reflecting the changes in angular sampling pattern.

With the exception of some retrievals at latitude 60 degrees south in the red band, and for five of the six biomes studied, nearly all albedos are within a 10 percent margin of relative error. In many cases, especially in the near-infrared, they are well within that margin. Errors in the near-infrared mostly show little variation with latitude, indicating robustness against the sampling effects occurring. In the red, the retrievals are relatively less stable, owing to the larger sensitivity of a small albedo to errors in reflectance. The retrievals for some biomes at some solar zenith angles are off by 10 to 30 percent. But still, the bulk of data falls within the 10 percent margin. It is interesting to note that in both bands the retrievals for a solar zenith angle of 30 degrees show less error than the retrievals at the mean solar zenith angle of the observations. This reflects the fact that the models fit moderate solar zenith angles better than large ones. Results at the prevailing solar zenith angle of observations are worse if that angle is large than when this result is extrapolated to a smaller angle. This bodes well for deriving albedo at a standardized, typical solar zenith angle, perhaps at 30 or 45 degrees.

White-sky albedo errors, being dependent on the accurate prediction of black-sky albedo at all solar angles, show in many cases larger errors than the black-sky albedo retrievals at the smaller solar zenith angles. Again, an improvement would be achieved if the model could be altered to fit BRDFs better at large zenith angles, but the accuracies achieved are still acceptable in view of the fact that any derivation of white-sky albedo necessarily involves a large amount of extrapolation of data in the absence of good sampling of the solar hemisphere.

Figure 5 compares Ambrals retrieval accuracies with those for the modified RPV and the modified Walthall models for a few selected cases showing typical results. The modified RPV model generally shows error patterns that are very similar to those of Ambrals, i.e., when one model has a problem the other one does too. This indicates that the problems encountered are based on a lack of required directional information in the angular sampling available, not in an inherent inability of the models to predict better results. Individual examples can be found in the full data set where either the Ambrals or the modified RPV model are doing better. There is a tendency, however, for modified RPV model retrievals to be more consistent in terms of the size of the error produced. The modified Walthall model generally does worse,

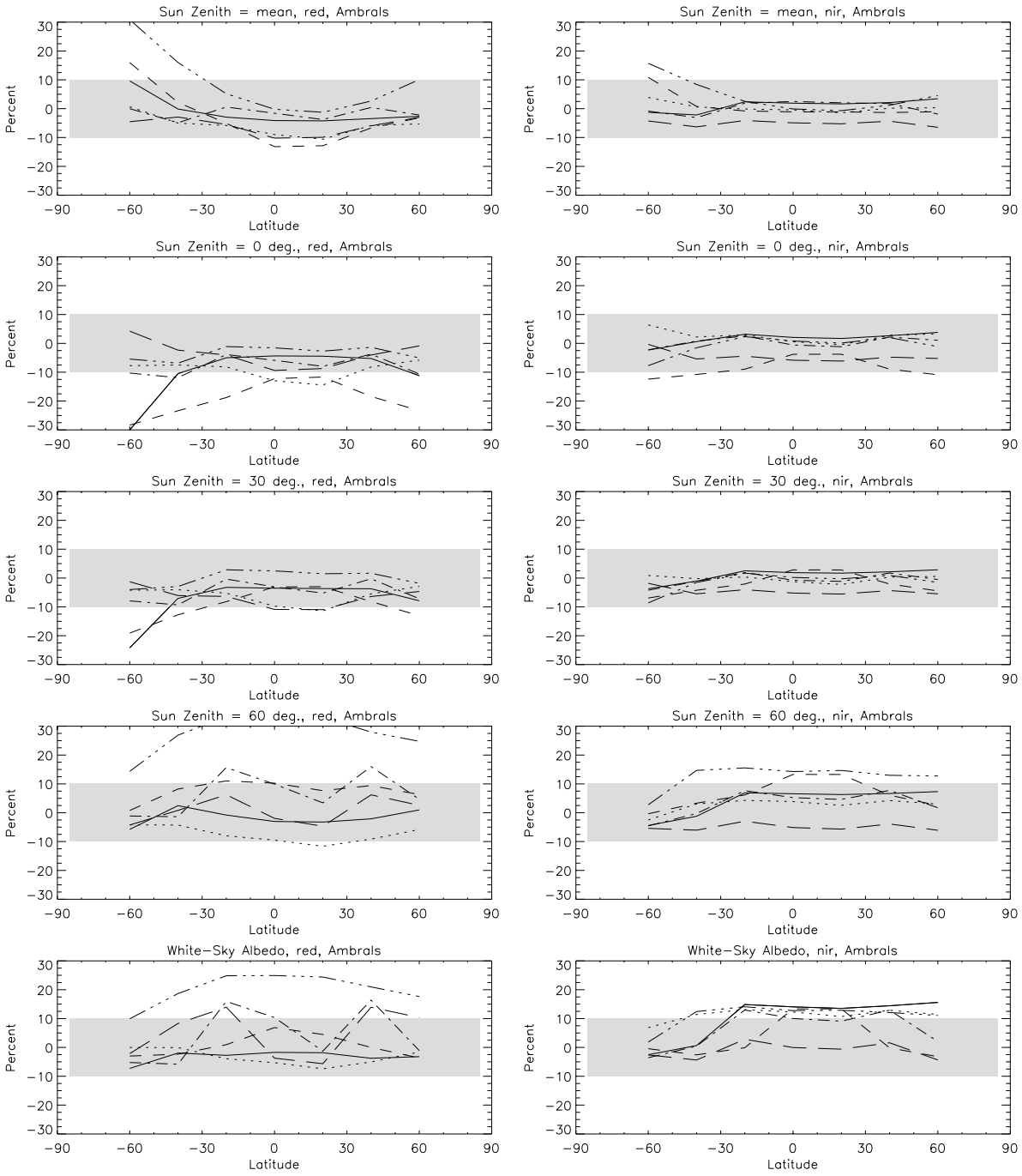

Figure 4: Black-sky and White-sky albedo relative retrieval errors for a 16-day period starting day of the year 96 using Ambrals in the red (left) and near infrared (right) wavebands as a function of latitude. Each panel shows results for each of the six BRDF types (land cover types). Black-sky albedos were calculated for the indicated solar zenith angles irrespective of the sun angle of observation, and at the mean sun angle. White-sky albedo is a constant. The shaded area shows the region of a 10 percent positive or negative error.

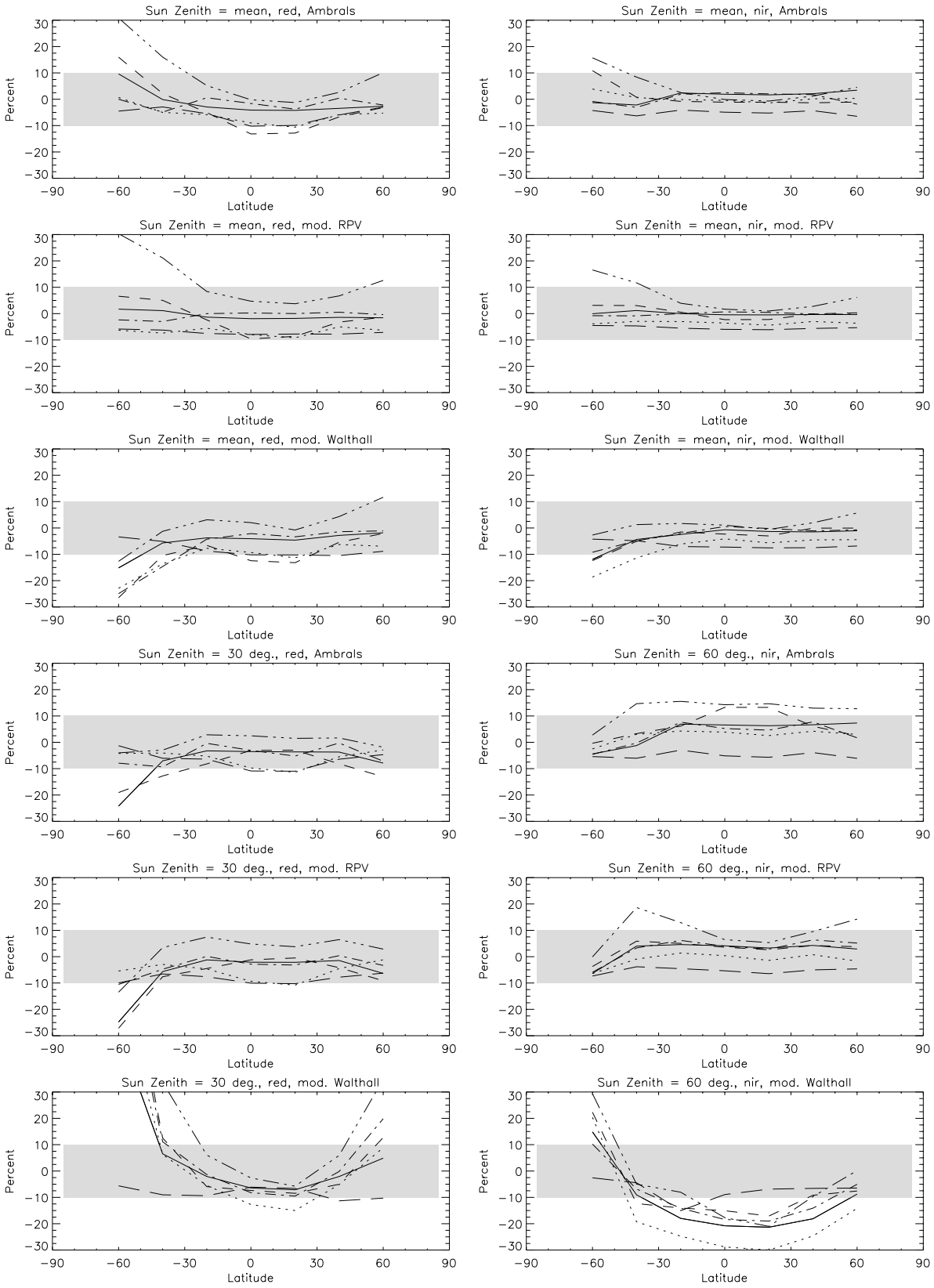

Figure 5: Selected black-sky and White-sky albedo relative retrieval errors for a 16-day period starting day of the year 96 using the Ambrals, the modified RPV and the modified Walthall models, shown as a function of latitude and for the selected wavebands and solar zenith angles indicated. Each panel shows results for each of the six BRDF types (land cover types). The shaded area shows the region of a 10 percent positive or negative error.

with a pattern of errors that is noticeably distinct from those of the semiempirical models. The empirical nature of this model clearly has a negative effect. By the same token, one may state that despite the very severe approximations made in deriving both the Ambrals and the modified RPV model, they do retain physical knowledge that allows extrapolation of the BRDFs studied to solar angles away from those of the observations. However, this finding needs to be qualified somewhat by the fact that these BRDFs inverted were derived from a numerical forward model that encorporates some of the same principles that were also applied in the inverse modeling, although they were fully developed in the complex forward model and strongly approximated in the simple retrieval models.

The overall conclusion, however, should be that in general albedo retrievals are possible from cloud-free MODIS and MISR sampling if a relative error margin of about 10 percent is acceptable. Depending on the application, this relative error will have to be qualified in terms of the absolute radiation contained in the respective waveband, albedos in the near-infrared being higher but solar irradiation in that band also being much lower than in the visible.

A systematic statistical analysis of albedo retrieval errors across all biomes, bands and sun angles will follow in the discussion section of this paper.

5. Overall BRDF and Albedo Retrieval Accuracies

The question asked at the outset of this paper was concerned with the accuracy of BRDF and albedo retrieval one may expect from angular sampling as will be provided by the EOS sensors MODIS and MISR. Inversions conducted for different sampling geometries, as they will occur as a function of latitude and time of year, and for different BRDF types (landcover types), show that in most cases, the values of reflectances and albedos can indeed be retrieved satisfactorily. Whether the errors remaining are sufficiently small depends on the accuracy required in a specific application of the data. Here, they are reported to allow such an evaluation, and to put error margins on the planned MODIS BRDF/Albedo Product, which will make use of the same combined MODIS and MISR sampling investigated in this study.

Whereas in the previous sections example results from inversions were shown for BRDF and albedo, an analysis of the results of the full study will now be given. Figure 6 shows the relative frequency with which errors occur for all cases (latitudes, days of year, biomes), binned to 5-percent bins, for nadir-view reflectances and albedos predicted at various solar zenith angles. The most obvious thing to notice is that the Ambrals and the modified RPV model produce a rather similar histogram of error magnitudes, whereas the modified Walthall model consistently produces larger errors more frequently. Errors larger than 15 percent still occur in a considerable number of cases, especially at large solar zenith angles. This happens despite the fact that the model has one free parameter more than the other two. Clearly, use of the modified Walthall model is not advised for best accuracy. Its main benefit is its one-line simplicity and attractive mathematical properties where some loss of accuracy can be accepted.

The bulk of errors for the semiempirical models is in the 10 percent range, with tails of the distribution spreading to 15 percent in some cases. While Ambrals is doing better than the modified RPV model in some cases, for example for nadir reflectance in the red band at all solar zenith angles, the modified RPV model is doing better in a number of other cases, most notably in the near-infrared. But these differences are not very large. White-sky albedo in the near-infrared, however, is predicted much more accurately by the modified RPV model due to a tendency of the Ambrals model to overestimate it.

A differently summarized overview over bottom-line BRDF and albedo retrieval accuracies is given in Table 1. For each of the three models, and for albedo and nadir-view reflectance at various solar zenith angles, in the red and near-infrared bands, the median relative error of retrieval is given in the center column to identify the typical error. The numbers to either side of that column give the error margins that encompass two thirds of the data. The two outermost respective columns give the best and the worst case

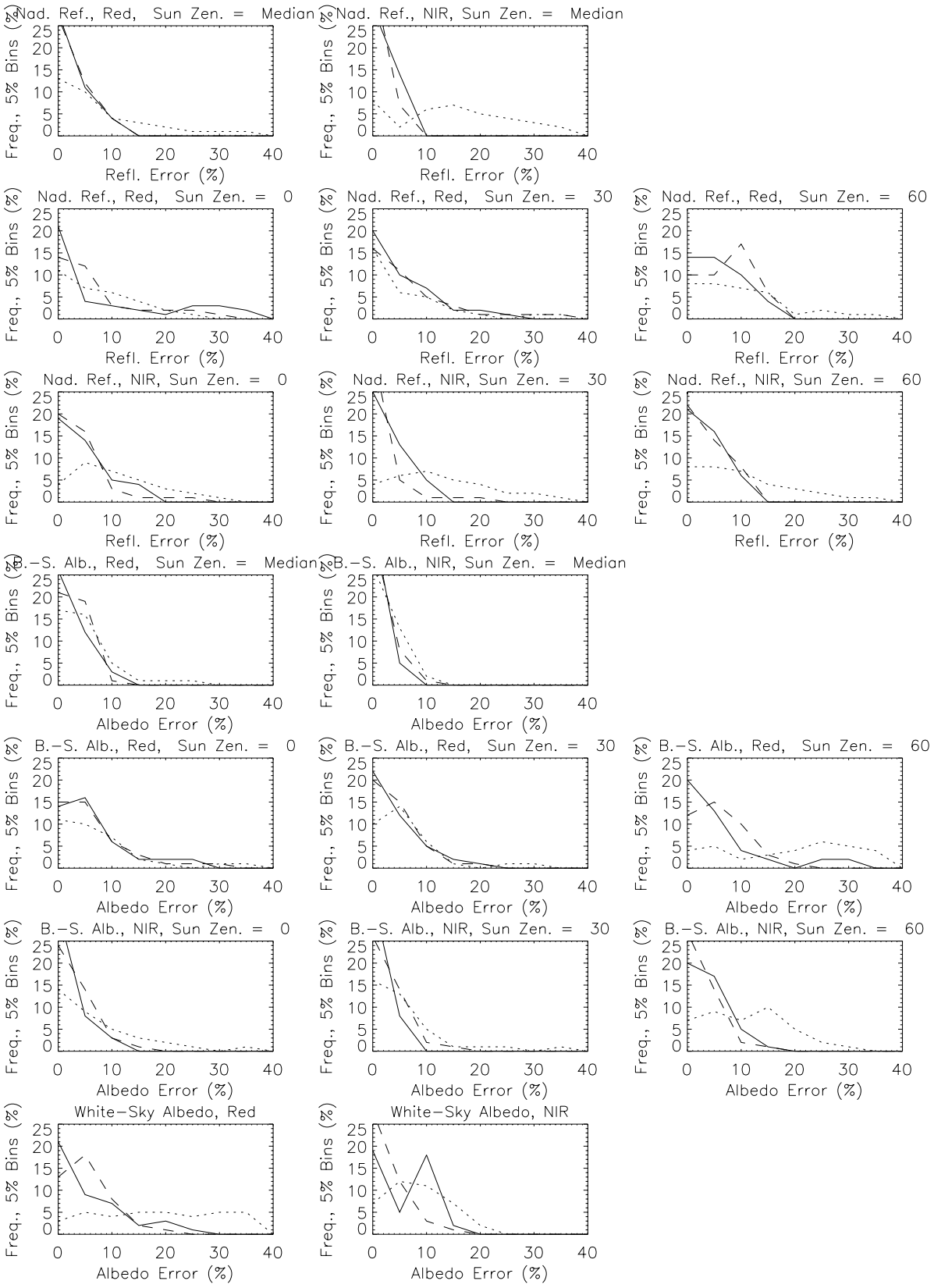

Figure 6: Histograms of the distribution of relative errors of retrieval for nadir-view reflectance and albedo for the Ambrals (solid line), modified RPV (dashed line) and modified Walthall model (dotted line) in the red and near-infrared. Histograms are based on data from all latitudes, all six BRDF types (biomes) and all days of the year tested. Results were obtained for the solar angles indicated, irrespective of the solar zenith angles of observation. Relative frequency is shown based on bins with a width of 5 percent.

Table 1: Predicted Retrieval Accuracies: All Latitudes, Times of Year and Biome Types. Median Error, Two-Thirds of Cases Range, and Best and Worst Error Found.

Model	Band	Solar Zenith Angle	Albedo Percentage of Data 0/6	1/6	3/6	5/6	6/6	Nadir Reflectance Percentage of Data 0/6	1/6	3/6	5/6	6/6
Ambrals	red	$\theta_s = 0$	0.0	3.7	7.5	16.0	33.2	0.0	1.1	5.5	28.7	50.1
		$\theta_s = 30$	0.0	2.5	4.8	11.0	24.2	0.0	1.2	5.4	14.5	41.0
		$\theta_s = 60$	0.0	2.3	6.0	16.0	42.6	0.0	2.1	7.9	11.9	21.8
		$\langle\theta_s\rangle_{obs}$	0.0	1.9	4.3	9.6	39.0	0.0	0.9	3.2	8.1	13.6
		$\int \theta_s$	0.0	1.4	5.3	14.2	31.4					
	nir	$\theta_s = 0$	0.0	0.8	3.0	6.4	17.3	0.0	0.8	6.1	13.9	38.3
		$\theta_s = 30$	0.0	0.6	2.5	5.4	14.4	0.0	1.3	4.6	8.8	28.7
		$\theta_s = 60$	0.0	2.5	5.4	8.8	19.1	0.0	1.2	5.2	9.6	15.2
		$\langle\theta_s\rangle_{obs}$	0.0	0.5	2.0	4.9	19.9	0.0	0.7	3.3	6.6	13.2
		$\int \theta_s$	0.0	1.6	8.1	13.4	16.7					
	red +nir	$\theta_s = 0$	0.0	1.6	4.8	11.6	33.2	0.0	1.0	5.9	17.8	50.1
		$\theta_s = 30$	0.0	1.2	3.7	7.6	24.2	0.0	1.2	4.9	11.6	41.0
		$\theta_s = 60$	0.0	2.4	5.7	12.6	42.6	0.0	1.5	6.5	11.2	21.8
		$\langle\theta_s\rangle_{obs}$	0.0	0.9	3.1	6.7	39.0	0.0	0.8	3.3	7.1	13.6
		$\int \theta_s$	0.0	1.5	6.0	13.8	31.4					
modified RPV	red	$\theta_s = 0$	0.0	2.2	6.3	15.4	43.2	0.0	2.4	7.2	28.2	59.8
		$\theta_s = 30$	0.0	1.8	5.6	11.4	33.6	0.0	1.6	6.6	19.7	48.6
		$\theta_s = 60$	0.0	2.2	7.9	14.1	32.6	0.0	3.8	10.3	14.6	23.7
		$\langle\theta_s\rangle_{obs}$	0.0	1.2	5.1	8.3	39.6	0.0	1.1	3.6	8.8	17.5
		$\int \theta_s$	0.0	3.1	7.4	13.1	27.7					
	nir	$\theta_s = 0$	0.0	1.3	4.6	8.6	25.5	0.1	2.2	5.5	11.5	34.2
		$\theta_s = 30$	0.0	0.6	3.4	7.7	23.3	0.0	1.3	2.8	7.0	29.9
		$\theta_s = 60$	0.0	1.9	4.5	6.7	19.7	0.0	1.4	5.3	10.3	15.8
		$\langle\theta_s\rangle_{obs}$	0.0	0.4	2.5	5.5	24.0	0.0	0.9	2.3	5.1	15.4
		$\int \theta_s$	0.0	1.4	3.9	6.7	18.3					
	red +nir	$\theta_s = 0$	0.0	1.7	5.5	12.8	43.2	0.0	2.2	6.1	20.3	59.8
		$\theta_s = 30$	0.0	1.2	4.8	9.8	33.6	0.0	1.4	4.3	14.1	48.6
		$\theta_s = 60$	0.0	2.0	5.3	11.7	32.6	0.0	2.0	7.7	12.9	23.7
		$\langle\theta_s\rangle_{obs}$	0.0	0.6	3.2	7.2	39.6	0.0	1.0	2.7	6.6	17.5
		$\int \theta_s$	0.0	2.0	5.4	10.6	27.7					
modified Walthall	red	$\theta_s = 0$	0.2	3.0	10.6	48.6	303.4	0.0	3.0	12.0	53.1	293.5
		$\theta_s = 30$	0.0	3.8	9.0	42.5	270.4	0.1	2.0	9.8	55.6	308.6
		$\theta_s = 60$	0.1	8.1	26.5	41.6	163.6	0.0	4.3	13.5	43.1	257.1
		$\langle\theta_s\rangle_{obs}$	0.0	2.9	6.7	11.8	46.9	0.0	2.3	8.7	35.8	131.2
		$\int \theta_s$	0.4	8.5	23.7	38.6	179.0					
	nir	$\theta_s = 0$	0.0	2.6	9.2	35.2	180.7	0.0	6.7	16.0	51.2	290.9
		$\theta_s = 30$	0.0	1.8	7.2	26.6	143.7	0.1	7.3	19.0	54.1	245.0
		$\theta_s = 60$	0.1	5.0	13.9	21.8	62.2	0.0	4.1	13.5	40.1	145.1
		$\langle\theta_s\rangle_{obs}$	0.0	1.1	3.5	7.4	31.6	0.1	3.4	18.4	33.7	76.1
		$\int \theta_s$	0.3	4.9	11.8	17.3	74.8					
	red +nir	$\theta_s = 0$	0.0	2.8	9.8	42.6	303.4	0.0	4.9	13.5	53.1	293.5
		$\theta_s = 30$	0.0	2.6	8.2	35.4	270.4	0.1	3.2	14.5	54.2	308.6
		$\theta_s = 60$	0.1	6.2	18.1	34.7	163.6	0.0	4.3	13.5	40.5	257.1
		$\langle\theta_s\rangle_{obs}$	0.0	1.6	5.0	10.2	46.9	0.0	3.0	14.5	34.8	131.2
		$\int \theta_s$	0.3	6.1	14.9	33.7	179.0					

Table 2: Summary of Predicted Retrieval Accuracies: All Latitudes, Times of Year, Biome Types and Solar Zenith Angles, Irrespective of the Sun Zenith Angle of Observation. Median and Two-Thirds of Cases Range, the Ranges Being With Respect to Solar Zenith Angle.

Model	Albedo		Nadir Reflectance	
Ambrals	2.0–8.1	(0.5–16.0)	3.2–7.9	(0.7–28.7)
mod. RPV	2.5–7.9	(0.4–15.4)	2.3–10.3	(0.9–28.2)
mod. Walthall	3.5–26.5	(1.1–48.6)	8.7–19.0	(2.0–55.6)

Table 3: Summary of Predicted Retrieval Accuracies as a Function of Cloud Probability: All Latitudes, Biome Types and Solar Zenith Angles for a 16-Day Time Period Beginning Day of Year 96, Irrespective of the Sun Zenith Angle of Observation. Median and Two-Thirds of Cases Range, the Ranges Being With Respect to Solar Zenith Angle.

Prob. of Cloud	Albedo		Nadir Reflectance	
0 %	2.0–7.8	(0.7–18.4)	3.2–9.2	(0.4–31.4)
25%	1.9–8.0	(0.8–17.9)	3.2–9.0	(0.5–30.8)
50 %	2.3–8.1	(0.7–18.6)	3.1–9.2	(0.7–31.2)
75 %	3.1–9.0	(0.7–18.7)	2.6–9.3	(0.7–29.6)

found in the whole set. Table 2 in turn summarizes Table 1 to allow a quick overview over the tendencies found. It lists the range of median errors found, the variation being with respect to sun angle, and the lowest and highest delimiters of the two-thirds of cases range at the different solar zenith angles for each of the three models.

It is clear from these numbers than the Ambrals and modified RPV models are doing similarly well. Ambrals retrievals seem to be slightly better, but not by much. The accuracy of albedo retrieval is between 2 and 8 percent for both models, that of nadir-view reflectance between 3 and 8 percent for the Ambrals model and between 2 and 10 percent for the modified RPV model. But in cases with retrieval problems (not the worst cases, but typical bad cases), errors can amount to some 30 percent for the modified RPV model where they are typically only some 15 percent for the Ambrals model. The modified Walthall model is clearly inferior in terms of retrieval accuracy. The median accuracy of albedo retrieval is between 4 and 26 percent, with typical problematic cases ranging to 50 percent in error, and nadir-view reflectance is retrieved to within only 9 to 19 percent, bad cases being off by up to 60 percent typically.

The accuracies given in Tables 1 and 2 are bottom-line accuracies calculated for full sampling in the absence of clouds. A careful study is required to assess how these accuracies change when observations are lost to clouds, and what impact errors in aerosol retrieval and atmospheric correction have. Only then will the picture be complete. However, in order to provide some idea of the stability of the inversions performed in this study and the relevance of the numbers found, Table 3 gives some results for the Ambrals model and a 16-day period beginning day of the year 96, using all six BRDF types (land cover types), all latitudes,

and the red and the near-infrared bands. The probability of an observation to be lost due to cloudiness was set in turn to 0, 25, 50 and 75 percent. Five realizations of each case were computed. In each of these, the number of observations varied, as did which observations were dropped, but the average number was close to three quarters, half, and one quarter of the full set. Observations were randomly dropped even though MISR observations are most likely to be dropped in multiples of 9 if they are dropped (since the multiangular observations are acquired simultaneously, which is not the case for MODIS). Inversions were preformed on each case and the error ranges given in Table 3 computed.

Table 3 shows that neither albedo retrieval errors nor nadir reflectance retrieval errors change much even when three quarters of all observations are dropped. The reason for this is that the most important factor in the inversions is not the number of observations but the range of angles they cover, which is mostly not affected by random dropouts of observations. The sensitivity of retrievals to various types of noise-like effects in the observations will grow as the number of observations drops, but a study by Wanner et al. (1996) and Lewis and Wanner (1997) has shown that noise sensitivity of Ambrals retrievals is rather good for combined MODIS and MISR sampling, noise mostly not being amplified into the BRDFs and albedos retrieved even with a loss of observations to clouds.

Consequently, it is safe to say that loss of observations to clouds are not a limiting factor with respect to the MODIS observations. And since at least two opportunities for a MISR observation occur in a 16-day time period, in most cases actual MODIS/MISR sampling should be even better than obtained from the computed random loss. With some caution, the bottom-line accuracies derived in this study may be taken as a preliminary indication of expected product accuracy of the MODIS BRDF/Albedo Product. Table 1 and Figure 6 give the full details.

6. Discussion and Conclusions

A word of caution is due with respect to the fact that this study was conducted in form of a model-to-model comparison. Since angular sampling has such a particular influence in the values retrieved, it is important to study retrieval accuracies using the actual sampling, not principal-plane sampling or cross-principal plane sampling, even though those too may give an indication of what is achievable. In the absence of the actual instruments, this makes necessary a study using simulation, such as this one, allowing to explore the full range of occurring situations. However, if an inverse model is not capable of producing good results, the reason may be sought with either the inverse model or the forward model. Particularly, deviations of the inverse from the forward model at large zenith angles, where theories involving projections are most likely to be overly idealistic, may be caused by either model. It would be wrong to necessarily construct the inversion models in such a way that it absolutely follows the forward model. Furthermore, in this study the forward model itself may have had some problems, for example due to the discreteness of the numerical scheme used. The BRDFs from DOM/RTCODE are rather similar across the biomes, either reflecting a similarity in the theories used for the different biomes or reflecting a general similarity in natural BRDFs once both shadowing and radiative transfer-type scattering are both taken into account at all levels.

However, it should also be pointed out that even after the MODIS and MISR instruments are operational, it will be very difficult to replace these error estimates from simulation with values actually measured. Any validation effort will necessarily be limited in the range of conditions covered, will have to deal with severe problems of scaling between local observations and the size of the sensor footprints (effectively one kilometer for the MODIS BRDF/Albedo Product), and be convolved with other uncertainties, stemming for example from differences in the spectral response or calibration of the ground and the space instruments. Most accuracies considered in this study are in the range of a few percent, which to detect requires excellent accuracy in the field.

In conclusion, it seems from this investigation that it is probable that BRDF and albedo will be retrievable

with reasonable accuracy from MODIS and MISR observations using either the Ambrals or the modified RPV model. Typical errors will be below 10 percent. It is good that the MISR BRDF/Albedo Product will be based on the modified RPV model while the MODIS BRDF/Albedo Product will use the Ambrals model, as both models are capable of producing reliable results and using both models in different products will maximize the material generated from which conclusions can be drawn. The resulting BRDFs and albedos can be assembled into databases that integrate knowledge over time, further minimizing the error involved. These databases may then serve for a characterization of the radiative state of the Earth's surface for biophysical, climate and weather modeling.

Acknowledgements. Special thanks are due to Ranga Myneni for allowing generous use of his DOM/RTCODE BRDF modeling algorithm, without which this work would not have been possible. Baojin Zhang at Boston University cooperated in early stages of this work. Thanks also to all members of the MODIS BRDF/Albedo team for discussions, especially Philip Lewis, Alan Strahler, and Xiaowen Li; and to Petra Lucht. This work was supported by NASA under NAS5-31369.

References

Barnsley, M. J., A. H. Strahler, K. P. Morris, and J.-P. Muller, Sampling the surface bidirectional reflectance distribution function (BRDF): Evaluation of current and future satellite sensors, *Remote Sens. Rev. 8*, 271–311, 1994.

Deschamps, P. Y., F. M. Breon, M. Leroy, A. Podaire, A. Bricaud, J. C. Buriez, and G. Seze, The POLDER mission: Instrument characteristics and scientific objectives, *IEEE Trans. Geosci. Remote Sens., 32*, 598–615, 1994.

Diner, D., C. J. Bruegge, J. V. Martonchik, G. W. Bothwell, E. D. Danielson, V. G. Ford, L. E. Hovland, K. L. Jones, and M. L. White, A multi-angle image spectroradiometer for terrestrial remote sensing with the Earth Observing System, *Int. J. Imag. Sys. Tech., 3*, 92–107, 1991.

Diner, D., J. V. Martonchik, C. Borel, S. A. W. Gerstl, H. R. Gordon, R. Myneni, B. Pinty, and M. M. Verstraete, MISR LEvel 2 Surface Retrieval Algorithm Theoretical Basis, *NASA EOS-MISR Document, JPL D-22401, Rev. B*, 78 pp.1996.

Engelsen, O., B. Pinty, M. M. Verstraete, and J. V. Martonchik, Parametric bidirectional reflectance factor models: evaluation, improvements and applications, *Report, Joint Research Centre of the European Commission, EU 16426,*, 114 pp., 1996.

Hu, B., W. Wanner, X. Li, and A. Strahler, Validation of kernel-driven semiempirical BRDF models for application to MODIS-MISR data, *Proc. Int. Geosci. Remote Sens. Symp. 96*, 1669–1671, 1996.

Hu, B., W. Wanner, X. Li, and A. Strahler, Validation of kernel-driven semiempirical models for global modeling of bidirectional reflectance, to be submitted to Remote Sens. Env., 1997.

Lewis, P., and W. Wanner, Noise sensitivity of BRDF and albedo retrieval from the Earth Observing System MODIS and MISR Sensors with respect to angular sampling, in preparation, 1997.

Leroy, M., J. L. Deuze, F. M. Breon, O. Hautecoeur, M. Herman, J. C. Buriez, D. Tanre, S. Bouffies, P. Chazette, and J.-L. Roujean, Retrieval of atmospheric properties and surface bidirectional reflectances over land from POLDER/ADEOS, *J. Geophys. Res., this issue*, 1997.

Li, X., and A. H. Strahler, Geometric-optical bidirectional reflectance modeling of the discrete crown vegetation canopy: effect of crown shape and mutual shadowing, *IEEE Trans. Geosci. Remote Sens., 30*, 276–292, 1992.

Martonchik, J. V., Determination of aerosol optical depth and land surface directional reflectances using multi-angle imagery, *J. Geophys. Res.*, in press, 1997.

Myneni, R. B., G. Asrar, and F. G. Hall, A three-dimensional radiative transfer method for optical remote sensing of vegetated land surfaces, *Remote Sens. Env., 41*, 105–121, 1992.

Nilson, T., and A. Kuusk, A reflectance model for the homogeneous plant canopy and its inversion, *Remote Sens. Env., 27*, 157–167, 1989.

Rahman, H., B. Pinty, and M. M. Verstraete, Coupled surface-atmosphere reflectance (CSAR) model, 2, Semiempirical surface model usable with NOAA advanced very high resolution radiometer data, *J. Geophys. Res., 98*, 20,791–20,801, 1993.

Roujean, J. L., M. Leroy, and P. Y. Deschamps, A bidirectional reflectance model of the earth's surface for the correction of remote sensing data, *J. Geophys. Res., 97*, 20,455–20,468, 1992.

Ross, J. K., *The Radiation Regime and Architecture of Plant Stands*, 392 pp., Dr. W. Junk Publishers, The Hague, 1981.

Running, S. W., C. O. Justice, V. Salomonson, D. Hall, J. Barker, Y. J. Kaufman, A. H. Strahler, A. R. Huete, J.-P. Muller, V. Vanderbilt, Z. M. Wan, P. Teillet, and D. Carneggie, Terrestrial remote sensing science and algorithms planned for EOS/MODIS, *Int. J. Remote Sens., 15*, 3587–3620, 1994.

Schaaf, C. B., and A. H. Strahler, Validation of bidirectional and hemispherical reflectances from a geometric-optical model using ASAS imagery and pyranometer measurements of a spruce forest, *Remote Sens. Environ., 49*, 138–144, 1994.

Schaaf, C. B., X. Li, and A. H. Strahler, Topographic effects on bidirectional and hemispherical reflectances calculated with a geometric-optical canopy model, *IEEE Trans. Geosci. Remote Sens., 32*, 1186–1193, 1994.

Strahler, A. H., C. B. Schaaf, J.-P. Muller, W. Wanner, M. J. Barnsley, R. d'Entremont, B. Hu, P. Lewis, X. Li, and E. V. Ruiz de Lope, MODIS BRDF/albedo product: Algorithm theoretical basis document, *NASA EOS-MODIS Doc.*, version 4.0, 1996.

Walthall, C. L., J. M. Norman, J. M. Welles, G. Campbell, and B. L. Blad, Simple equation to approximate the bidirectional reflectance from vegetation canopies and bare soil surfaces, *Appl. Opt., 24*, 383–387, 1985.

Wanner, W., X. Li, and A. H. Strahler, On the derivation of kernels for kernel-driven models of bidirectional reflectance, *J. Geophys. Res., 100*, 21077–21090, 1995.

Wanner, W., P. Lewis, and J.-L. Roujean, The influence of directional sampling on bidirectional reflectance and albedo retrieval using kernel-driven models, *Proc. Int. Geosci. Remote Sens. Symp. 96*, 1408–1410, 1996.

Wanner, W., A. H. Strahler, B. Hu, X. Li, C. L. Barker Schaaf, P. Lewis, J.-P. Muller, and M. J. Barnsley, Global retrieval of bidirectional reflectance and albedo over land from EOS MODIS and MISR data: theory and algorithm, *J. Geophys. Res.*, in press, 1997.

APPENDIX C:
NOISE SENSITIVITY OF BRDF AND ALBEDO RETRIEVAL FROM THE EOS-MODIS AND MISR SENSORS WITH RESPECT TO ANGULAR SAMPLING (PAPER BY LEWIS AND WANNER)

PROGRESS REPORT (Nov. 96):
Tables and figures final; text will be completely revised

Noise Sensitivity of BRDF and Albedo Retrieval From the Earth Observing System MODIS and MISR Sensors With Respect to Angular Sampling

Philip Lewis[1] and Wolfgang Wanner[2]

[1] *Remote Sensing Unit, Dept. of Geography, University College London, London, UK*
[2] *Center for Remote Sensing and Dept. of Geography, Boston University, Boston, MA*

Abstract

The sensitivity of the Ambrals semiempirical BRDF model to random noise in observed multiangular reflectances is investigated. The mathematical properties of kernel-driven BRDF models allow to derive analytically so-called weights of determinations or noise inflation factors that quantify the expected noise found in retrieved parameters like nadir-view reflectance or albedo at various solar zenith angles, or in the BRDF model parameters. The study is carried out using simulated angular sampling as is to be expected from the MODIS and MISR instruments to be flown on the EOS-AM platforms as a function of latitude, day of year and sampling period. A similar study is carried out for comparison using the modified RPV BRDF model. Results show that for both models the retrieved parameters reflectance and albedo the noise amplification factors are less than one (less noise present than was in the original data, i.e., the retrievals are stable with respect to random noise). The BRDF model parameters themselves, especially for the modified RPV model, are found to be more susceptible to noise. Differences in noise sensitivity between different model variants and sampling scenarios are further explored. This study is relevant with respect to the reliability to be expected from the planned operational BRDF/albedo products from the MODIS and MISR instruments.

1. Introduction

Global space-based retrievals of the bidirectional reflectance distribution function (BRDF) and albedo over land will be possible in the near future using the Earth Observing System's (EOS) MODIS and MISR sensors or the POLDER instrument. BRDF information is useful for normalizing satellite-acquired data sets and for deriving key surface parameters, mainly atmospherically corrected albedo for use in climate studies.

Little work, however, has been done on the sensitivity of BRDF and albedo retrievals to angular sampling patterns even though the impact of these on product accuracy is possibly substantial. With any instrument, the angular distribution of samples obtainable in a given time period will vary with geographic latitude and time of year, and be also determined by instrument and orbit characteristics. Cloud masking will further reduce the set of available angular reflectances. In this paper we evaluate in a practical case the impact of angular sampling effects on BRDF and albedo derivation.

Two effects mainly have an influence on retrieval accuracy as a function of angular sampling:
(1) Sensitivity to random noise. Analysis is carried out under the assumption that the RMSE found in

inverting a model against observations is due to random "noise-like" errors in the observed reflectances, due for example to fluctuations in surface properties, misregistration, atmospheric correction errors etc.
(2) Misfit sensitivity. Analysis is carried out under the assumption that the RMSE found in inversion is due to an inherent partial inability of the model used to fit the observations even in the absence of "noise", and to infer completely from limited angular sampling the BRDF shape observed. Investigating this effect is important in view of the many assumptions that are commonly made in operationally feasible BRDF models.

In this paper, we focus on the noise sensitivity analysis alone, although the misfit analysis is of equal importance. We study the behavior of the semiempirical Ambrals BRDF model (Wanner et al., 1995, 1997) under conditions of sampling by MODIS and MISR, and how the semiempirical Rahman model (Rahman et al., 1993) behaves under the same circumstances.

2. The Experiment

We here investigate sampling effects with respect to the MODIS BRDF/albedo product (Strahler et al., 1996; Wanner et al., 1997), using the sampling patterns and BRDF models characterizing it. The product is slated for production at a spatial resolution of one kilometer once every 16 days and in seven spectral bands from combined MODIS-AM and MISR data starting in 1998. The MODIS-AM sensor is an across-track imager with a swath width of 2330km, and a repeat rate shorter than 2 days (mostly shorter than 1 day). MISR is an along-track imager with a swath width of 364km using four fore-, four aft- and one nadir-pointing camera. The two-look repeat rate is 16 days. In this time, each sensor produces a string of observations across the viewing hemisphere with rather constant relative azimuth and solar zenith angles. The two strings from the two instruments are nearly orthogonal; their respective azimuthal distance from the principal plane varies with latitude and time of year, as does the mean solar zenith of the observations and the number of observations from MODIS.

The analysis was carried out for the Ambrals BRDF model that will be used in the production of the MODIS BRDF/albedo product. The kernel combinations used in that model are: RossThick-LiSparse, RossThin-LiSparse, RossThin-LiDense, and RossThick-LiDense (Wanner et al., 1995). These are capable of modelling a wide variety of volume and surface scattering behavior and which will be employed depending on the scattering behavior observed.

Retrievals investigated are for nadir-view reflectance and directional-hemispherical ("black-sky") albedo. Both of these quantities are studied for retrievals at the mean sun angle of the observations ("interpolation") and for nadir sun zenith angle ("extrapolation", the amount of extrapolation depending on the sun angle of observations, which depends on the latitude and the time of year of the observations). Additionally, bihemispherical albedo ("white-sky albedo") is studied.

MODIS and MISR sampling was simulated using the Xsatview software (Barnsley et al., 1994). The viewing and illumination geometries were constructed for 9 latitudes between 80 degrees south and 80 degrees north, and for 8 different 16-day time periods throughout the year.

3. Noise Sensitivity of the Ambrals Model

3.1. Method

The behavior of kernel-driven linear models under the conditions of limited and varying angular sampling can be studied analytically due to the mathematical form of these models. It is given by the the so-called "weights of determination", calculated using theory that originates with Gauss (Whittaker and Robinson, 1960). Kernel-driven models give the reflectance R in form of a sum, $R = \sum f_i k_i$, where f_i are the model

parameters and k_i are mathematical functions ("kernels") giving basic BRDF shapes depending only on sampling geometry.

The theory of least squares and related statistical analyses permit the derivation of unbiased estimates of model parameters and linear combinations of model parameters (such as reflectances at given angles and albedos for kernel-driven models). The techniques also directly provide estimates of the variance in these quantities. An overview of the relevant tools for analysis is provided below, but it is worth first considering the nature of "error" in this context. The theory used here and that used in most model inversions in the field of BRDF modelling is based on the assumption that the model is suitable for modelling the reflectance at some given location on the globe. Thus, if a model is "fitted" (in the sense of providing unbiased estimates of the model parameters) to a set of sample observations, then the model should be capable of predicting the reflectances (or derived quantities such as albedo-related terms) at viewing and illumination angles other than those sampled. The theory assumes that any deviation from a perfect fit in an over-constrained case (number of samples larger than number of model parameters) is due to error in observation. Related statistical theory tends to assume further that the variation in reflectance at each observation angle is normally distributed and of equal variance over the reflectance function (if the variance of the reflectance varies in some predictable way over the observation angles, this can be taken into account by weighting the observations). The "error" in a model fit term which is minimized in "fitting" the model, the root mean squared error (RMSE), provides an estimate of this variance in observation. Such fluctuations may indeed arise, due, for example, to uncertainty in atmospheric correction, registration or resampling. Some of these fluctuations may cause normally distributed variation in the data, and others, such as poor specification of the atmospheric intrinsic path radiance, may cause bias. The former is well-treated in the approach followed in this paper, and the latter may be taken into account in describing the additional expected error if an estimate of the bias is produced.

The key to understanding the behavior of kernel-driven linear models in the presence of random noise in the observed data under the conditions of limited and varying angular sampling is the variation of the so-called "weights of determination" of the model parameters, derived reflectances and derived albedo measures found from model inversion. These weights allow an estimation of the expected error in the terms under consideration, which can be expressed as (Whittaker and Robinson, 1960)

$$\epsilon_u = e\sqrt{\frac{1}{w_u}}, \tag{1}$$

where e is the estimate of standard error in the observed data (approximated by the RMSE in model fitting), and $1/w_u$ is the weight of determination of term u under the sampling configuration considered. The weight of determination is formed through

$$\frac{1}{w_u} = [U]^T[M^{-1}][U], \tag{2}$$

where U is a vector composed of the weighting of the kernels in some linear combination of the kernels which results in the term u under consideration, and M^{-1} is the inverse matrix providing the solution of the least-squares inversion problem for the linear model.

For example, to obtain the weight of determination of the parameter $f_0 = f_{iso}$ of a kernel-driven model, $[U]^T = (1, 0, 0)$. The weight of determination of directional-hemispherical reflectance at solar zenith angle θ_s is formed from $[U]^T = (1, \overline{k_1(\theta_s)}, \overline{k_2(\theta_s)})$, where $\overline{k_i}$ are the respective directional-hemispherical integrals of the kernels used. The weight of determination of bihemispherical reflectanc is formed from $[U]^T = (1, \overline{\overline{k_1}}, \overline{\overline{k_2}})$, where two bars tand for the respective bihemispherical integral. The weight of determination of the reflectance at some combination of viewing and illumination angles, $(\theta_v, \theta_s, \phi)$, is given by forming $[U]^T = (1, k_1(\theta_v, \theta_s, \phi), k_2(\theta_v, \theta_s, \phi))$.

The weight of determination depends on the sampling scheme under consideration because M^{-1} depends on it. The weight of determination also depends on the number of samples, N, and contains the factor $1/\sqrt{N}$.

Increasing N decreases the expected error because the errors are assumed to be randomly distributed at each observation angle. Thus, we can already begin to understand that factors such as cloud cover, which will reduce N from the maximum ideal number considered in this study to N', will tend to increase the expected error even if the angular distribution of samples remains roughly the same. The increase in each term under consideration is given by $\sqrt{N/N'}$.

Note that this analysis is independent of any specific BRDF function.

3.2. Results for the Ambrals Model

In an extensive investigation, we have studied the sensitivity to random noise of the several Ambrals BRDF model variants listed above using sampling for a variety of combinations of the MODIS and MISR sensors, and for different periods of data accumulation. Table 1 lists the weights of determination found for albedo and nadir view reflectance retrieval in interpolation and extrapolation for the different Ambrals model kernel combinations. Nearly all numbers are smaller than 1, indicating stability with respect to noise amplification in deriving the respective quality.

Table 2 investigates median error ranges (the ranges reflecting variations with kernel combination used; the median being with respect to latitude and day of year) for different sampling scenarios using MODIS and MISR on the EOS-AM-1 platform and MODIS on the PM platform. The MISR BRDF/albedo product, which will be produced using the BRDF model by Rahman et al. (1993), will be based on a 9-day sampling period, whereas the MODIS BRDF/albedo product will be built from data acquired during 16-day periods. Since the RossThick and LiDense kernels are least independent in their angular characteristics, the RossThick-LiDense kernel combination is most susceptible to noise of all combinations. Therefore, we list results separately for using this combination and for using those kernels separately along with the other kernel combinations. The lower part of the table lists relative changes in accuracy of the different sampling schemes as measured against the combined MODIS and MISR 16-day sampling.

Table 2 shows that albedo and nadir-view reflectance may be stably retrieved both in interpolation and extrapolation of the solar zenith angle. This is also true for 9-day MISR sampling, showing that MISR angular sampling is very suitable for these retrievals. Using MODIS alone introduces susceptibility to noise that is not desired. The MODIS-PM instrument is a partial, but not a full substitute for the MISR instrument, the advantage of MODIS-PM being, however, that it will feature the same 7 land-designated spectral bands as the MODIS-AM instrument, whereas MISR has only 4 bands.

Table 3 lists the worst-case ranges of the noise sensitivities found. "Worst-case" refers to the most unfavorable choice of kernel combination; the numbers given are the range numbers that include two thirds of the data for all latitudes and times of year.

Figure 1 shows the weights of determination found for the different retrievals when using the RossThick-LiSparse model, chosen as a typical example. Curves represent different days in the first half of the year. Panel (f) shows the error expected when extrapolating black-sky albedo in sun zenith angle for different latitudes and sampling in the first 16-day period of the year. One can see that extrapolation towards nadir is less problematic than extrapolation to large zenith angles for all latitudes, the beginning of the rise being determined by the sun zenith angle at which the observations were made.

Overall, the noise sensitivity of the Ambrals BRDF model with respect to BRDF and albedo retrieval at the sun zenith angles investigated is such that in the absence of clouds noise-like effects in the observations lead to a usually much smaller error in the derived quantities than was present in the reflectances. Under conditions where observations will be lost to clouds, the sensitivity will increase, but the noise inflation factor will still be mostly smaller than unity.

Figure 2 shows the noise sensitivity of the model parameters themselves (note that the isotropic parameter is identical with nadir-view, nadir-sun reflectance, shown in Figure 1). They are more susceptible to noise than the derived quantities due to possible tradeoffs between parameter values that do not affect, for example,

the value of albedo. This means that while albedo and reflectance retrievals are robust, interpretation of the model parameters themselves, desired with respect to correlating them with land cover types, is more problematic. See also the numbers in Tables 1, 2 and 3.

4. Noise Sensitivity of the modified RPV model

The noise sensitivity of the RPV BRDF model by Rahman et al. (1993) as modified by Martonchik (Engelsen et al., 1996) was also investigated for comparison and in order to reveal whether the properties found are related to the Ambrals model in particular or whether they might pertain to 3-parameter models in general.

The modified RPV model is not fully linear, making the analytical investigation of noise sensitivity along the lines of the Ambrals BRDF model impossible. However, an equivalent weight of determination may be constructed from the RMSE and the variation found in the derived quantity, albedo or reflectance. This was done by computing 250 realizations of noisy data for each of 5 magnitudes of noise up to 5 percent absolute of the reflectance (keeping the resulting reflectance is non-negative).

Due to the nonlinear nature of the modified RPV model, the analysis will also depend on land cover type and wave band. The analysis was carried out for the red and the near-infrared using four different data sets measured by Kimes (1983) and Kimes et al. (1985, 1986), namely BRDF observations of corn, a plowed field, a hardwood forest and a grass lawn. These represent four types of BRDFs, a broadleaf crop, a barren scene, a forested scene, and a grass-like land cover.

Table 4 gives ranges of the inferred equivalent weights of determination. Numbers are similar to those found for the Ambrals BRDF model, showing that both models do a good job in the stability of the retrievals with respect to random noise.

Figure 3 shows red and near-infrared weights of determinations as a function of latitude for a 16-day period beginning the first day of the year for the four land cover types used (solid and dotted lines). Also given is the result for the RossThick-LiSparse Ambrals model kernel combination (dashed line), showing that where one model has increased sensitivity to noise the other one does, too.

Figure 2 shows the sensitivity of the three modified RPV model parameters. The second and third parameters, the two describing BRDF shape, are extremely susceptible to noise. This does not translate to noisy retrievals of reflectance and albedo, but will make very difficult using and interpreting them directly. The cause of this sensitivity is probably internal redundancy in the way these parameters affect overall BRDF shape, perhaps caused by the hotspot term the model contains that allows tradeoffs between parameters under limited angular sampling. However, since the model retrieves albedo and reflectance very well, this does not constitute a major problem in terms of physical quantities to be retrieved.

A more detailed investigation is under way.

5. Conclusions

Retrievals of BRDF and albedo using the Ambrals BRDF model is stable against random noise-like variations in the reflectances used that may be due for example to fluctuations in surface properties, misregistration, atmospheric correction errors etc. This holds both for retrieval of BRDF and albedo at the mean sun angle of observation and for extrapolation of the retrieval to a nadir sun zenith angle. Where the Ambrals BRDF model shows increased susceptibility to noise, the modified RPV model does, as well, indicating that the source of the problem lies in the geometric distribution of angular samples available, not with the model. Generally, the modified RPV model is as capable of retrieving BRDF and albedo from MODIS and MISR sampling as the Ambrals BRDF model. The respective model parameters themselves are more noisy than the derived quantities BRDF and albedo for both models, but much more so for two of the three parameters of the modified RPV model. In terms of using different instruments for sampling, a combination

of MODIS and MISR leads to excellent retrievals in terms of noise sensitivity. Using MISR only is also feasible. Using MODIS alone may represent a problem due to the less favorable angular sampling properties of this instrument.

Acknowledgments
We thank Mike Barnsley and Kevin Morris for providing the Xsatview software for orbital modeling, without which this work would have been impossible. This work was partly supported by NASA under NAS5-31369.

References

Barnsley, M. J., A. H. Strahler, K. P. Morris, and J.-P. Muller, Sampling the surface bidirectional reflectance distribution function (BRDF): Evaluation of current and future satellite sensors, *Remote Sens. Rev. 8*, 271–311, 1994.

Engelsen, O., B. Pinty, M. M. Verstraete, and J. V. Martonchik, Parametric bidirectional reflectance factor models: evaluation, improvements and applications, *Report, Joint Research Centre of the European Commission, EU 16426,*, 114 pp., 1996.

Kimes, D. S., Dynamics of directional reflectance factor distribution for vegetation canopies, *Appl. Opt., 22(9)*, 1364–1372, 1983.

Kimes, D. S., W. W. Newcomb, C. J. Tucker, I. S. Zonneveldt, W. van Wijngaarden, J. de Leeuw, and G. F. Epema, Directional reflectance factor distributions for cover types of Northern Africa, *Remote Sens. Env., 18*, 1–19, 1985.

Kimes, D. S., W. W. Newcomb, R. F. Nelson, and J. B. Schutt, Directional reflectance distributions of a hardwood and a pine forest canopy, *IEEE Trans. Geosci. Remote Sens., 24*, 281–293, 1986.

Rahman, H., B. Pinty, and M. M. Verstraete, Coupled surface-atmosphere reflectance (CSAR) model, 2, Semiempirical surface model usable with NOAA advanced very high resolution radiometer data, *J. Geophys. Res., 98*, 20,791–20,801, 1993.

Strahler, W. Wanner, A. H., C. B. Schaaf, J.-P. Muller, M. J. Barnsley, R. d'Entremont, B. Hu, P. Lewis, X. Li, and E. V. Ruiz de Lope, MODIS BRDF/albedo product: Algorithm theoretical basis document, *NASA EOS-MODIS Doc.*, version 4.0, 1996.

Wanner, W., X. Li, and A. H. Strahler, On the derivation of kernels for kernel-driven models of bidirectional reflectance, *J. Geophys. Res., 100*, 21077–21090, 1995.

Wanner, W., A. H. Strahler, B. Hu, X. Li, C. L. Barker Schaaf, P. Lewis, J.-P. Muller, and M. J. Barnsley, Global retrieval of bidirectional reflectance and albedo over land from EOS MODIS and MISR data: theory and algorithm, *J. Geophys. Res.*, in press, 1997.

Whittaker, E., and G. Robinson, *The Calculus of Observations*, Blachie and Son, Glasgow, 397 pp., 1960.

Table 1: Weights of Determination for MODIS-AM/MISR 16-Day Sampling: Typical Small, Median and Large Error for Different Kernel-Driven BRDF Models

MODIS–AM+MISR 16-Day Sampling	kernel 1	kernel 2	low	median	high	low	median	high
			Nadir-View Reflectance			Black-Sky Albedo		
Interpolation	RossThin		0.17	0.21	0.24	0.14	0.17	0.19
$\theta_s = \langle\theta_s\rangle$	RossThick		0.17	0.18	0.21	0.12	0.16	0.17
	LiSparse		0.14	0.19	0.25	0.13	0.17	0.18
	LiDense		0.15	0.18	0.19	0.12	0.16	0.18
	RossThin	LiSparse	0.18	0.23	0.27	0.14	0.17	0.19
	RossThin	LiDense	0.17	0.22	0.24	0.15	0.18	0.20
	RossThick	LiSparse	0.18	0.23	0.28	0.13	0.17	0.18
	RossThick	LiDense	0.17	0.19	0.22	0.13	0.16	0.18
Extrapolation	RossThin		0.19	0.23	0.25	0.15	0.17	0.19
$\theta_s = 0$	RossThick		0.16	0.17	0.19	0.16	0.18	0.21
	LiSparse		0.38	0.44	0.53	0.16	0.18	0.28
	LiDense		0.48	0.62	0.71	0.18	0.21	0.28
	RossThin	LiSparse	0.38	0.45	0.55	0.16	0.18	0.33
	RossThin	LiDense	0.73	0.93	1.08	0.19	0.28	0.49
	RossThick	LiSparse	0.40	0.46	0.55	0.17	0.21	0.36
	RossThick	LiDense	1.03	1.35	1.71	0.39	0.52	0.63
						White-Sky Albedo		
Global, $\int \theta_s d\theta_s$	RossThin					0.14	0.31	0.64
	RossThick					0.14	0.18	0.34
	LiSparse					0.18	0.30	0.43
	LiDense					0.13	0.17	0.23
	RossThin	LiSparse				0.19	0.36	0.64
	RossThin	LiDense				0.21	0.42	0.82
	RossThick	LiSparse				0.19	0.34	0.58
	RossThick	LiDense				0.16	0.36	1.05
			Parameter f_{vol}			Parameter f_{geo}		
Parameters	RossThin		0.04	0.14	0.25			
	RossThick		0.32	0.89	1.74			
	LiSparse					0.18	0.27	0.31
	LiDense					0.34	0.46	0.57
	RossThin	LiSparse	0.05	0.15	0.30	0.19	0.28	0.36
	RossThin	LiDense	0.07	0.17	0.29	0.45	0.60	0.69
	RossThick	LiSparse	0.33	0.89	1.76	0.20	0.27	0.31
	RossThick	LiDense	0.62	1.86	4.14	0.60	0.86	1.34

Table 2: Median Weights of Determination for Different EOS Sensor Combinations: Smallest and Largest Median Error, and Percentage Deviation From MODIS-MISR Sampling

		MODIS-AM/ MISR 16–day	MISR 9–day	MODIS-AM 16–day	MISR 16–day	MODIS-AM/PM 16–day	MODIS-AM/ /PM/MISR 16–day
Models: All 3-Parameters Models							
Interpolation	Rnad	0.19–0.23	0.27–0.30	0.35–0.40	0.26–0.31	0.20–0.23	0.13–0.16
$\theta_s = \langle\theta_s\rangle$	bsa	0.16–0.18	0.21–0.25	0.32–0.55	0.21–0.21	0.18–0.29	0.11–0.14
Extrapolation	Rnad	0.45–1.35	0.61–2.00	1.17–6.61	0.58–1.49	0.67–3.50	0.36–1.11
$\theta_s = 0$	bsa	0.18–0.52	0.25–0.71	0.33–2.54	0.25–0.63	0.19–1.32	0.13–0.43
Global, $\int \theta_s d\theta_s$	wsa	0.34–0.42	0.42–0.56	0.99–1.60	0.34–0.42	0.55–0.95	0.27–0.38
Parameters	f_{vol}	0.15–1.86	0.22–2.45	0.39–7.23	0.16–1.84	0.23–4.20	0.12–1.65
	f_{geo}	0.27–0.86	0.37–1.22	0.68–4.56	0.28–0.88	0.39–2.43	0.22–0.77
Models: All 3-Parameter Models, with Ross-Thick/Li-Dense replaced by Ross-Thick and Li-Dense separately							
Interpolation	Rnad	0.18–0.23	0.25–0.30	0.30–0.40	0.23–0.31	0.17–0.23	0.12–0.16
$\theta_s = \langle\theta_s\rangle$	bsa	0.16–0.18	0.21–0.25	0.25–0.55	0.20–0.21	0.15–0.29	0.10–0.14
Extrapolation	Rnad	0.17–0.93	0.24–1.24	0.28–3.45	0.23–1.09	0.16–1.94	0.12–0.77
$\theta_s = 0$	bsa	0.18–0.28	0.25–0.37	0.29–0.82	0.24–0.36	0.17–0.45	0.12–0.23
Global, $\int \theta_s d\theta_s$	wsa	0.17–0.42	0.23–0.56	0.31–1.60	0.21–0.42	0.18–0.95	0.12–0.38
Parameters	f_{vol}	0.15–0.89	0.22–1.25	0.39–2.01	0.16–0.97	0.23–1.19	0.12–0.73
	f_{geo}	0.27–0.60	0.37–0.86	0.68–2.32	0.28–0.63	0.39–1.28	0.22–0.49
Models: All 3-Parameter Models, with Ross-Thick/Li-Dense replaced by Ross-Thick and Li-Dense separately							
Interpolation	Rnad	0, 0	+38, +30	+66, +73	+27, +34	−6, 0	−34, −31
$\theta_s = \langle\theta_s\rangle$	bsa	0, 0	+31, +38	+56, +205	+25, +16	−7, +61	−38, −23
Extrapolation	Rnad	0, 0	+41, +33	+64, +270	+35, +17	−6, +108	−30, −18
$\theta_s = 0$	bsa	0, 0	+38, +32	+61, +192	+33, +28	−6, +60	−34, −18
Global, $\int \theta_s d\theta_s$	wsa	0, 0	+35, +33	+82, +280	+23, 0	+5, +126	−30, −10
Parameters	f_{vol}	0, 0	+46, +40	+160, +125	+6, +8	+53, +33	−20, −18
	f_{geo}	0, 0	+37, +43	+151, +286	+3, +5	+44, +113	−19, −19

Rnad = reflectance at nadir view angle; bsa = black-sky albedo; wsa = white-sky albedo; f_{vol} = volume scattering kernel coefficient; f_{geo} = surface scattering kernel coefficient.

Table 3: Ranges of Weights of Determination for Different EOS Sensor Combinations: Smallest and Largest Error in the Worst Case, and Percentage Deviation From MODIS-MISR Sampling

		MODIS–AM + MISR 16–day	MISR 9–day	MODIS–AM 16–day	MISR 16–day	MODIS–AM+PM 16–day	MODIS–AM +PM+MISR 16–day
Models: All 3-Parameter Models							
Interpolation	Rnad	0.18–0.28	0.25–0.36	0.29–0.54	0.25–0.38	0.17–0.28	0.12–0.18
$\theta_s = \langle\theta_s\rangle$	bsa	0.15–0.20	0.20–0.29	0.40–0.72	0.17–0.24	0.23–0.41	0.12–0.15
Extrapolation	Rnad	1.03–1.71	1.45–2.41	2.95–9.59	1.12–2.23	1.61–5.44	0.90–1.51
$\theta_s = 0$	bsa	0.39–0.63	0.53–0.94	0.80–4.01	0.51–0.76	0.45–1.95	0.29–0.61
Global, $\int \theta_s d\theta_s$	wsa	0.21–1.05	0.28–1.47	0.76–2.90	0.24–1.74	0.47–1.43	0.17–0.81
Parameters	f_{vol}	0.62–4.14	0.87–5.83	2.97–13.07	0.68–7.11	1.63–6.60	0.52–3.10
	f_{geo}	0.60–1.34	0.87–1.84	2.01–7.07	0.62–1.88	1.18–3.56	0.56–1.06
Models: All 3-Parameter Models, with Ross-Thick/Li-Dense replaced by Ross-Thick and Li-Dense separately							
Interpolation	Rnad	0.18–0.28	0.25–0.36	0.29–0.44	0.25–0.38	0.17–0.25	0.12–0.18
$\theta_s = \langle\theta_s\rangle$	bsa	0.15–0.20	0.20–0.29	0.40–0.72	0.17–0.24	0.23–0.41	0.12–0.15
Extrapolation	Rnad	0.73–1.08	0.96–1.58	1.47–5.72	0.77–1.54	0.86–3.18	0.60–1.05
$\theta_s = 0$	bsa	0.19–0.49	0.25–0.66	0.30–2.54	0.26–0.57	0.17–1.47	0.13–0.43
Global, $\int \theta_s d\theta_s$	wsa	0.21–0.82	0.28–1.11	0.66–2.42	0.24–0.92	0.40–1.41	0.17–0.67
Parameters	f_{vol}	0.33–1.76	0.48–2.48	1.21–3.52	0.37–3.28	0.72–1.97	0.28–1.08
	f_{geo}	0.45–0.69	0.62–0.95	0.99–3.73	0.47–0.98	0.58–1.99	0.40–0.59
Models: All 3-Parameter Models, with Ross-Thick/Li-Dense replaced by Ross-Thick and Li-Dense separately							
Interpolation	Rnad	0, 0	+38, +28	+61, +57	+38, +35	−6, −11	−34, −36
$\theta_s = \langle\theta_s\rangle$	bsa	0, 0	+33, +44	+166, +259	+13, +19	+53, +104	−20, −26
Extrapolation	Rnad	0, 0	+31, +46	+101, +429	+5, +42	+17, +194	−18, −3
$\theta_s = 0$	bsa	0, 0	+31, +34	+57, +418	+36, +16	−11, +200	−32, −13
Global, $\int \theta_s d\theta_s$	wsa	0, 0	+33, +35	+214, +195	+14, +12	+90, +71	−20, −19
Parameters	f_{vol}	0, 0	+45, +40	+266, +100	+12, +86	+118, +11	−16, −39
	f_{geo}	0, 0	+37, +37	+119, +440	+4, +42	+28, +188	−12, −15

Rnad = reflectance at nadir view angle; bsa = black-sky albedo; wsa = white-sky albedo; f_{vol} = volume scattering kernel coefficient; f_{geo} = surface scattering kernel coefficient.

Table 4: Inferred Equivalent Weights of Determination for the modified RPV model: Smallest and Largest Median Error, and Smallest and Largest Error in the Worst Case

MODIS–AM/MISR 16-Day Sampling		Red Band median	Red Band worst-case range	NIR Band median	NIR Band worst-case range
Interpolation	Rnad	0.21–0.28	0.20–0.31	0.19–0.22	0.16–0.26
$\theta_s = \langle\theta_s\rangle$	bsa	0.08–0.16	0.14–0.18	0.04–0.06	0.05–0.09
Extrapolation	Rnad	0.32–0.49	0.38–0.76	0.31–0.49	0.38–0.76
$\theta_s = 0$	bsa	0.11–0.20	0.17–0.39	0.08–0.13	0.07–0.33
Global, $\int \theta_s d\theta_s$	wsa	0.19–0.23	0.16–0.49	0.17–0.19	0.10–0.36
Parameters	r_0	0.17–0.29	0.23–0.51	0.16–0.25	0.19–0.47
	k	1.70–9.86	4.37–15.25	0.89–1.41	0.98–2.00
	w_1	3.12–12.12	5.96–28.20	1.15–2.71	1.70–4.02
Land cover types (Kimes et al.): Corn, Lawn, Plowed Field, Hardwood Forest					

Rnad = reflectance at nadir view angle; bsa = black-sky albedo; wsa = white-sky albedo; r_0 = base reflectance coefficient; k = BRDF slope coefficient; w_1 = forward/backward scattering coefficient.

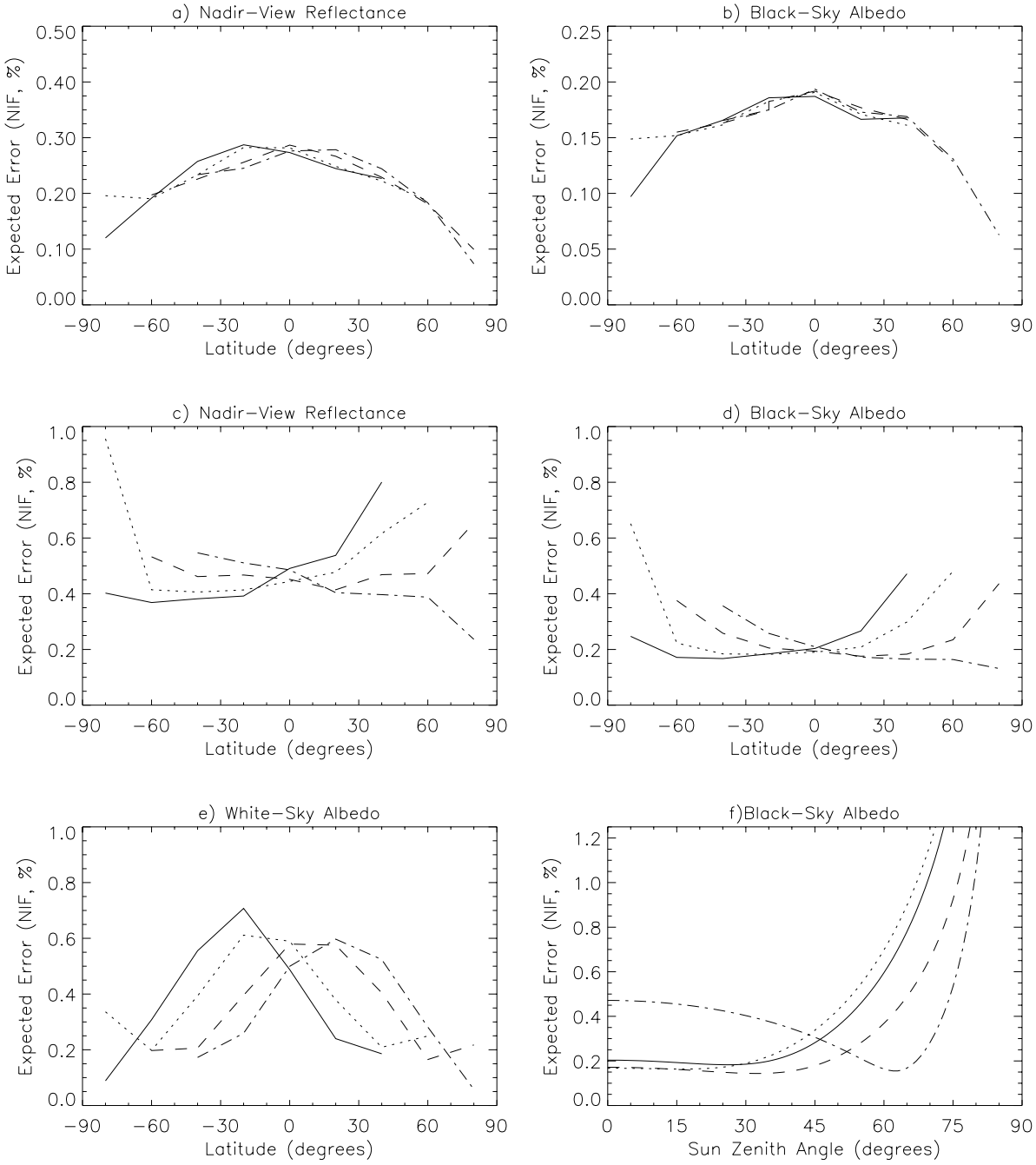

Figure 1: Noise sensitivity of the Ambrals BRDF model using the example of the RossThick-LiSparse kernel combination. Weights of determination ("Noise inflation factors", NIF) are shown as a function of latitude for different 16-day time periods throughout the first half of the year. Panel (f) shows the noise sensitivity of black-sky albedo extrapolation as a function of sun zenith angle for different latitudes and for sampling during the first 16-day period of the year.

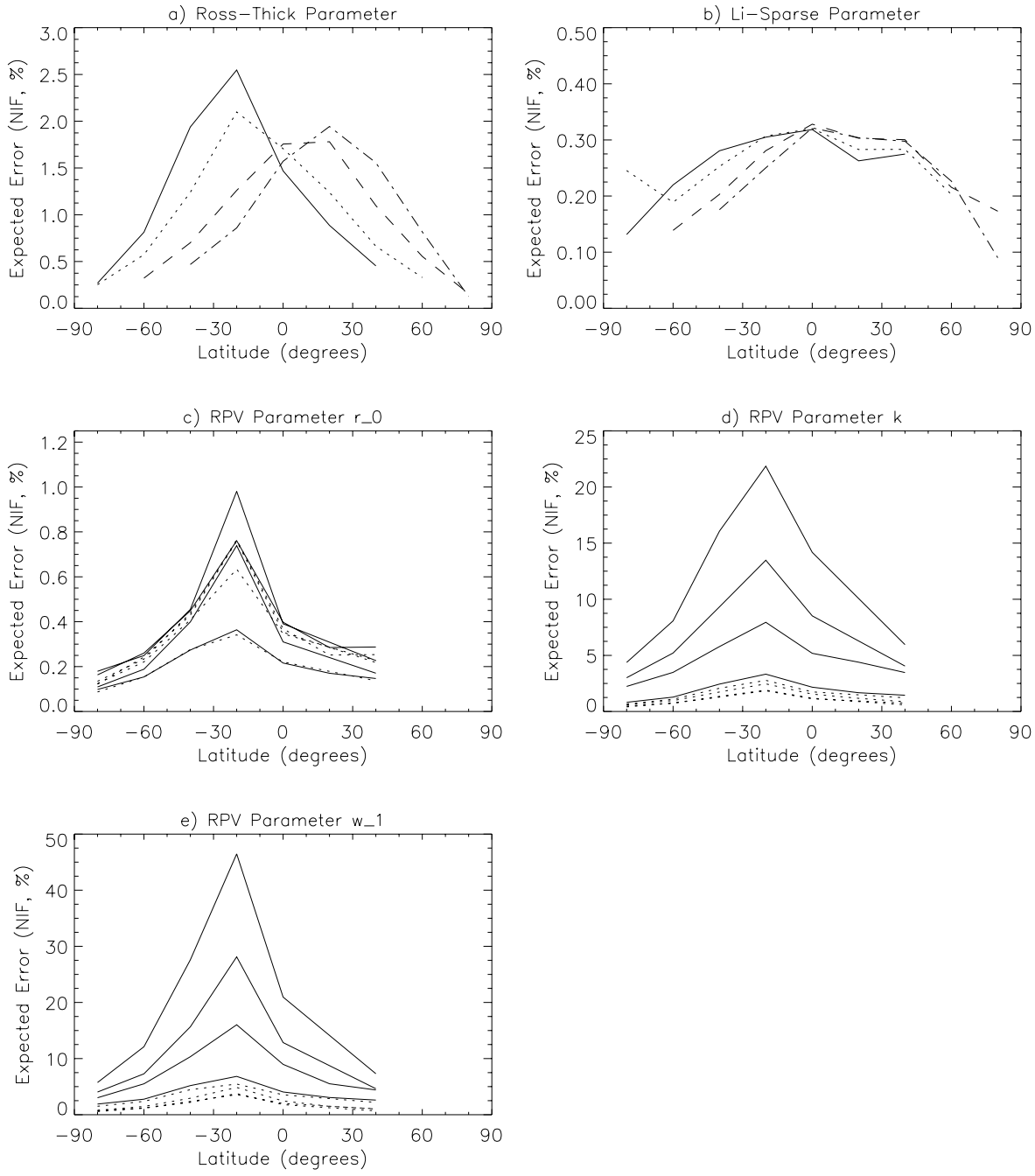

Figure 2: Noise sensitivity of the model parameters for the Ambrals BRDF model using the example of the RossThick-LiSparse kernel combination and the modified RPV BRDF model. Weights of determination ("Noise inflation factors", NIF) are shown as a function of latitude; for the Ambrals model they are shown for different 16-day time periods throughout the first half of the year, for the modified RPV model for sampling of the first of these 16-day periods and for the red and near-infrared band of four different land cover types (Ambrals model analysis is independent of band or land cover type due to the mathematical properties of kernel-driven models).

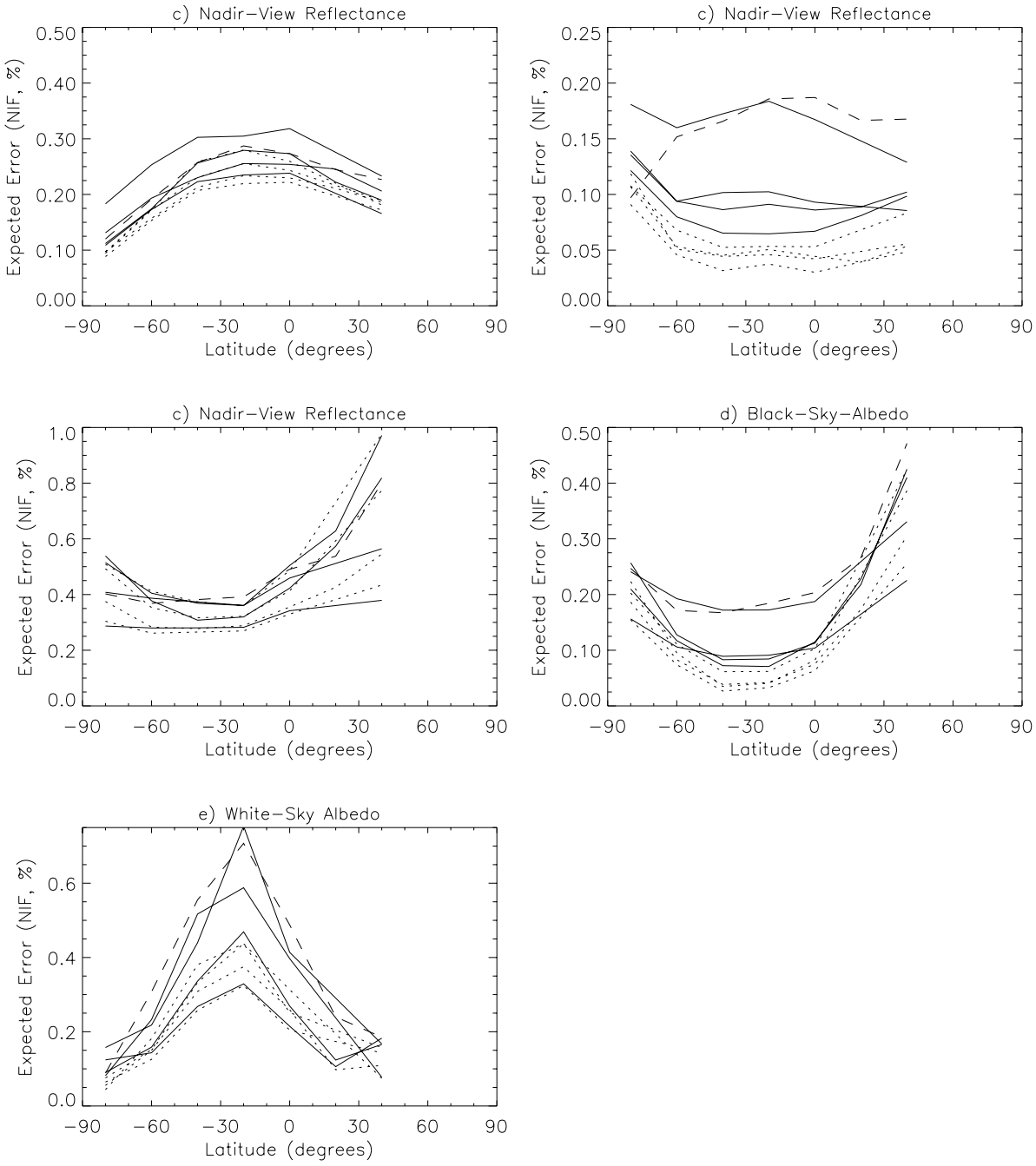

Figure 3: Noise sensitivity of the modified RPV BRDF model. Inferred equivalent weights of determination ("Noise inflation factors", NIF) are shown as a function of latitude for the first 16-day period of the year and for the red and near-infrared band of four different land cover types (solid and dotted lines). Also shown is are the weights of determination for the Ambrals BRDF models using the example of the RossThick-LiSparse kernel combination (dashed lines).

APPENDIX D:
THE SENSITIVITY OF ATMOSPHERIC CORRECTION OF REFLECTANCES TO THE SURFACE BRDF (PAPER BY HU, WANNER AND STRAHLER)

Draft manuscript (Nov. 96): to be revised

The Sensitivity of Atmospheric Correction of Reflectances to the Surface BRDF

Baoxin Hu, Wolfgang Wanner, and Alan H. Strahler

Center for Remote Sensing and Department of Geography, Boston University, Boston, MA

Abstract

This paper systematically studies the relationship between surface BRDF (Bidirectional Reflectance Distribution Function) retrieval and atmospheric correction. The study uses the atmospheric correction scheme of the Moderate Resolution Imaging Spectroradiometer (MODIS), and angular sampling expected for MODIS and MISR (Multiangle Imaging Spectro-Radiometer) for different land cover types and optical depths of aerosols. The results show the following two points. 1). Even for a non-turbid atmosphere, the assumption of a Lambertian surface in atmospheric correction causes large errors in the retrieved surface reflectances, such as from 1.7% to 7.6% in the red band. Thus, it is necessary to consider the surface anisotropic BRDF in atmospheric correction. 2). Surface BRDF retrieval and atmospheric correction can be coupled in a converging iteration loop, which improves the quality of atmospheric correction and of subsequent BRDF retrieval. For example, performing two steps of the iteration loop is already sufficient to obtain a mean error of only 0.89% in the retrieved surface reflectances for the atmosphere with the aerosol optical depth of 0.4 in the red band.

1. INTRODUCTION

In the solar spectrum, the signal received by a remote sensor doesn't reflect the true reflectance characteristics of surface objects, due to atmospheric effects. Thus, it is necessary to remove atmospheric effects in remote sensing applications.

Atmospheric effects on upward radiance for a cloudless sky can be computed as a solution to the atmospheric radiative transfer (RT) equation. The reflectance properties of surface objects provide a lower boundary condition for the RT equation. Most objects have anisotropic reflectances, which can be described by the bidirectional reflectance distribution function (BRDF). Generally, the RT equation is solved with a nonuniform and non-Lambertian boundary surface. The research of Case et al. (1953) indicated that decoupling the atmospheric RT from the transfer within surface objects is rigorously possible without the loss of accuracy, only if the boundary conditions for the atmospheric RT equation are appropriately specified. But the reflectance properties of the boundary surface can only be retrieved from the remotely sensed data after the removal of atmospheric effects. To resolve this interdependency between surface BRDF retrieval and atmospheric correction, most atmospheric correction methods assume that the surface is Lambertian. The atmospheric correction scheme of the MODIS (Moderate Resolution Imaging Spectroradiometer) couples atmospheric correction and surface BRDF retrieval by performing an iteration loop. In this scheme, atmospheric correction is first performed on MODIS observations under the assumption of an isotropic surface BRDF; the reflectances are then used to retrieve a new BRDF, and atmospheric correction is updated based on the new BRDF (Vermote et al., 1995).

In theory, this problem of specifying the correct boundary conditions at the atmosphere-surface interface is eliminated when a coupled system of atmosphere and the earth surface is considered for the RT analysis. A single radiative transfer model that includes radiative transfer in the atmosphere as well as at the Earth's surface is developed for a coupled system. But a coupled system is very complicated, and the discontinuity of the interface between the atmosphere and surface objects is handled in present coupled atmosphere-surface

RT equations as an area of multiple reflections between the atmosphere and any surface object (Myneni, et al., 1991; Liang et al., 1993). In addition, solving coupled RT equations requires many approximations and a large number of calculations (Asrar, 1989).

In this paper, we focus on atmospheric correction methods which decouple the atmospheric RT from the RT within surface objects. The important question for these atmospheric correction methods is whether it is necessary to take surface anisotropic reflectance properties into consideration in atmospheric correction, and if so, how to do it.

The research of Lee and Kaufman (1986) indicates that even for a nonturbid atmosphere, the assumption of a Lambertian surface leads to large errors in predicted upward radiance in the backscattering portion of the hemisphere, especially for large solar zenith angles. Their research is based on a savanna data set (Kriebel, 1977). Vermote et al. (1995) analyze the effect of surface anisotropic reflectances on atmospheric correction by using a Hapke model (Pinty et al, 1989). The model parameters are determined by fitting a field-measured directional reflectance data set of a plowed field (Kimes, 1985). Their results show that an adequate surface BRDF for use in atmospheric correction can be retrieved from the results of the atmospheric correction assuming a Lambertian surface. This iteration ultimately causes much smaller errors in the surface reflectances than the use of an atmospheric correction with the assumption of a Lambertian surface does. For example, the error is reduced from $10\% - 15\%$ to $2\% - 3\%$, when the aerosol optical depth is 0.23. We have conducted similar research using Ross-thick–Li-sparse model (Wanner et al., 1995) based on three simulated land cover types (tree-dominated, crop-dominated, and tree and crop half-mixed, respectively) and the angular sampling of MODIS/MISR over latitude 45^o north during a 9-day period around March 25 (Strahler et al., 1995). In our results, the assumption of an isotropic surface boundary in the atmospheric correction calculation leads to an error of about $2\% - 16\%$ in the retrieved surface reflectance in the red band for an atmosphere with aerosol optical depths at $550nm$ of 0.15, 0.3 and 0.5. A single iteration of a coupled surface BRDF retrieval and atmospheric correction iteration loop reduces the error to a range from 0.4% to 6.2%. All of this research indicate the necessity of taking surface BRDF into account in atmospheric correction. But this work is based on several specific cases with limited land cover types and angular samplings.

In this study, we systematically analyze the relationship between the surface BRDF retrieval and atmospheric correction by investigating the sensitivity of the retrieved surface reflectance to the input surface reflectance properties based on the atmospheric correction scheme of MODIS.

2. Theoretical Basis and Simulation data

In the atmospheric correction algorithm of MODIS (Vermote et al., 1995), the reflectance at the top of the atmosphere for the visible and near-infrared bands are expressed as

$$\begin{aligned}\rho_{toa}(\mu_s,\mu_v,\phi) &= \rho_0 + e^{-\tau/\mu_v}e^{-\tau/\mu_s}\rho_s(\mu_s,\mu_v,\phi) + e^{-\tau/\mu_v}t_d(\mu_s)\bar{\rho} + e^{-\tau/\mu_s}t_d(\mu_v)\bar{\rho}' \\ &\quad + t_d(\mu_s)t_d(\mu_v)\bar{\bar{\rho}} + \frac{(e^{-\tau/\mu_s}+t_d(\mu_s))(e^{-\tau/\mu_v}+t_d(\mu_v))S(\bar{\bar{\rho}})^2}{1-S\bar{\bar{\rho}}} \qquad (1)\end{aligned}$$

where ρ_{toa} is the reflectance at the top of the atmosphere; ρ_0 is the intrinsic atmospheric reflectance; ρ_s is the surface reflectance; S is the reflectance of the atmosphere for isotropic light entering the base of the atmosphere; μ_s is the cosine of the solar zenith angle, and μ_v is the cosine of the view zenith angle; ϕ is the azimuthal difference between the sun and view zenith angle; $e^{-\tau/\mu_s}$ and $t_d(\mu_s)$ are the downward direct and diffuse transmittance of the atmosphere along the path of the incoming solar beam, respectively; $e^{-\tau/\mu_v}$ and $t_d(\mu_v)$ are the upward direct and diffuse transmittance of the atmosphere in the viewing direction, respectively; τ is the atmospheric optical depth; $\bar{\rho}$, $\bar{\rho}'$, and $\bar{\bar{\rho}}$ are the surface hemispherical-directional, directional-hemispherical, and hemispherical-hemispherical reflectances, respectively, and couple

the atmospheric optical parameters and the surface reflectance properties. They are expressed in Equation (2-4).

$$\bar{\rho}(\mu_s, \mu_v, \phi) = \frac{\int_0^{2\pi}\int_0^1 \mu L\downarrow(\mu_s, \mu, \phi')\rho_s(\mu_s, \mu_v, \phi' - \phi)d\mu d\phi'}{\int_0^{2\pi}\int_0^1 \mu L\downarrow(\mu_s, \mu, \phi')d\mu d\phi'} \tag{2}$$

$$\bar{\rho}'(\mu_s, \mu_v, \phi) = \bar{\rho}(\mu_v, \mu_s, \phi) \tag{3}$$

$$\bar{\bar{\rho}} = \overline{\bar{\rho}'(\mu_s, \mu_v, \phi)} \approx \frac{\int_0^1\int_0^{2\pi}\int_0^1 \rho_s(\mu, \mu', \phi)\mu\mu' d\mu d\mu' d\phi}{\int_0^1\int_0^{2\pi}\int_0^1 \mu\mu' d\mu d\mu' d\phi} \tag{4}$$

where, $L\downarrow(\mu_s, \mu, \phi')$ is the downwelling diffuse irradiance with the sun at μ_s.

From these equations, we can note that, given atmospheric optical parameters and a series of surface reflectances estimated by other products or calculated by a BRDF model describing the bidirectional reflectances of the surface object, the coupled terms can be calculated and the atmospherically corrected surface reflectances can be obtained by solving Equation (1). Operationally, a BRDF model and the model parameters are first determined by the prior knowledge of surface objects or a prior product, and then these coupled terms are calculated. To give more weight to the actual observations than to the estimated surface BRDF used in the calculation of these coupled terms, equation (1) can be modified as follows:

$$\begin{aligned}\rho_{toa} &= \rho_0 + e^{-\tau/\mu_v}e^{-\tau/\mu_s}\rho_s + \rho_s[e^{-\tau/\mu_v}t_d(\mu_s)\bar{\rho^*} + e^{-\tau/\mu_s}t_d(\mu_v)\bar{\rho'^*} + t_d(\mu_s)t_d(\mu_v)\bar{\bar{\rho}^*} \\ &\quad + \rho_s\frac{(e^{-\tau/\mu_s} + t_d(\mu_s))(e^{-\tau/\mu_v} + t_d(\mu_v))S(\bar{\bar{\rho}^*})^2}{1 - S\bar{\bar{\rho}}}]\end{aligned} \tag{5}$$

$$\begin{aligned}\bar{\rho^*} &= \frac{\bar{\rho}}{{\rho_s}^m} \\ \bar{\rho'^*} &= \frac{\bar{\rho'}}{{\rho_s}^m}, \\ \bar{\bar{\rho}^*} &= \frac{\bar{\bar{\rho}}}{{\rho_s}^m}\end{aligned} \tag{6}$$

where, ${\rho_s}^m$ is a predicted surface reflectance, for example taken from a BRDF model. In this modified approach, only the shape of the surface BRDF influences the correction process and not the actual magnitude of the estimated surface BRDF. ρ_s can be obtained by solving equation (5).

When the surface is Lambertian, $\bar{\rho^*} = \bar{\rho^{*\prime}} = \bar{\bar{\rho}^*} = 1$ and $\bar{\bar{\rho}} = \rho_s$. Thus, equation (5) can be simplified as

$$\rho_{toa} = \rho_0 + \frac{(e^{-\tau/\mu_s} + t_d(\mu_s))(e^{-\tau/\mu_v} + t_d(\mu_v))\rho_s}{1 - S\rho_s} \tag{7}$$

So, under the assumption of a Lambertian surface, ρ_s can easily be calculated using equation (7).

We accomplished this study using 6S (Vermote et al., 1994). In its forward mode, 6S can calculate the reflectance at the top of the atmosphere at a given viewing and illumination geometry according to equation (1). 6S also performs atmospheric correction in its inverse mode. Here we use its atmospheric correction based on the assumption of a Lambertian surface according to equation (7). This method is called a Lambertian-based atmospheric correction. We have added an atmospheric correction method which considers the surface BRDF based on equation (5) and uses a BRDF model, Ambrals (Algorithm for Modis Bidirectional Reflectance Anisotropics of the Land Surface) (Strahler et al., 1996). This method is called BRDF-based atmospheric correction.

In this study, we use the forward mode of 6S to calculate simulated observation data (ρ_{toa}) of MODIS and MISR using equation (1). To make our simulation convincing, the following various conditions are used

in this research.

1). Angular sampling. We use the angular samplings of MODIS and MISR for geographic locations from latitude 60^o south (-60^o) to latitude 60^o north (+60^o) at intervals of 15^o during a 16-day period around March 12. These angular samplings provide a good coverage of the view angle hemisphere, and a range of sun zenith angle from 20^o to 60^o.

2). Surface cover types. Four typical land cover types are analyzed here. They are a plowed field, a hard wheat field with 11 percent of coverage, a grass lawn (vegetation coverage: 97%; LAI: 9.9) and a hardwood forest (Kimes et al., 1983, 1985, and 1986). Bidirectional reflectances at a given angular sampling are calculated by fitting Ambrals to these field-measured data sets and determining the model parameters for these land cover types in the red and near-infrared bands. The solid lines in Figure 1 and Figure 2 show the BRDF plots in the principal plane in the red and near-infrared bands, respectively. As can be seen, these BRDF shapes are typical of most land cover types. For example, in the red band, there is a strong hotspot in the surface BRDF of bare soil and the field with a sparse vegetation coverage, and an evident bowl shape and hotspot for the dense crop field, grass lawn, and forest.

3). Atmospheric conditions. The simulated atmospheric conditions are for a continental aerosol model and the aerosol optical depths at $550nm$ of 0.1, 0.2 and 0.4. Based on some measurement data of aerosol optical depths (Kaufman et al., 1994), an optical depth of about 0.1 is typical for semidesert areas (without dust outbreaks) and for land areas in high latitudes ($> 30^o$), and optical depths of about $0.2-0.3$ are typical for tropic forest area during the dry season. Also research on maximum aerosol optical depths derived from NOAA AVHRR global coverage data indicates that aerosol optical depths are often over 0.3, with the highest value of about 2.0 occurring over south America and Africa (Vermote et al., 1996).

To clearly show the atmospheric effects, we calculate and display the root mean square error (rmse) between the true surface reflectances (ρ_s) and those at the top of the atmosphere (ρ_{toa}) at every given angular sample in the top plots in Figure 3 and Figure 4. Figure 5 and Figure 6 show the plots of the reflectances in the principal plane in the red and near-infrared band, respectively, to display how atmospheric scattering affects the shape of the surface BRDF. As anticipated, 1). the errors are larger in the red band than in the near infrared band, because atmospheric scattering decreases as wavelength increases, and the effect of the path radiance of the atmosphere is larger in relative to the smaller reflectances of vegetated land covers in the red band than to their larger reflectances in the near infrared band; 2). the errors increase with the increasing of the optical depth of aerosols (even for the atmosphere with the aerosol optical depth of 0.1, the errors are still very large, ranging from 3.0% in the hard wheat field to 124% in the hardwood forest in the red band), and the shape of the surface BRDF at the top of the atmosphere is far different from that of the true one, due to the effect of atmospheric scattering. These results show that atmospheric effects on remotely sensed data should be removed in remote sensing applications where absolute surface reflectances are needed.

3. The sensitivity of the retrieved surface reflectance to the input surface reflection properties

From equation (5), one can see that the surface BRDF influences the atmospheric correction through the terms $\bar{\rho}^*$, $\bar{\rho'}^*$ and $\bar{\bar{\rho}}^*$. To obtain the relationship between atmospheric correction and the surface BRDF retrieval, we investigate the sensitivity of the retrieved surface reflectance to these ratios. Assuming that an error occurs separately and simultaneously in $\bar{\rho}^*$, $\bar{\rho'}^*$, and $\bar{\bar{\rho}}^*$ on the order of 1%, we can calculate the rmse caused in the retrieved surface reflectances for a given angular sampling. For different angular sampling and land cover types, the sensitivity of the retrieved surface reflectance to these ratios is different. The mean values and ranges based on all the various cases studied are shown in Figure 7 and Figure 8 for the red and near-infrared bands, respectively.

In Figure 7 and Figure 8, the x-axis shows the relative errors(%) in input $\bar{\rho^*}$, $\bar{\rho'^*}$, $\bar{\bar{\rho}}^*$ and all them combined; the y-axis shows the mean rmse (%) between the true surface reflectances and the retrieved values, caused by these errors. The error bars show the range of the rmse in various cases investigated (different land cover types and latitudes). From these plots, one can see that the sensitivity of the retrieved surface reflectance is nearly linear to any error occurring in $\bar{\rho^*}$, $\bar{\rho'^*}$ and $\bar{\bar{\rho}}^*$. The approximate slope degree is shown in Table 1 and Table 2 for the red and near-infrared bands, respectively. One can also see that the retrieved surface reflectance is more sensitive to $\bar{\rho^*}$ and $\bar{\rho'^*}$ than to $\bar{\bar{\rho}}^*$. This is because the contributions of the surface hemispherical-directional reflectance (relating to $\bar{\rho^*}$) and directional-hemispherical reflectance (relating to $\bar{\rho'^*}$) to the upward radiance are larger than that of the surface hemispherical-hemispherical reflectance (relating to $\bar{\bar{\rho}}^*$). And the retrieved surface reflectance is much more sensitive to all them combined than to one of them. For example, for an aerosol optical depth of 0.2 in the red band, when a 8% error occurs in $\bar{\rho^*}$, $\bar{\rho'^*}$, and $\bar{\bar{\rho}}^*$, the error caused in the retrieved surface reflectance is 1.17%, 1.18%, and 0.44%, respectively. But, when the error simultaneously occurs in them, the error caused in the retrieved surface reflectance is 2.71%. Finally, one can see that the sensitivity of the retrieved surface reflectance to these ratios is larger in the red band than in the near-infrared band and increases as the optical depth of aerosols increases, and that the error bars indicate that the sensitivity of the retrieved surface reflectance to these ratios varies with the land cover types and angular samplings.

In the following, we will analyze the relationship between the surface BRDF retrieval and atmospheric correction by considering these results and atmospheric correction methods.

3.1. Lambertian-based atmospheric correction

A Lambertian-based atmospheric correction assumes the surface is Lambertian, where $\bar{\rho^*}$, $\bar{\rho'^*}$ and $\bar{\bar{\rho}}^*$ equal 1. We calculate the rmse in $\bar{\rho^*}$, $\bar{\rho'^*}$ and $\bar{\bar{\rho}}^*$ caused by this assumption for a given angular sampling. Column IV of Table 1 and Table II shows the mean rmses of all cases here (different land cover types and altitudes) for $\bar{\rho^*}$, $\bar{\rho'^*}$ and $\bar{\bar{\rho}}^*$ and their ranges (in brackets). Referring to the degrees in slope, we can see that the errors in $\bar{\rho^*}$, $\bar{\rho'^*}$ and $\bar{\bar{\rho}}^*$ will lead to large errors in the retrieved surface reflectance, such as from 1.8% to 7.7% for the aerosol optical depth of 0.1 in the red band. These points can be demonstrated by carrying out a Lambertian-based atmospheric correction.

We performed a Lambertian-based atmospheric correction for the ρ_{toa} calculated above using the inverse mode of 6S according to equation (7). Table 3 shows the mean and range values of the rmse(%) between the true surface reflectances and the retrieved values from this Lambertian-based atmospheric correction for a given angular sampling, and for the various cases. As the table shows, even in a non-turbid atmosphere, the error in the retrieved surface reflectance is still very large. For example, when the aerosol optical depth is 0.1, the mean value of the error is 1.90% and its maximum is as high as 4.10% in the near-infrared band, and the error increases to the mean value of 3.21% with the maximum of 7.66% in the red band. Furthermore, as the aerosol optical depth increases from 0.1 to 0.4, the mean error increases from 3.21% to 7.46% in the red band, and from 1.90% to 5.02% in the near-infrared band. Finally, the large error range indicates that the error varies with land cover types and angular samplings (i.e. the BRDF shapes). This point can clearly be seen from the middle plots in Figure 3 and Figure 4. For different land cover types at different angular samplings, the BRDF shape is different. Thus the error caused by the assumption of a Lambertian surface is different. The farther away from isotropy the surface BRDF shapes are, the larger the error is. Among these land cover types, the plowed field has the strongest anisotropic reflectance characteristics, thus the error caused in the plowed field is largest. The differences in the error caused in the surface reflectance in different cases become larger with the increasing of the optical depths of aerosols.

To see how the Lambertian-based atmospheric correction affects the BRDF shape, we show the BRDF plots in the principal plane in Figure 1 and Figure 2, where those with the dotted lines are retrieved from the Lambertian-based atmospheric correction. From these plots, we can note that the Lambertian-based

atmospheric correction distorts the BRDF shapes and the largest errors occur at the hotspot and bowl edge area. But the BRDF shapes retrieved from the Lambertian-based atmospheric correction are indeed nearer to the true ones than an isotropic line.

Surface reflectances retrieved from atmospheric correction are usually used to invert a BRDF model and then retrieve some biophysical parameters of surface objects and calculate the surface albedo. So, we also calculate the rmses between the true model parameters and their retrieved values, and between the true surface albedo and its predicted value by the inverted BRDF model. The results are shown in Table 3.

From Table 3, we can see that the errors in the retrieved model parameters are very large, such as 13.58% for the aerosol optical depth of 0.1 in the red band. The albedo predicted by the retrieved BRDF model deviates from its true value by 0.03% to 4.88% in the red band for various cases (different latitudes, land cover types and aerosol optical depths), and by 0.21% to 4.61% in the near-infrared band.

From the above analysis of surface reflectances at given angular samples, BRDF model parameters and surface albedos, we can see that one should take the surface BRDF into account in atmospheric correction.

3.2. The coupled surface BRDF retrieval and atmospheric correction loop

The coupled surface BRDF retrieval and atmospheric correction iteration loop uses a surface BRDF in atmospheric correction as a lower boundary condition in the atmospheric correction. As in all iteration procedures, initial values of input surface reflectance properties are first determined, and then the iteration is performed and the estimated values are updated. The iteration is continually performed until a desirable result is obtained. Here, the initial values of $\bar{\rho}^*$, $\bar{\rho'}^*$ and $\bar{\bar{\rho}}^*$ are estimated from the results of a Lambertian-based atmospheric correction. So, the first iteration of the loop consists of using Ambrals to fit the reflectances retrieved from the Lambertian-based atmospheric correction to obtain model parameters. Based on these model parameters and the atmospheric optical parameters, the estimated $\bar{\rho}^*$, $\bar{\rho'}^*$ and $\bar{\bar{\rho}}^*$ can be calculated. Then BRDF-based atmospheric correction of ρ_{toa} is performed. From the previous calculations, we know, this Lambertian-based atmospheric correction leads to large errors in the model parameters (Table 3). However, the errors caused in $\bar{\rho}^*$, $\bar{\rho'}^*$ and $\bar{\bar{\rho}}^*$ by using these model parameters is acceptable.

Column V of Table 1 and Table 2 show the errors between the true $\bar{\rho}^*$, $\bar{\rho'}^*$ and $\bar{\bar{\rho}}^*$ and the estimated values from a Lambertian-based atmospheric correction. Compared with Column IV (the errors in $\bar{\rho}^*$, $\bar{\rho'}^*$ and $\bar{\bar{\rho}}^*$ caused by the assumption of a Lambertian surface in the Lambertian based atmospheric correction), the errors in Column V are smaller, thus causing smaller errors in the retrieved surface reflectance (referring to the slope degrees). But when the optical depth of aerosols is large, such as 0.4, the errors in the retrieved surface reflectance are still large, such as a mean value of about 2.50% in the red band (referring to the slope degrees).

The errors caused in the retrieved surface reflectances, BRDF model parameters and surface albedos after performing the first iteration are shown in Table 4. Compared with the errors caused by the Lambertian-based atmospheric correction in Table 3, the errors shown in Table 4 caused by the first iteration are much smaller. For example, in the red band, the mean error in the retrieved surface reflectance decreases from 3.21% – 7.46% to 0.49% – 2.64%. Also the ranges of these errors are smaller, which can be seen in the bottom plots in Figure 3 and Figure 4. This is because the surface reflectance properties used in the first iteration are nearer to the true ones than those used in Lambertian-based atmospheric correction, thus the difference in the extent to which the estimated BRDF shapes deviates from the the actual ones for different cases is decreased. After the first iteration, the surface BRDF shape in the principal plane is much nearer to the true one than it is after a Lambertian-based atmospheric correction. This is demonstrated in Figure 1 and Figure 2, where the dashed lines are the results after the first iteration.

From Table 4, one can also note that the errors are still large in the retrieved surface reflectances, such as over 2.00% in the red band in some cases when the aerosol optical depth is larger than 0.2. Therefore, we explored the effects of a second iteration in this procedure.

In this step, the Ambrals BRDF models are fitted to the surface reflectances retrieved from the first iteration. Because the errors in the model parameters inverted from the first iteration are much smaller than those from the Lambertian-based atmospheric correction, in this step the errors in $\bar{\rho}^*$, $\bar{\rho'}^*$ and $\bar{\bar{\rho}}^*$ calculated based on these model parameters should be smaller than those in the first iteration. Thus the errors caused in the retrieved surface reflectances are smaller than those occurring after the first iteration. This is demonstrated by the values in column VI of Table 1 and Table 2 , and Table 5. The mean errors in $\bar{\rho}^*$, $\bar{\rho'}^*$ and $\bar{\bar{\rho}}^*$ decrease from 4.08%, 4.02% and 6.99% in the first iteration to 1.45%, 1.46% and 2.39% in the second iteration, for an atmosphere with the aerosol optical depth of 0.4 in the red band. Correspondingly, the mean errors in the retrieved surface reflectances decrease from 2.64% to 0.90%. The errors caused in the model parameters and surface albedos also decrease. However, the error ranges in the retrieved surface reflectances tell us that for certain extreme cases (such as MODIS/MISR looks over 60^o north and south), the error of the retrieved surface reflectances of the plowed field is over 3.60% in the red band. Actually, depending on specific land cover types and the angular sampling, the iteration loop may need to be performed more than two times. Thus the convergency of the iteration loop should be considered.

Because of the complication of the algorithm, we can not obtain proofs mathematically. Thus, in this study, we iteratively perform the iteration loop several times for an aerosol optical depth of 0.4. For every step, we use Ambrals to fit the reflectances retrieved from the last step and do a BRDF-based atmospheric correction based on the inversion results. The rmse between the true surface reflectances and the retrieved values, and the relative change in the model parameters between the adjacent steps, decreases as more iterations are performed. After 5 iterations, the relative change in the model parameters decreases to 0.5% and the mean error in the retrieved surface reflectances decrease to near-infrared band than in the red band.

In summary, surface BRDF retrieval and atmospheric correction can be coupled in a converging iteration loop, which can improve the quality of atmospheric correction of reflectances.

4. DISCUSSION

4.1. The effect of skylight on atmospheric correction

From equation (2), we know the calculation of $\bar{\rho}$ requires knowledge of the downward radiation. Thus in a BRDF-based atmospheric correction, the exact distribution of skylight need to be known. Here we will investigate the assumption that the skylight is isotropic, so that we can save a large amount of calculation time. We use the model parameters retrieved from Lambertian-based atmospheric correction and assume the skylight is isotropic to calculate the estimated $\bar{\rho}^*$. Table 6 is the mean rmse and dynamic range between the estimated $\bar{\rho}^*$ and the true values. Compared with column V in Table 1 and Table 2 where the skylight is exactly calculated, the estimated error in $\bar{\rho}^*$ increases from $0.77\% - 5.66\%$ to $5.16\% - 16.02\%$ to the aerosol optical depth of 0.1 in the red band. Thus the corresponding error caused in the surface reflectances by the error in $\bar{\rho}^*$ increases from $0.08\% - 0.57\%$ to $0.52\% - 1.60\%$. Thus we should avoid the assumption of an isotropic skylight in atmospheric correction.

4.2. Comparison between the BRDF-based atmospheric correction using absolute surface BRDF and that using surface BRDF shape

Table 1 and Table 3 show the rmse between the true ratio of the surface albedo to its bidirectional reflectance, $\bar{\bar{\rho}}^*$, and the estimated ratio from the results of the Lambertian-based atmospheric correction, and that between the true surface albedo, $\bar{\bar{\rho}}$, and its estimated values from the results of the Lambertian-based atmospheric correction, respectively. From these results, we can note that the rmse in $\bar{\bar{\rho}}$ is smaller than that in $\bar{\bar{\rho}}^*$. Similarly, we also calculate the estimated errors in $\bar{\rho}$ and $\bar{\rho'}$ in the first iteration of the loop. The results are shown in Table 7. Compared with column V of Table 1, the errors in $\bar{\rho}$ and $\bar{\rho'}$ are

smaller than those in $\bar{\rho}^*$ and $\bar{\rho'}^*$. So a question remains, is the BRDF-based atmospheric correction based on Equation (7) better than that based on Equation (1)? To answer this question, we analyze the sensitivity of the retrieved surface reflectance to $\bar{\rho}$, $\bar{\rho'}$ and $\bar{\bar{\rho}}$ according to Equation (1) under the same simulation conditions as those in the above sensitivity analysis. Figure 7 shows the results in the red band. Comparing Figure 7 and Figure 5, one can see that the surface reflectance is more sensitive to $\bar{\rho}$, $\bar{\rho'}$ and $\bar{\bar{\rho}}$ than to $\bar{\rho}^*$, $\bar{\rho'}^*$ and $\bar{\bar{\rho}}^*$. Thus even though the estimated errors in $\bar{\rho}$, $\bar{\rho'}$ and $\bar{\bar{\rho}}$ are smaller than those in $\bar{\rho}^*$, $\bar{\rho'}^*$ and $\bar{\bar{\rho}}^*$, the error caused in the surface reflectances is larger by the errors in $\bar{\rho}$, $\bar{\rho'}$ and $\bar{\bar{\rho}}$ than by the errors in $\bar{\rho}^*$, $\bar{\rho'}^*$ and $\bar{\bar{\rho}}^*$. The BRDF-based atmospheric correction using the estimated surface BRDF shapes is better than that using absolute surface BRDF.

5. Conclusions

In this study, we analyze the sensitivity of atmospherically corrected reflectances to surface BRDF. Decoupling atmospheric correction and the surface anisotropic BRDF leads to large errors in the retrieved surface reflectances. In addition to atmospheric optical parameters, surface BRDF shape determines the size of the error, varying from 2.41% to 11.64% in the red band for the atmosphere with the aerosol optical depth of 0.2. The farther away from isotropy the BRDF shape is, the larger the error becomes. The surface BRDF retrieval and atmospheric correction can be coupled in a converging iteration loop. The initial values of surface reflectance properties are derived from the atmospheric correction with the assumption of a Lambertian surface. The accuracy of the estimated surface reflectance properties increases as more iterations are performed, thus the error in the retrieved surface reflectance decreases. However, one or two iterations are already sufficient to obtain a mean error of only 0.89% in the red band even with an atmospheric optical depth of 0.4.

As one notes, all the error values in this study are based on the assumption that the exact atmospheric optical parameters are known. This does not hold in actual applications. In the future, we will further analyze the effect of the uncertainty of atmospheric optical parameters on the sensitivity of atmospheric correction of reflectances to the surface BRDF.

We wish to thank Xiaowen Li, Crystal Schaaf, and other members of the MODIS BRDF/albedo team for their support and numerous discussions. This work was supported by NASA under NAS5-31369.

REFERENCES

Asrar, Ghassem, Theory and Applications of Optical Remote Sensing, A Wiley-Interscience Publication, 1989.

Case, R.M., F. de Hoffmane and G. Placzek, Introduction to the theory of neutron diffusion, vol.1, Los Alamos Scientific Laboratory, 1953.

Lee, T. Y. and Y. J. Kaufman, Non-Lambertian effects in remote sensing of surface reflectance and vegetation index, IEEE trans. Geosci. Remote Sens., 24, 699-708, 1986.

Liang S. and A. H. Strahler, Calculation of the angular radiation distribution for a coupled atmosphere and canopy, IEEE trans. Geosci. Remote Sens., 31, 491-502, 1993.

Kaufman Y. J., A. Gitelson, A. Karnieli, E. Ganor, R. S. Fraser, T. Nakajima, S. Mattoo, and B. N. Holben, Size distribution and scattering phase function of aerosol particles retrieved from sky brightness measurements, J. Geophys. Res., 100, 10341-10356, 1994.

Kimes, D. S., A. G. Kerber and P. J. Seller, Dynamics of directional reflectance factor distribution for vegetation canopies, Appl. Opt., 22(9), 1364-1372, 1983.

Kimes, D. S., W. W. Newcomb, C. J. Tucker, I. S. Zonneveldt, W. van Wijngaarden, J. de Leeuw, and G. F. Epema, Directional reflectance factor distributions for cover types of Northern Africa, Remote Sens. Environ 18, 1-19,1985.

Kimes, D. S., W. W. Newcomb, R. F. Nelson, and J. B. Schutt, Directional reflectance distributions of a hardwood and a pine forest canopy, IEEE Trans. Geosci. Remote Sens. GE-24, 281-293, 1986.

Kriebel, K. T., Measured spectral bidirectional reflection properties of four vegetated surfaces, Appl. Optics, 17(2), 352-259, 1978.

Myneni, R. B. and J. Ross, Photon-Vegetation Interactions", Springer- Verlag, 1991.

Pinty, B., Verstraete, M. M. and Dickinso, R. E., A physical model for predicting bidirectional reflectances over bare soil, Remote Sens. Env., 27, 273-288, 1989.

Strahler, A. H., Barnsley M. J., d'Entremont R., Hu B., Lewis P., Li X., Muller J., Schaaf, C. B., Wanner W. and Zhang B., MODIS BRDF/ Albedo Product: Algorithm Theoretical Basis Document Version 3.2, NASA EOS-MODIS, 1995.

Vermote, E. F., D. Tanre, Deuze, J. L. Herman, M. and Morcrette, J. J., Second Simulation of the Satellite Signal in the Solar Spectrum (6S), 6S User Guide Version 0, NASA-Goddard Space Flight Center-Code 923, Greenbelt, MD 20771, 1994.

Vermote, E. F., L. A. Remer, C. O. Justice, Y. J. Kaufman, and D. Tanre, Algorithm technical background Document: atmospheric correction algorithm, Modis Science Team and Associates, 1995.

Vermote, E. F., N. El Saleous, C. O. Justice, Y. J. Kaufman, J. L. Privette, L. Remer, J. C. Roger, and D. Tanre, Atmospheric correction of visible to middle infrared EOS-MODIS data over land surface: background, operational algorithm and validation, J. Geophys. Res., in press, 1996.

Wanner, W., X. Li, A. H. Strahler, On the derivation of kernels for kernel-driven models of bidirectional reflectance, J. Geophys. Res., 100, 21077-21089, 1995.

Table 1 The rmse(%) in $\bar{\rho^*}$, $\bar{\rho'^*}$ and $\bar{\bar{\rho}^*}$ in the red band

		slope degree	Lambertian assumption	BRDF(I)	BRDF (II)
$\bar{\rho^*}$	$\tau = 0.1$	0.10	$13.42(7.06 - 27.68)$	$2.09(0.77 - 5.66)$	$0.28(0.09 - 0.94)$
	$\tau = 0.2$	0.15	$12.35(6.31 - 26.86)$	$2.78(1.00 - 7.84)$	$0.62(0.17 - 1.95)$
	$\tau = 0.4$	0.20	$11.99(6.19 - 27.92)$	$4.08(1.51 - 11.82)$	$1.45(0.43 - 4.75)$
$\bar{\rho'^*}$	$\tau = 0.1$	0.10	$13.35(6.99 - 28.50)$	$1.85(0.62 - 5.97)$	$0.29(0.09 - 1.07)$
	$\tau = 0.2$	0.15	$12.10(6.00 - 26.83)$	$2.56(0.89 - 8.32)$	$0.60(0.18 - 2.28)$
	$\tau = 0.4$	0.20	$11.58(5.59 - 26.88)$	$4.02(1.51 - 12.13)$	$1.46(0.45 - 5.33)$
$\bar{\bar{\rho}^*}$	$\tau = 0.1$	0.03	$23.91(14.34 - 56.53)$	$2.95(1.11 - 8.24)$	$0.43(0.16 - 1.36)$
	$\tau = 0.2$	0.05	$23.91(14.34 - 56.53)$	$4.15(1.65 - 12.17)$	$0.92(0.35 - 3.03)$
	$\tau = 0.4$	0.12	$23.91(14.34 - 56.53)$	$6.99(2.84 - 19.02)$	$2.39(0.88 - 7.47)$

BRDF (I) and BRDF (II) represent the first and second iteration of the surface BRDF retrieval and atmospheric correction loop, respectively.

Table 2 The rmse(%) in $\bar{\rho^*}$, $\bar{\rho'^*}$ and $\bar{\bar{\rho}^*}$ in the near-infrared band

		slope degree	Lambertian assumption	BRDF(I)	BRDF (II)
$\bar{\rho^*}$	$\tau = 0.1$	0.06	$12.56(6.99 - 23.79)$	$1.11(0.51 - 2.92)$	$0.12(0.04 - 0.47)$
	$\tau = 0.2$	0.10	$11.92(6.57 - 23.71)$	$1.74(0.82 - 4.62)$	$0.28(0.11 - 1.32)$
	$\tau = 0.4$	0.16	$11.64(5.85 - 24.98)$	$2.69(1.24 - 7.72)$	$0.67(0.32 - 2.04)$
$\bar{\rho'^*}$	$\tau = 0.1$	0.06	$11.19(4.40 - 25.06)$	$0.91(0.32 - 3.31)$	$0.10(0.04 - 0.34)$
	$\tau = 0.2$	0.10	$10.34(4.25 - 24.23)$	$1.45(0.39 - 5.24)$	$0.25(0.09 - 0.90)$
	$\tau = 0.4$	0.16	$9.89(4.33 - 24.54)$	$2.56(0.85 - 8.42)$	$0.67(0.29 - 2.53)$
$\bar{\bar{\rho}^*}$	$\tau = 0.1$	0.03	$20.49(11.24 - 55.51)$	$1.64(0.64 - 4.63)$	$0.17(0.07 - 0.58)$
	$\tau = 0.2$	0.05	$20.49(11.24 - 55.51)$	$2.70(1.05 - 7.62)$	$0.45(0.19 - 1.70)$
	$\tau = 0.4$	0.10	$20.49(11.24 - 55.51)$	$4.45(1.26 - 12.90)$	$1.14(0.53 - 3.45)$

BRDF (I) and BRDF (II) represent the first and second iteration of the surface BRDF retrieval and atmospheric correction loop, respectively.

Table 3 The rmse(%) between the true BRDF, BRDF model parameters and surface albedo and their retrieved values from the Lambertian-based atmospheric correction

item	wavelength	$\tau = 0.1$	$\tau = 0.2$	$\tau = 0.4$
BRDF	red	3.21 (1.71-7.66)	4.73 (2.41-11.64)	7.46 (3.78-18.25)
	nir	1.90 (0.93-4.10)	3.05 (1.51-6.96)	5.02 (2.55-12.32)
model parameters	red	13.58 (10.40-22.48)	17.83 (10.87-30.01)	30.17 (24.85-41.67)
	nir	8.65 (5.82-10.83)	13.28 (9.51-19.96)	22.85 (16.74-31.44)
albedo	red	1.12 (0.03-2.95)	1.49 (0.10-3.43)	1.75 (0.20-4.88)
	nir	1.45 (0.21-2.55)	1.88 (0.41-3.01)	2.33 (0.10-4.62)

Table 4 The rmse(%) between the true BRDF, BRDF model parameters and surface albedo and their retrieved values from the first iteration of the coupled surface BRDF retrieval and atmospheric correction loop

item	wavelength	$\tau = 0.1$	$\tau = 0.2$	$\tau = 0.4$
BRDF	red	0.49 (0.16-1.85)	1.05 (0.32-3.92)	2.64 (0.84-9.08)
	nir	0.17 (0.09-0.60)	0.45 (0.26-1.34)	1.25 (0.56-1.64)
model parameters	red	1.66 (1.12-2.65)	3.69 (2.56-5.69)	9.72 (6.99-14.49)
	nir	0.74 (0.34-1.16)	1.87 (0.94-2.78)	5.17 (3.00-7.99)
albedo	red	0.36 (0.01-0.86)	0.68 (0.01-1.66)	1.33 (0.10-3.21)
	nir	0.15 (0.00-0.33)	0.32 (0.02-0.70)	0.70 (0.02-1.74)

Table 5 The rmse(%) between the true BRDF, BRDF model parameters and surface albedo and their retrieved values from the second iterations of the coupled surface BRDF retrieval and atmospheric correction loop

item	wavelength	$\tau = 0.1$	$\tau = 0.2$	$\tau = 0.4$
BRDF	red	0.07 (0.02-0.31)	0.23 (0.07-0.99)	0.90 (0.25-3.63)
	nir	0.02 (0.01-0.06)	0.07 (0.02-0.25)	0.34 (0.13-1.19)
model parameters	red	0.21 (0.11-0.46)	0.77 (0.43-1.14)	3.30 (1.96-8.11)
	nir	0.06 (0.02-0.14)	0.26 (0.10-0.40)	1.25 (0.56-2.22)
albedo	red	0.06 (0.01-0.15)	0.15 (0.01-0.43)	0.48 (0.01-1.35)
	nir	0.02 (0.00-0.03)	0.05 (0.00-0.11)	0.23 (0.01-0.88)

Table 6 The rmse(%) in $\bar{\rho}^*$ in the first iteration under the assumption of an isotropic skylight

wavelength	$\tau = 0.1$	$\tau = 0.2$	$\tau = 0.4$
red	9.22 (5.16-16.02)	8.54 (4.29-15.76)	7.20 (3.48-12.33)
nir	10.03 (3.49-17.60)	9.33 (2.61-16.28)	8.22 (2.03-5.64)

Table 7 The rmse(%) in $\bar{\rho}$ and $\bar{\rho'}$ in the red band in the first iteration of the coupled surface BRDF retrieval and atmospheric correction loop

	$\tau = 0.1$	$\tau = 0.2$	$\tau = 0.4$
$\bar{\rho}$	1.78 (0.80-4.56)	2.63 (1.28-5.17)	3.87 (2.15-8.10)
ρ'	1.71 (0.81-4.36)	2.47 (1.34-5.00)	3.77 (2.21-7.94)

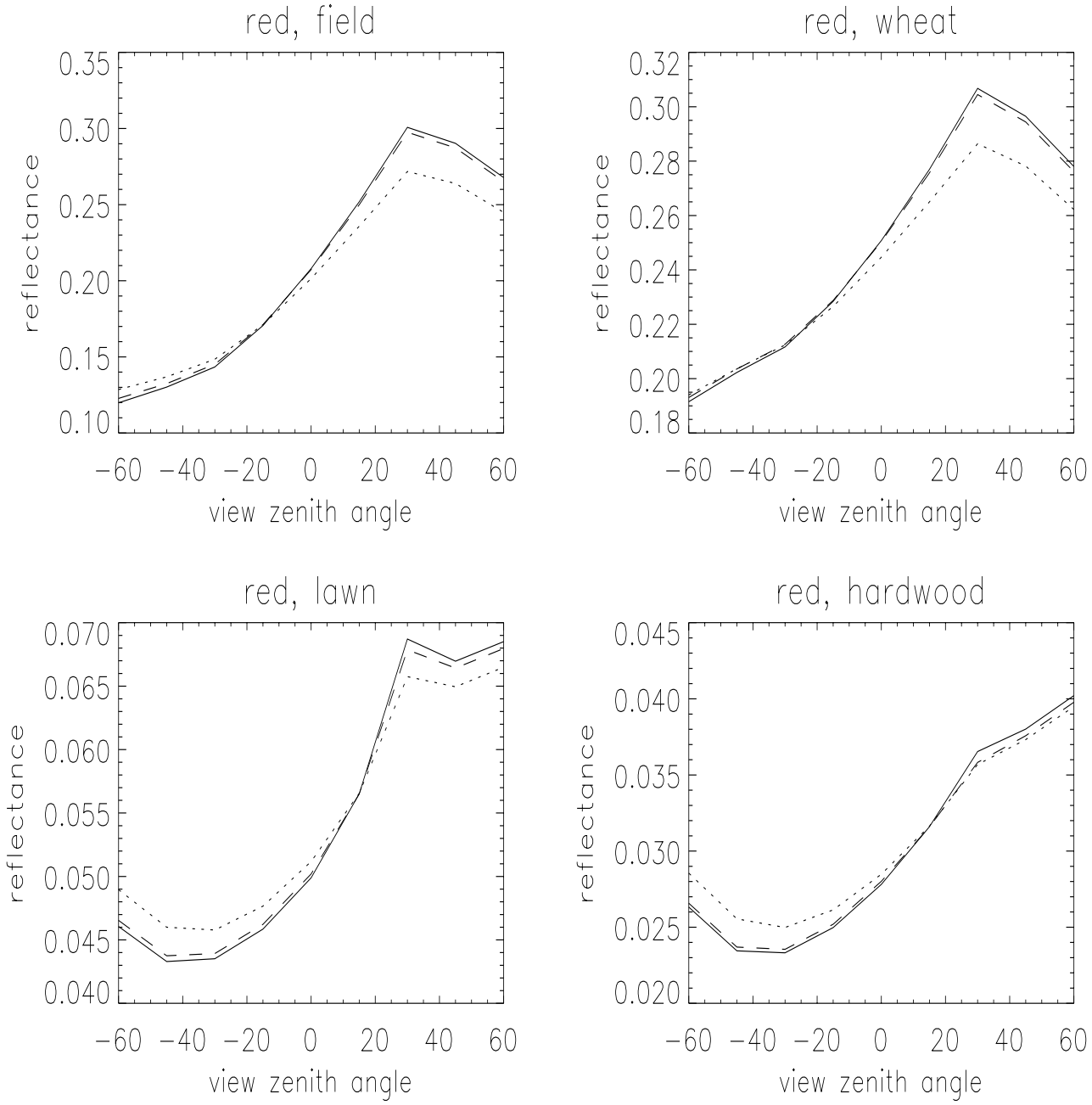

Fig. 1 The BRDF in the Principal Plane for selected Kimes data in the red band, where the sun zenith angle is 30^o and aerosol optical depth is 0.2. solid line: true value; dotted line: the retrieved values through Lambertian-based atmospheric correction; dashed: the retrieved values through the first step of the surface BRDF retrieval and atmospheric correction loop

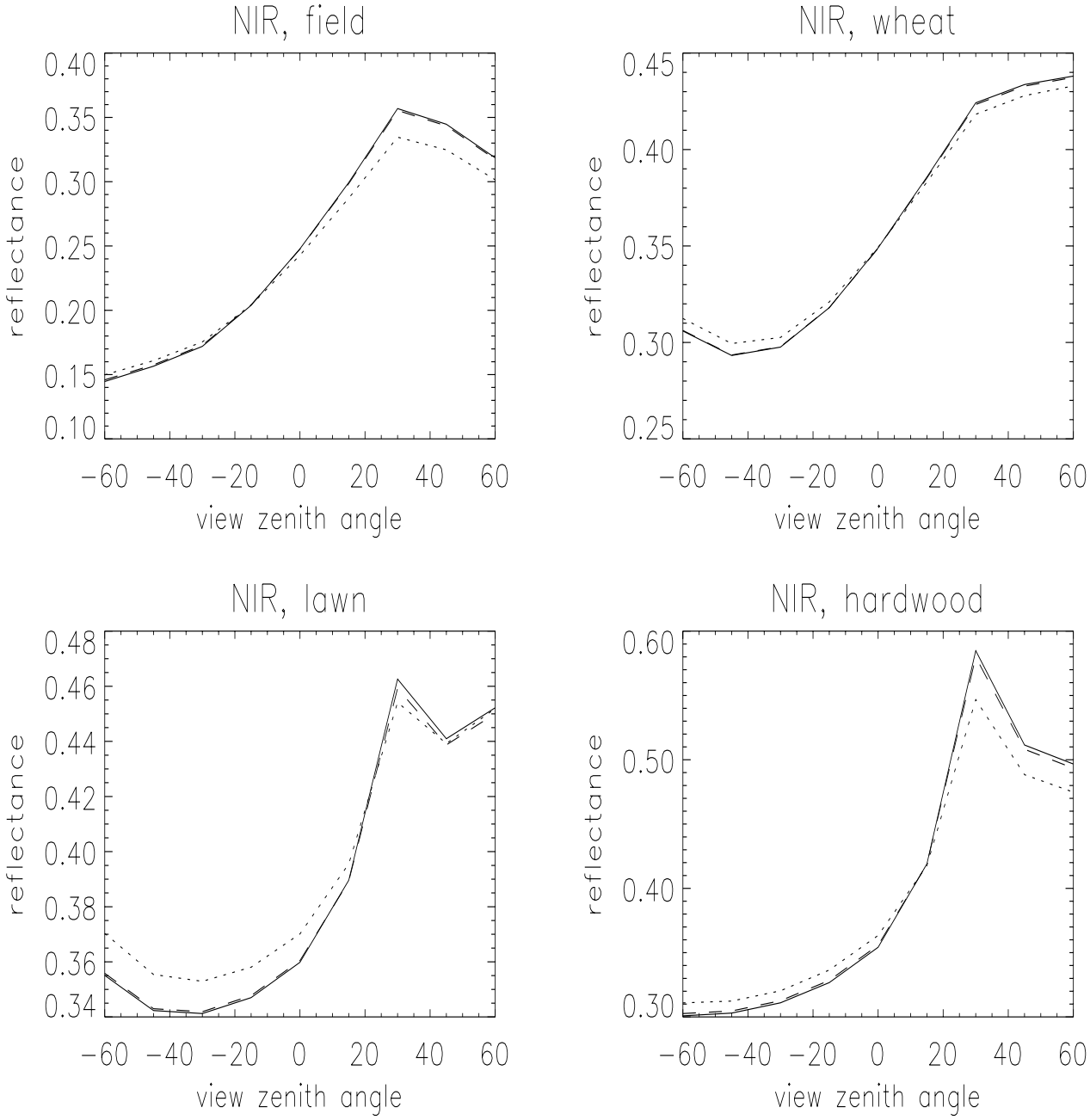

Fig. 2 The BRDF in the Principal Plane for selected Kimes data in the near-infrared band, where the sun zenith angle is 30^o and aerosol optical depth is 0.2. solid line: true value; dotted line: the retrieved values through Lambertian-based atmospheric correction; dashed: the retrieved values through the first step of the surface BRDF retrieval and atmospheric correction loop

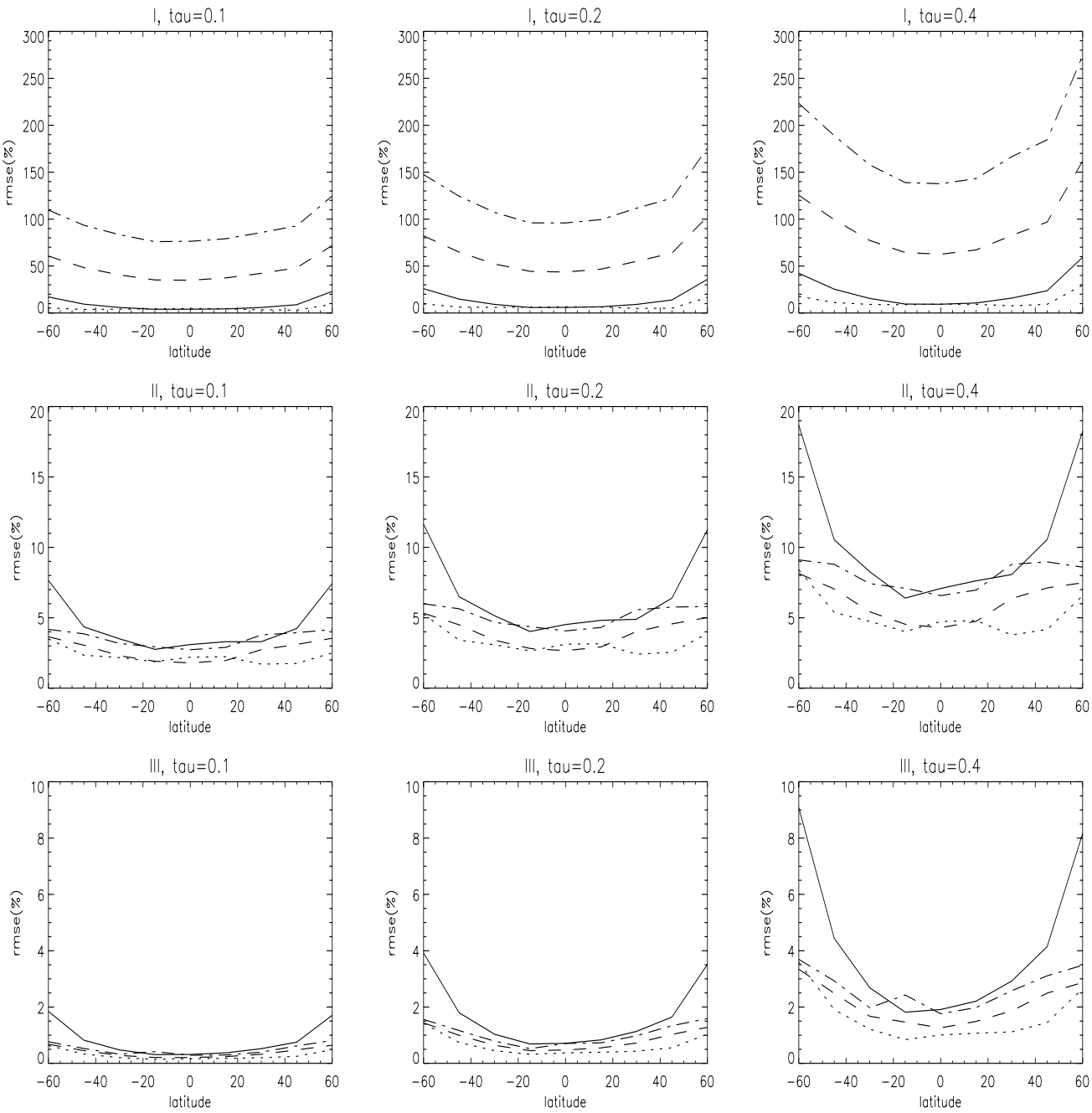

Fig. 3 The rmse between the retrieved surface reflectances and their true values in the red band. solid line: plowed field; dotted line: hard wheat; dashed line: grass lawn; dash-dotted line: hardwood. I, II and III denote the rmse between the true surface reflectances and the reflectances at the top of the atmosphere, the retrieved reflectances from Lambertian-based atmospheric correction, and the retrieved reflectances from the first step of the surface BRDF retrieval and atmospheric correction iteration loop, respectively.

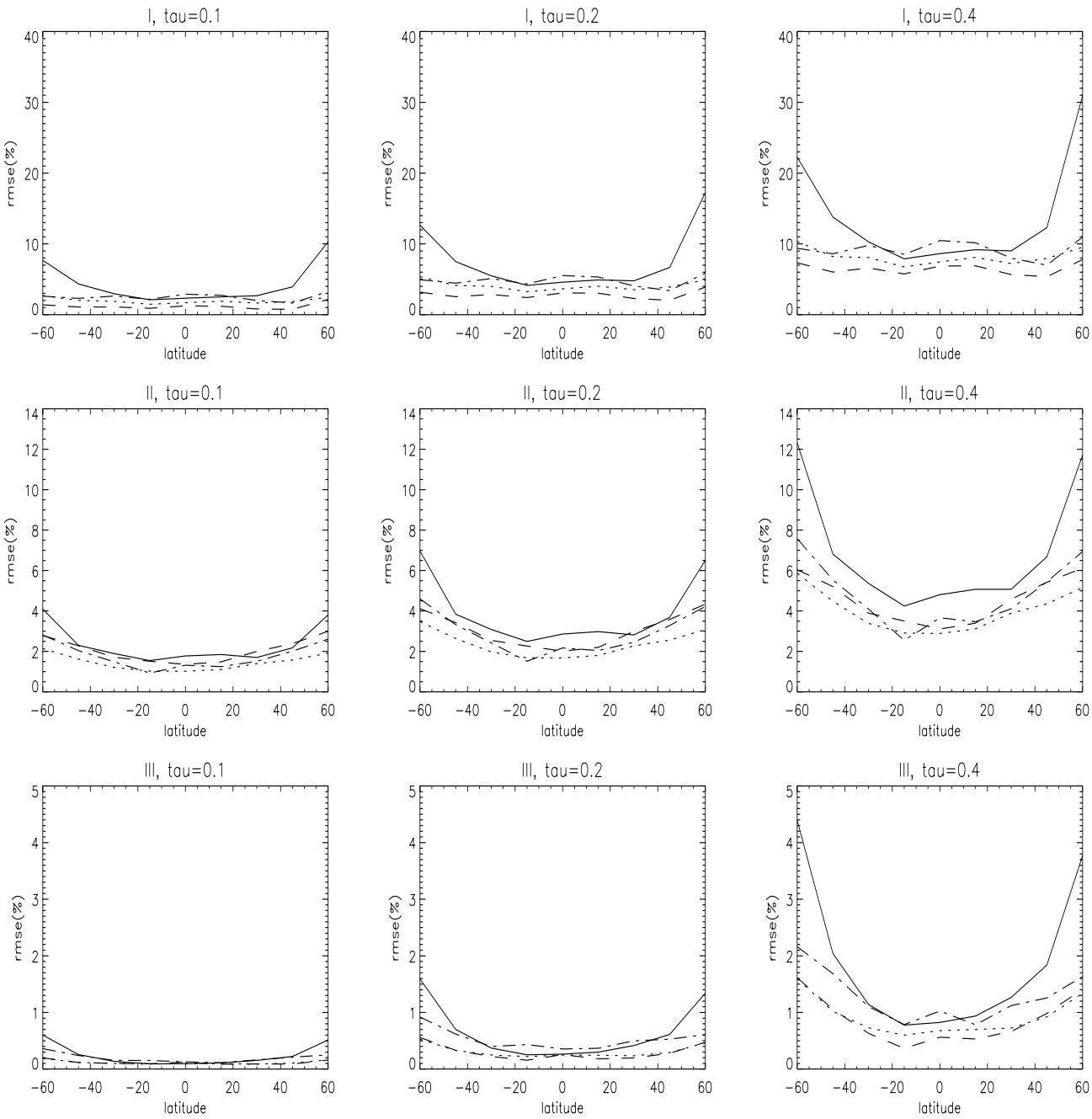

Fig. 4 The rmse between the retrieved surface reflectances and their true values in the near-infrared band. solid line: plowed field; dotted line: hard wheat; dashed line: grass lawn; dash-dotted line: hardwood. I, II and III denote the rmse between the true surface reflectances and the reflectances at the top of the atmosphere, the retrieved reflectances from Lambertian-based atmospheric correction, and the first step of the the surface BRDF retrieval and atmospheric correction iteration loop, respectively.

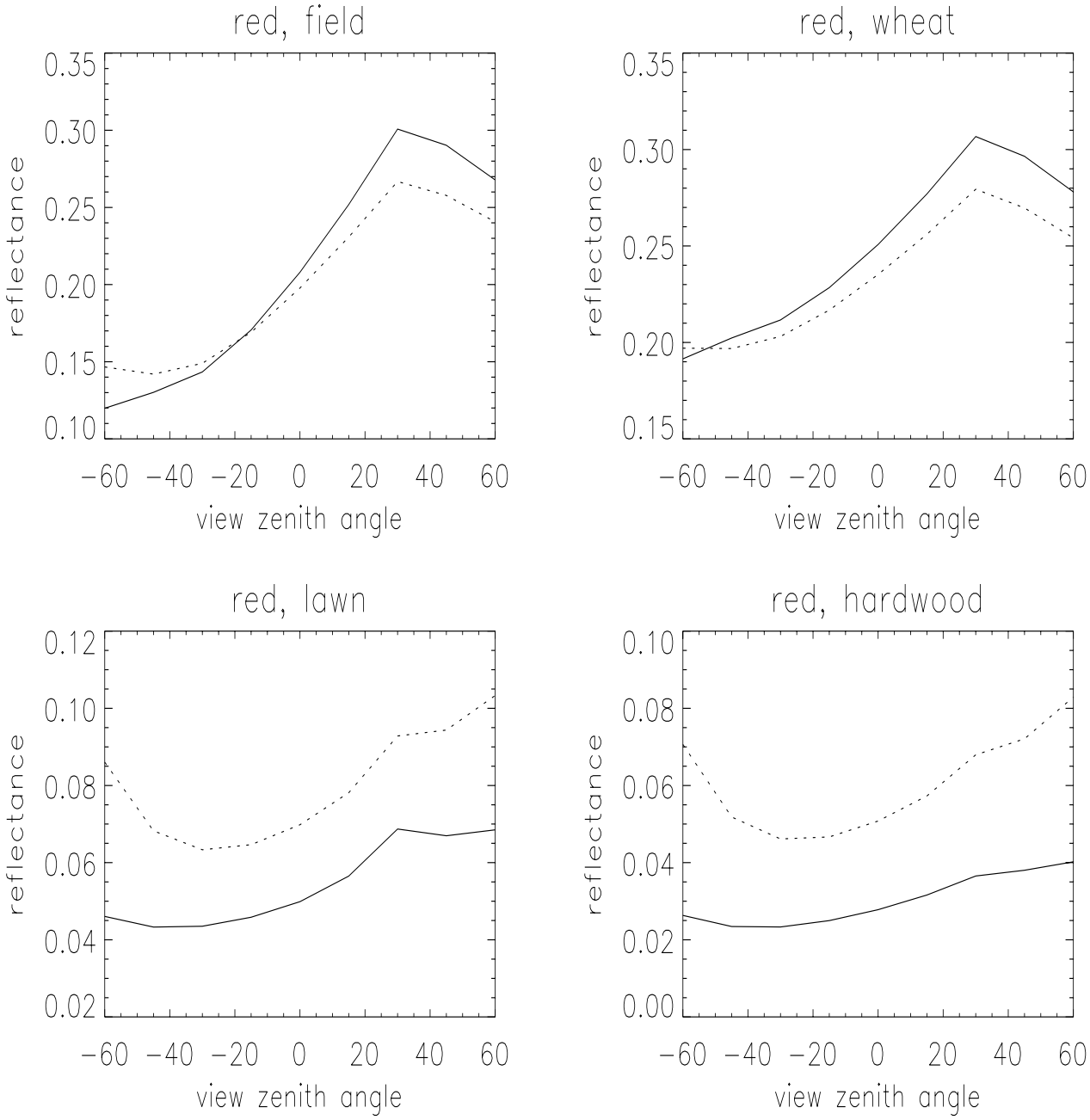

Fig. 5 The BRDF in the Principal Plane for selected Kimes data in the red band, where the sun zenith angle is 30^o and aerosol optical depth is 0.2. solid line: true value; dotted line: the value at the top of atmosphere.

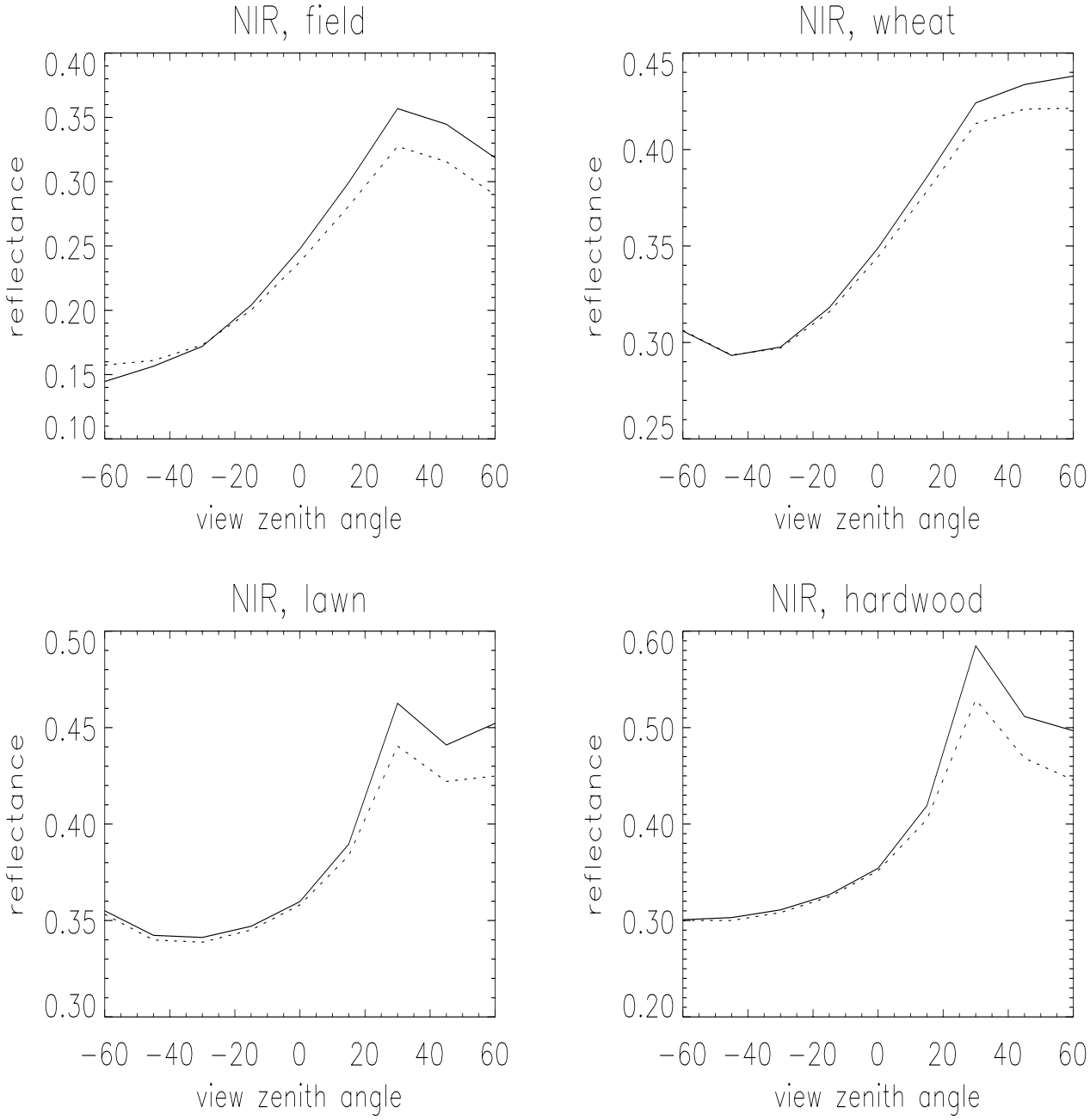

Fig. 6 The BRDF in the Principal Plane for selected Kimes data in the near-infrared band, where the sun zenith angle is 30^o and aerosol optical depth is 0.2. solid line: true value; dotted line: the value at the top of atmosphere.

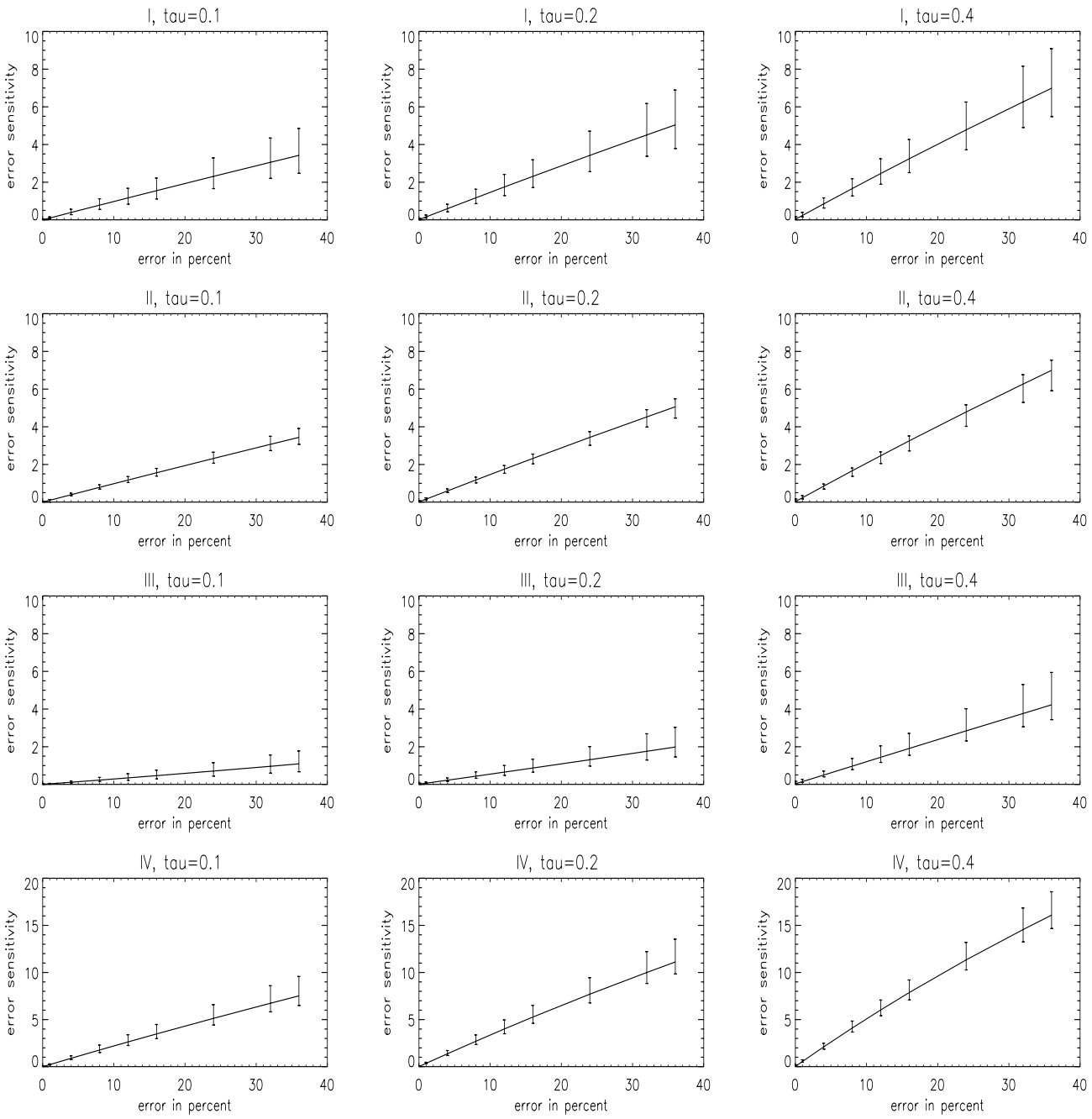

Fig. 7 The sensitivity of the retrieved surface reflectances to $\bar{\rho^*}$(I), $\bar{\rho'^*}$(II), $\bar{\bar{\rho}}^*$ (III) and all of them togather (IV) in the red band

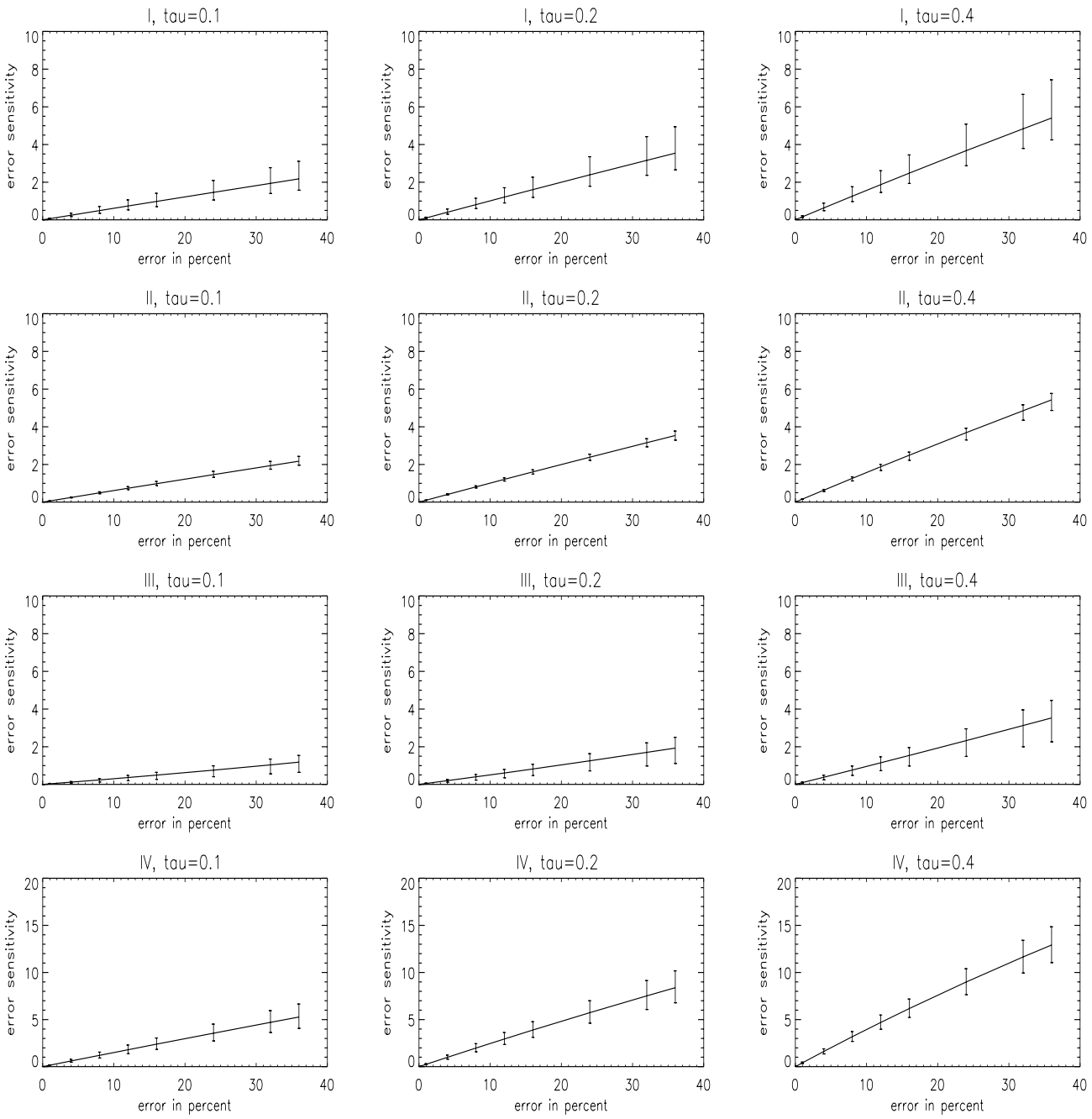

Fig. 8 The sensitivity of the retrieved surface reflectances to $\overline{\rho^*}$(I), $\overline{\rho'^*}$(II), $\overline{\overline{\rho^*}}$ (III), and all of them togather (IV) in the near infrared band

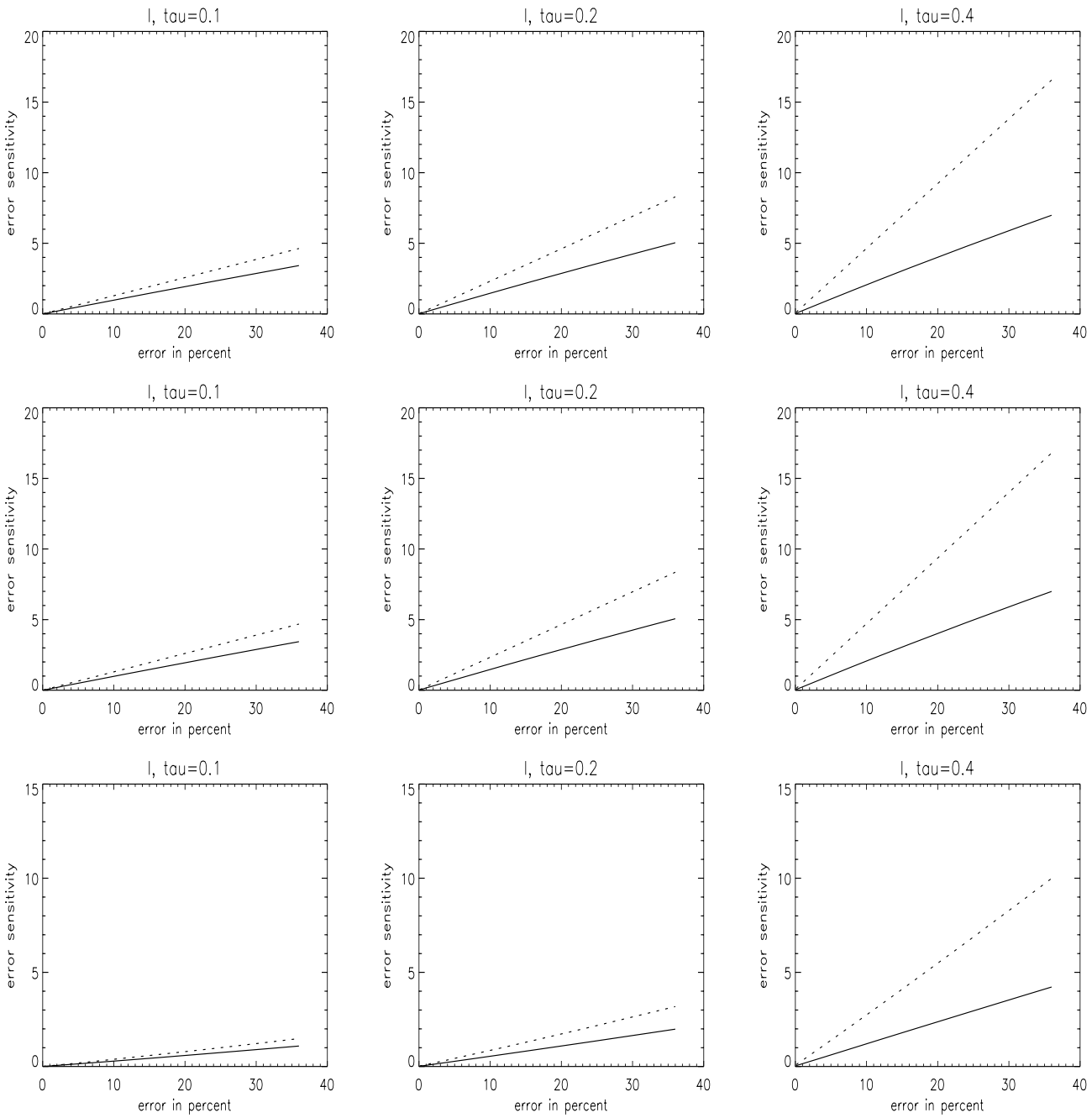

Fig. 9 The comparison between the sensitivity of the retrieved surface reflectances to $\overline{\rho}$(I), $\overline{\rho'}$(II), $\overline{\overline{\rho}}$ (III) (dashed lines) and the sensitivity of the retrieved surface reflectances to $\overline{\rho^*}$(I), $\overline{\rho'^*}$(II), $\overline{\overline{\rho^*}}$ (III) (solid lines) in the red band.

APPENDIX E:
GLOBAL RETRIEVAL OF BIDIRECTIONAL REFLECTANCE AND ALBEDO OVER LAND FROM EOS MODIS AND MISR DATA: THEORY AND ALGORITHM (PAPER BY WANNER ET AL., JGR, 1997)

Accepted for publication by JGR (1997) – will be revised slightly.

Global Retrieval of Bidirectional Reflectance and Albedo over Land From EOS MODIS and MISR Data: Theory and Algorithm

W. Wanner, A. H. Strahler, B. Hu
Department of Geography and Center for Remote Sensing, Boston University, Boston, Massachusetts.

P. Lewis
Remote Sensing Unit, University College London, London, UK.

J.-P. Muller
Department of Photogrammetry and Surveying, University College London, London, UK.

X. Li, C. L. Barker Schaaf
Department of Geography and Center for Remote Sensing, Boston University, Boston, Massachusetts.

M. J. Barnsley Department of Geography, University of Wales, Singleton Park, Swansea, SA2 8PP, UK.

Abstract

This paper describes the theory and the algorithm to be used in producing a global bidirectional reflectance distribution function (BRDF) and albedo product from data to be acquired by the moderate resolution imaging spectroradiometer (MODIS) and the multiangle imaging spectroradiometer (MISR), both to be launched in 1998 on the AM-1 satellite platform as part of NASA's Earth Observing System (EOS). The product will be derived using the kernel-driven semiempirical Ambrals BRDF model, utilizing five variants of kernel functions characterizing isotropic, volume and surface scattering. The BRDF and the albedo of each pixel of the land surface will be modeled at a spatial resolution of one kilometer and once every 16 days in seven spectral bands spanning the visible and the near-infrared. The BRDF parameters retrieved and recorded in the MODIS BRDF/albedo product will be intrinsic surface properties decoupled from the prevailing atmospheric state and hence suited for a wide range of applications requiring characterization of the directional anisotropy of earth surface reflectance. A set of quality control flags accompanies the product. An initial validation of the Ambrals model is demonstrated using a variety of field-measured data sets for several different land cover types.

1. Introduction

This paper reports on the status of the science and algorithms to be employed in the routine production of a global 1-km land surface bidirectional reflectance distribution function (BRDF) and albedo data product to be generated beginning in mid-1998. This product will be derived from the combined data of the moderate resolution imaging spectroradiometer (MODIS) [*Running et al.*, 1994] and the multiangle imaging spectroradiometer (MISR) [*Diner et al.*, 1991], two key sensors of NASA's Earth Observing System (EOS) on the AM-1 platform. Produced through the MODIS project, it will be available for use in atmospheric correction problems, earth radiation budget studies, and climate and climate change investigations. It will also allow some inference of land surface properties for use in global land cover classification and biophysical databases for vegetation modeling. Furthermore, it will be employed in the angular correction of MODIS and similar imagery.

Section 2 of this paper gives an overview of BRDF applications, with an emphasis on the coupling between the atmosphere and surface reflectance. In section 3, the MODIS BRDF/albedo product will be discussed with re-

spect to sensor characteristics and the Ambrals BRDF models to be used. Section 4 introduces the algorithm that was developed for the processing, explains the processing philosophy, and describes the product produced. Section 5 offers an outline of current model and planned product validation, and discusses the possible relationship of the BRDF model kernels used to land cover type. The paper closes with conclusions.

2. Multiangle Effects in Remote Sensing

2.1. Bidirectional Reflectance

The observation that the reflectance of most natural surfaces is anisotropic in nature is relevant to remote sensing because under such circumstances the reflectance of a surface depends both on the viewing and on the illumination angle. With natural scenes, this directional anisotropy is caused by the way in which shadows cast by an ensemble of objects such as plants, buildings or topographic slopes are hidden or emerge as a function of the observation angle, and by the intrinsic directionality of material in the scene, for example the leaves of the plants. Mathematically, it is described by the BRDF [*Nicodemus et al.*, 1977].

Variations of view angle across images and between images occur naturally due to a wide swath width (as for the advanced very high resolution radiometer (AVHRR) or MODIS) or to along-track off-nadir viewing capabilities (as for the along-track scanning radiometer, ATSR-2, or MISR). Variations in the solar angle are caused by variations in the time of day, season and latitude of observations, and are also determined by orbital characteristics of the satellite. Unless corrections for the BRDF are made, comparisons of surface reflectance observations across images from such instruments or between them are difficult or impossible. A simple example is given by the problem of mosaicking together AVHRR data from different orbits to obtain a composite image, where the orbital border will be visible due to the difference in the sun-view geometry in the two or several parts (see *Li et al.* [1996] for an illustration).

The need to take BRDF effects into account when conducting land surface studies, for example land cover classification, has increasingly been recognized [e.g., *Wu et al.*, 1994; *Cihlar et al.*, 1995; *Gutman*, 1994; *Moody and Strahler*, 1994]. It is known that current vegetation indices retain some angular effects due to the differences in the BRDF of different wavebands [e.g., *Wu et al.*, 1994]. It may even be desirable to standardize observations to angles where no observations were acquired, for example to nadir view and/or sun angle [*Leroy and Roujean*, 1994].

The BRDF may also be used to derive albedos, which are mathematically defined as weighted integrals (averages) of the BRDF. Surface albedos play an important role in global and regional climate since they determine the surface energy balance, for example the heat fluxes linked to evapotranspiration [*Kustas et al.*, 1989]. The BRDF and its integrals are also important for atmospheric correction in remote sensing [*Kaufman*, 1989], where errors of up to 10 percent or more may be made when BRDF effects are disregarded. We will discuss albedos and atmospheric correction in more detail further on. Recently there have also been indications that knowledge of the BRDF function can be valuable in cloud detection [*d'Entremont et al.*, 1995, 1996; see also *DiGirolamo and Davies*, 1994], opening up the possibility of improved cloud detection in the absence of thermal data.

Finally, the BRDF can be interpreted to infer land surface properties. Since the angular dependence of the reflectance is driven by the optical properties of the scattering medium and by its three-dimensional structure, one may attempt to retrieve the dominant parameters describing these properties from the observed BRDF functions.

Initially, such retrievals will be experimental, and the main focus of BRDF/albedo work will be on semiempirical descriptors of the BRDF that can be used for angle corrections and albedo calculations without requiring detailed physical modeling of the scene viewed. This is the path taken by the MODIS BRDF/albedo product. As more experience is accumulated, however, and as more computer power becomes available, more elaborate retrievals of physical parameters may be attempted [*Goel*, 1989; *Pinty and Verstraete*, 1991]. The MODIS land cover product [*Strahler et al.*, 1995b] will make use of reflectances corrected for angular effects but will also take into consideration the observed BRDF shape itself.

2.2. Surface BRDF-Atmosphere Coupling

Atmospheric correction algorithms for operational processing are commonly based on expressing the total transmittance of radiation from the top of the atmosphere to the ground as the sum of a direct and a diffuse component (see *Kaufman* [1989] for a general treatment of atmospheric correction in remote sensing). One then arrives at expressions such as the one suggested by Li [cf. *Strahler et al.*, 1995a], which is similar to the formulation to be used for MODIS atmospheric correction in the visible and near-infrared [see *Vermote et al.*, 1995, 1996]. We have:

$$\rho_{\mathrm{toa}} = \rho_{\mathrm{path}} + \frac{\mathbf{t}(\mu_s)\mathbf{R}\mathbf{t}(\mu_v) - e^{-\tau/\mu_s}|\mathbf{R}|e^{-\tau/\mu_v}}{1 - \overline{\overline{\rho_s}}\rho_a}, \quad (1)$$

where μ_s is the cosine of the solar zenith angle, μ_v that of the view zenith angle, ρ_{toa} the reflectance at the top of the atmosphere, ρ_{path} the reflectance due to path radiance, ρ_a the downward hemispherical reflectance of the atmosphere

for isotropic light entering at its base, $\rho_s(\mu_s, \mu_v, \phi)$ the directional surface reflectance (surface BRDF), with ϕ the relative azimuth between sun and view zenith (θ_s and θ_v), and τ the optical thickness; the vector $\mathbf{t}$ and matrix $\mathbf{R}$ are given by

$$\mathbf{t}(\mu) = \left[e^{-\tau/\mu}, t_d(\mu)\right], \tag{2}$$

and

$$\mathbf{R} = \begin{bmatrix} \rho_s & \rho_b(\mu_s) \\ \overline{\rho_s}(\mu_s; \mu_v, \phi) & \overline{\overline{\rho_s}} \end{bmatrix}. \tag{3}$$

In these expressions, t_d is the diffuse transmittance of the atmosphere, ρ_b is the directional-hemispherical integral ("black-sky albedo") of the BRDF,

$$\rho_b(\mu_s) = \frac{1}{\pi} \int_0^{2\pi} \int_0^{\pi/2} \rho_s \cos(\theta_v) \sin(\theta_v) d\theta_v d\phi, \tag{4}$$

$\overline{\rho_s}(\mu_s; \mu_v, \phi)$ is the diffuse irradiance that is directly scattered into the viewing direction (μ_v, ϕ) under illumination from μ_s,

$$\overline{\rho_s}(\mu_s; \mu_v, \phi) = \frac{\int_0^{2\pi} L_\downarrow(\mu_s; \mu, \phi') \rho_s(\mu, \mu_v, \phi' - \phi) \cos(\theta) d\theta d\phi'}{\int_0^{2\pi} L_\downarrow(\mu_s; \mu, \phi') \cos(\theta) d\theta d\phi'}, \tag{5}$$

with $L_\downarrow(\mu_s; \mu, \phi')$ the downwelling diffuse irradiance distribution with the sun at μ_s, and $\overline{\overline{\rho_s}}$ is the diffuse-to-diffuse reflectance under illumination from μ_s,

$$\overline{\overline{\rho_s}} = \frac{1}{\pi} \int_0^{\pi/2} \overline{\rho_s}(\mu_s; \mu, \phi) \cos(\theta) \sin(\theta) d\theta d\phi. \tag{6}$$

Note that $\mathbf{t}(\mu_s)$ and $\mathbf{t}(\mu_v)$ contain only atmospheric properties, namely the direct and diffuse parts of the transmittance, while $\mathbf{R}$ contains only surface reflectance properties, although partly under the prevailing conditions of diffuse illumination, which depend on the atmospheric condition. The determinant, $|\mathbf{R}|$, has the physical meaning of a correction term for using ρ_s in multiple bouncing between surface and atmosphere.

These equations clearly demonstrate the coupling between surface reflectance properties and atmospheric radiative transport. Given the atmospheric parameters, the BRDF ρ_s can be retrieved only if the integral reflectance expressions occurring are known, which in turn depend on the BRDF and the atmospheric state.

Approximations that can be made are to simplify the treatment of multiple scattering to be mainly based on the terms involving $t_d(\mu_s)t_d(\mu_v)$, or to approximate $\overline{\rho_s}$ by ρ_b. However, the error made can be significant under turbid conditions [*Lewis and Barnsley*, 1994]. Approximating $\overline{\overline{\rho_s}}$ by the bihemispherical integral of the BRDF (the "white-sky albedo" ρ_w, which is the normalized integral of $\rho_b(\theta_s)\cos(\theta_s)$ over the sun zenith) is less problematic, since the multi-bounce radiation between surface and atmosphere will tend to an isotropic distribution.

If a simultaneous, iterative retrieval of surface reflectance and the coupling integrals is not possible, approximate values will have to be used for the BRDF integrals. In practice, these may be taken from previous retrievals or estimated from the surface reflectance and ancillary data. In the past, the most commonly used assumption has been that the surface is Lambertian, which breaks the coupling but introduces a potentially important error, as is demonstrated in the next section.

2.3. Magnitude of BRDF Effects in Atmospheric Correction

Work by *Lee and Kaufman* [1986] showed that even in nonturbid conditions the assumption of a Lambertian surface leads to large errors in predicted upward radiance in the backscattering portion of the hemisphere (the situation is much more favorable in the forescattering direction), especially for large solar zenith angles (e.g., 60°). This study was conducted for a savanna data set [*Kriebel*, 1978]. In a more recent study, *Vermote et al.* [1995, 1996] performed atmospheric corrections of reflectance data that were obtained from a Hapke model [*Pinty et al.*, 1989] fitted to directional reflectances of a plowed field with the sun at 30° zenith angle [*Kimes*, 1985]. Corrections were carried out first using the assumption of a Lambertian surface, then repeated using the BRDF reconstructed from that "Lambertian" retrieval. In this manner a one-step iteration was carried out. The respective solutions were compared for three different optical depths. For a nonturbid atmosphere, $\tau = 0.01$, the Lambertian assumption does not lead to serious errors. For $\tau = 0.23$ the relative error is already about 10–15 percent at view zenith angles of $\pm 60°$, and less at smaller angles. The error of the solution after one iteration is reduced to about 3–4 percent. In a turbid situation, $\tau = 0.5$, the error made with the Lambertian assumption is large, about 30 percent at $+60°$ (forescattering), and 12 percent at $-60°$, with smaller errors at smaller view zenith angles. After the first iteration, this error is reduced to 20 percent and 5 percent, respectively. A second iteration, based on the BRDF from the first iteration, reduces the error to 14 percent and 1 percent, respectively.

We have conducted a similar study using a Ross-thick+Li-sparse kernel-driven BRDF model [*Wanner et al.*, 1995a]. Three different types of BRDF were investigated: strong volume scattering (a croplike canopy), strong geometric-optical scattering (a sparse woodland canopy), and an intermediate case. The atmospheric model used was a US standard atmosphere and continental aerosol, and the 6S atmospheric correction code was used [*Vermote et al.*, 1996]. Table 1 shows the ranges of RMS error, in per-

cent, that were observed for these cases for different optical depths, and when using a Lambertian assumption for atmospheric correction and when not, performing a one-step iteration. Results are given for the red and near-infrared wavebands, and for the surface BRDF and the bihemispherical integral of the BRDF (the white-sky albedo). In both cases, the errors which arise clearly increase with optical depth, but are noticeably smaller in the non-Lambertian case when compared to that using the Lambertian assumption. Employing an isotropic surface reflectance in atmospheric correction, errors in the surface reflectance between about 2 percent and 16 percent are made. A one-loop correction, however, reduces the errors to a range from 1 to 3 percent in all but the most turbid case, where the errors are also reduced considerably. The situation is similar with the bihemispherical reflectance. The error made is reduced by a significant factor if a one-step iteration loop is performed.

These results show clearly that errors of up to 10 percent, and at some angles and under turbid conditions more, occur if BRDF effects are not taken into account in atmospheric correction. The difference between the first and second iteration in the turbid case of the study of *Vermote at al.* [1995] illustrates that even using a BRDF that is only approximately correct can be improved upon noticeably by using a BRDF that is closer to the real anisotropy. The conclusion from all the studies is that it is worthwhile, even necessary, to use BRDF corrections in atmospheric correction, unless the conditions are not very turbid. It also is clear that the size of the error that remains depends on the accuracy of the BRDF used. However, an iteration in one or two steps leads to sufficiently accurate results, and should thus always to be carried out in operational atmospheric correction where BRDF information is available. Given the central importance of surface reflectance to most of the goals to be achieved in optical remote sensing, this implies that deriving a BRDF/albedo product is key to obtaining accurate results from remotely sensed optical data.

This brief review has focused on the specific case of the atmospheric correction problem. But by implication, similar effects are to be expected in principle for radiation budget studies and the radiation treatment in climate and weather models. Clearly, the anisotropic nature of the reflectance of the earth's surface plays a role in shaping the energy flux in the atmosphere close to the surface, and needs to be taken into consideration in any surface data retrieval or radiative tranfer modeling.

2.4. Albedo

Integrals of the BRDF play a role beyond that of atmospheric correction. Good accuracy of global albedo values is required for global and regional climate and climate change studies. *Zhang et al.* [1995] point out that over land the average shortwave reflectivity of clouds is only 1.5 times higher than that of the surface, making surface albedo an important influence. These authors go on to state that current uncertainty in land surface albedo is more important than current uncertainty in cloud albedo with respect to determining net surface shortwave fluxes. With respect to climate models, *Henderson-Sellers and Wilson* [1983] state that an absolute accuracy of 5 percent is required for a global albedo data set. The albedo values used by different climate models for identical regions still differ by several percent (see *Li and Garand* [1994] for an overview). *Gutman* [1994] addresses the problem that albedo over dark targets, like rainforests, is more problematic than over land covers with higher reflectivity, and that errors here can easily be 20 percent. *Sellers* [1993] cites a need for a 2 perdent absolute accuracy for global albedo in climate models. Thus, there is a longstanding need for highly accurate albedo data. To meet this need is a prime objective for remote sensing, one that has not been fully met up to date.

In attempts to bridge this gap, global albedo has been derived using a number of techniques utilizing radiation flux and budget assessments, but hitherto not from bidirectional reflectance distribution functions. *Zhang et al.* [1995] assume Lambertian reflectance in their study of surface and top-of-atmosphere radiative fluxes. The albedos used are based on a few land cover classes and wind speeds over oceans, and are given as a function of solar zenith angle and season. Dropping the Lambertian assumption will be the obvious next step in the development. A method also discussed by *Zhang et al.* [1995] is to use albedos derived from the earth radiation budget experiment (ERBE) to fit measurements at hand, depending on land cover type. *Li and Garand* [1994] investigate deriving surface albedo from top-of-atmosphere albedos in a clear sky situation, and find an accuracy of a few percent. They point out that bidirectional effects have not been given proper attention even though they are among the decisive factors in determining surface albedo from satellite measurements. These authors also use a Lambertian albedo for the land surface. The albedos of the International Satellite Land Surface Climatology Project (ISLSCP) data sets [*Sellers et al.*, 1994] are derived using a two-stream approximation. Problems with directional effects in AVHRR data in general and their influence on surface albedo estimates are discussed by *Gutman* [1994] and *Cihlar, Manak and Voisin* [1994].

As a consequence, current coarse land cover-based and radiation flux-derived albedo estimates will in future be replaced by albedo products derived from directional reflectance measurements utilizing BRDF models of the land surface, such as the MODIS BRDF/albedo product. These new products will also have the advantage of having much

finer spatial resolution than that of current data (2.5° × 2.5° for ERBE; 1° × 1° for the ISLSCP data base). This will allow not only a closer correlation of albedos with land cover classes, which is needed for parameterizations in the land surface schemes of climate models, but also quantifications of subgrid variability and derivation of better coarse-scale averages.

3. The MODIS BRDF/Albedo Product

3.1. Product Outline

The MODIS BRDF/albedo product will provide the full surface BRDF as well as black-sky (directional) and white-sky (diffuse) albedos, these albedos being intrinsic surface albedos. It will be produced from combining MODIS and MISR data, at a spatial resolution of 1 km, and over land only, globally. BDRF and albedos will be provided in 7 spectral bands ranging from 0.47 to 2.13μm (see *Running et al.* [1994]) and in three broadbands ranging from 0.3 to 0.7μm, from 0.7 to 3.0μm, and from 0.3 to 3.0μm. The product will be produced once every 16 days (the EOS-AM-1 platform and MISR 2-look repeat rate) and will be based on the semiempirical Ambrals BRDF model [*Wanner et al.*, 1995a; *Strahler et al.*, 1995a; *Lewis*, 1995]. Results from inverting the empirical modified Walthall BRDF model [*Walthall et al.*, 1985; *Nilson and Kuusk*, 1989] will also be recorded. A separate quarter-degree resolution product will be provided for global modeling purposes. This product will also carry information on subscale variability. Principal Investigators on the MODIS BRDF/albedo product are A. H. Strahler of Boston University and J.-P. Muller of University College London.

3.2. Angular Sampling from MODIS and MISR

Two key issues for a BRDF/albedo product are the angular sampling coverage available and the expected rate of loss of angular data due to cloud cover. Angular sampling is given by instrumental and orbital characteristics [*Barnsley et al.*, 1994]. The EOS-AM-1 platform carrying both MODIS and MISR will have a polar orbit with a 10:30 morning equatorial crossing time. The PM-1 platform, to be launched in the year 2000 with a second MODIS sensor, will have a 13:30 early afternoon crossing time. Data from this second MODIS will be included in the MODIS BRDF/albedo processing chain once it is available.

The MODIS sensor will image the earth's surface across-track with a swath width of 2330 km [*Running et al.*, 1994]. The viewing zenith angle will vary between ±55°, or about ±61° at the surface. The repeat cycle is two days at most, and less than one day at latitudes greater than about 30°. Orbital overlap thus makes it well suited for accumulating multiangle reflectance data over a period of time. Spatial resolution at nadir is 250 meters for the red and near infrared bands and 500 meters for the other land bands.

MISR will image along-track using nine separate push-broom cameras [*Diner et al.*, 1991]. Four of these are aft-looking, four fore-pointing, and one is nadir-viewing. Observations will be made in four spectral bands at visible and near infrared wavelengths that are similar to those of MODIS. The potential spatial resolution of MISR observations is 275 m, but data will be made available at a standard spatial resolution of 1.1 km. MISR's swath width is 364 km, allowing for a 9-day global repeat cycle, with the 2-repeat cycle being 16 (not 18) days at the equator.

Angular sampling sufficient for BRDF model inversions will be achieved by combining data from MODIS and MISR in the four corresponding spectral bands, and by accumulating data over a period of 16 days. In the absence of clouds, this leads to between 30 multiangular observations available at the equator, and about 55 observations at 60 degrees latitude, subject to variation with season. Using a coarse statistic of mean global cloud cover probability [*Wylie and Menzel*, 1989; *Wylie et al.*, 1994] as a function of latitude, one may predict that generally about 15 to 20 multiangular observations will be available at all latitudes except at the equator, where abundance of cloudy conditions is likely to create problems.

With this number of observations available on average, sufficient angular coverage for a BRDF model inversion is to be expected in most cases. Since MODIS scans across-track and MISR along-track, the respective views will generally represent different parts of the BRDF [*Barnsley et al*, 1994]. When one sensor views the cross-principal plane of the BRDF, the other views the principal plane, and vice versa. Figure 1 illustrates this, showing two typical cases for a particular latitude and time of year. With two sweeps across it, sampling of the viewing hemisphere is good in all cases. Sampling of the illumination hemisphere, however, is limited. Any one string of MISR data is acquired for only one solar zenith angle, while the MODIS observations display a small but valuable variation in that angle during the sampling period.

3.3. Kernel-Based Semiempirical BRDF Models

The MODIS BRDF/albedo product will be based on a semiempirical, kernel-based modeling approach introduced by *Roujean et al.* [1992] for top-down BRDF modeling. Mathematically, this type of model has the following form (here using two kernels and a constant):

$$R(\theta_i, \theta_v, \phi) = f_i + f_v k_v(\theta_i, \theta_v, \phi) + f_s k_s(\theta_i, \theta_v, \phi), \quad (7)$$

where R is the reflectance, k_v and k_s are kernel functions, and f are the weights of these functions (the model parameters). The kernels depend only on the viewing and illumination geometry. They describe basic BRDF shapes into which the full BRDF may be decomposed.

In this kernel-based BRDF model, the BRDF is given as a linear superposition of kernel shapes, which are chosen to represent different types of scattering with typical influences on the BRDF. In the above formulation, for example, k_v stands for volume scattering as described by radiative transfer theories, and k_s for surface scattering as derived from geometric-optical theories. The kernel that goes with the constant f_i is the isotropic Lambertian kernel, unity. Although the kernel functions used can be empirical (as in the Walthall model [*Walthall et al.*, 1985]), they are best derived from a physical theory through approximation, making the resulting model semiempirical. Mathematically, the weights f may be expressed in terms of physical properties of a scene, such as leaf area index, shape and height of trees, surface reflectance, etc. Through inversion, however, only the three quantities f are retrieved, providing the relative influence of the respective type of scattering on the directional signal observed, and allowing a rough characterization of the structural characteristics of the surface observed.

The kernel-based approach to BRDF modeling has been discussed and justified by *Roujean et al.* [1992] and *Wanner et al.* [1995a]. Depending on the scene, it may be understood in different ways. In a mixed scene composed of two areas with different BRDFs, for example a grassland-forest mixed pixel, the superposition represents the respective areal contributions of the mainly shadow-driven (geometric-optical) BRDF of the forest and the turbid medium-type BRDF of the grassland. Adjacency effects are neglected, which is admissible unless the mosaic is very fine or the zenith angle very large. But even in a homogeneous scene, volume and surface scattering may still be both present. For example, in a forest canopy the geometric scattering is given by the inter-crown gaps, whereas the volume scattering is given by the gaps between the leaves. The superposition then describes first and second-order scattering, while neglecting the coupling of the two. From a practical standpoint, it is perhaps most accurate to say that the BRDF observed is decomposed into the two components represented by the two basic types of scattering. Volume and surface scattering produce BRDF functions that are semi-orthogonal due to an increase in reflectance with zenith angle in the former and a decrease in the latter case.

Kernel-driven models have been proven successful in application to AVHRR, advanced solid state array spectroradiometer (ASAS), laboratory and field-measured multiangular reflectance data and have been shown to fit observed BRDF data well [*Roujean et al.*, 1992; *Leroy and Roujean*, 1994; *Wu et al.*, 1995; *Wanner et al.*, 1995b; [*Privette and Vermote*, 1995; *Strahler et al.*, 1995c; *Li et al.*, 1996; *Barnsley et al.*, 1996b; *Hu et al.*, 1996; *White et al.*, 1996]. Some examples of the latter will be given in section 5. A kernel-based model is also being used for the BRDF/albedo product of the polarization and directionality of the earth's radiation (POLDER) project [*Deschamps et al.*, 1994; *Leroy et al.*, 1996].

3.4. The Ambrals BRDF Model

The kernel-based BRDF model to be used for production of the MODIS BRDF/albedo product was chosen to be the Ambrals BRDF (Algorithm for MODIS bidirectional reflectance anisotropy of the land surface) BRDF model, as defined by the kernels used in it. The rationale for choosing this model is given in section 3.5. The kernels used are based on theory by *Roujean et al.* [1992], *Ross* [1981], *Li and Strahler* [1992], Li [*Strahler et al.*, 1994; *Wanner et al.*, 1995a] and *Cox and Munk* [1954].

The Ambrals model provides two choices each for the volume scattering and the surface scattering kernel. The kernels to be used in a particular case depend on the characteristics of the multiangular observations available. The two kernel expressions derived for volume scattering are based on two different approximations to a single-scattering radiative transfer theory of *Ross* [1981], one for large values of the leaf area index ("thick" approximation) [*Roujean et al.*, 1992], one for small values ("thin" approximation) [*Wanner et al.*, 1995a]. For geometric surface scattering, two types of Li-kernels are available. These were derived from the geometric-optical mutual shadowing BRDF model for forest canopies by *Li and Strahler* [1992]. The first of these is an approximation for "sparse" spacing of discrete objects (crowns), the second for "dense" spacing of objects (crowns) [*Strahler et al.*, 1994; *Wanner et al.*, 1995a]. The Li-sparse kernel is mainly driven by the way shadows emerge and are hidden in the scene, while the Li-dense kernel is dominated by the sunlit crowns as seen under conditions of mutual shadowing in both viewing and illumination directions. For MODIS BRDF/albedo processing, the Li-sparse kernel is formulated to represent spheroids that are relatively close to the ground ($b/r = 1$, $h/b = 2$, where b is the crown vertical radius, r the crown horizontal radius, and h the height to center-of-crown). The Li-dense kernel is formulated to represent prolate crowns that are situated some distance above the ground ($b/r = 2.5$, $h/b = 2$). For general use of the Ambrals model, other choices of these parameters can be made.

In cases where the forward-scattering direction of the BRDF has been sampled, a Cox-Munk kernel has been developed [*Strahler et al.*, 1995a, update] to model contributions from sub-resolution water bodies, flooded fields, and

melting ice. This kernel is based on a theory of sunglint on the ocean by *Cox and Munk* [1954]. A wind speed parameter of 5 m/s is used.

Figure 2 shows the shape of these five Ambrals model kernels on the principal plane for three different solar zenith angles. Kernels may be normalized before use to have comparable ranges of values or integrals. Note that volume scattering and surface scattering kernels are, to a large degree, linearly independent.

Using these kernels, the Ambrals BRDF model can acquire five distinct forms, Which allows good fits to the variety of BRDF shapes expected from global BRDF observations at the kilometer scale. The Ross-thin kernel is combined with either the Li-sparse or the Li-dense kernel, as is the Ross-thick kernel. The Cox-Munk kernel is combined with the Li-sparse kernel. These five model variants, also listed in Table 2, will be used to produce the MODIS BRDF/albedo product. Tests have shown that for a variety of land cover types at least one of these models provides a good fit, although for some land cover types several models may do well due to the fact that they share the kernel that accounts for most of the BRDF shape (see section 5 of this paper, and [*Wanner et al.*, 1995b, *Hu et al.*, 1996]).

3.5. Rationale in Choosing the Ambrals BRDF Model

Quite a number of BRDF models are available in the literature, ranging from simple empirical to rather complex numerical models that more closely represent the physical features of the plant types being modeled (*Strahler* [1994] gives an overview). The majority of these were derived from a forward-modeling perspective. Geometric and optical properties of vegetation are used to compute the most prominent features of radiation scattering and shadow casting in plant canopies, and to derive the BRDF. While being very valuable in providing an insight into the physics of the interaction of light with vegetation, they are not ideally suited for remote sensing applications. Forward modeling represents a bottom-up approach, while remote sensing requires dealing with the inverse problem. The perspective that needs to be at the core of the modeling is top-down.

The rationale for choosing the Ambrals BRDF model for the operational inversions of MODIS BRDF/albedo processing is outlined by four requirements that were met by this model.

(1) The model is required to be reflectance-based to eliminate the need to rely on ancillary databases of vegetation properties, soil brightnesses, etc. Global databases of these properties do not exist currently with the required spatial resolution and mostly are of unknown quality. Furthermore, the approach chosen should be flexible enough to model the BRDFs of the major types of vegetation and non-vegetated surfaces. This, to some extent, precluded the use of just one single BRDF model for all land cover types.

The Ambrals model meets these requirements in that the inversion of three parameters is achievable from the available multiangular sampling, and that no additional parameters need to be pre-determined. It has been successfully applied to a number of observed BRDF data set [*Privette and Vermote*, 1995; *Strahler et al.*, 1995c; *Wanner et al.*, 1995b; *Hu et al.*, 1996; *White et al.*, 1996]. A similar model is to be used for operational BRDF retrievals or POLDER [*Leroy et al.*, 1996].

(2) The model used should be robust in several respects. It should be robust with respect to inversion from limited angular sampling and robust against noise in the input data. It is essential that it should not assume that the pixels viewed possess a homogeneous land cover (an assumption implicit in most BRDF models). Globally, the number of mixed pixels heterogeneous at the 100-meter-scale is large. Also the BRDF model needs to be able to model BRDF effects caused by hilly and rugged topography and by rough soil surfaces.

Due to the top-down modeling approach taken in kernel-driven models, discussed in the previous section, the Ambrals BRDF model meets these requirements well. Noise sensitivity is discussed in section 3.7.

(3) There should be a mathematically clear way of scaling the model spatially. The MODIS BRDF/albedo product will be generated at a spatial resolution of 1 kilometer, but the results may be applied at coarser resolutions up to climate-model resolutions of 2.5 degrees or more. Since the BRDF is a nonlinear function of at least 3 angles, such spatial scaling is not a straightforward operation, and neither is the spatial averaging of albedos when taking a varying BRDF effect into account.

The Ambrals model scales spatially due to its linear properties: the parameters of the model at a coarser spatial scale may be expressed through weighting of the parameters of each kernel according to their proportion of area. This will allow degrading the MODIS BRDF/albedo product to any resolution desired for a specific modeling purpose.

(4) The model must have a speedy inversion. This excludes the use of numerical inversion techniques, typically required for the inversion of physical and numerical BRDF models (cf. *Goel* [1989]). Currently, only a model that has a mostly analytical inversion is a feasible candidate.

The Ambrals model may be inverted analytically by solving the set of linear equations derived from minimizing an appropriate error function through matrix inversion [*Lewis*, 1995]. The model inverts extremely rapidly for this reason and is consequently ideally suited for large-scale global BRDF inversion.

3.6. Albedo From MODIS

The influence of atmospheric state on the radiative fluxes at the surface becomes an issue when deriving albedo. Albedo is defined as the ratio between the hemispherical upwelling and downwelling fluxes, the latter depending on the amount of diffuse scattering occurring in the atmosphere due to its aerosol and water vapor load. This makes the albedo itself dependent on the atmospheric state at the time of observation. Albedo in this form, while characterizing accurately the radiative fluxes at the time of observation, is not directly usable in biospheric and climate modeling, where the atmosphere applied and/or computed may be different from that observed and may vary as a simulation proceeds. What is needed for modeling is an average or hemispherical reflectance in form of an intrinsic surface property that is not dependent on a particular atmosphere and time.

In order to meet this demand, the MODIS BRDF/albedo product will provide two measures of albedo in form of the directional-hemispherical and bihemispherical integrals of the BRDF, derived through the Ambrals BRDF model from atmospherically corrected reflectances. These albedo measures then are intrinsic properties of the surface. They represent the following two cases. The directional-hemispherical integral (4), called the "black-sky albedo," represents the case of single-beam irradiation in the absence of diffuse skylight, that is, the situation of a perfectly clear sky. The bihemispherical albedo, called the "white-sky albedo," given by (6), with $\overline{\rho_s}$ replaced by ρ_b and the integration over θ_s, represents the case of perfectly diffuse illumination, that is, the case of a perfectly turbid atmosphere, similar to an overcast situation. The albedo under conditions of atmospheric scattering of light will then be a value between these two extreme cases and depend on the actual aerosol and water vapor loading.

It may be noted that the black-sky albedo is a function of solar zenith angle, whereas the white-sky albedo is a constant. It is an advantageous property of kernel-based models that the black-sky albedo may be formulated as a linear combination of the BRDF model parameters and the black-sky integrals of the kernels. Since these integrals may be pre-computed and tabulated, the black-sky albedo can be generated from known model parameters at any solar zenith angle without numerical integration [*Lewis*, 1995] using a very compact look-up table that will be provided with the product.

Black-sky and white-sky albedo will be given in all seven MODIS land bands, spanning from 0.47 to 2.13μm. They will also be derived in three broad bands, from $0.4-0.7$ μm, $0.7-3.0$ μm, and $0.4-3.0$ μm, which are useful to climate modeling, where the wavelength domain is commonly partitioned in this manner [*Dickinson*, 1983]. In the shortwave region, vegetation dominantly absorbs radiation, whereas in the longerwave region it is mainly scattered. Broadband albedos are not simply spectral averages of the albedo. They are defined such that, given a downwelling broadband flux, the corresponding broadband upwelling flux is derived.

Narrowband-to-broadband albedo conversion will be achieved by weighting the narrowband albedos by their associated proportion of downwelling solar irradiance. This method has been used with nadir Landsat measurements [*Brest and Goward*, 1987] and was shown to be satisfactory by *Ranson et al.* [1991], although *Starks et al.* [1991] report a case where a significant bias occurred. Since the downwelling solar irradiance depends on the atmospheric state during observation there is an undesirable dependence of the broadband albedos on that state. We currently are considering resolving this situation by using the irradiance found from applying molecular scattering alone (clean-sky case). However, the spectral albedos will be provided by the MODIS BRDF/albedo product as well, so individual researchers will always be able to carry out their own conversions.

Table 3 shows sample results illustrating the potential accuracy achievable in narrowband-to-broadband albedo conversion using the 7 MODIS land bands for three different land cover types. The broadband albedos derived from splines to the spectral values are within 1 or 2 percent of the real values.

3.7. Sensitivity of BRDF and Albedo Retrievals to Angular Sampling and Noise

The behavior of the Ambrals BRDF model under inversion was studied in detail under conditions of angular sampling as expected from MODIS and MISR. Two types of studies were carried out. The first is a study of the influence of random noise on the accuracy of the inversion. The second is a study of how well a BRDF derived from a limited set of angular reflectances interpolates and extrapolates to angles not observed. Both of these extensive studies will be reported in full detail elsewhere. Here, only a brief overview over the main results can be given.

Both the noise sensitivity and the interpolation/extrapolation accuracy study were conducted using simulated 16-day MODIS and MISR cloud-free viewing and illumination geometries simulated by the Xsatview software by Barnsley and Morris [*Barnsley et al.*, 1994]. Investigations were carried out as a function of latitude and day of the year. The quantities studied were nadir-view reflectance and black-sky albedo at the prevailing mean sun angle of observations ("interpolation") and for a fixed nadir or 10° sun zenith angle ("extrapolation"). White-sky albedo and the model parameters themselves were also investigated.

The noise sensitivity study was carried out by taking advantage of the linear mathematical properties of kernel-

driven models that allow an analytical analysis following methods developed by Gauss [*Whittaker and Robinson*, 1960]. The diagonal elements of the inversion matrix found in the minimization problem, which depend only on the kernel values at the angles sampled, may be used to compute so-called "weights of determination," or "noise inflation factors" [*Wanner et al.*, 1996]. These factors indicate how random uncertainty in the reflectances sampled translates into uncertainty in the BRDF and in albedo. Noise inflation factors depend on the sampling geometry alone, i.e., for MODIS and MISR sampling they vary with latitude and time of year; but for kernel-based models they do not depend on wavelength or the type of BRDF viewed. The study conducted shows that both interpolated and extrapolated nadir-view reflectances and black-sky albedos as well as the white-sky albedo have median noise inflation factors of less than 0.5, and worst values of less than about 1, demonstrating that the inversions are stable with respect to random noise.

In the presence of clouds, these factors are expected to increase with the square root of the number of observations, provided that the angular coverage of the samples does not change significantly. A comparison of the Ambrals noise sensitivity with the corresponding sensitivity of the semiempirical 3-parameter BRDF model by *Rahman et al.* [1993] shows that both models behave very similarly. The study was also carried out using MODIS-only and MISR-only sampling. Results demonstrated that the quality of a MODIS-only product is greatly enhanced by adding MISR data. The noise inflation factor may be used as a quantitative indicator of sampling quality in operational BRDF inversions and will be carried by the MODIS BRDF/albedo product.

For the interpolation and extrapolation error study, a three-dimensional discrete ordinate numerical BRDF forward model by *Myneni et al.* [1992] was used to create surface reflectances at the angles sampled by MODIS and MISR over 16 days. The study was carried out for BRDFs of six different biome types (grassland, shrubs, broadleaf crops, savanna, broadleaf forest, conifers) and for red and near-infrared wavelengths. Upon inversion of the Ambrals BRDF model, results were compared with those known from the forward model. At the mean sun zenith angle of the observations the predicted nadir-view reflectance and black-sky albedo were found to have a median deviation from the true value of about 3 to 4 percent. At a sun zenith angle of 10°, reflectance showed a median deviation of about 6 percent, whereas black-sky albedo was accurate to about 5 percent. This shows that while interpolation can be carried out with good precision, extrapolation depends more on favorable sampling conditions. White-sky albedo could be determined with a median accuracy of 6 percent. Since these numbers are the results of model-to-model comparisons, they should be interpreted with caution; problems can be due to either model. In cases with unfavorable sampling, errors of up to 10 or 20 percent may occur.

Table 4 summarizes the noise sensitivity and the interpolation/extrapolation study results. The results in both cases are medians over all cases investigated. The ranges given are chosen to include two thirds of all relevant data.

4. The Algorithm

4.1. BRDF/Albedo in the MODIS Production Chain

The MODIS BRDF/albedo product is generated as part of the surface reflectance processing chain for the MODIS instrument, which runs from calibration and geolocation through atmospheric correction, gridding and resampling to BRDF and albedo retrieval. The latter relies on atmospherically corrected surface reflectance data from both MODIS and MISR and atmospheric coupling descriptors for updating atmospheric corrections where necessary after the initial BRDF retrievals. Product generation is supported and gaps are filled by having available current land cover and topographic information, the BRDF/albedo results from the previous production cycle and a global database of accumulated BRDF/albedo knowledge that will be built over time.

MODIS level-2 reflectances that have been cloud cleared and atmospherically corrected are binned into the MODIS level-3 grid over a period of 16 days and combined with all MISR observations acquired during that time. The data are averaged to a spatial resolution of one kilometer, where each observation is weighted by the respective overlap between the grid cell and the observation footprint. Quality information associated with the data is translated to quality coefficients that are used to weight individual observations in the subsequent BRDF inversion. This allows special consideration of data where, for example, atmospheric correction was difficult or aerosol information was taken from standard tables because no aerosol retrievals were available.

The directional observations thus assembled are then analyzed by inverting the five model variants listed in Table 2 to find the Ambrals kernel combination that describes the observations best. BRDF model inversion is carried out by straightforward matrix inversion. The four bands common to MODIS and MISR are inverted first. The model chosen from this analysis is then applied to the three remaining bands, in which only MODIS data are available. The model parameters found are written to output along with extensive quality control data and other information necessary for an assessment of the product. Integration of the BRDF is carried out to provide black-sky and white-

sky albedos. Use of a digital terrain database will allow correction for BRDF effects created by topographic shading some time after the launch of AM-1. Initially, the BRDF derived will characterize the combined BRDF of vegetation/soil and topography.

The Ambrals model kernel combination that describes the observations best is selected from among the five model variants available as follows. Generally, the kernels to be used will be chosen to provide the fit with the smallest root band-averaged mean squared error (RMSE) when inverting the available multiangular reflectances. The two cases where an exception is made are if the RMSE found is large, or angular sampling coverage is bad enough to mistrust the inversion, either because observations span only a small angle range or their number is too small. In these cases information from the supporting ancillary databases is used to limit the inversion. If angular sampling is good but the RMSE found is high, the kernel combination suggested by the ancillary data (previous BRDF, BRDF accumulated database, land cover type, topography) is used instead of the best-fitting model variant if the resulting RMSE is not much worse. The model parameters are still derived from a full inversion of the reflectances.

If angular sampling is bad or the number of reflectances available is too small, a full inversion cannot be trusted and gaps in the product would result. In this case, the BRDF kernel combination and model parameters suggested by the ancillary databases will be used, but the magnitude of the BRDF (the isotropic constant of the model) will be adjusted to the observed reflectances. Through this the shape but not the magnitude of the BRDF will be fixed. This procedure also guarantees that the reflectance information available in cases not permitting a full BRDF inversion will not be simply lost but used to the extent possible.

In each case, the source of the resulting BRDF information will be recorded so that users can filter the output according to their needs. The ancillary database accumulating BRDF knowledge over time, keyed by season, and the relationships between land cover type and BRDF used will be established post-launch from the data observed and updated at intervals.

Since the Ambrals model allows adapting the kernels used to the specifics of the land cover types viewed by giving a choice of kernels, the mathematical expressions used on adjacent pixels may be slightly different. While this is expected to provide the best BRDF and albedo information on a per-pixel basis, it may also cause difficulties in mapping between pixels and where a much simpler uniform approach is desired. As a consequence, the MODIS BRDF/albedo product will always also provide the full inversion results for the modified Walthall BRDF model [*Walthall et al.*, 1985; *Nilson and Kuusk*, 1989]. This model is purely empirical and is expected to produce results of reduced accuracy, particularly under conditions of sparse angular sampling. But the simplicity of the mathematical expression used and the fact that it will be the same for all pixels are attractive to applications where a reduced accuracy is acceptable.

Product generation rules are the following. If less than 8 observations are available in the 16-day period, or they are clustered in a small region of angle space, this will be deemed insufficient for a full inversion. Angular coverage will be monitored through the determinant of the inversion matrix, which reflects the power of a given sampling to discriminate the model parameters. If the looks are all at very high zenith angles, production continues but the appropriate quality flags are set to indicate this situation. Similarly, the quality of the product will be lower if no MISR data are available. If the supporting inputs of land cover, digital terrain and ancillary accumulated BRDF database are not available, production continues with lower quality, since these inputs are supportive only. No BRDF is derived over oceans or inland water, although pixels with subresolution water content will be processed. For snow we expect the Ross kernels to apply, but this will be investigated. Processing of areas covered by sea ice is under consideration.

Details about the algorithm, its theoretical basis, and its dependence on other products may be found in the NASA Algorithm Technical Basis Document [*Strahler et al.*, 1995a], available on the internet at http://spso.gsfc.nasa.gov/atbd/pg1.html.

4.2. Output Product and Quality Flags

BRDF inversion results will be given in form of identifiers determining the Ambrals model kernel combination used for each pixel and the list of model parameters found for each band for the Ambrals and the modified Walthall model. Black-sky albedo at any solar zenith angle and white-sky albedo for both models can be constructed with almost no computational effort directly from the model parameters using a small look-up table of precomputed kernel integrals that will be provided to users with the product. Broadband albedos will be given in a similarly parameterized form.

Quality and product information will be comprised of the following: an overall quality indicator; a flag detailing the source of the BRDF given (new full inversion, limited inversion or taken from ancillary database); the quality of the fit over wavelengths; view and sun angle coverage; the mean sun angle of the observations; flags indicating whether topographic effects are expected in the BRDF, whether MISR data was available and whether atmospheric correction was updated; and the land/water and data availability mask. The RMSE of the inversions, a quantitative descriptor of the quality of the angular sam-

pling found, and a parameter describing the relative contribution of surface and volume scattering to the scene are also recorded.

In addition to this one-kilometer BRDF/albedo product, a product spatially degraded to a quarter-degree resolution will be produced for direct use in climate models. This product will also carry information on the subgrid variability of albedo.

4.3. The Ambrals BRDF Inversion and Modeling Tool

The production algorithm has been programmed to provide maximum efficiency through avoiding multiple evaluation of expressions shared by several kernels, and through look-up table approaches to kernel value retrieval and albedo calculations. One 16-day BRDF/albedo product at full resolution and in all seven bands will have a total file size of approximately 35 GByte. This size also applies to the BRDF knowledge database to be created. The processing power required to produce the 16-day product in real-time is currently estimated at about 300 million floating point operations per second. Preparing the input data for BRDF/albedo processing requires additional resources.

A user working with the product will need to be able to reconstruct the BRDF from the parametrization provided by the MODIS BRDF/albedo product. For this, an algorithm is required that allows forward modeling of each of the models used in the inversion. The Ambrals code will be provided in a form that allows forward and inverse BRDF modeling of kernel-driven models, provides a selection of science options, numerical BRDF integration, and permits easy adding of new models. This code can also be used to degrade the product to coarser spatial resolutions and derive the corresponding albedos. The Ambrals code, together with a user guide, is presently available from the authors upon request for BRDF modeling work and preparation of BRDF-dependent algorithms.

5. Validation

5.1. Validation Outline

Validation of the BRDF/albedo product will be performed in three respects. First, the semiempirical BRDF models need to be validated for as many types of land cover as possible to assure that they provide adequate mathematical descriptions of occurring BRDF shapes. This is done using field-measured, laboratory-measured and numerically simulated BRDFs.

Second, large-scale BRDF and albedo retrievals need to be demonstrated given the constraints of sampling, atmospheric correction and temporal composition of data occurring in a remote sensing situation. This is done using multiangular data from airborne sensors and from AVHRR.

Third, the quality and accuracy of the product need to be monitored during post-launch product generation. This validation will be part of a MODIS-wide and EOS-wide validation and quality assurance effort based on tower measurements, aircraft campaigns and intercomparisons with the results obtained from other space-based sensors.

5.2. Model Validation

Basic model validation was carried out by applying the Ambrals BRDF model to multiangle reflectance data measured in the field for a variety of land cover types. Here we demonstrate this work by giving a few examples, selected to represent four distinct categories of land cover types: forests; barren or sparsely vegetated lands; grasses and grasslike crops; and broadleaf crops. The data sets used include two soybean data sets observed by *Ranson et al.* [1985] using an Exotech Model 100 radiometer. They represent canopy coverages of 72 and 99 percent and solar zenith angle ranges from 20° to 49° and 31° to 61°, respectively. Inversion was carried out using all four bands observed, including the red and near-infrared. An aspen and a spruce forest data set were selected from measurements by *Deering et al.* [1995] using a PARABOLA instrument, and the red and near-infrared channel were used for inversions. The solar zenith angle range was 45° to 59° and 36° to 59°, respectively. All other data were acquired by *Kimes* [1983] and *Kimes et al.* [1985, 1986] at solar zenith angles ranging from 25° to 79°, varying from one data set to another. The whole of the viewing hemisphere was sampled for all data sets.

Evaluations were carried out for the red and near-infrared (NIR) channels. Table 5 lists the data sets, gives the model with the lowest root of the band-averaged squared deviation between modeled and observed reflectances (RMSE), and the coefficients of linear correlation between the modeled and observed reflectances in the red and in the NIR band. The RMSEs are found to be between 1.1 and 4.6 percent, which is satisfactory, and the correlation coefficients commonly are larger than 0.8 or even 0.9. These results are typical for those found for a number other data sets (including AVHRR, airborne POLDER, ASAS and field-measured data) using variants of the Ambrals model used here [*Privette and Vermote*, 1995; *Hu et al.*, 1996; *White et al.*, 1996]. The corn data set has rather large irregular variations in the observed reflectance, which explains the low red band correlation coefficient for this one data set.

Figure 3 shows the correlation between observed and modeled reflectances for one example from each of the four land cover groups. Even though there are some deviations, the modeled reflectances generally follow the observed val-

ues. It is interesting that the unvegetated plowed field data set is described well by the geometric-optical theory of shadowing provided by the Li-sparse kernel. This is not unexpected. Geometric-optical theories are based on relative geometric proportions and thus scale, and the plowed field consists of shadow-casting clumps of earth sitting on the ground. Note that in the cases of irrigated wheat and the plowed field there are some reflectances that are noticeably larger than the others, and that these are modeled correctly.

Figure 4 shows the RMSE for each of five BRDF models tested for three examples of each land cover group (the Cox-Munk/Li-sparse model was not used since it is only applicable to scenes involving a water component). Obviously, all data sets are fit well by at least one of the models. In a number of cases, one type of model fits the data better than another. Examples include the models containing the Li-sparse kernel for the barren or sparsely vegetated land cover types, the Li-dense kernel for the hardwood forest, and the Ross-thick kernel for the orchard grass and the second soybean data set. In some other cases, all models provide good fits, as for the aspen data set, the grass lawn, and the corn. This may be explained by a low variance of reflectances in the particular angular ranges sampled, which places a large emphasis on the isotropic constant of the models. The empirical modified Walthall model performs fairly well in some cases, showing a lower RMSE than the best semiempirical model. But this result is valid for the relatively good angular sampling that characterizes these validation data sets. Remotely sensed data will be much sparser in angle space, which is when the physical basis of the semiempirical models will give them an important advantage.

An important question is whether the differences in the RMSE found between model variants translate to noticeable differences in derived reflectances and albedos. If this were not the case, all model variants could be considered equally capable of modeling the BRDF of different land cover types, and using only one of them would be sufficient. But there is indeed a difference between kernel combinations. Figure 5 shows this for two examples, the hardwood forest data and one of the soybean datasets. In the forest case, the models containing the Li-dense kernel clearly have a smaller RMSE. But the white-sky albedo is nearly the same for all model variants. This may be caused by the term $\cos\theta_v \sin\theta_v \cos\theta_i \sin\theta_i$ that occurs in the bihemispherical albedo integral. Values of the BRDF at very small and very large zenith angles, where the dependence of the BRDF on angle is strongest, have only a weak effect on the albedo. In the case of the soy dataset, however, the opposite effect occurs. There is a noticeable difference in albedo between models based on the Ross-thin and those based on the Ross-thick kernel even though the RMSEs of all model variants are similar.

The isotropic model constant f_i (nadir sun and view reflectance) shows, in this example, large differences between model variants for the case where the albedo varies little, but only small variation in the case where the albedo differs across kernel combinations. These and similar findings for other datasets lead to the conclusion that choosing the correct model is important for generating accurate results. Using just one BRDF model or model variant will lead to results of varying quality for different land cover types. This situation will be aggravated under conditions of more limited sampling than is the case for these well-sampled field-measured data sets.

The feasibility of using kernel-based semiempirical models for modeling bidirectional reflectance data has also been shown by several authors using a model similar to the Ambrals model, employing the Ross-thick kernel and a geometric-optical kernel by *Roujean et al.* [1992]. *Leroy and Roujean* [1994] were able to correct noise-like temporal variations in AVHRR data that were due to varying angles of observations. *Wu et al.* [1995] successfully modeled AVHRR data for several different land cover types. *Li et al.* [1996] are able to remove mosaicking borders from an AVHRR NDVI image of Canada that were due to directional differences between overpasses. *Privette and Vermote* [1995] conclude that kernel-based models of the Ambrals model type perform satisfactorily for atmospheric correction purposes on an AVHRR desert scene. *Barnsley et al.* [1996b] apply the Roujean model and the modified Walthall model to multiangle images obtained by ASAS during the HAPEX-Sahel campaign. They show that the first parameter of the semiempirical model, which is the reflectance for nadir view and sun, is the most stable parameter in the retrieval and matches spatially with the nadir-view images acquired. Maps of albedo are produced from the model inversions. Inversions of a soybean and a nasturtium dataset observed in a Chinese laboratory that acquires rapid multiangle reflectance measurements has produced satisfactory results both when angular sampling was dense and when it was sparse [*Strahler et al.*, 1995c].

The conclusions to be drawn from these validation investigations are the following. First of all, the kernel-driven semiempirical Ambrals BRDF model to be used in the MODIS BRDF/albedo algorithm is capable of fitting bidirectional reflectance data sets well. Second, different kernel combinations fit different data sets best. Using a small number of distinct kernel variants is therefore advisable if both albedo and the BRDF are to be derived with low errors. And finally, the modified Walthall model, to be used as a uniform model parallel to the Ambrals model, is capable of fitting the data sets tested here as well, but it is expected to perform less well for inversion of the more limited angular sampling encountered from MODIS/MISR.

Additional field-measured BRDF data sets are expected to be available for continued model validation. The BRDF laboratory in Changchun, China, [*Strahler et al.*, 1995c; *Liang et al.*, 1996] will provide additional BRDF measurements in the future. Data acquired during the BOREAS campaigns are beginning to be available, such as the PARABOLA data sets by *Deering et al.* [1995], two of which were used in this paper. Artificial data sets have been created by *Soffer et al.* [1995] using model trees in a laboratory, and by *Lewis and Muller* [1992] using Monte Carlo ray-tracing. BRDF data sets generated numerically for several different biome types from a 3D-radiative transfer code by *Myneni et al.* [1992] are being employed for a detailed study of model properties that will be reported elsewhere.

5.3. Relationship of BRDF to Land Cover

In Figure 4, there is an indication of distinctive patterns characterizing each land cover type group. In the case of the hardwood forest, clearly the two models involving the Li-dense kernel are much favored over those involving the Li-sparse kernel. This corresponds to the fact that the forest observed was indeed dense in nature. There is little difference between the model using the Ross-thick kernel and the model using the Ross-thin kernel. This may be explained by the fact that scattering is dominated by geometric optics, leading to a small weight given to the volume scattering kernel. It does not matter which one is chosen. The case is less clear for the pine and the aspen data sets, but the aspen does show a slight improvement of fits if the Ross-thick kernel is used. Although it might well be expected from the scene type, this data set lacks a distinct hotspot, perhaps due to instrument characteristics.

All the examples given for barren or sparsely vegetated covers show a distinct preference for the Li-sparse kernel, which is driven by shadowing. The plowed field consisted of clumps of earth on the ground, leading to strong surface scattering effects. The annual grass data set was acquired at a site with less than 5 percent of vegetation cover, where 40 percent of the surface was covered by stones and pebbles [*Kimes and Sellers*, 1985]. The steppe grass site had clumps of grass, and the total cover was 18 percent. Obviously, the structured surface of these land covers is best represented by strong shadow-driven geometric-optical scattering.

Two of the three data sets given for dense grasses and grasslike crops show a preference for models containing the Ross-thick kernel, as might be expected for dense horizontally layered canopies that show little shadowing. In the broadleaf crops group, two of the three examples given are modeled well by all models. They lack angular variation in the angle intervals sampled, resulting in a strong isotropic contribution to overall fitting that renders the contributions from the respective kernels less important. One set, however, shows the influence of both shadowing and volume scattering in being modeled best by the Ross-thick/Li-dense model.

We think that there is an indication in this data that where mutual shadowing of crowns plays a role, as in most forests, models containing the Li-dense kernel will be chosen, whereas in scenes where shadows are dominant, models using the Li-sparse kernel are preferred. These scenes would then be sparse forests or brushlands, and rock-strewn deserts, rough (plowed) terrain or clumped vegetation, respectively. When the Ross-thick kernel is chosen over the Ross-thin kernel, or all models perform well, a dense layered canopy with no individual crowns is observed. The Ross-thin kernel is expected to be applicable to scenes with a thin but horizontally continuous layer of leaves over a rather solid background, which can be the ground or dense underlying vegetation.

Table 6 summarizes these correspondences in a tentative list of land covers likely to be associated with models containing specific kernels. Whether the relationships speculated upon here hold with any consistency, and whether the differences are distinct enough to allow reliable inference of surface structural properties, remains to be seen when much more extensive data sets than are now available can be studied. But the fact that surface structure determines the angular dependence of the reflectance, as is known from physical reflectance forward modeling, should make a retrieval of at least general structural information of the type discussed here possible [*Goel*, 1989; *Pinty and Verstraete*, 1991]. If the classes obtained from such an analysis are not congruent with the classes derived from spectral land cover classifications, the combination of directional and spectral information should allow for more accuracy in land cover classification. An example is the distinction between dense and sparse forests, or between dense brush and sparse forest, which may have similar spectral properties but distinct bidirectional characteristics. A study by *Barnsley et al.* [1996a] shows that while the spectral information content of a scene of arable farmland obtained with the airborne multispectral scanner Daedalus is greater than the directional information content, the multiangle properties of the data nevertheless provide an important means of distinguishing between the occurring land cover types. For this reason, the MODIS land cover product will make use of BRDF-derived information where feasible [*Strahler at al.*, 1995b].

5.4. Pre-Launch Product Prototyping

Several projects are close to completion that apply the Ambrals BRDF model to AVHRR data over large regions, demonstrating and testing the MODIS algorithm. It is beyond the scope of this paper to report this work in detail.

A study led by d'Entremont [*d'Entremont et al.*, 1995, 1996] is targeted at inversions of AVHRR multiangle imagery for the whole of New England. Maps of albedo and kernel combinations chosen have been derived. A project conducted by Lewis includes large-area AVHRR data inversions for different times of the year for the Sahel region of Africa. A similar investigation, led by X. Li, is under way for a large area surrounding the site of Three Gorges dam project on the Yangtse river in China. These scientific studies, which also serve to prototype the MODIS BRDF/albedo product, demonstrate the feasibility of the approach and have been successful in generating BRDF and albedo images of large areas. Validation of the results obtained is the next step. In the Sahel region, for example, both ground-measured and airborne sensor multiangular data have also been evaluated for comparison.

Other sources of large-area data that will be used when they become available are data from the POLDER instrument, launched in August 1996, and the SPOT-VEGETATION sensor, also to be launched before the AM-1 platform. These data sets, observed from space, will be complemented by more limited datasets acquired from airborne sensors. Here, several campaigns have been carried out and will be carried out in the future with the ASAS, the MODIS airborne simulator (MAS), the compact airborne spectrographic imager (CASI) and the airborne POLDER sensors over a variety of sites. Work on processing these data is under way. Semiempirical models will be and are being applied to these data sets to optimize the algorithm for deriving BRDF and albedo from MODIS/MISR. AirMISR is a MISR-like instrument that will be very relevant to BRDF studies once it is operational in 1997.

5.5. Post-Launch Product Validation

In the post-launch phase, a coordinated effort for validating the radiometric products of MODIS and EOS as a whole will be undertaken. Validation of BRDF and albedo is tied into validation of calibration, atmospheric correction, and several higher-order products. This effort is currently being developed in the EOS project.

A number of tower sites will be equipped with radiometers monitoring upwelling and downwelling radiances on a continuous basis. At a minimum, these sensors will record broadband hemispherical fluxes. Spectral measurements will be made whereever possible. A selected number of sites will also feature directional measurements. The status of the land cover around the towers and atmospheric properties over the towers will be measured simultaneously. Tower sites will be chosen to represent major land cover types. One problem with many current sites observing aerosols, for example, is that little attention is given to the upward fluxes coming back from the surface (e.g., rooftop instruments will not do).

The observations obtained at a tower site will be scaled to the footprint size of the space-based sensor through occasional aircraft overflights that relate site properties to surrounding areas. Additionally, sites will be chosen to be homogeneous in land cover type. Scaling may also be inferred from using data from sensors with different resolutions.

An important part of post-launch product monitoring will also be cross-comparing the MODIS BRDF/albedo product with the corresponding MISR surface product and the POLDER BRDF and albedo product. Use of data comparable data from meteorological satellites for validation purposes will also be investigated.

6. Conclusions

Surface reflectance is a key quantity in optical remote sensing. A multitude of derived parameters and estimates are based on surface reflectance, for example land cover classifications, snow and ice maps, and vegetation state parameters. However, since the reflectance of the land surface is anisotropic in nature, retrieval of the bidirectional reflectance distribution function is essential for an exact interpretation of the data, and for characterizing average reflectance in form of albedo measures. In addition, BRDF and albedo are required for accurate computations of radiative transport in the atmosphere, providing the directional characteristics and the magnitude of scattering at the lower boundary. This is of importance in atmospheric correction and in the radiation transfer schemes of climate and weather models.

The MODIS BRDF/albedo product will provide this information to a wide variety of users as part of the EOS-MODIS standard product catalogue. The expected uses comprise correction of images for directional effects; standardizing images to common viewing and illumination geometries; deriving vegetation indexes free of directional effects; providing lower boundaries for atmospheric correction and radiation budget investigations; retrieving precise measures of land surface albedo; inferring land surface structural characteristics, especially of vegetation and topography; and as an input to land cover classification. A possible future application is in cloud detection.

The MODIS BRDF/albedo product will employ the Ambrals kernel-based semiempirical BRDF model, making use of a total of five different available kernel functions, and the modified Walthall model for modeling the multiangle data. These models have been shown to fit a variety of observed multiangular data sets well. Besides possessing beneficial computational qualities, such as analytical inversion, direct spatial scaling and generic accommodation of mixed pixels, their physical basis allows for credible

extrapolation of the BRDF to angles not covered by the observations. The BRDFs found will be integrated to provide integral measures of albedo that do not depend on atmospheric state.

The combination of these activities, it is hoped, will contribute to the goal of EOS, to further the understanding of the earth system in a time of potentially large changes induced by human activity. The production of a routine global BRDF and albedo product will lead to an increased understanding of the role that directional anisotropy in the reflectance of the earth's surface plays in the global energy system.

Acknowledgments. We would like to thank Jordan Borak for generating the data for the narrowband-to-broadband conversions shown in Table 3, Baojin Zhang for work on model inversion accuracy under varying angular sampling, and Jim Tallent for taking the beta-version of the Ambrals code to version 1. This work was supported in the US by NASA under NAS5-31369, and in the UK by NERC under the TIGER-SVATS programme and the European Union under the 3rd Famework Human Capital and Mobility Programme.

Barnsley, M. J., A. H. Strahler, K. P. Morris, and J.-P. Muller, Sampling the surface bidirectional reflectance distribution function (BRDF): Evaluation of current and future satellite sensors, *Remote Sens. Rev. 8*, 271–311, 1994.

Barnsley, M. J., D. Allison, and P. Lewis, On the information content of multiple-view-angle (MVA) images, *Int. J. Remote Sens.*, in press, 1996a.

Barnsley, M. J., P. Lewis, M. Sutherland, and J.-P. Muller, Estimating land surface albedo in the HAPEX-Sahel southern super-site: Inversion of two BRDF models against multiple angle ASAS images, *J. Hydrol.*, in press, 1996b.

Brest, C. L., and S. N. Goward, Deriving surface albedo measurements from narrow band satellite data, *Int. J. Remote Sens., 8*, 351–367, 1987.

Cihlar, J., D. Manak, and N. Voisin, AVHRR bidirectional reflectance effects and compositing, *Remote Sens. Env., 48*, 77–88, 1994.

Cox, C., and W. H. Munk, The measurement of the roughness of the sea surface from photographs of the sun glitter, *J. Opt. Soc. Am., 44*, 838–850, 1954.

Deering, D. W., S. P. Ahmad, T. F. Eck, and B. P. Banerjee, Temporal attributes of the bidirectional reflectance for three boreal forest canopies, *Proc. Int. Geosci. Remote Sens. Symp. 95*, 1239–1241, 1995.

Deschamps, P. Y., F. M. Breon, M. Leroy, A. Podaire, A. Bricaud, J. C. Buriez, and G. Seze, The POLDER mission: Instrument characteristics and scientific objectives, *IEEE Trans. Geosci. Remote Sens., 32*, 598–615, 1994.

Dickinson, R. E., Land surface processes and climate-surface albedos and energy, *Adv. Geophys., 25*, 305–353, 1983.

DiGirolamo, L., and R. Davies, A band-difference angular signature technique for cirrus cloud detection, *IEEE Trans. Geosci. Remote Sens., 32*, 890–896, 1994.

Diner, D., C. J. Bruegge, J. V. Martonchik, G. W. Bothwell, E. D. Danielson, V. G. Ford, L. E. Hovland, K. L. Jones, and M. L. White, A multi-angle image spectroradiometer for terrestrial remote sensing with the Earth Observing System, *Int. J. Imag. Sys. Tech., 3*, 92–107, 1991.

d'Entremont, R. P., C. B. Schaaf, and A. H. Strahler, Cloud detection and land surface albedos using visible and near-infrared bidirectional reflectance distribution models, *Proc. SPIE Symp. Sat. Remote Sens., 2586*, 1995.

d'Entremont, R. P., C. B. Schaaf, and A. H. Strahler, Using infrared cloud clearing techniques in the estimation of AVHRR-based bidirectional reflectance distributions functions, *Proc. 8th Conf. Sat. Met. Oceanog.*, 334–338, 1996.

Goel, N. S., Inversion of canopy reflectance models for estimation of biophysical parameters from reflectance data, in *Theory and Applications of Optical Remote Sensing*, pp. 205–251, J. Wiley & Sons, New York, 1989.

Gutman, G., Normalization of multi-annual global AVHRR reflectance data over land surfaces to common sun-target-sensor geometry, *Adv. Space Res., 14(1)*, 121–124, 1994.

Henderson-Sellers, A., and M. F. Wilson, Surface albedo for climate modeling, *Rev. Geophys. Space Sci., 21*, 1743–1778, 1983.

Hu, B., W. Wanner, X. Li, and A. Strahler, Validation of kernel-driven semiempirical BRDF models for application to MODIS-MISR data, *Proc. Int. Geosci. Remote Sens. Symp. 96*, 1669–1671, 1996.

Kaufman, Y. J., The atmospheric effect on remote sensing and its correction, in *Theory and Applications of Optical Remote Sensing*, pp. 336–428, J. Wiley & Sons, New York, 1989.

Kimes, D. S., Dynamics of directional reflectance factor distribution for vegetation canopies, *Appl. Opt., 22(9)*, 1364–1372, 1983.

Kimes, D. S., W. W. Newcomb, C. J. Tucker, I. S. Zonneveldt, W. van Wijngaarden, J. de Leeuw, and G. F. Epema, Directional reflectance factor distributions for cover types of Northern Africa, *Remote Sens. Env., 18*, 1–19, 1985.

Kimes, D. S., W. W. Newcomb, R. F. Nelson, and J. B. Schutt, Directional reflectance distributions of a hardwood and a pine forest canopy, *IEEE Trans. Geosci. Remote Sens., 24*, 281–293, 1986.

Kimes, D. S., and P. J. Sellers, Inferring hemispherical reflectance of the earth's surface for global energy budgets from remotely sensed nadir or directional radiance values, *Remote Sens. Env., 18*, 205–223, 1985.

Kriebel, K. T., Measured spectral bidirectional reflection properties of four vegetated surfaces, *Appl. Optics, 17(2)*, 253–259, 1978.

Kustas, W. P., R. D. Jackson, and G. Asrar, Estimating surface energy-balance components from remotely sensed data, in *Theory and Applications of Optical Remote Sensing*, pp. 604–627, J. Wiley & Sons, New York, 1989.

Lee, T. Y., and Y. J. Kaufman, Non-Lambertian effects in remote sensing of surface reflectance and vegetation index, *IEEE Trans. Geosci. Remote Sens., 24*, 699–708, 1986.

Leroy, M., and J.-L. Roujean, Sun and view angle corrections on reflectances derived from NOAA/AVHRR data, *IEEE Trans. Geosci. Remote Sens., 32*, 684–697, 1994.

Leroy, M., J. L. Deuze, F. M. Breon, O. Hautecoeur, M. Herman, J. C. Buriez, D. Tanre, S. Bouffies, P. Chazette, and J.-L. Roujean, Retrieval of atmospheric properties and surface bidirectional reflectances over land from POLDER/ADEOS, *J. Geophys. Res., this issue*, 1996.

Lewis, P., The utility of kernel-driven BRDF models in global BRDF and albedo studies, *Proc. Int. Geosci. Remote Sens. Symp. 95*, 1186–1187, 1995.

Lewis, P., and M. J. Barnsley, Influence of sky radiance distribution on various formulations of earth surface albedo, *Proc. 6th Int. Symp. Phys. Meas. Sign. Remote Sens.*, 707–715, 1994.

Lewis, P., and J.-P. Muller, The advanced radiometric ray-tracer: ARARAT for plant canopy reflectance simulation, *Proc. 29th Conf. Int. Soc. Photogramm. Remote Sens.*, 26–34, 1992.

Li, X., and A. H. Strahler, Geometric-optical bidirectional reflectance modeling of the discrete crown vegetation canopy: effect of crown shape and mutual shadowing, *IEEE Trans. Geosci. Remote Sens., 30*, 276–292, 1992.

Li, Z., and L. Garand, Estimation of surface albedo from space: A parametrization for global application, *J. Geophys. Res., 99*, 8335–8350, 1994.

Li, Z., X. Zheng, L. Moreau, and H. Ly, Detection and correction of bidirectional effects in AVHRR measurements over northern regions, *IEEE Trans. Geosci. Remote Sens.*, in press, 1996.

Liang, S., A. H. Strahler, Q. Zhu, and X. Jin, Comparisons of radiative transfer models of vegetation canopies and laboratory measurements, *IEEE Trans. Geosci. Remote Sens.*, in press, 1996.

Moody, A., and A. H. Strahler, Characteristics of composited AVHRR data and problems in their classification, *Int. J. Remote Sens., 15*, 3473–3491, 1994.

Myneni, R. B., Asrar, G., and F. G. Hall, A three-dimensional radiative transfer method for optical remote sensing of vegetated land surfaces, *Remote Sens. Env., 41*, 105–121, 1992.

Nilson, T., and A. Kuusk, A reflectance model for the homogeneous plant canopy and its inversion, *Remote Sens. Env., 27*, 157–167, 1989.

Nicodemus, F. E., J. C. Richmond, J. J. Hsia, I. W. Ginsberg, and T. Limperis, Geometrical considerations and nomenclature for reflectance, *Nat. Bureau Stand. Report, NBS MN-160*, 52 pp., 1977.

Pinty, B., and M. M. Verstraete, Extracting information on surface properties from bidirectional reflectance measurements, *J. Geophys. Res, 96*, 2865–2874, 1991.

Pinty, B., M. M. Verstraete, and R. E. Dickinson, A physical model for predicting bidirectional reflectance over bare soil, *Remote Sens. Env., 27*, 273–288, 1989.

Privette, J. L., and E. F. Vermote, Fitting remote sensing data with linear bidirectional reflectance models, *Proc. SPIE Symp. Sat. Remote Sens., 2586*, 172–179, 1995.

Rahman, H., B. Pinty, and M. M. Verstraete, Coupled surface-atmosphere reflectance (CSAR) model, 2, Semiempirical surface model usable with NOAA advanced very high resolution radiometer data, *J. Geophys. Res., 98*, 20,791–20,801, 1993.

Ranson, K. J., L. L. Biehl, and M. E. Bauter, Variation in spectral response of soybeans with respect to illumination, view and canopy geometry, *Int. J. Remote Sens., 6*, 1827–1842, 1985.

Ranson, K. J., J. R. Irons, and C. S. T. Daughtry, Surface albedo from bidirectional reflectance, *Remote Sens. Env., 35*, 201–211, 1991.

Ross, J. K., *The Radiation Regime and Architecture of Plant Stands*, 392 pp., Dr. W. Junk Publishers, The Hague, 1981.

Roujean, J. L., M. Leroy, and P. Y. Deschamps, A bidirectional reflectance model of the earth's surface for the correction of remote sensing data, *J. Geophys. Res., 97*, 20,455–20,468, 1992.

Roujean, J.-L., D. Tanre, F.-M. Breon, and J.-L. Deuze, An improved land surface parameters retrieval from POLDER bidirectional measurements during HAPEX-Sahel, *Proc. Int. Geosci. Remote Sens. Symp. 95*, 1293–1295, 1995.

Running, S. W., E. R. Hunt, R. Nemani, and J. Glassy, MODIS leaf area index and fraction photosynthetically active radiation: Algorithm theoretical basis document, *NASA EOS-MODIS Doc.*, 21 pp., 1995.

Running, S. W., C. O. Justice, V. Salomonson, D. Hall, J. Barker, Y. J. Kaufman, A. H. Strahler, A. R. Huete, J.-P. Muller, V. Vanderbilt, Z. M. Wan, P. Teillet, and D. Carneggie, Terrestrial remote sensing science and algorithms planned for EOS/MODIS, *Int. J. Remote Sens., 15*, 3587–3620, 1994.

Sellers, P. J., Remote sensing of the land surface for studies of global change, *NASA/GSFC Int. Sat. Land Surf. Clim. Proj. Report*, 1993.

Sellers, P. J., C. J. Tucker, G. J. Collatz, S. O. Los, C. O. Justice, D. A. Dazlich, and D. A. Randall, A global 1 degree by 1 degree NDVI data set for climate studies, Part 2, The generation of global fields of terrestrial biophysical parameters from NDVI, *Int. J. Remote Sens., 15*, 3519–3545, 1994.

Soffer, R. J., J. R. Miller, W. Wanner, and A. Strahler, Winter boreal forest canopy BRF results: Comparisons between airborne data, laboratory simulations and geometrical-optical model data, *Proc. Int. Geosci. Remote Sens. Symp. 95*, 800–802, 1995.

Starks, P. J., J. M. Norman, B. L. Blad, E. A. Walter-Shea, and C. L. Walthall, Estimation of shortwave hemispherical reflectance (albedo) from bidirectionally reflected radiance data, *Remote Sens. Env., 38*, 123–134, 1991.

Strahler, A. H., Vegetation canopy reflectance modeling – recent developments and remote sensing perspectives, *Proc. 6th Int. Symp. Phys. Meas. Sign.*, 593–600, 1994.

Strahler, A. H. X. Li, S. Liang, J.-P. Muller, M. J. Barnsley, and P. Lewis, MODIS BRDF/albedo product: Algorithm technical basis document, *NASA EOS-MODIS Doc.*, version 2.1, 55 pp., 1994.

Strahler, A. H., M. J. Barnsley, R. d'Entremont, B. Hu, P. Lewis, X. Li, J.-P. Muller, C. B. Schaaf, W. Wanner, and B. Zhang, MODIS BRDF/albedo product: Algorithm theoretical basis document, *NASA EOS-MODIS Doc. and update*, version 3.2, 65 pp., 1995a.

Strahler, A. H., A. Moody, E. Lambin, A. Huete, C. Justice, J.-P. Muller, S. Running, V. Salomonson, V. Vanderbilt, and Z. Wan, MODIS land cover product: Algorithm technical basis document, *NASA EOS MODIS Doc.*, version 3.1, 42 pp., 1995b.

Strahler, A. H., W. Wanner, Q. Zhu, and X. Jin, Bidirectional reflectance modeling of data from vegetation obtained in the Changchun Solar Simulation Laboratory, *Proc. Int. Geosci. Remote Sens. Symp. 95*, 1965–1967, 1995c.

Vermote, E. F., L. A. Remer, C. O. Justice, Y. J. Kaufman, and D. Tanre, MODIS atmospheric correction algorithm: spectral reflectances, Algorithm technical basis document, *NASA EOS MODIS Doc.*, version 2.0, 42 pp. 1995.

Vermote, E. F., N. El Saleous, C. O. Justice, Y. F. Kaufman, J. L. Privette, L. Remer, J. C. Roger, and D. Tanre, Atmospheric correction of visible to middle infrared EOS-MODIS data over the land surface: background, operational algorithm and validation, *J. Geophys. Res., this issue*, 1996.

Vermote, E. F., D. Tanre, J. L. Deuze, M. Herman, and J. J. Morcrette, Second simulation of the satellite signal in the solar spectrum: an overview, *IEEE Trans. Geosci. Remote Sens.*, in press, 1996.

Walthall, C. L., J. M. Norman, J. M. Welles, G. Campbell, and B. L. Blad, Simple equation to approximate the bidirectional reflectance from vegetation canopies and bare soil surfaces, *Appl. Opt., 24*, 383–387, 1985.

Wanner, W., X. Li, and A. H. Strahler, On the derivation of kernels for kernel-driven models of bidirectional reflectance, *J. Geophys. Res., 100*, 21077–21090, 1995a.

Wanner, W., A. H. Strahler, J.-P. Muller, M. Barnsley, P. Lewis, X. Li, and C. L. Barker Schaaf, Global mapping of bidirectional reflectance and albedo for the EOS MODIS project: the algorithm and the product, *Proc. Int. Geosci. Remote Sens. Symp. 95*, 525–529, 1995b.

Wanner, W., P. Lewis, and J.-L. Roujean, The influence of directional sampling on bidirectional reflectance and albedo retrieval using kernel-driven models, *Proc. Int. Geosci. Remote Sens. Symp. 96*, 1408–1410, 1996.

Whittaker, E., and G. Robinson, *The Calculus of Observations*, Blachie and Son, Glasgow, 397 pp., 1960.

White, H. P., R. Soffer, J. R. Miller, and W. Wanner, Semiempirical modeling of bidirectional reflectance utilizing the MODIS BRDF/albedo algorithm models *Proc. Int. Geosci. Remote Sens. Symp. 96*, 1411–1413, 1996.

Wu, A., Z. Li, and J. Cihlar, Effects of land cover type and greenness on advanced very high resolution radiometer bidirectional reflectances: Analysis and removal, *J. Geophys. Res., 100*, 9179–9192, 1995.

Wylie, D. P., and W. P. Menzel, Two years of cloud cover statistics using VAS, *J. Climate, 2*, 380–392, 1989.

Wylie, D. P., W. P. Menzel, H. M. Woolf, and K. I. Strabala, Four years of global cirrus cloud statistics using HIRS, *J. Climate, 7*, 1972–1986, 1994.

Zhang, Y.-C., W. B. Rossow, and A. A. Lacis, Calculation of surface and top of atmosphere radiative fluxes from physical quantities based on ISCCP data sets, 1. Method and sensitivity to input data set uncertainties, *J. Geophys. Res., 100*, 1149–1165, 1995.

Table 1: Percent RMS Error Ranges in BRDF and Bihemispherical Albedo Retrieval Using Lambertian and Non-Lambertian Assumptions in Atmospheric Correction and Different Optical Depths τ.

		$\tau = 0.15$		$\tau = 0.30$		$\tau = 0.50$	
	Band	Lambertian	non-Lamb.	Lambertian	non-Lamb.	Lambertian	non-Lamb.
BRDF	red	2.3–5.2	0.4–1.3	5.9–10.6	0.7–2.9	7.4–16.2	1.6–5.9
	NIR	1.5–5.7	0.1–0.7	2.7–7.7	0.4–2.5	4.1–14.2	1.2–6.2
Bihem.	red	1.8–7.1	0.2–1.4	0.8–9.5	0.3–1.7	1.8–14.6	0.3–3.6
Albedo	NIR	1.0–1.9	0.2–0.8	1.0–3.0	0.3–0.6	0.5–5.1	0.5–1.5

The ranges given correspond to three different shapes of the BRDF: one that is dominated by volume scattering, one that is dominated by surface scattering, and one that is a mix of the two.

Table 2: Ambrals Model Kernel Combinations to be Used in Generating the MODIS BRDF/Albedo Product.

	Model	Applicable Scene Type	LAI	b/r	h/b
1.	Ross-thin/Li-sparse	scenes dominated by weak volume scattering and simultaneous shadowing	low or very high	1.0	2.0
2.	Ross-thin/Li-dense	scenes dominated by weak volume scattering and simultaneous mutual shadowing	low or very high	2.5	2.0
3.	Ross-thick/Li-sparse	scenes dominated by volume scattering and simultaneous shadowing	moderate	1.0	2.0
4.	Ross-thick/Li-dense	scenes dominated by volume scattering and simultaneous mutual shadowing	moderate	2.5	2.0
5.	Cox-Munk/Li-sparse	scenes dominated by shadowing and simultaneous forward scattering	N/A	1.0	2.0

Note that for each model, the weights attributed to the individual kernels can still range from making volume scattering dominant over surface scattering or vice versa. This may be due to the respective areal proportions of the scene components, or to a mix of the two scattering types in a homogeneous scene.

Table 3: Spectral-to-Broadband Albedo Conversion: Accuracy of Results Based on 7-Band Splines as Compared to Exact Results.

	Exact Results			Band-Based, Deviations		
Cover	total	vis	IR	total	vis	IR
Type	0.4-2.2μm	0.4-0.7μm	0.7-2.2μm	0.4-2.2μm	0.4-0.7μm	0.7-2.2μm
grass	0.22	0.058	0.34	-0.9%	+0.5%	-1.2%
soil	0.18	0.10	0.24	-0.4%	-3.2%	+0.4%
snow	0.84	0.99	0.72	-2.1%	-0.2%	-4.0%

Table 4: Expected BRDF/Albedo Product Accuracy: Median Values and Ranges for 16-Day MODIS and MISR Sampling at Different Latitudes and Times of Year.

Quantity Investigated		Noise Inflation Factor	Interpolation/Extrapolation Error (percent)
Interpolation (sun zenith = mean of obs.)	nadir reflectance	0.21 (0.18–0.28)	3.3 (0.7–8.1)
	black-sky albedo	0.17 (0.15–0.20)	3.1 (0.5–9.6)
Extrapolation (sun zenith = nadir/10°)	nadir reflectance	0.45 (0.17–1.08)	5.9 (0.8–28.7)
	black-sky albedo	0.23 (0.18–0.49)	4.8 (0.8–16.0)
Combined (all sun zeniths)	white-sky albedo	0.31 (0.17–0.82)	6.0 (1.4–14.2)

Table 5: Sample Ambrals Model Fit Accuracies Using Field-Measured BRDFs of Several Different Land Cover Types in the Red and NIR Bands.

Cover Type	Source	Best-fit Kernels	RMSE (%)	r (red,%)	r (NIR,%)
Needleleaf and Broadleaf Forests					
Dense hardwood forest	Kimes	Ross-thick/Li-dense	3.0	0.90	0.89
Dense pine forest	Kimes	Ross-thin/Li-dense	4.1	0.78	0.72
Aspen forest	Deering	Ross-thick/Li-sparse	2.5	0.92	0.88
Spruce forest	Deering	Ross-thick/Li-sparse	1.1	0.95	0.94
Barren, Soil, Sparse Vegetation					
Plowed Field	Kimes	Ross-thick/Li-sparse	1.6	0.98	0.98
Annual grass (cover. ¡5%)	Kimes	Ross-thick/Li-sparse	2.3	0.95	0.88
Steppe grass (coverage 18%)	Kimes	Ross-thick/Li-sparse	2.4	0.89	0.92
Grasses, Grasslike Crops					
Grass lawn	Kimes	Ross-thin/Li-dense	4.6	0.72	0.84
Irrigated wheat	Kimes	Ross-thick	3.7	0.91	0.92
Orchard grass	Kimes	Ross-thick/Li-sparse	3.1	0.84	0.91
Broadleaf Crops					
Soybeans (coverage 72%)	Ranson	Ross-thick/Li-sparse	1.7	0.75	0.89
Soybeans (coverage 99%)	Ranson	Ross-thick	1.1	0.91	0.93
Soybeans (coverage 90%)	Kimes	Ross-thick/Li-sparse	4.3	0.78	0.81
Corn (coverage 25%)	Kimes	Ross-thin/Li-dense	2.8	0.47	0.75

Sources: Deering = *Deering et al.* [1995]; Ranson = *Ranson et al.* [1985]; Kimes = *Kimes* [1983], *Kimes et al.* [1985, 1986].

Table 6: Expected Relationship Matrix of Ambrals Kernels to Land Cover Types.

Models composed of the following two kernels (left+down):	Li-sparse kernel: sparse distinct crowns/objects	Li-dense kernel: dense distinct crowns/objects	low weight for Li-kernels: no distinct crowns
low weight for Ross-kernels: no leaf-level scattering	plowed fields, rock-strewn lands, rugged topography; mosaics of these with sparse woodlands	dense buildings	Lambertian surface
Ross-thin kernel: thin layer of leaves	sparse woodlands or brush, no understory, deciduous forests in winter, young broadleaf crops	forests, dense brush; mosaics of these with sparse grass	sparse grass
Ross-thick kernel: thick layer of leaves	sparse woodlands or brush with understory, broadleaf crops, clumps of vegetation; mosaic of grasses or other dense layered vegetation and trees	grasses, dense vegetation; mosaics of these with forests	grasses, grasslike crops
Cox-Munk kernel: specular reflectance	subpixel water, ice, irrigated fields with sparse forest, brush or rugged topography	N/A	water, ice

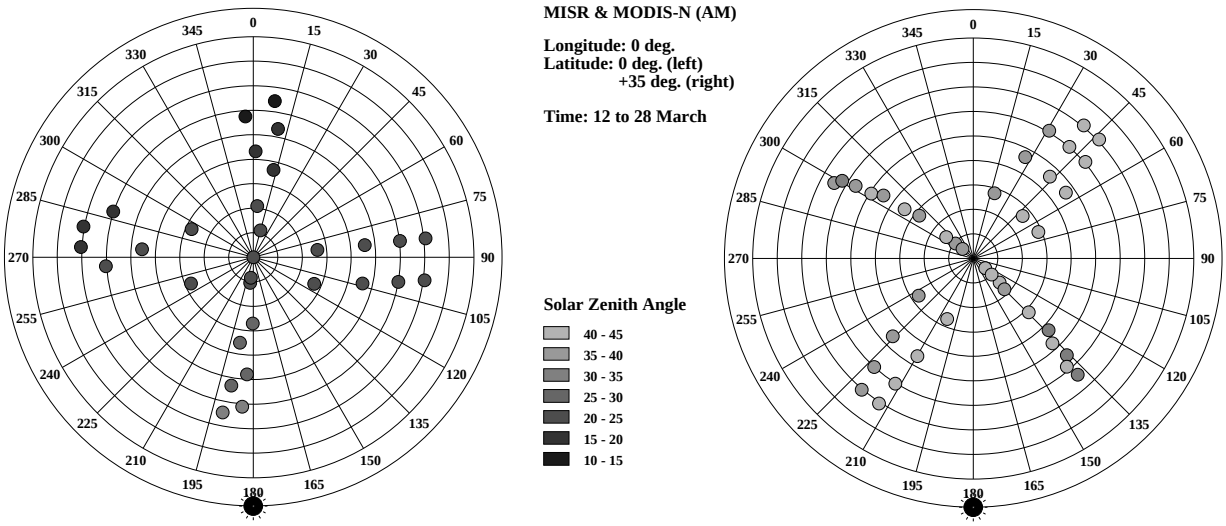

Figure 1: Distribution of observations from MODIS and MISR in the viewing hemisphere. The time period is 12 March to 28 March (16 days). The left plot is for the equator; MODIS observations are close to the principal plane, MISR observations are on the cross-principal plane. The right plot is for a latitude of 35° north; both MODIS and MISR are sampling away from the principal plane, with MISR a little closer to it. Further north MISR is closer to the principal plane. The solar zenith angle range in both cases is about 15 degrees. Data and plots produced by the Xsatview software (M. Barnsley and K. Morris, University College London) from approximate representations of the satellite orbits.

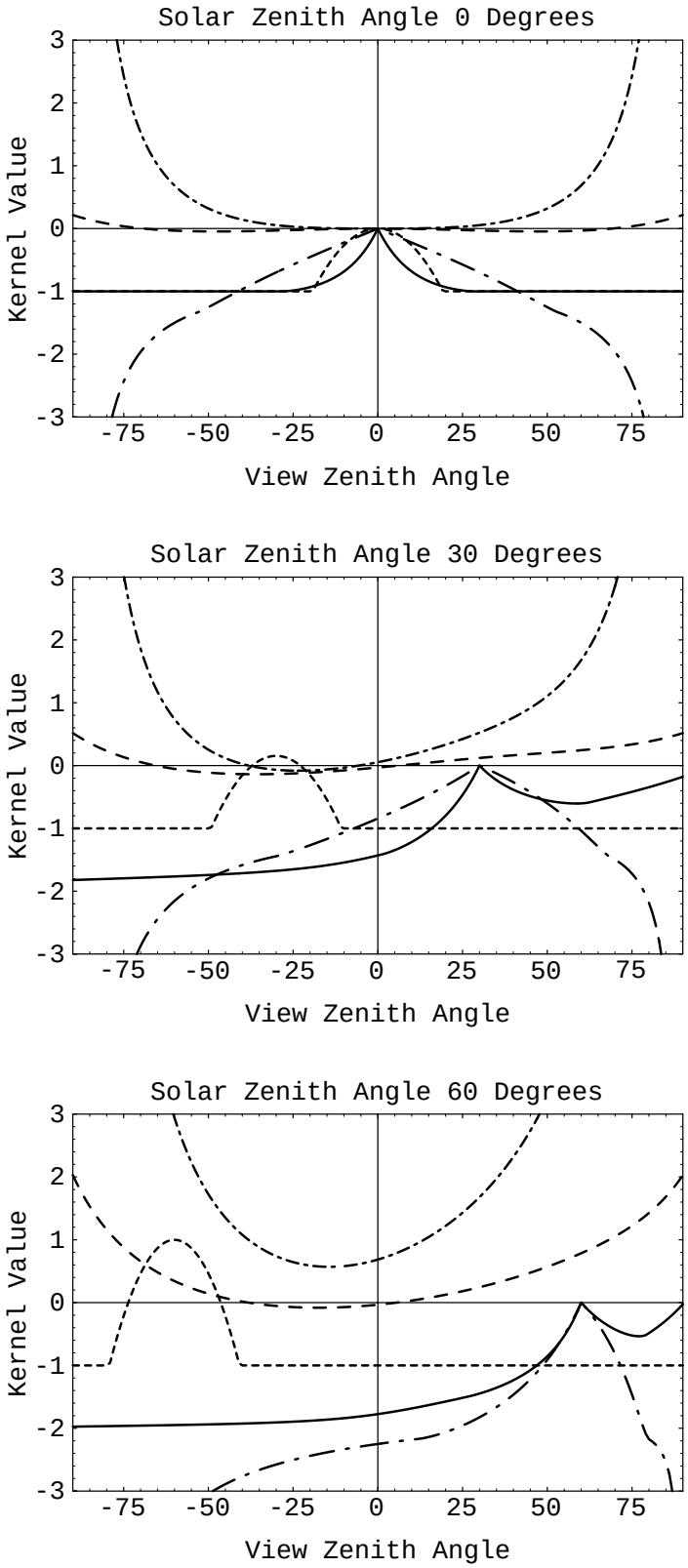

Figure 2: Principal plane values of the kernels for three different solar zenith angles. Dash-dot pattern, Ross-thin; dash pattern, Ross-thick; short dash pattern, specular; solid, Li-dense; long dash-dot, Li-sparse. The Li-sparse kernel is calculated for $b/r = 1$ and $h/b = 2$ (round, low crown), the Li-dense kernel for $b/r = 2.5$ and $h/b = 2$ (prolate, high crown).

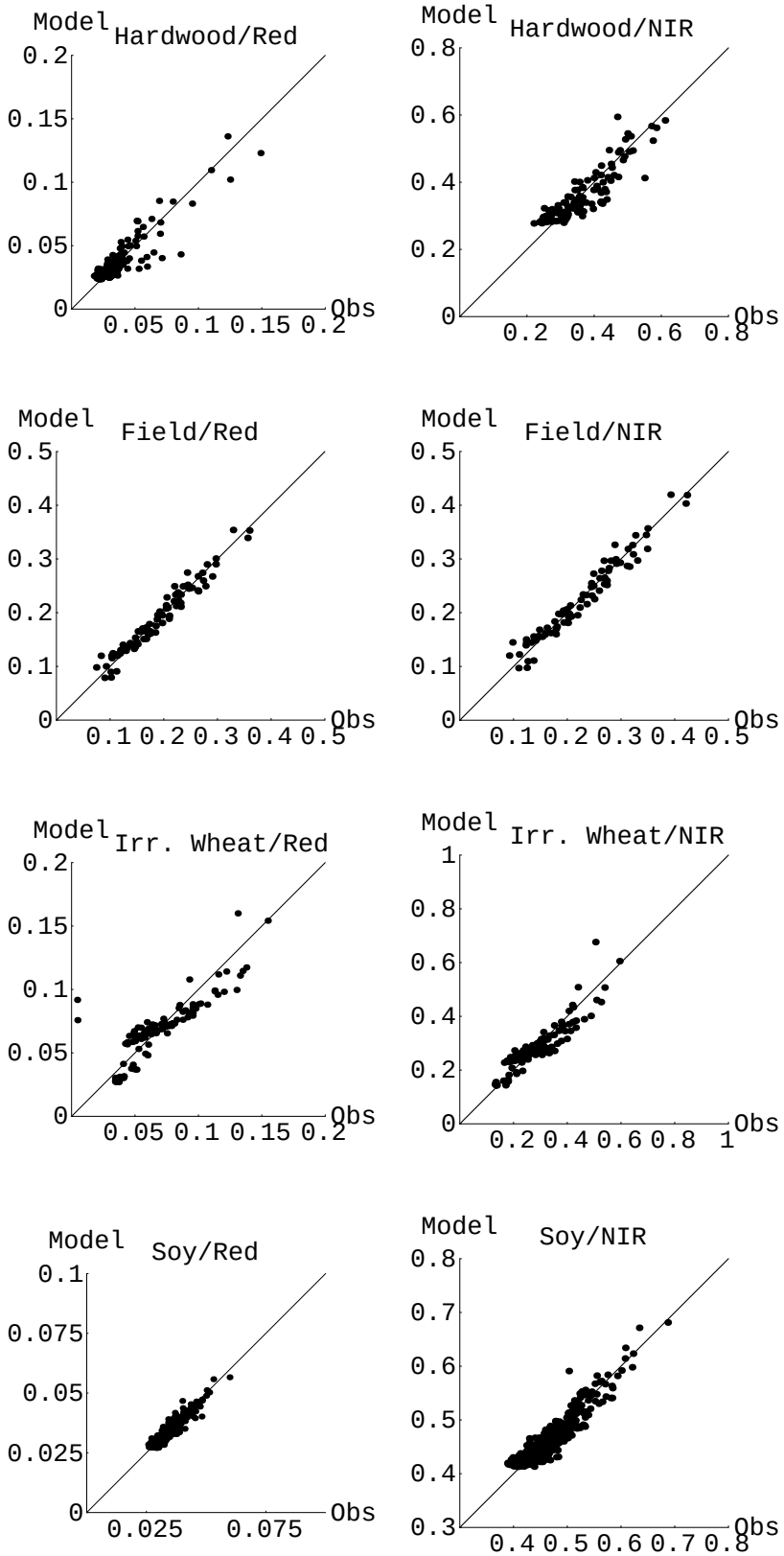

Figure 3: Observed versus modeled reflectances in the red and near-infrared bands for four distinct types of land cover. Forests are represented by a dense hardwood forest (coverage 79 percent), barren terrain by a plowed field, grasslike vegetation by dense (irrigated) wheat (coverage 70 percent, leaf area index 4.0), and broadleaf non-forest vegetation by a soybean data set (coverage 99 percent, leaf area index 2.9). The first three data sets were observed by *Kimes et al.* [1985, 1986], the latter by *Ranson et al.* [1985]. In the first data set, the Li-dense kernel is predominant, in the second the Li-sparse kernel. In the third and fourth data sets the Ross-thick kernel is predominant.

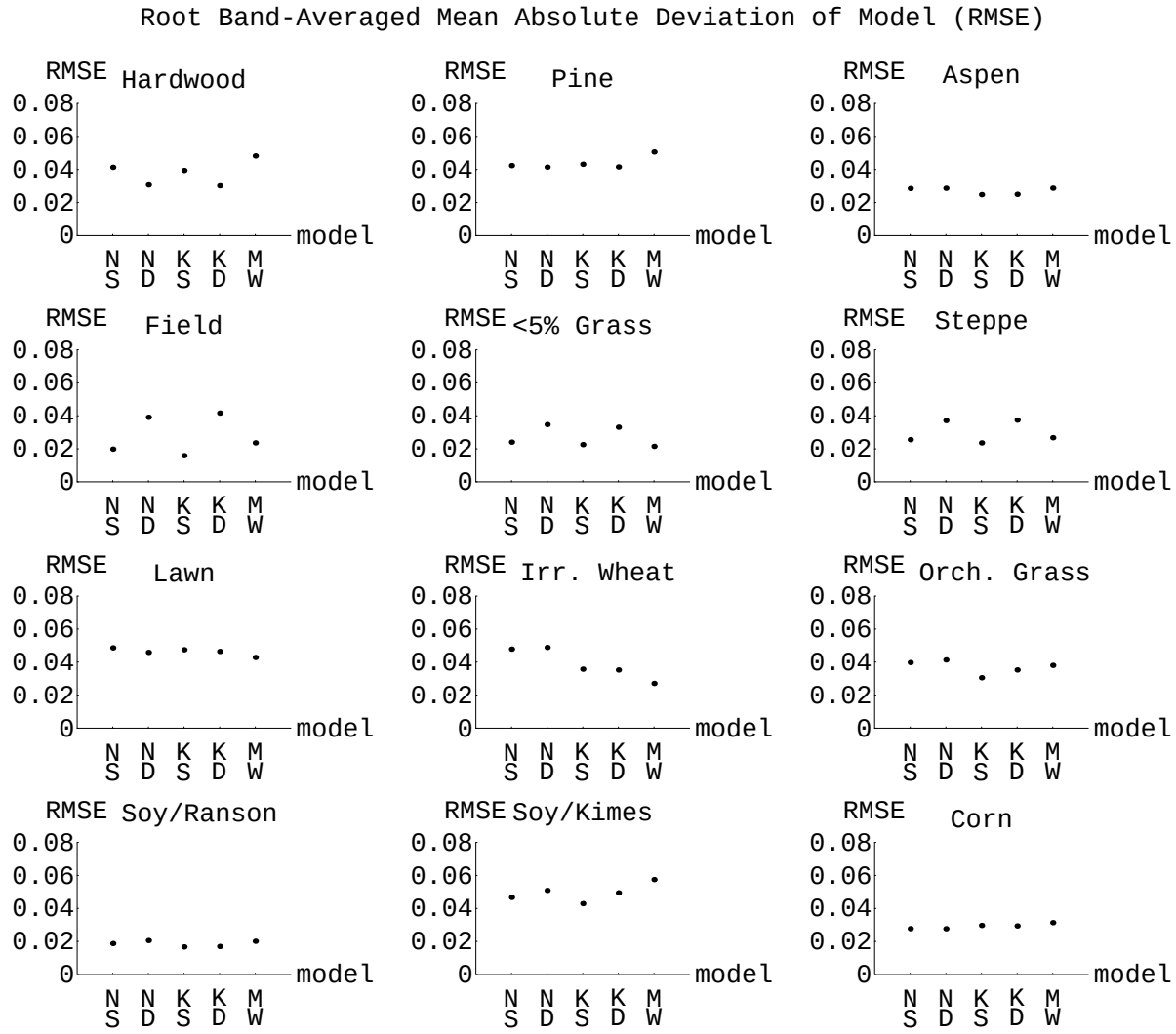

Figure 4: Root band averaged mean square errors (RMSE) of fitting five kernel-based BRDF model variants to bidirectional reflectance data measured by *Kimes* [1983], *Kimes et al.* [1985, 1986], *Deering et al.* [1995] and *Ranson et al.* [1985] for 4 different land cover types: top, forests; second row, barren or sparsely vegetated; third row, grasses and grasslike crops; bottom, broadleaf crops. Model codes are: N, Ross-thin; K, Ross-thick; S, Li-sparse; D, Li-dense; MW, modified Walthall.

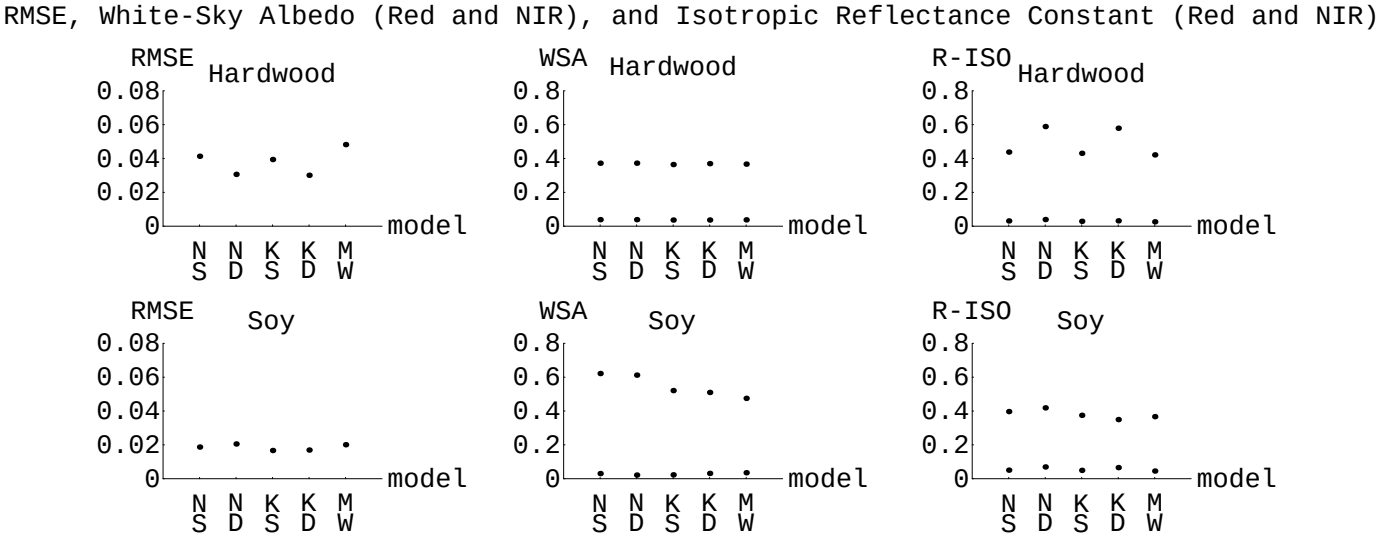

Figure 5: Root band-averaged mean square errors (RMSE), white-sky albedo (WSA) and the isotropic model constant f_i (nadir sun and view reflectances, R-ISO) of five kernel-based BRDF model variants to bidirectional reflectance data measured by *Kimes et al.* [1986], and *Ranson et al.* [1985] for two different land cover types: forest and broadleaf crop. Model codes are: N, Ross-thin; K, Ross-thick; S, Li-sparse; D, Li-dense; MW, modified Walthall.

APPENDIX F:
ASAS SCALING EXPERIMENTS FOR BRDF MODEL INVERSION (SUMMARY OF A PAPER BY MULLER AND DISNEY)

ASAS Scaling Experiments for BRDF Model Inversion (Summary of a Paper by Muller and Disney)

It is extremely difficult to extrapolate surface canopy directional reflectance measurements to pixel IFoVs of 250m–1km which will be available with MODIS/MISR. Similarly it is important to establish what the linearity ranges of BRDF model inversions are if we are to set up a global validation network for MODIS/MISR-based BRDF or albedo.

There are two sources of airborne data which can be used to establish the scaling properties of the "Ambrals" models: ASAS (Irons et al., 1991) and POLDER (Roujean et al., 1996) .

Preliminary results are presented here for the use of ASAS data to investigate these scaling properties. A more comprehensive description of these experimental results will be described in (Muller and Disney, 1997).

ASAS data has been geometrically registered to sub-pixel accuracy using the methods described in (Allison et al., 1994; Allison and Muller, 1992; Barnsley et al., 1995) . A schematic diagram of the method is shown in Figure 1.

Two sites have been studied to date from the HAPEX-SAHEL experiment (Prince et al., 1995) : the Southern Supersite millet area (hereafter referred to as SSS) and the West Central Supersite savannah/millet area (hereafter referred to as WCSS).

The data were all atmospherically corrected using the "6S" scheme with the atmospheric optical depth measurements performed by Halthore (see (Brown de Coulstoun et al., 1996)) by employing the US Standard atmosphere (1961) with a desert type aerosol. The aforementioned authors have suggested the use of a tropical standard atmosphere with continental aerosol model which we have tested and which yields better results. The data is currently being re-processed using this new atmospheric correction data. An example of the "at surface" reflectance is shown for the SSS in Figure 2.

The resultant "at surface" reflectance data were spatially degraded using spatial averaging from the original 3m resolution to 30m, 90m, 240m and 480m. The 9 look angles of ASAS only covered a 1.92 x 1.92 km area so the results at 480m are only marginal. In future the POLDER data with 100m pixels over these same areas will be used to study the scaling up to 1km.

Each set of surface directional reflectances were then inverted using the "Ambrals" models to provide a per-pixel based model inversion. The BRDF models were solely chosen based on their minimum rmse. The results for all four TM-equivalent spectral bands (blue, green, red and NIR) are shown in Figures 3–5 for the SSS and Figures 10–12 for the WCSS, where only resolutions 3m, 90m and 240m were selected here to serve as examples of the more extensive studies. For each model inversion an image was created of the rmse which are shown in Figures 7–9 for SSS and Figures 14–16 for the WCSS.

Histograms of the occurrence of each of the 9 models for each spectral band are shown in Figure 6 for the SSS and Figure 13 for the WCSS.

The SSS model inversions and more clearly in the rmse results show artifacts associated with the number of looks which were available outside of the central region which appear to have an impact on model selection from 3m to 30m. The WCSS show no such artifacts. The SSS millet area indicates that as the resolution is degraded the RossThickLiDense kernels are preferentially chosen over the modified Walthall model. A similar behavior is also observed for the WCSS savannah/millet area with some slight evidence for a change to RossThin at 480m.

The implications of this are that field canopy data or data taken from ASAS may produce different model inversion results than that observed at MODIS/MISR wavelengths. This will be tested for all 6 HAPEX-SAHEL sites in future and the results compared with those from the POLDER instrument.

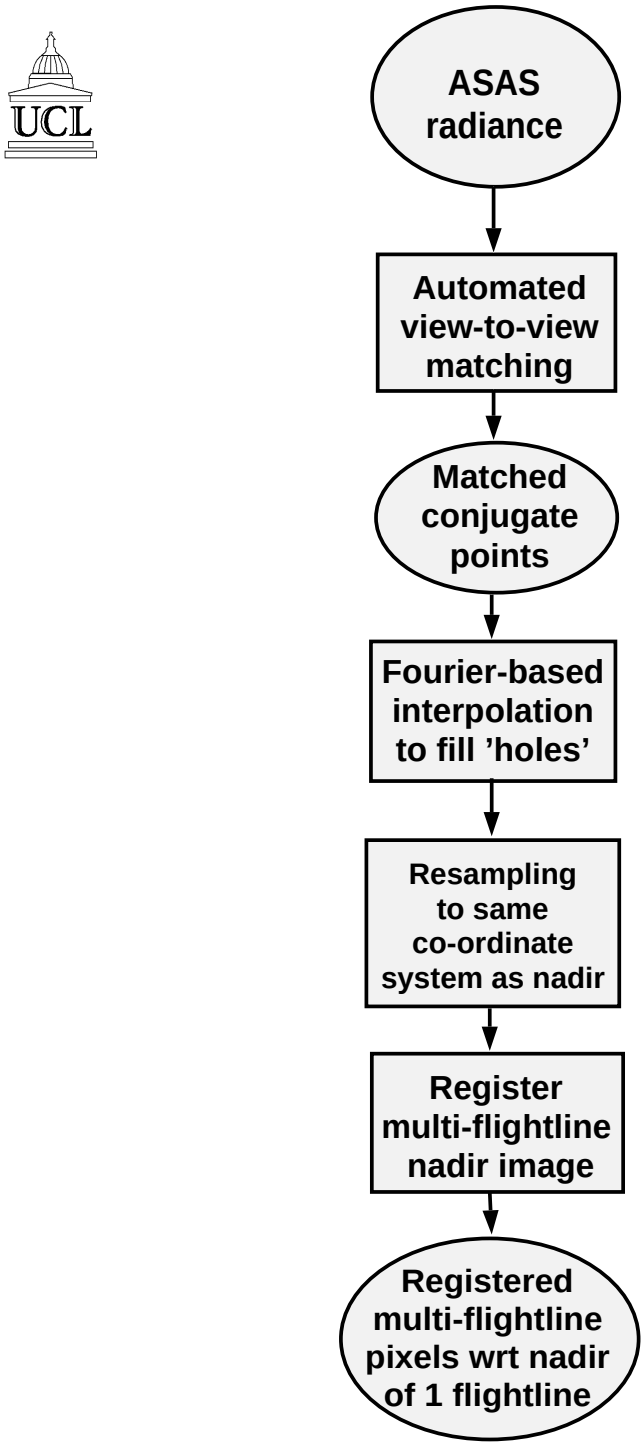

Figure 1: Schematic diagram of sub-pixel registration scheme employed to register multi-flightline ASAS data to the same (nadir) image pixel co-ordinate system.

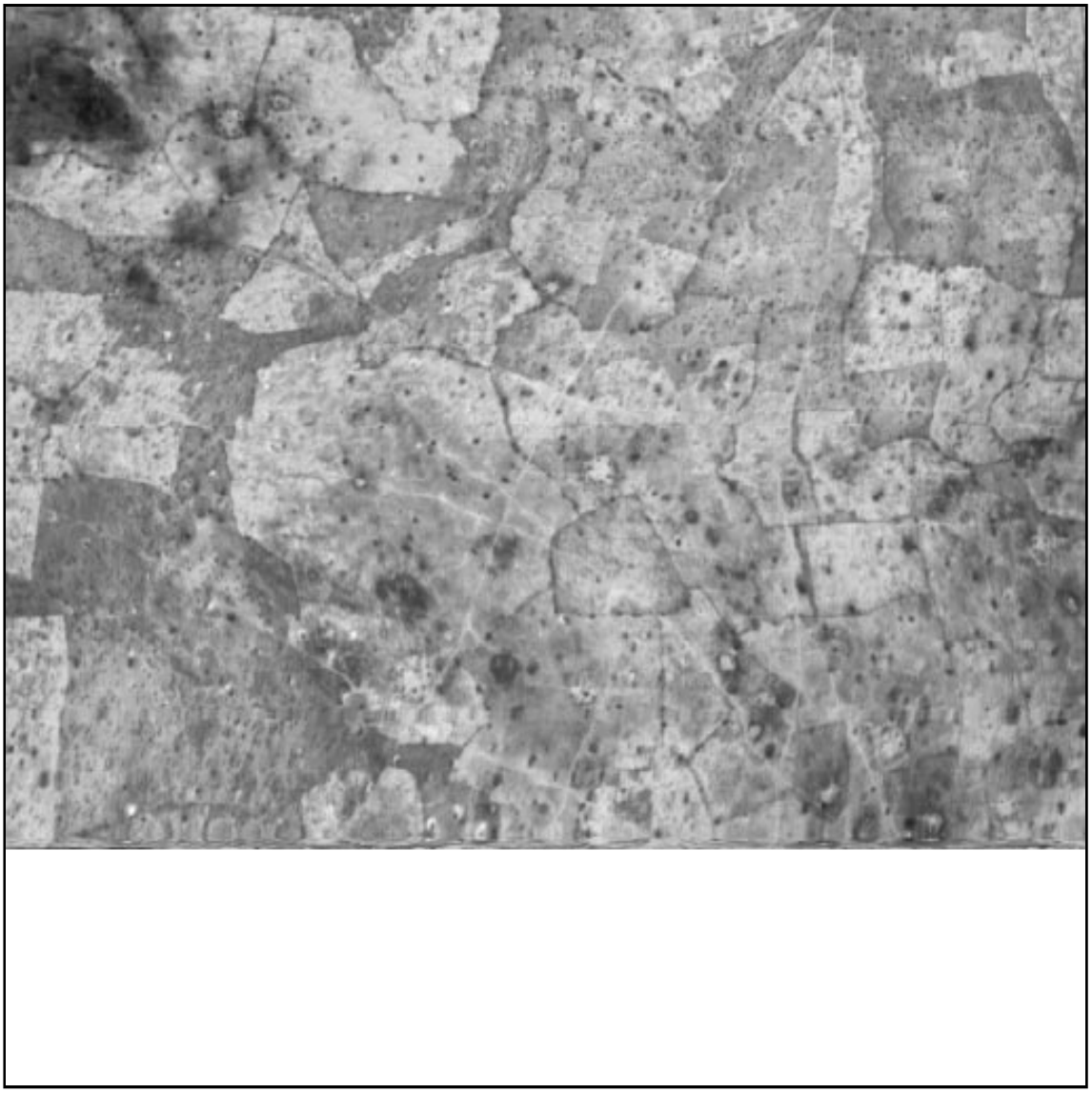

ASAS SSS Millet reflectance image - line 101, row 1, nadir, 3/9/92, green band

Figure 2: Green band (TM 2) ASAS image of nadir for the HAPEX-SAHEL Southern Supersite (SSS) acquired on 3 September 1992.

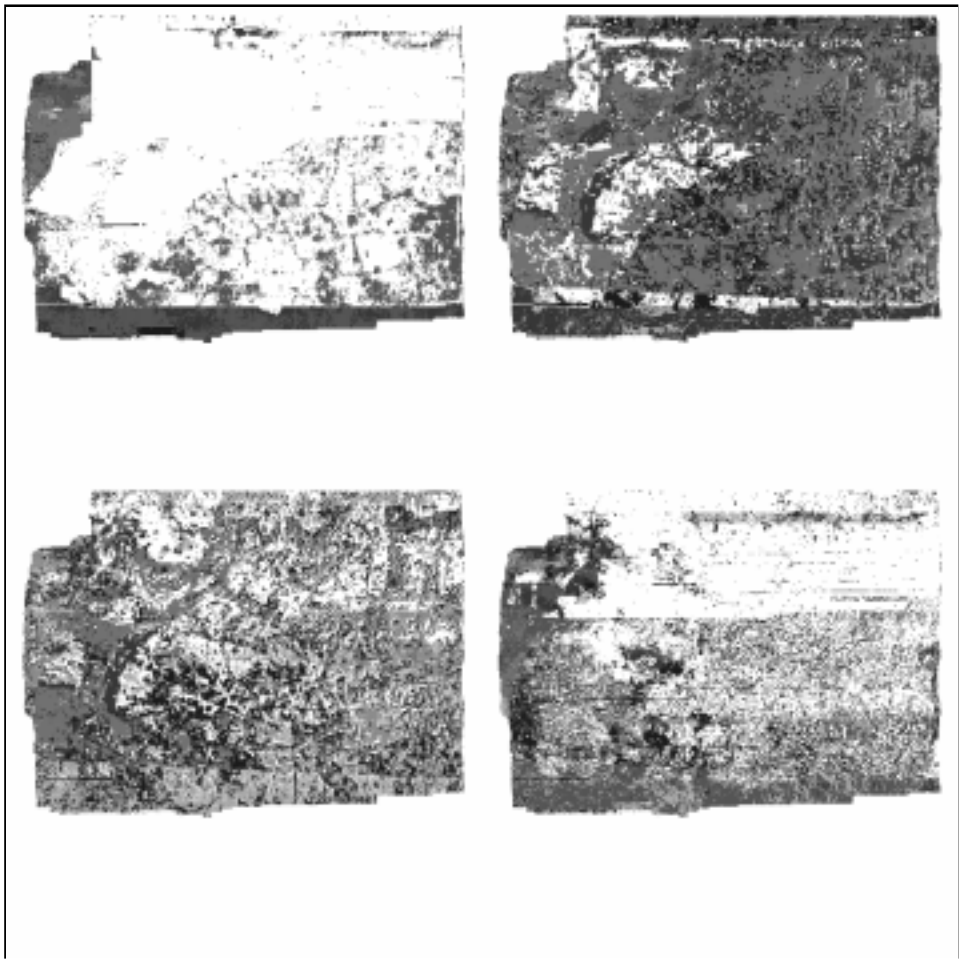

Figure 3: Mosaic of four band inversion SSS images showing model selection for each original 3m pixel from "Ambrals". Notice the dominance of the modified Walthall model selection at the blue and NIR wavelengths.

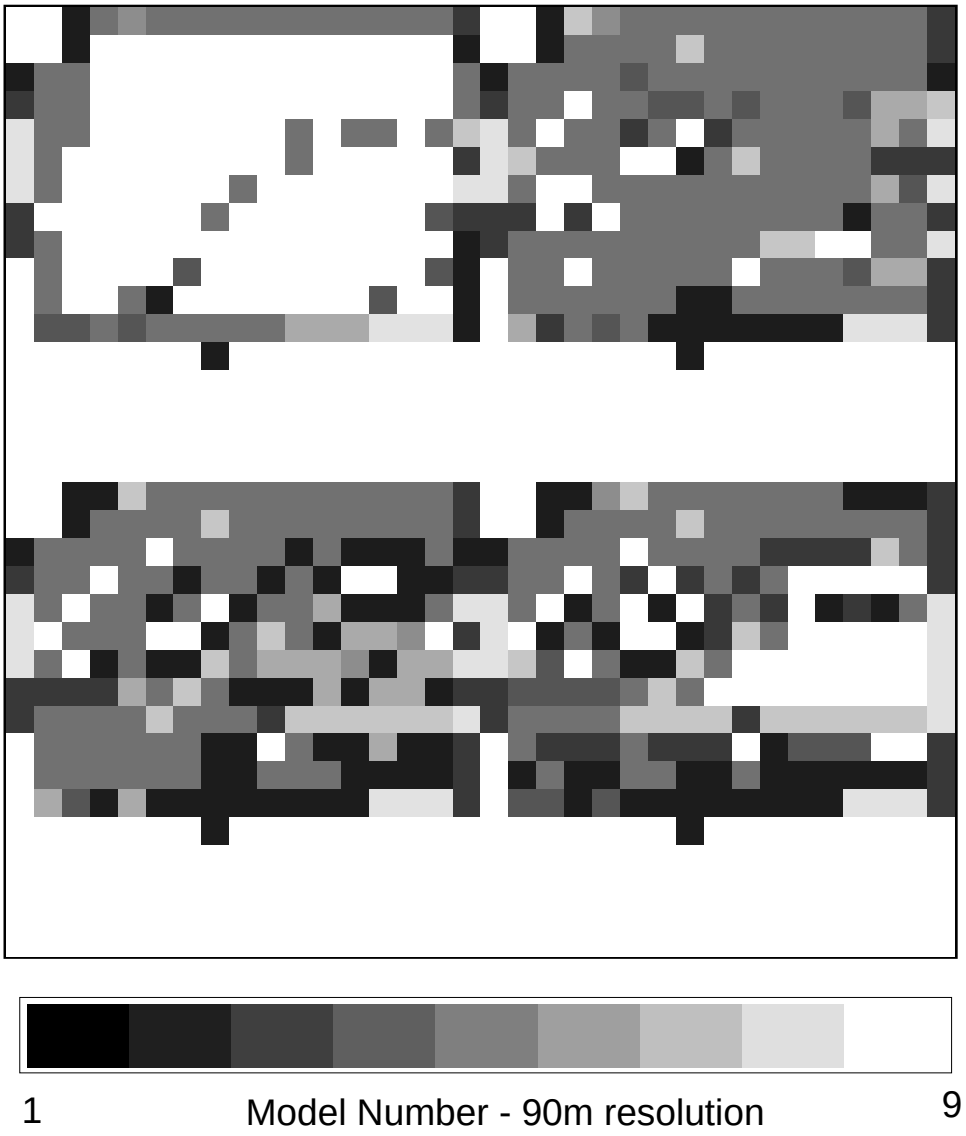

Figure 4: Mosaic of four band inversion SSS images showing model selection for each original 90m averaged pixels from "Ambrals". Notice the dominance of the modified Walthall model selection at the blue wavelength.

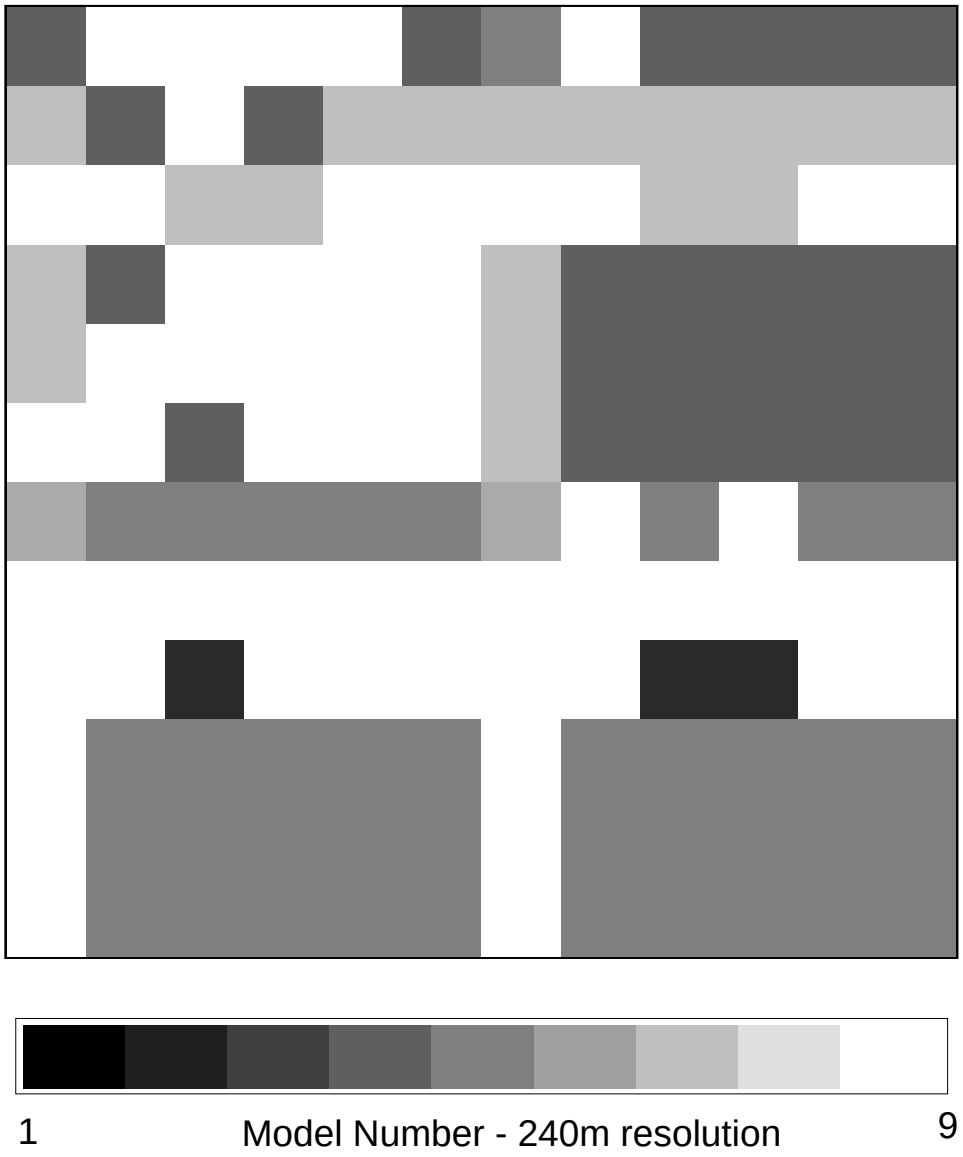

Figure 5: Mosaic of four band inversion SSS images showing model selection for each original 240m averaged pixels from "Ambrals". Notice the dominance of the modified Walthall model selection at the blue wavelength.

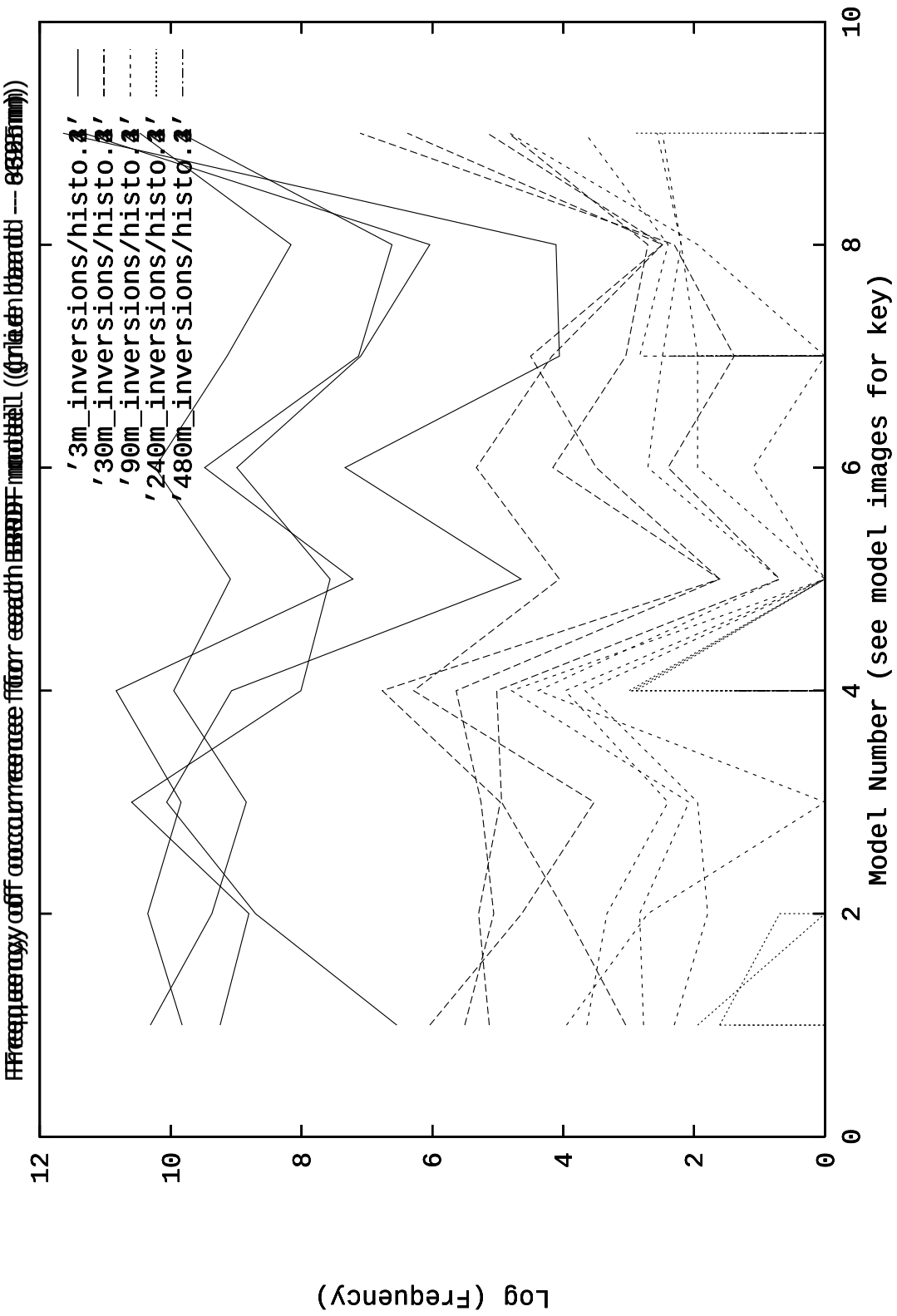

Figure 6: Mosaic of four band inversion SSS histograms showing frequency distribution of model selection. Notice the dominance of the RossThickLiDense kernels which are selected at resolutions ¿30m and for lower resolution the modified Walthall are preferentially selected.

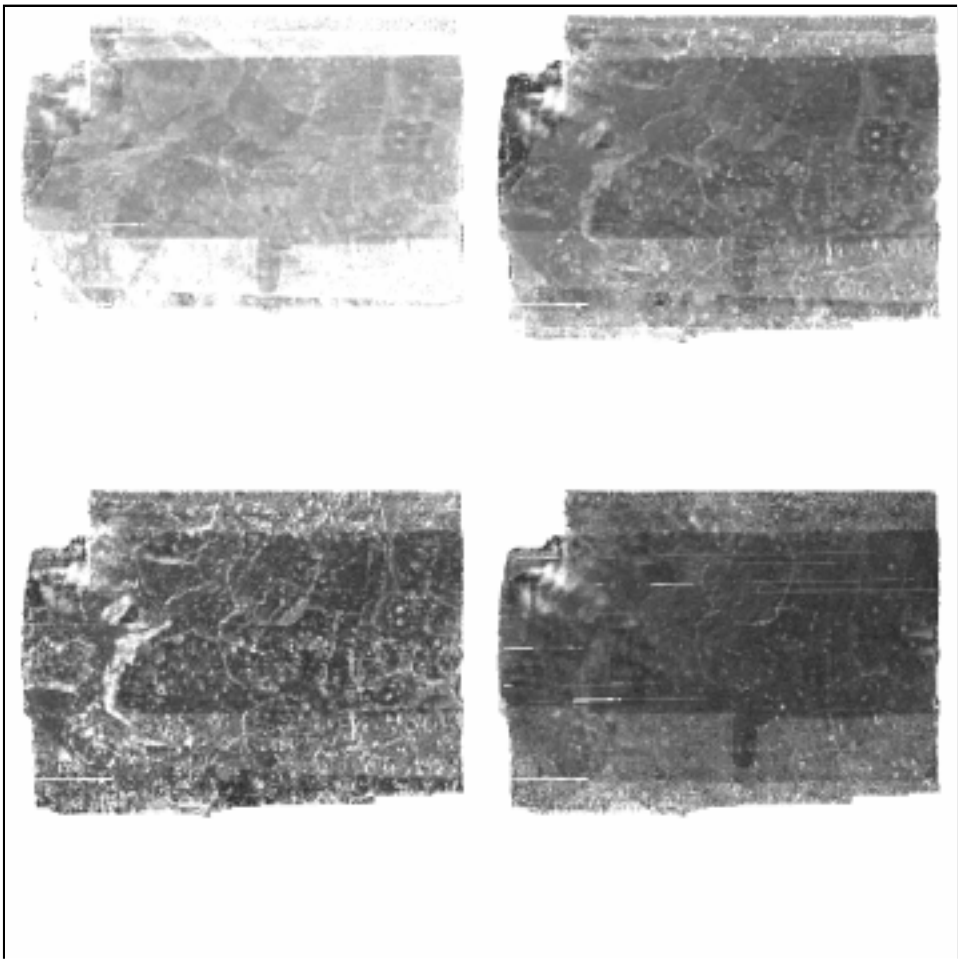

0 RMSE - 3m resolution 0.1

SSS Millet - blue, green, red and nir bands, in raster order, showing the spatial variation of the rmse on which the choice of each model is made.

Stats of each frame:

Blue:	n = 154722 mean = .0047 SD = .002 Min. = 9.3e-05 Max. = .032
Green:	n = 154722 mean = .0040 SD = .001 Min. = 1.4e-04 Max. = .046
Red:	n = 154722 mean = .0052 SD = .002 Min. = 1.7e-04 Max. = .65
NIR:	n = 154722 mean = .0070 SD = .004 Min. = 6.5e-04 Max. = .10

Figure 7: Mosaic of four band SSS rmse showing the rmse with 3m inversions for each model selected. Notice the banding across the centre which represents a greater number of looks than other areas.

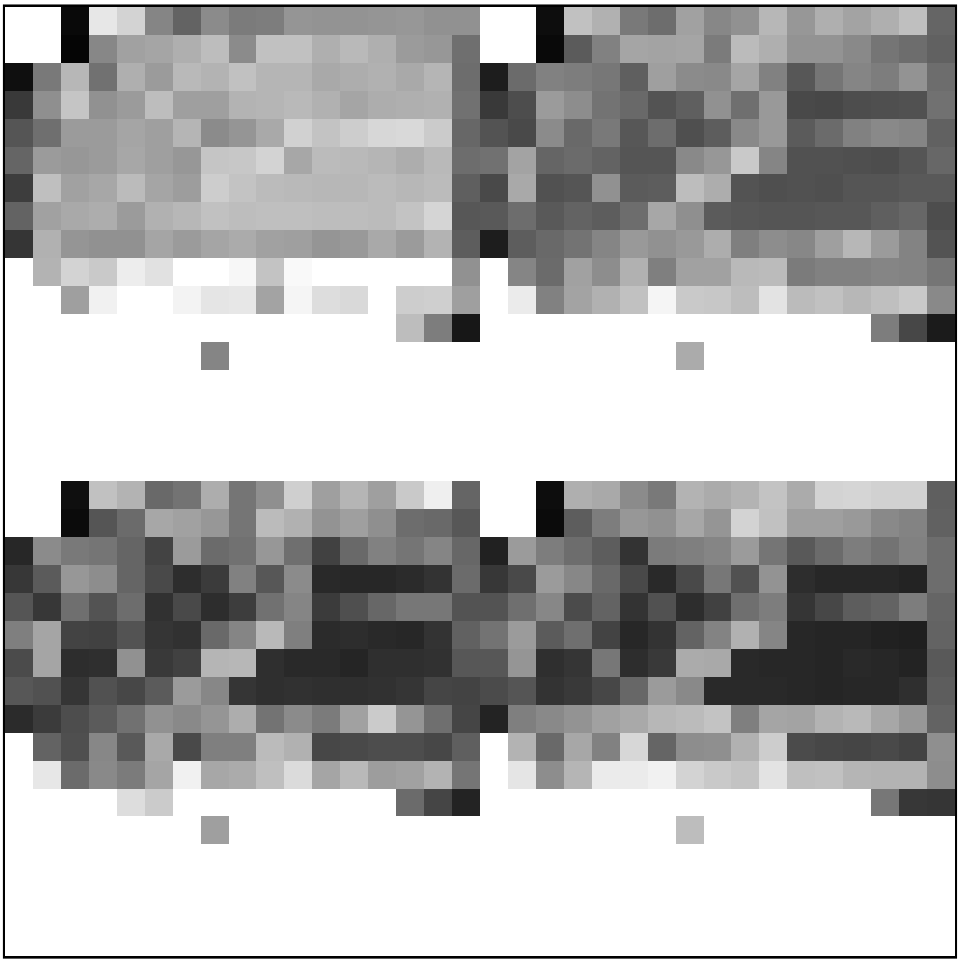

0 RMSE - 90m resolution .051

SSS Millet - blue, green, red and nir bands, in raster order, showing the spatial variation of the rmse on which the choice of each model is made.

Stats of each frame:

Blue: n = 198 mean = .0036 SD = .001 Min. = 1.4e-04 Max. = .0097
Green: n = 198 mean = .0050 SD = .003 Min. = 3.8e-04 Max. = .0178
Red: n = 198 mean = .0073 SD = .005 Min. = 7.0e-04 Max. = .030
NIR: n = 198 mean = .0130 SD = .009 Min. = 13e-04 Max. = .051

Figure 8: Mosaic of four band SSS rmse showing the rmse with 90m inversions for each model selected. Notice the banding is reduced with respect to 3m and 30m inversions across the centre which represents a greater number of looks than other areas.

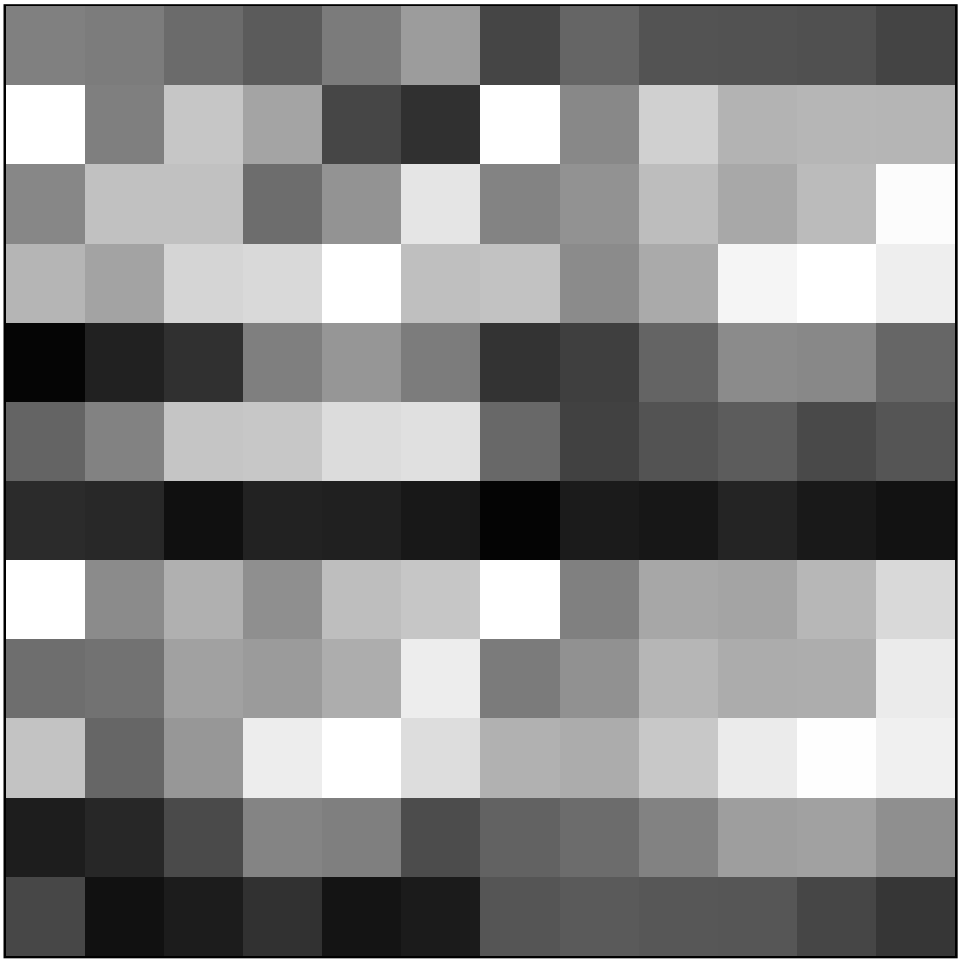

SSS Millet - blue, green, red and nir bands, in raster order, showing the spatial variation of the rmse on which the choice of each model is made.

Stats of each frame:

Blue:	n = 36 mean = .0039 SD = .0007 Min. = 2.1e-03 Max. = .0052
Green:	n = 36 mean = .0066 SD = .0016 Min. = 3.3e-03 Max. = .0096
Red:	n = 36 mean = .0104 SD = .0032 Min. = 6.0e-03 Max. = .0170
NIR:	n = 36 mean = .0190 SD = .0060 Min. = 8.0e-03 Max. = .0291

Figure 9: Mosaic of four band SSS rmse showing the rmse with 90m inversions for each model selected. Notice the banding has now disappeared.

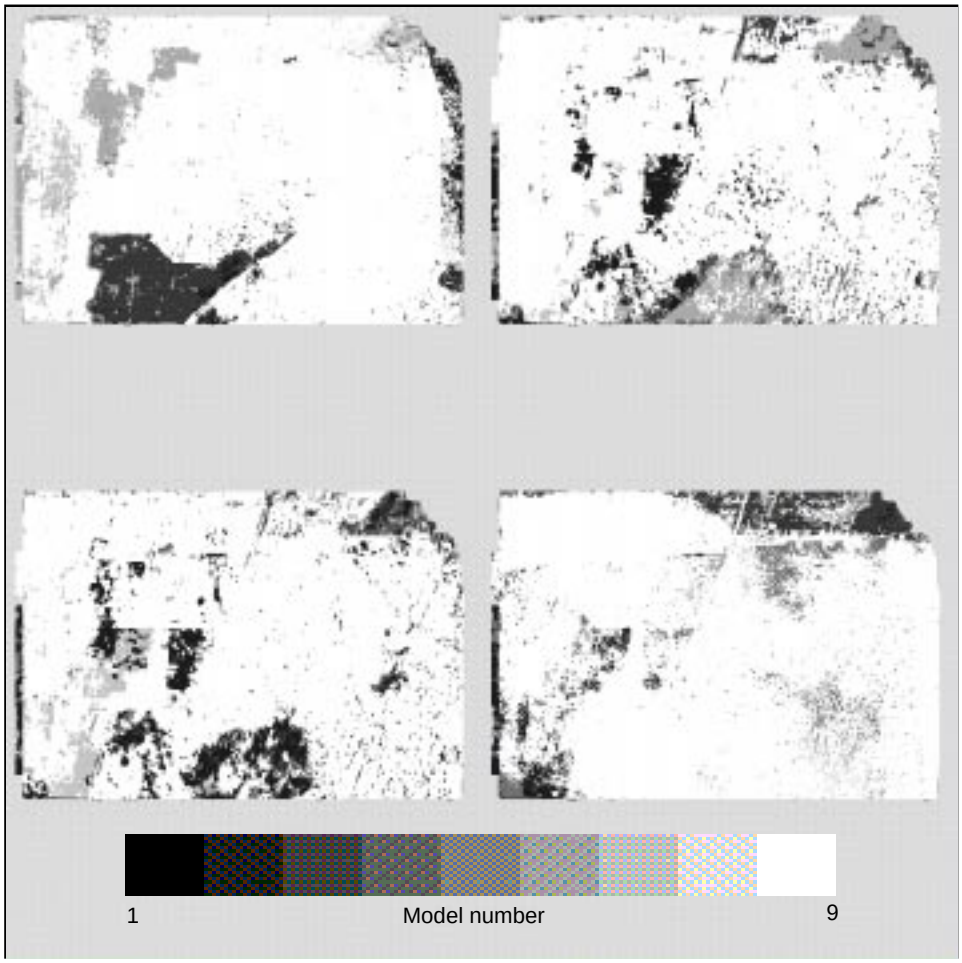

WCSS Fallow - model choice at full (3m) resolution

Blue, green, red and NIR bands, in raster order, showing the spatial variation of the 'best' choice of model in each band, where choice was made on the basis of lowest rmse in each pixel. It is (unsurprisingly) dominated by the Walthall model.

Models are:

1. Isotropic LiDenseModis
2. " LiSparseModis
3. " RossThick
4. " RossThin
5. " RossThick LiDenseModis
6. " RossThick LiSparseModis
7. " RossThin
8. " RossThin LiSparseModis
9. " Walthall (4 parameter)

Figure 10: Mosaic of four band inversion WCSS images showing model selection for each original 3m pixel from "Ambrals". Notice the dominance of the modified Walthall model selection at all wavelengths and the strong contrast only for the lower left corner at blue wavelengths.

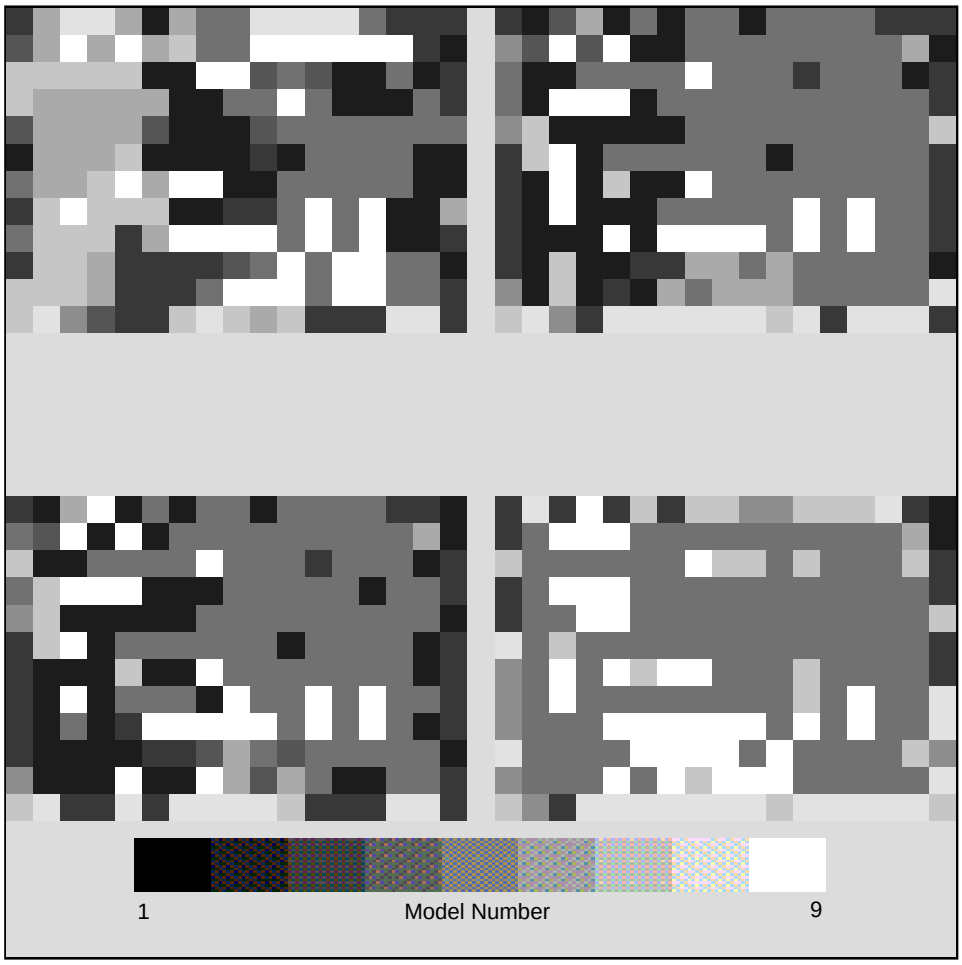

WCSS Fallow - model choice at 90m resolution

Blue, green, red and NIR bands, in raster order, showing the spatial variation of the 'best' choice of model in each band, where choice was made on the basis of lowest rmse in each pixel. It is (unsurprisingly) dominated by the Walthall model.

Models are:

1. Isotropic LiDenseModis
2. " LiSparseModis
3. " RossThick
4. " RossThin
5. " RossThick LiDenseModis
6. " RossThick LiSparseModis
7. " RossThin
8. " RossThin LiSparseModis
9. " Walthall (4 parameter)

Figure 11: Mosaic of four band inversion WCSS images showing model selection for each original 90m pixel from "Ambrals". Notice the dominance of the RossThickLiDense model selection at all wavelengths.

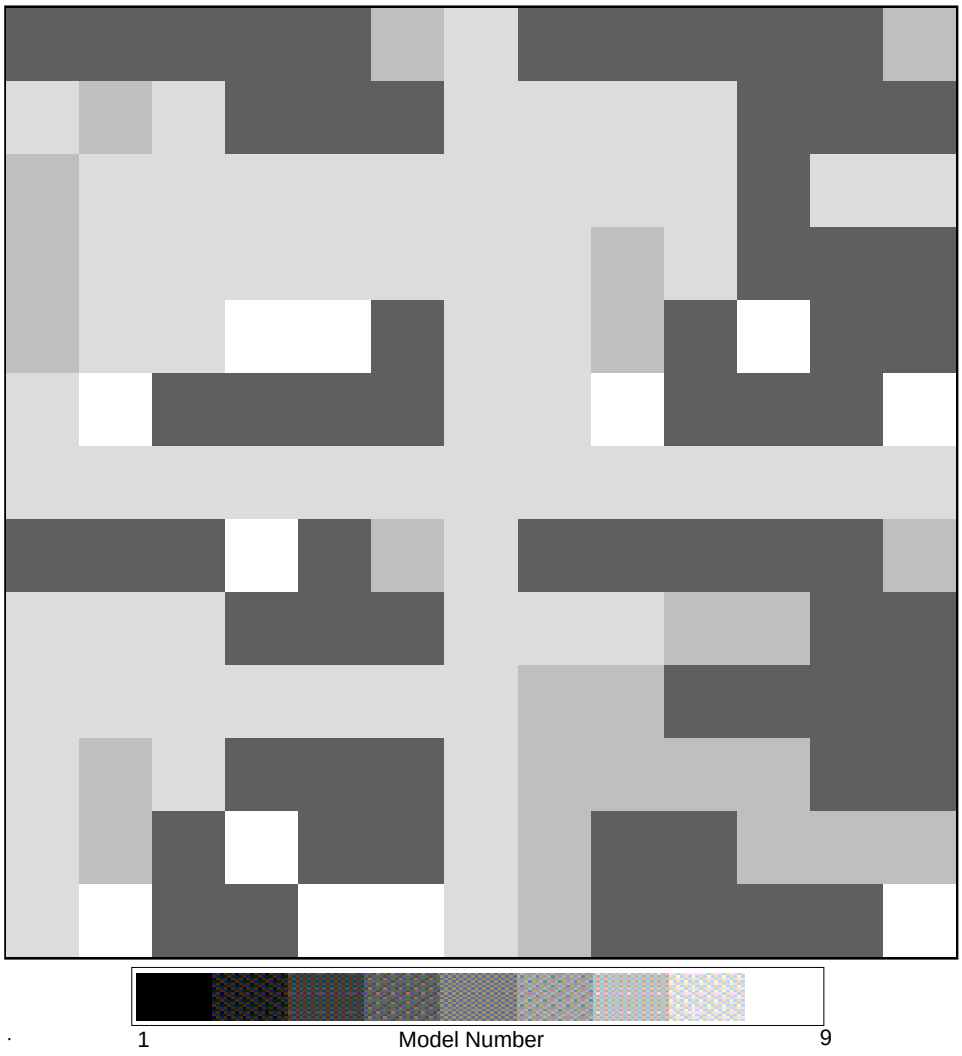

Blue, green, red and NIR bands, in raster order, showing the spatial variation of the 'best' choice of model in each band, where choice was made on the basis of lowest rmse in each pixel. It is (unsurprisingly) dominated by the Walthall model.

Models are:

1. Isotropic LiDenseModis
2. " LiSparseModis
3. " RossThick
4. " RossThin
5. " RossThick LiDenseModis
6. " RossThick LiSparseModis
7. " RossThin
8. " RossThin LiSparseModis
9. " Walthall (4 parameter)

Figure 12: Mosaic of four band inversion WCSS images showing model selection for each original 240m pixel from "Ambrals". Notice the dominance of the RossThickLiDense model selection at all wavelengths.

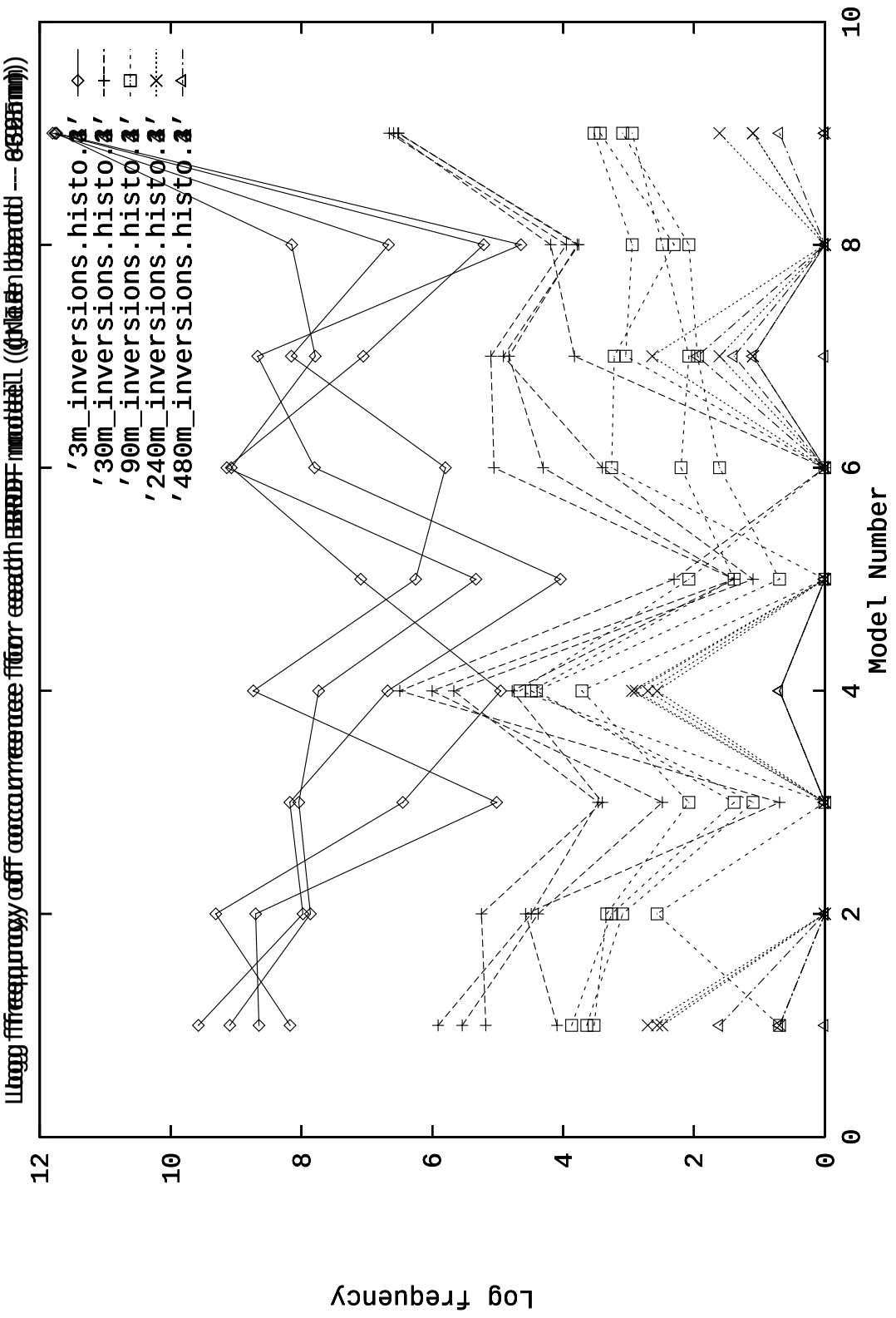

Figure 13: Mosaic of four band inversion WCSS histograms showing frequency distribution of model selection. Notice the dominance of the Walthall model kernels up to 30m and then the RossThickLiDense kernels up to 240m and the RossThin model at 480m.

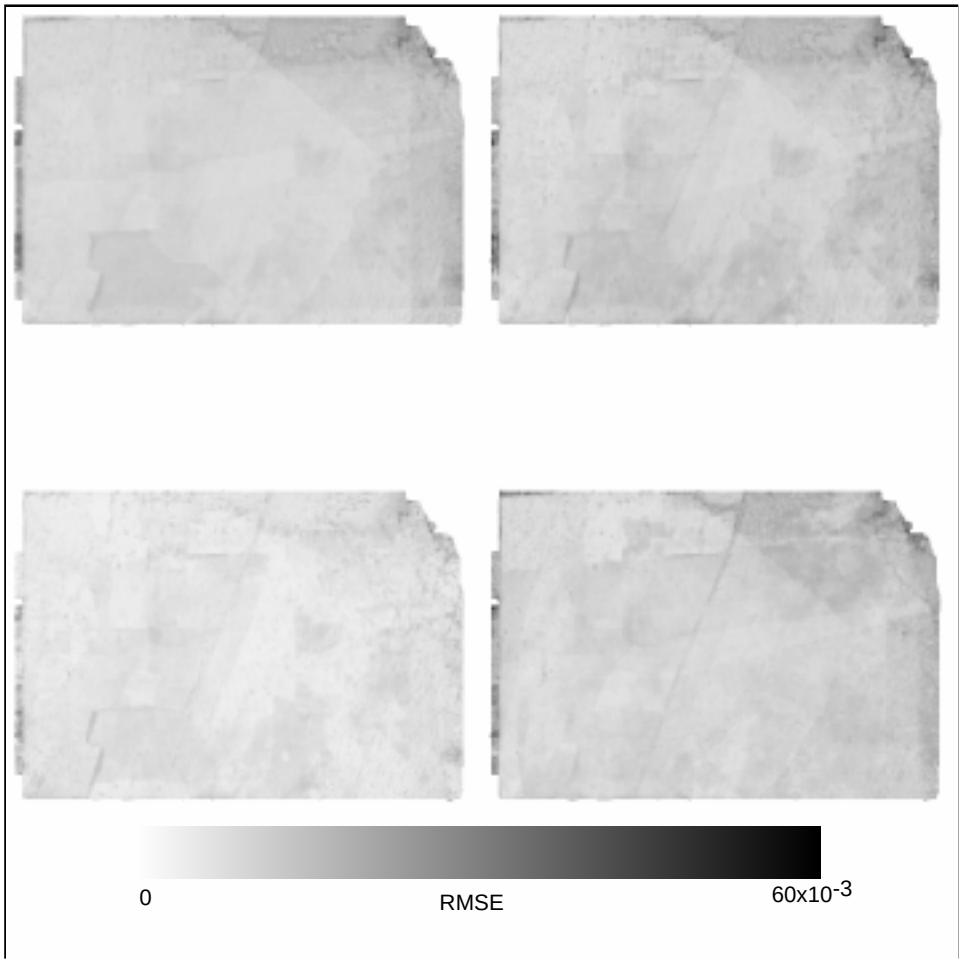

WCSS Fallow - rmse in model selection at 3m resolution

Blue, green, red and NIR bands, in raster order, showing the spatial variation of the rmse, on which the choice of model is made. NB ***the greyscale is inverted*** i.e. darker areas correspond to higher rms errors.

Stats of each frame:

Blue: n=156946 mean=.003763 SD=.001034 Min=.001197 Max=.020071
Green: n=156946 mean=.004807 SD=.001323 Min=.001312 Max=0.02363
Red: n=156946 mean=.006201 SD=.002015 Min=.001677 Max=.054222
NIR: n=156946 mean=0.00771 SD=.002307 Min=.003115 Max=.040761

Figure 14: Mosaic of four band WCSS rmse showing the rmse with 3m inversions for each model selected. Notice the lack of any banding as most of the area was covered with the same number of looks.

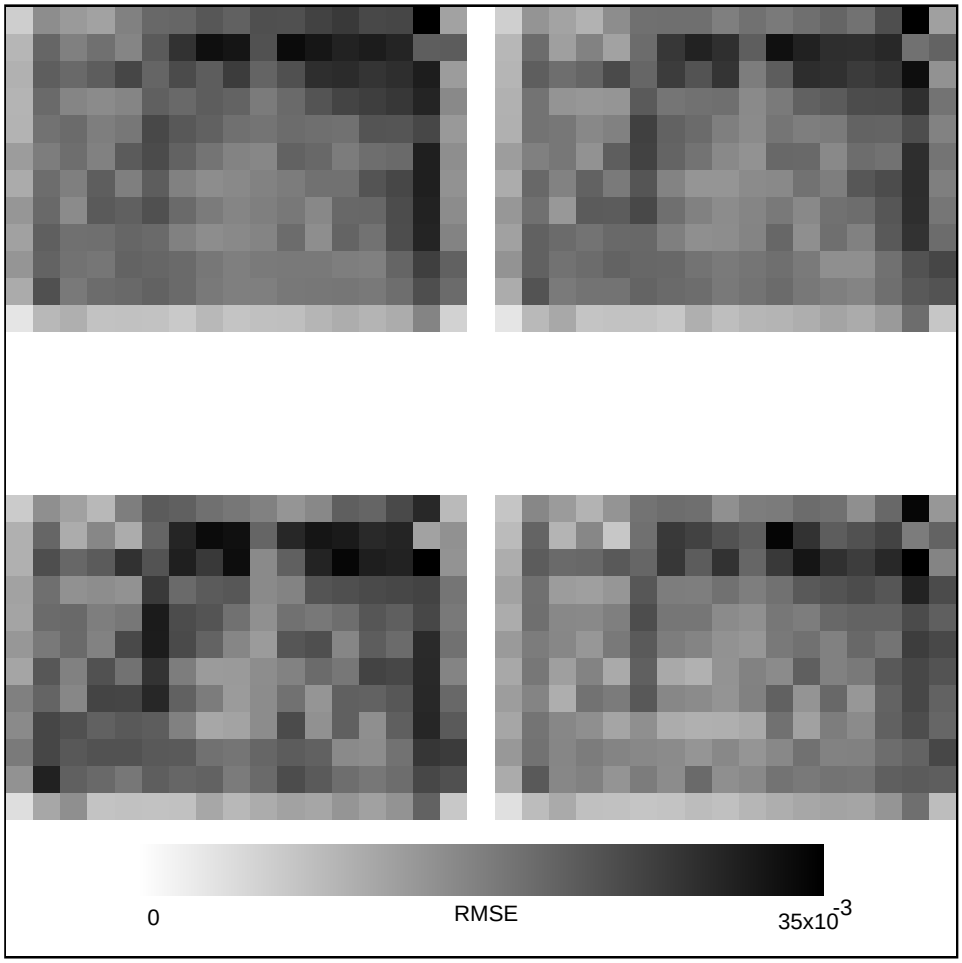

WCSS Fallow - rmse in model selection at 90m resolution

Blue, green, red and NIR bands, in raster order, showing the spatial variation of the rmse, on which the choice of model is made. NB ***the greyscale is inverted*** i.e. darker areas correspond to higher rms errors.

Stats of each frame:

Blue: n=1674 mean=.003866 SD=.001333 Min=.000174 Max=.012121
Green: n=1674 mean=.005179 SD=.001816 Min=.000282 Max=.016755
Red: n=1674 mean=.006593 SD=.002422 Min=.000247 Max=.019871
NIR: n=1674 mean=.008743 SD=.003382 Min=.000203 Max=.031837

Figure 15: Mosaic of four band WCSS rmse showing the rmse with 90m inversions for each model selected.

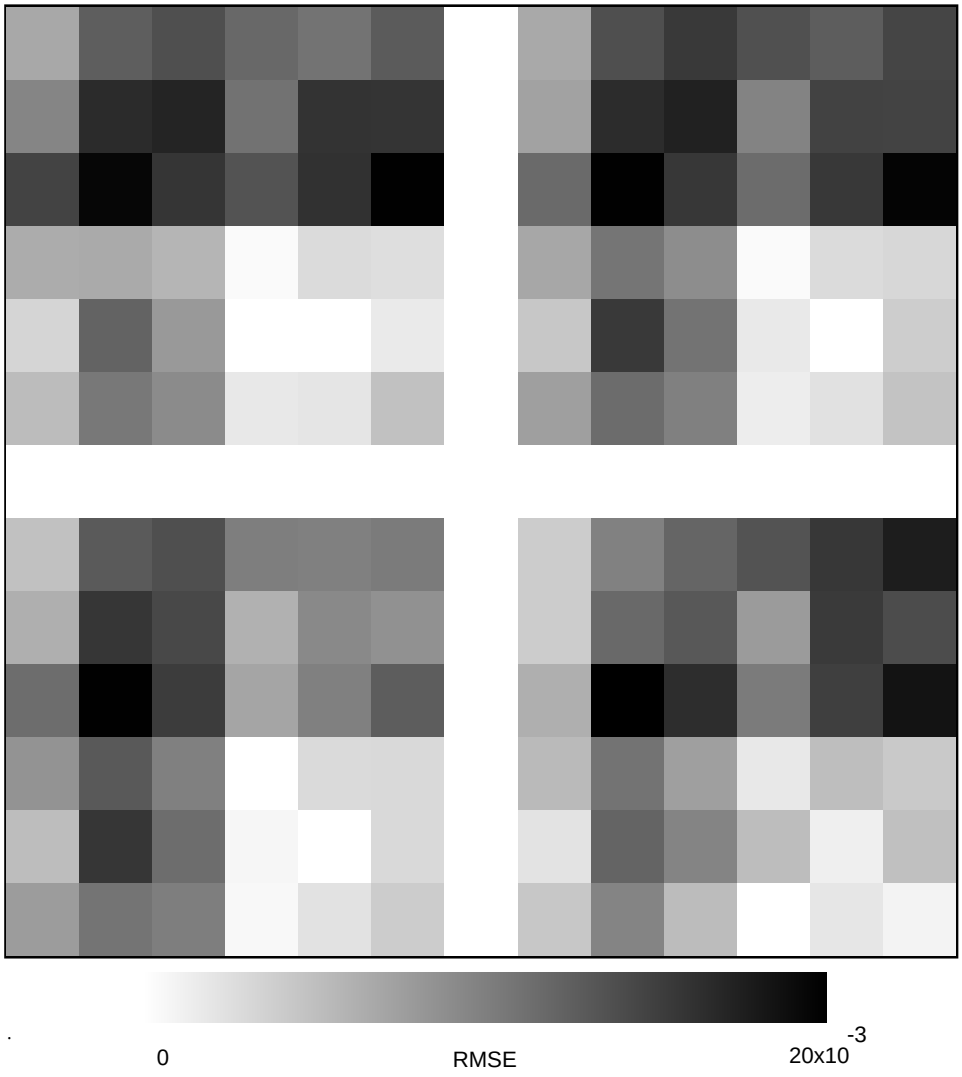

WCSS Fallow - rmse in model selection at 240m resolution

Blue, green, red and NIR bands, in raster order, showing the spatial variation of the rmse, on which the choice of model is made. NB ***the greyscale is inverted*** i.e. darker areas correspond to higher rms errors.

Stats of each frame:

Blue: n=36 mean=.004195 SD=.001338 Min=.002073 Max=.006569
Green: n=36 mean=.006229 SD=.001743 Min=.003191 Max=.009263
Red: n=36 mean=.009075 SD=.002667 Min=.004554 Max=0.01508
NIR: n=36 mean=.011941 SD=.002479 Min=.008005 Max=.016868

Figure 16: Mosaic of four band WCSS rmse showing the rmse with 240m inversions for each model selected.

APPENDIX G:
LANDSAT-TM SPECTRAL ALBEDO EXTRACTION (SUMMARY OF A PAPER BY DISNEY, MULLER ET AL.)

Landsat-TM Spectral Albedo Extraction (Summary of a Paper by Disney, Muller et al.)

An attempt has been made to use the ASAS "at surface" reflectances to create a large area BRDF/albedo map for use in scaling studies and simulation studies for GCM and hydrological applications. See (Disney et al., 1997; Muller et al., 1997b) for a fuller discussion.

The overall processing scheme is shown in Figure 1 which includes details of the atmospheric correction scheme for the ASAS data. (see Appendix XXX for a fuller discussion of this issue).

The resultant ASAS "at surface" radiances for each of the 4 TM spectral bands (1–4) were spatially degraded to TM 30m resolution and registered to the geocoded surface reflectance TM pixels provided by the NASA EDC DAAC to support MODIS Land group validation efforts. The radiometric range of the pixels from ASAS were then adjusted to fit the TM values. All of these pixels were then used as training statistics for the 3 regions covered in the SSS (millet, savannah/fallow and tiger bush). A Maximum Likelihood classification was then performed of the TM pixels using these training statistics and for each classified pixel, the original albedo value associated with that pixel was used to predict a spectral albedo for all the classified TM pixels.

The resultant TM spectral albedo maps are shown in Figure 2 (using the modified Walthall model) and for the RossThick-LiSparse model in Figure 3. Notice the AGRYMET agricultural square which is clearly in both images as well as the tiger bush in the lower left corner. The spectral albedo values are different dependent on the model with the RossThick-LiSparse model values being higher.

In future the "Ambrals" model inversions will be used from the 30m scaling experiments to repeat the experiment. Narrowband to broadband conversion will be made using the method proposed by (Brest and Goward, 1987) and the resultant broadband albedos will be compared to field solarimeter-based albedos provided by Simon Allen and his colleagues (Allen et al., 1994) at the Institute of Hydrology, Wallingford for validation. A similar procedure will also be tested using the POLDER data.

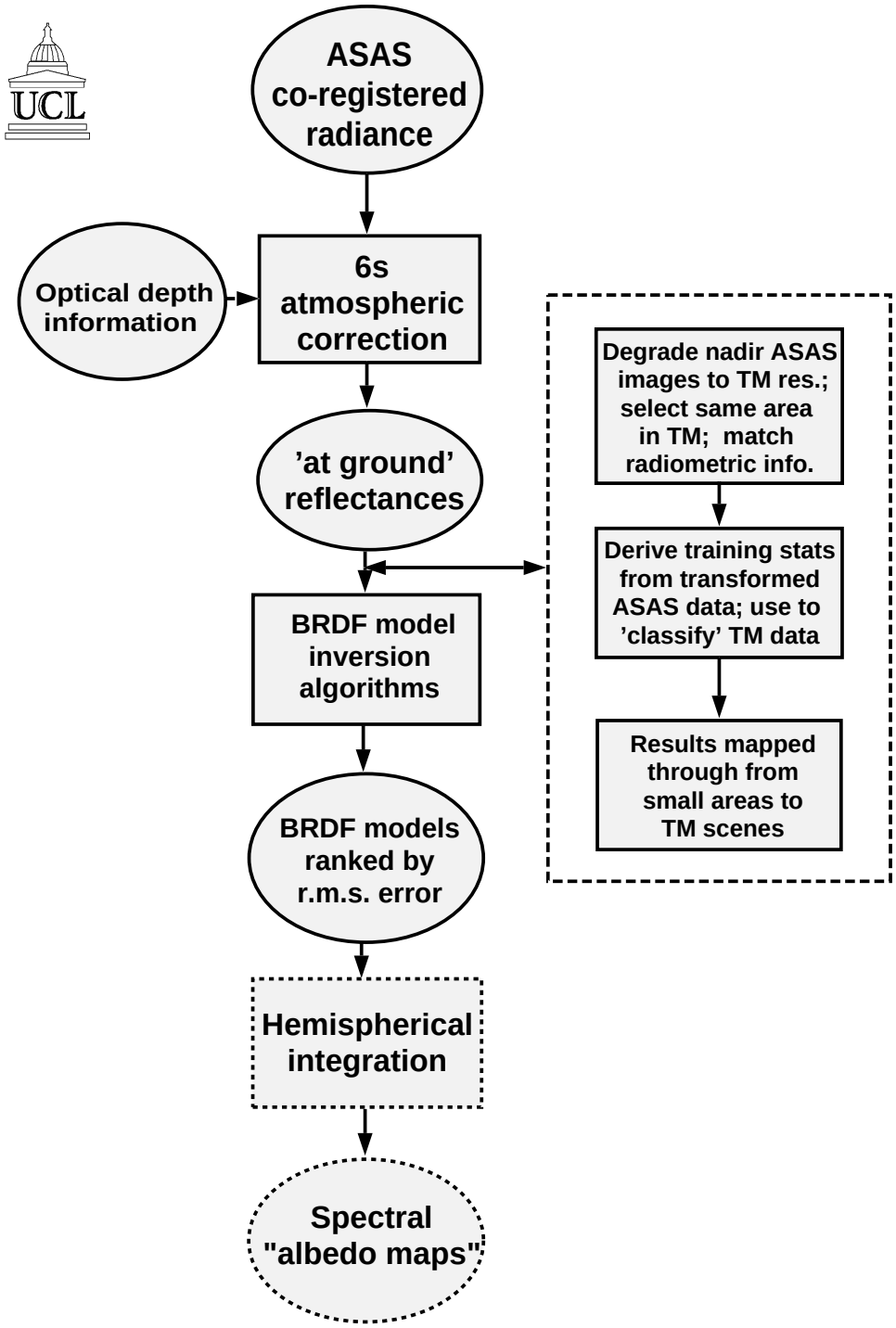

Figure 1: Schematic flow diagram of the LANDSAT-TM spectral albedo derivation using the ASAS directional reflectances including the production of "at surface" reflectances using the atmospheric optical depth measurements from Halthore.

Albedo maps of SSS at TM resolution

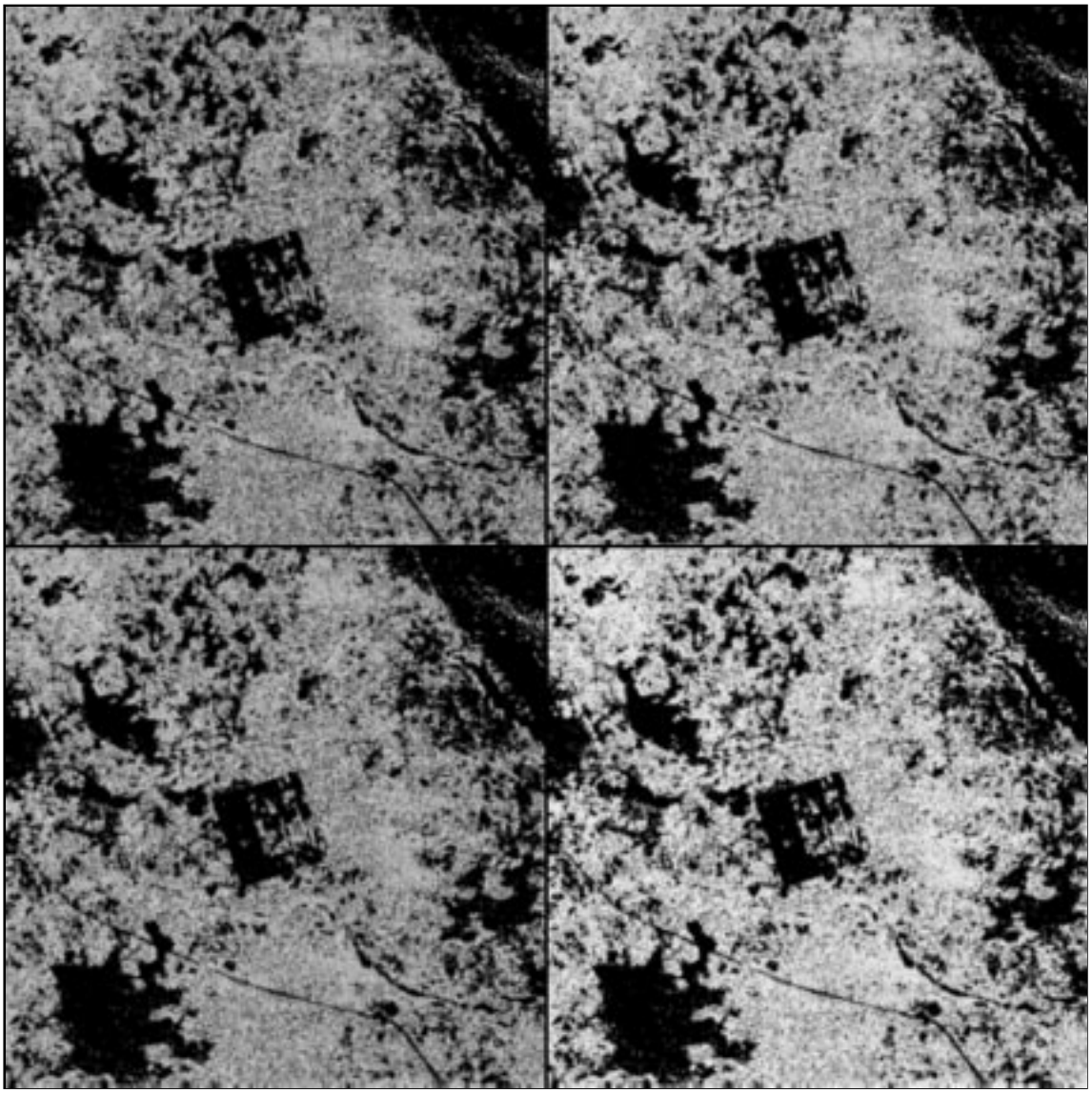

Figure 2: Mosaic of LANDSAT-TM spectral albedos for the four spectral bands using a modified Walthall inversion model for the ASAS "at surface" directional reflectances.

Bands 1, 2, 3 and 4 (left to right, top to bottom) of albedo, mapped from ASAS model inversions up to TM-scale. The BRDF kernels used in this case were the Isotropic, WalthallLinMultCos, WalthallSqMult and WalthallSqSum (i.e. Modified walthall model).

A 3 x 3 convolution filter was passed over the images to remove high frequency noise in the images.

The stats of the raw images are as follows:

Band 1 - n=129414 mean=.048008 SD=.018297 Min=7.96096e-05 Max=.082251
Band 2 - n=129414 mean=.120139 SD=0.03855 Min=.000873 Max=.177322
Band 3 - n=129414 mean=.181225 SD=.061481 Min=.000972 Max=.290579
Band 4 - n=129414 mean=.348764 SD=.094025 Min=.005047 Max=.439253

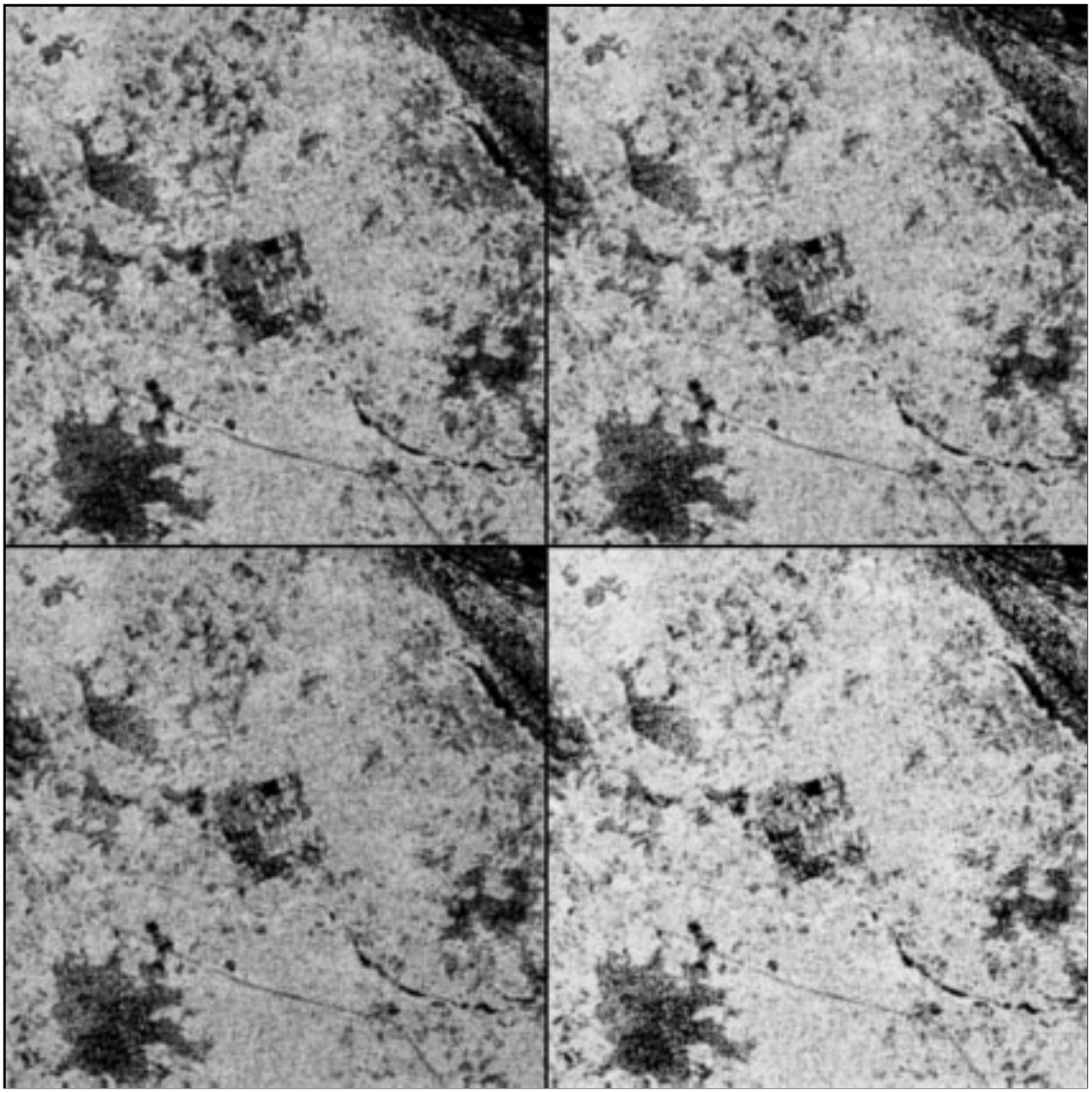

Figure 3: Mosaic of LANDSAT-TM spectral albedos for the four spectral bands using a RossThickLiSparse model inversion for the ASAS "at surface" directional reflectances. Notice the higher values of spectral albedo values over the DOE-1 modified Walthall in isotropic, RossThick and LiSparseModis.

Bands 1,2,3 and 4 (left to right, top to bottom) of albedo, mapped from ASAS model inversions up to TM-scale. The BRDF kernels used in this case were the isotropic, RossThick and LiSparseModis.

A 3 x 3 convolution filter was passed over the images to remove high frequency noise in the images.

The stats of the raw images are as follows:

Band 1 - n=175011 mean=.049615 SD=.018106 Min=.000334 Max=.082018
Band 2 - n=175011 mean=.118947 SD=.035053 Min=.000972 Max=.177611
Band 3 - n=175011 mean=.180364 SD=.057442 Min=.001486 Max=.295627
Band 4 - n=175011 mean=.351156 SD=.072161 Min=.004554 Max=.446293

APPENDIX H:
MONTE CARLO-RAY TRACING SIMULATIONS OF ASAS (SUMMARY OF A PAPER BY MULLER, DISNEY AND LEWIS)

Monte Carlo-Ray Tracing Simulations of ASAS (Summary of a Paper by Muller, Disney and Lewis)

To understand the relationship of the semi-empirical parameters to field-based biophysical measurements, a Monte Carlo ray-tracing system (Burgess et al., 1995; Lewis and Muller, 1990; Lewis and Muller, 1992; Lewis et al., 1991) is being employed to simulate radiance fields both at the "above canopy" level and at airborne altitudes. The objective is to understand the role of leaf-level and soil-level variations in reflectance and its relationship to the underlying biophysical properties of the vegetation (especially LAI) which appear as parameters in the semi-empirical kernels of "Ambrals".

Millet plants have been geometrically modelled using biometric measurements of tiller/leaf shape and form made at the SSS millet site by Lewis, Barnsley and Morris in September 1992. Six different plants have been modelled.

Leaf directional reflectance and transmittance measurements were made in the field but these proved unreliable. Instead the PROSPECT model was used to simulate a Lambertian leaf reflectance using a Chlorophyll content of 0.75.

Figure 1 shows an example of the resultant MCRT simulations for a perfectly diffuse "white" sky. as a function of solar zenith angle at the 4 TM spectral band equivalents. A Lambertian spectral reflectance was used for the underlying soil taken from the HSIS database. The "hot spot" region was sampled at higher angular sampling. 100 plant models were simulated on a regular grid-spacing of 1.5m using all 6 plant models randomly placed in the grid. The resultant simulation shows the averaged results for the whole area and clearly shows the "hot spot" and the variation of behavior as a function of wavelength.

The effect of using a directional soil reflectance data-set from Wim van Leeuven (van Leeuwen et al., 1996) shows the importance of including a directional soil reflectance model. Figure 2 shows a comparison of two MCRT simulation at ASAS 3m pixel size at the ASAS viewing angles. The first with the HSIS Lambertian soil reflectance and the second using the field spectro-radiometric data.

Finally, a comparison was made between a MCRT simulation at 3m at the ASAS viewing angles using the directional soil reflectance data and the actual ASAS data in Figure 3. The agreement is reasonable for NIR but becomes poorer as we move towards the blue. The reason for this lies both in the difficulty in atmospherically correcting the ASAS data and the artificial grid layout of the synthetic plant models.

In future, stereo photogrammetric measurements acquired by Lewis, Barnsley and Morris in September 1992 will be used to increase the realism of the plants as well as the individual plant spatial distribution to try to improve the agreement with the ASAS data. This is discussed in more detail in (Muller et al., 1997a).

The MCRT and Botanical Plant Modelling System allows for the calculation of plant biophysical data such as LAI which will be compared to the values derived from the semi-empirical kernels of "Ambrals"

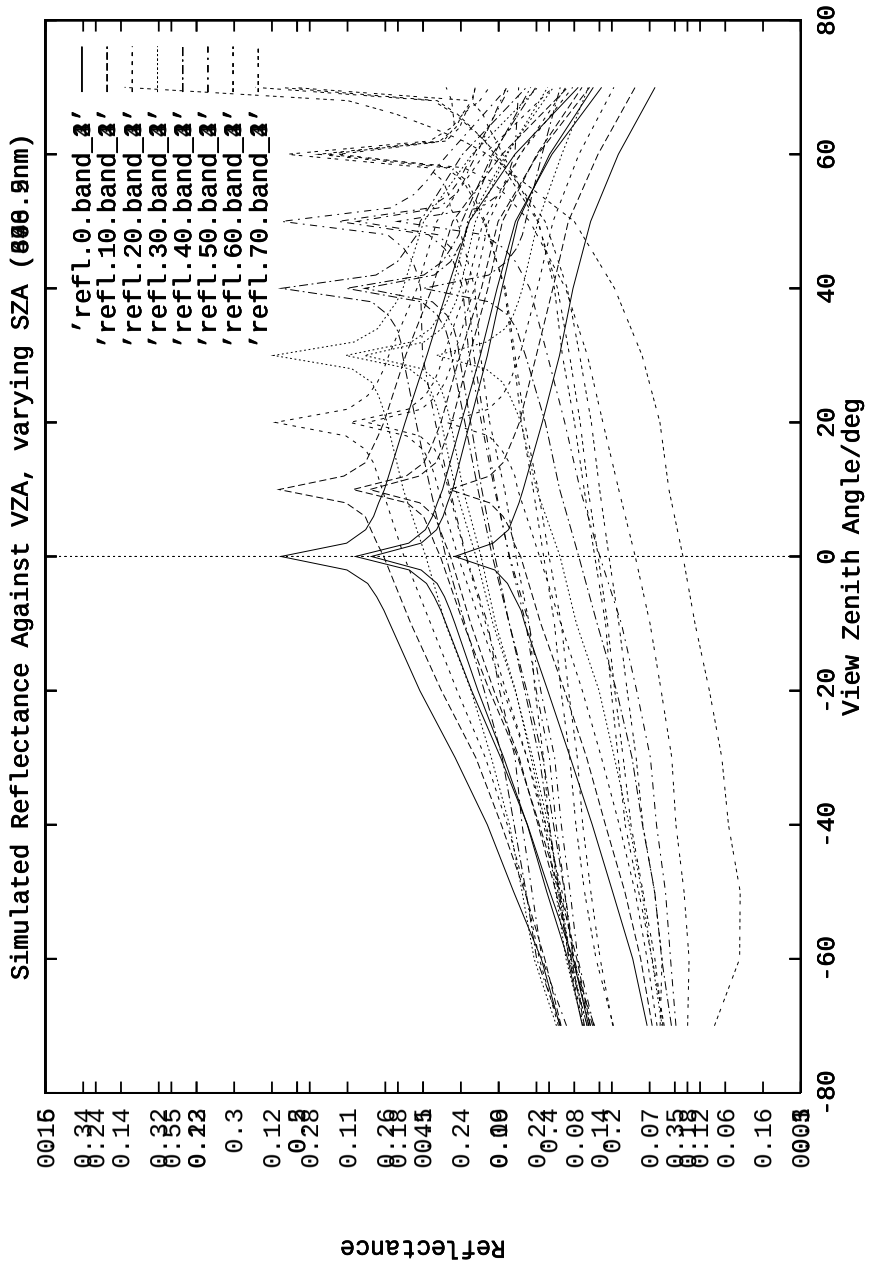

Figure 1: Monte Carlo ray-traced simulations of directional reflectance plots as a function of solar zenith angle using all 6 plant models randomly placed on a 10 x 10 grid. The values shown here are the mean value for the whole area. A white (single diffuse) sky has been used. View and solar zenith angle sampling is at 10 degrees except around the ± 10 degrees of the "hot spot" where the sampling is at 2 degrees. The plants are modelled geometrically from biometric field measurements. The leaf reflectance/transmittance is assumed isotropic and is derived from the PROSPECT model. The soil reflectance measurements are taken from the HSIS data-base.

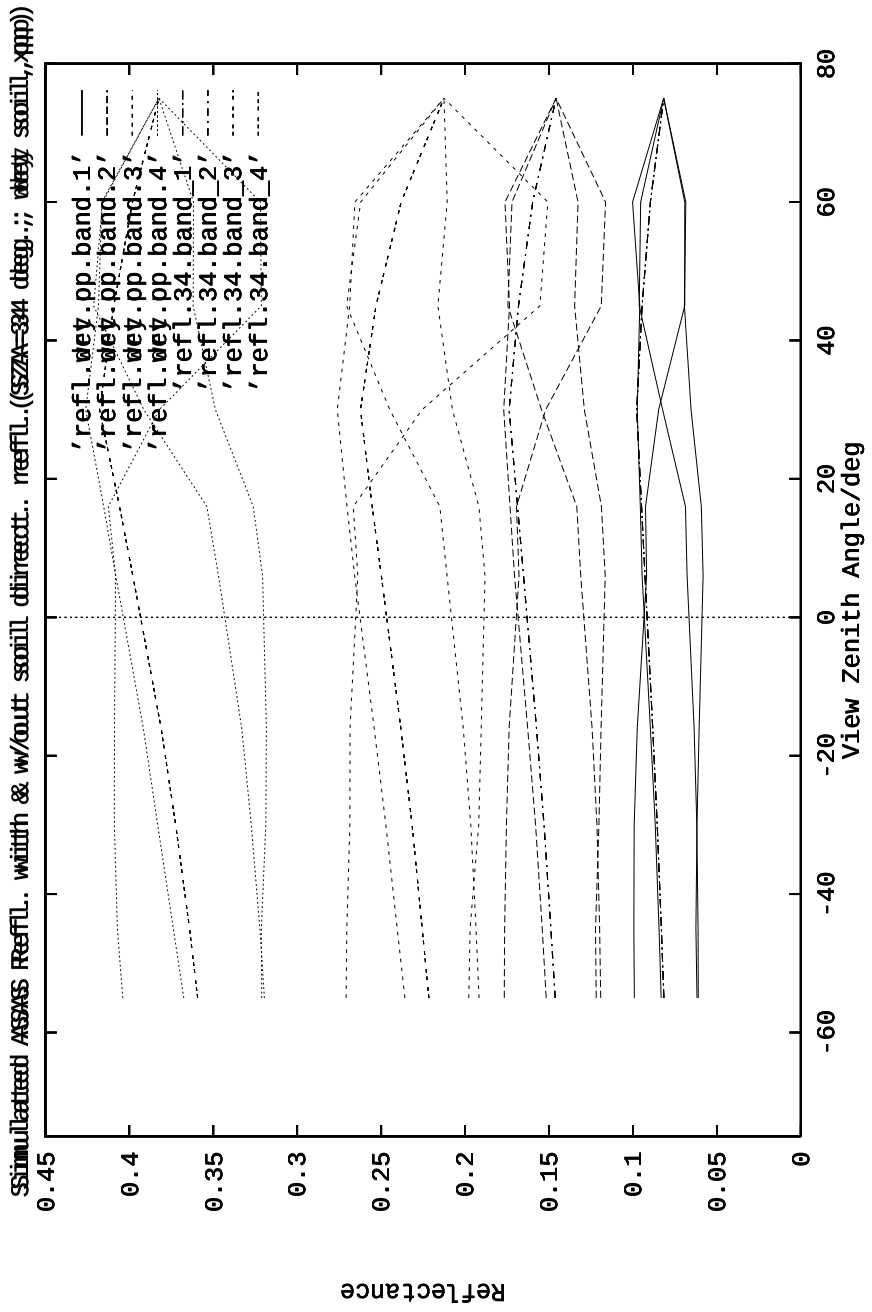

Figure 2: Monte Carlo ray-traced simulations at the ASAS view angles of directional reflectance plots as a function of solar zenith angle using all 6 plant models randomly placed on a 10 x 10 grid. The values shown here are the mean value for a 3m area. A white (single diffuse) sky has been used. Solar zenith angle sampling is at 34 degrees. The plants are modelled geometrically from biometric field measurements. The leaf reflectance/transmittance is assumed isotropic and is derived from the PROSPECT model. The soil reflectance measurements are taken from the HSIS database and are compared with the Spectron SE-590 spectro-radiometric data taken by Wim van Leeuven from the WCSS.

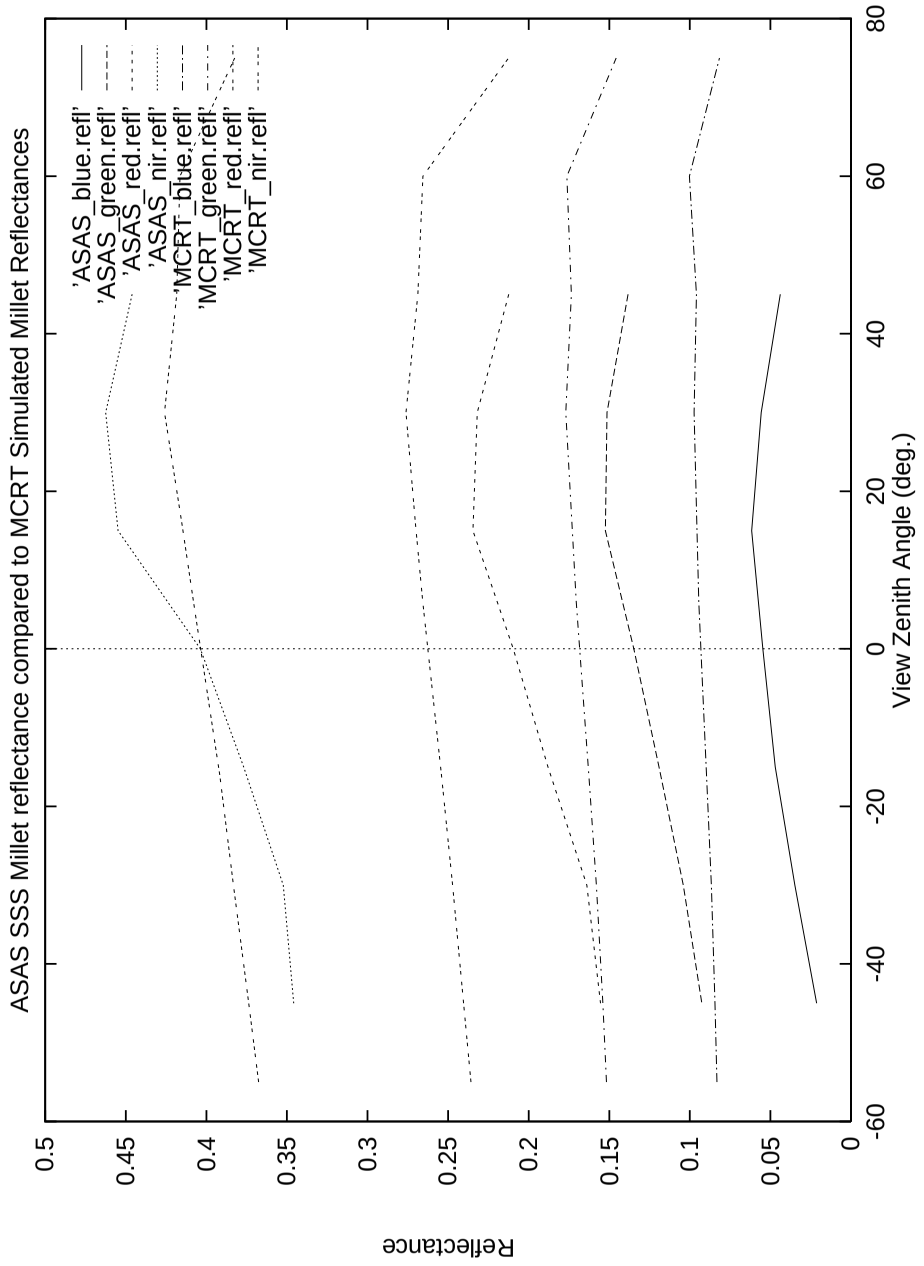

Figure 3: Comparison of ASAS "at surface" reflectance from the SSS with MCRT simulations of the same area. The MCRT simulations uses all 6 plant models randomly placed on a 10 x 10 grid. The values shown here are the mean value for a 3m area. A white (single diffuse) sky has been used. The plants are modelled geometrically from biometric field measurements. The leaf reflectance/transmittance is assumed isotropic and is derived from the PROSPECT model. The soil reflectance measurements are taken from the Spectron SE-590 spectro-radiometric data taken by Wim van Leeuven from the WCSS.

APPENDIX I:
MONITORING LAND SURFACE DYNAMICS IN THE HAPEX-SAHEL AREA USING KERNEL-DRIVEN BRDF MODELS AND AVHRR DATA (SUMMARY OF A PAPER BY RUIZ DE LOPE AND LEWIS)

Monitoring Land Surface Dynamics in the HAPEX-Sahel Area Using Kernel-Driven BRDF Models and AVHRR Data (Summary of a Paper by Ruiz de Lope and Lewis)

As part of an European Union consortium investigating land cover change in the Sahel, researchers at UCL have also been investigating the application of the Ambrals BRDF model to AVHRR data. Six months (May–October 1992) of LAC derived surface reflectance data of the HAPEX-Sahel grid square have been processed using the model and aspects of model fit and model selection investigated (Lewis and de Lope, 1996).

The results indicate that the Ambrals kernels are able to describe the shape of the BRDF (processed on a 16-day window, 1-day step, moving window) well over the period of study. Relatively large errors in model fit can, however, occur during the rainy season, due to variations in the surface reflectance on a sub-16-day timescale. In spite of this, the trends in normalized reflectance, albedo and BRDF model parameters are generally well-maintained. The temporal trajectory of these model parameters is currently being investigated with a view to providing information on variations in the surface cover.

The main kernel selection criterion in Ambrals, the RMSE in model fit, is found in many cases not to provide very consistent results (either temporally and spatially). It is understood that Ambrals will have to make use of additional information in aiding kernel selection, and so the team at UCL have been investigating the issues involved. Currently, an approach that considers temporal consistency in the main selection criterion, weighted by the RMSE is being tested. Early results indicate that this is indeed promising, and that it can be implemented efficiently within Ambrals.

In addition to this research, work is currently underway testing the application of Ambrals to the AVHRR Pathfinder (PAL) dataset for Africa north of the Equator. Two years of data have been processed so far (1989 and 1992) and the 1992 results compared with the LAC data over HAPEX-Sahel described above. While many of the trends observed appear to be similar in the two datasets, the magnitude of the trends are very different, probably mainly due to the poor atmospheric correction of the data (PAL corrects for only Rayleigh scattering and ozone absorption).

Were here present selected figure from this work. Figures 1a and 1b show the modeled values of millet reflectance for AVHRR band one for restricted sampling in May using the derived Ross-Thick and Li-Dense kernels. The reflectance values were modeled under the same viewing and illumination angles as the AVHRR data were measured. Additionally, each graph shows a continuous extrapolation of reflectance values under constant solar zenith and relative azimuth angles (equivalent to their monthly averages) in order to facilitate interpretation of the BRDF trends. Figure 1c illustrates the case of June. Figure 2a and 2b show similar plots for tiger bush and fallow as land covers. Figures 3a to 3c show differences in the black-sky albedo as a function of solar zenith angle found for different selections of kernels with similarly small RMSEs; Figure 3a shows a case with large discrepancies, Figures 3b and 3c with small ones.

Figure 4 shows a temporal profile of RMSE obtained from fitting the AVHRR band 1 data from the Central East millet site to the model variants using a 29-day window. The symbols indicate the vlue of the RMSE obtained for the kernel combinations providing good fits, usually two-parameter model variants. Figure 5a shows the temporal profiles of normalized reflectance (bidirectional reflectance at the 6-month period average solar zenith for nadir viewing) for the Central East millet site. Figure 5b shows the isotropic parameter, which is equivalent to the nadir bidirectional reflectance for nadir illumination, and, as such, is an extrapolated quantity. These figurs show that kernel selection is less important for interpolated results than for extrapolated retrievals.

Figures 6a and 6b show the results of applying the minimum-RMSE criterion for model selection to the retrieval of AVHRR band 1 normalized reflectance of the millet Central East site. The symbols appearing in the bar labeled "RMSE selection" represent the model selected each date.

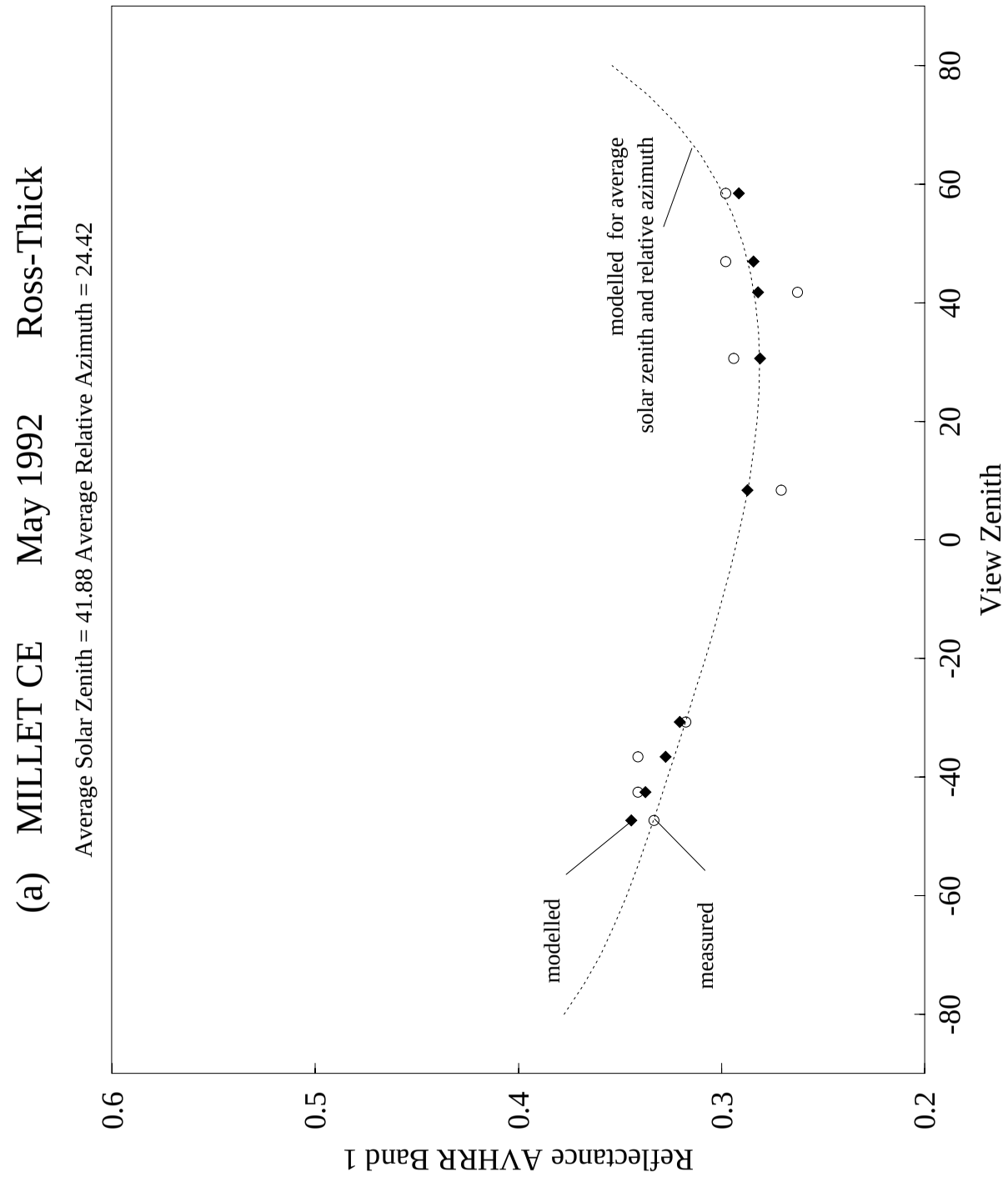

Figure 1: Part (a)

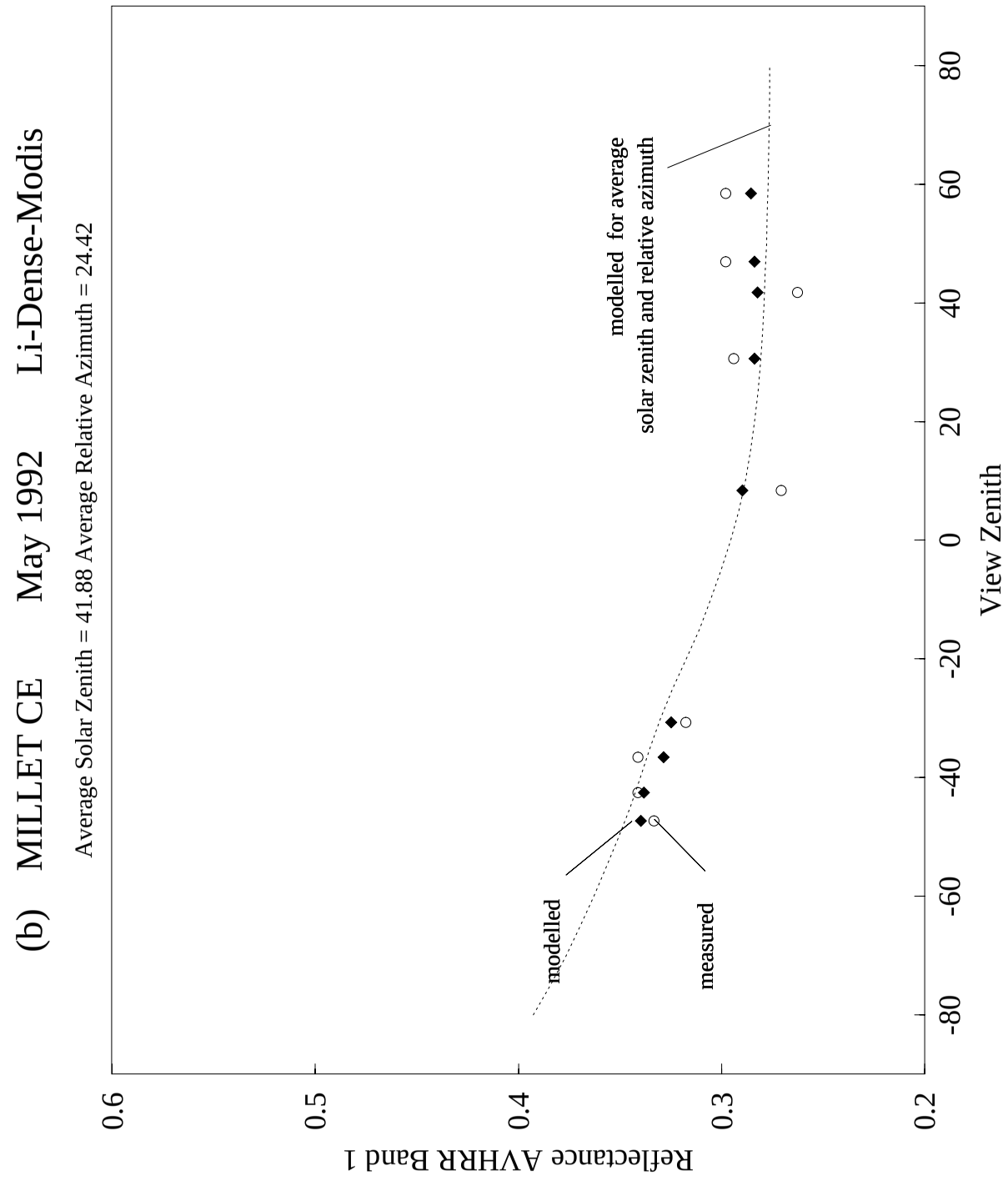

Figure 1: Part (b)

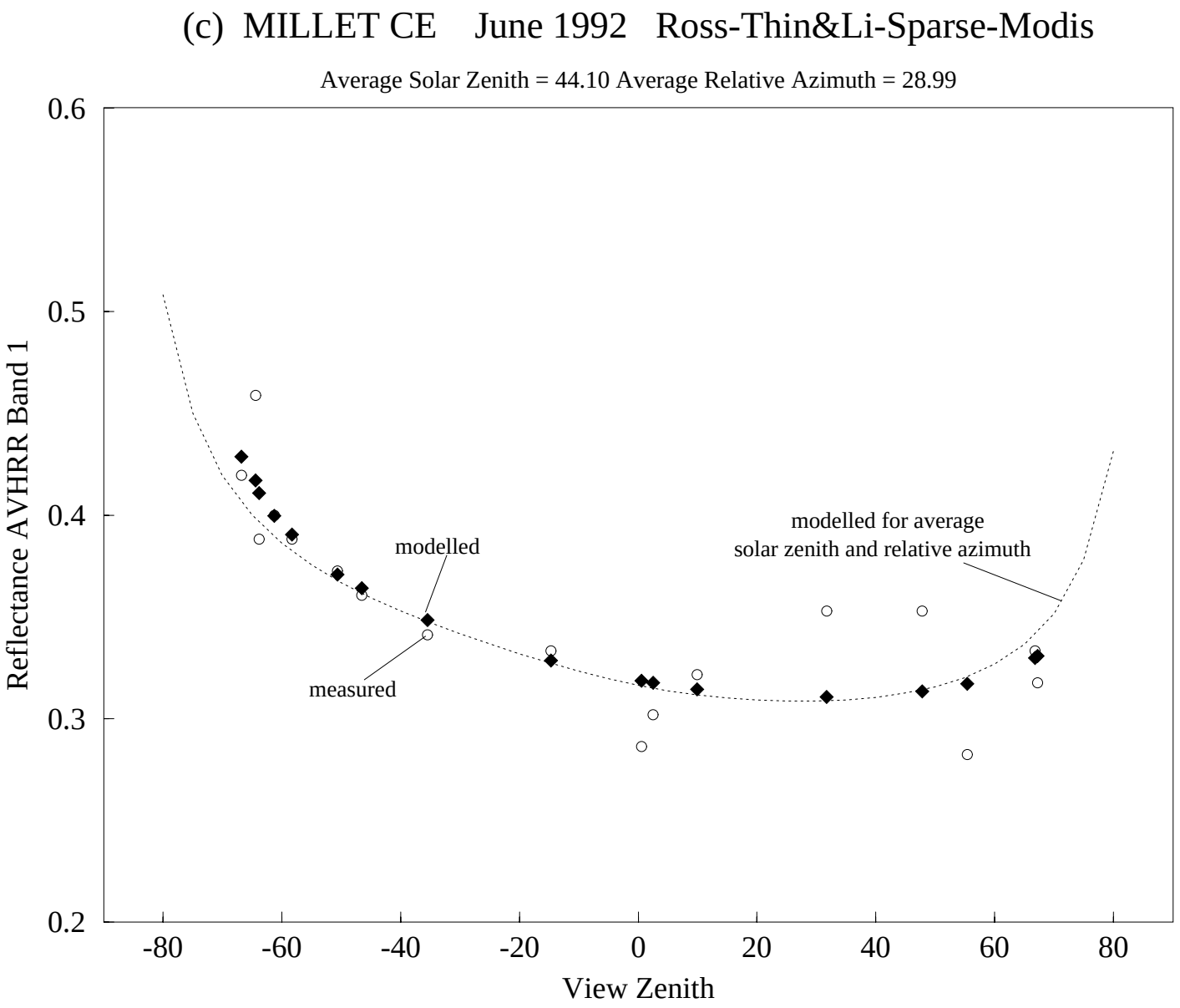

Figure 1: Part (c)

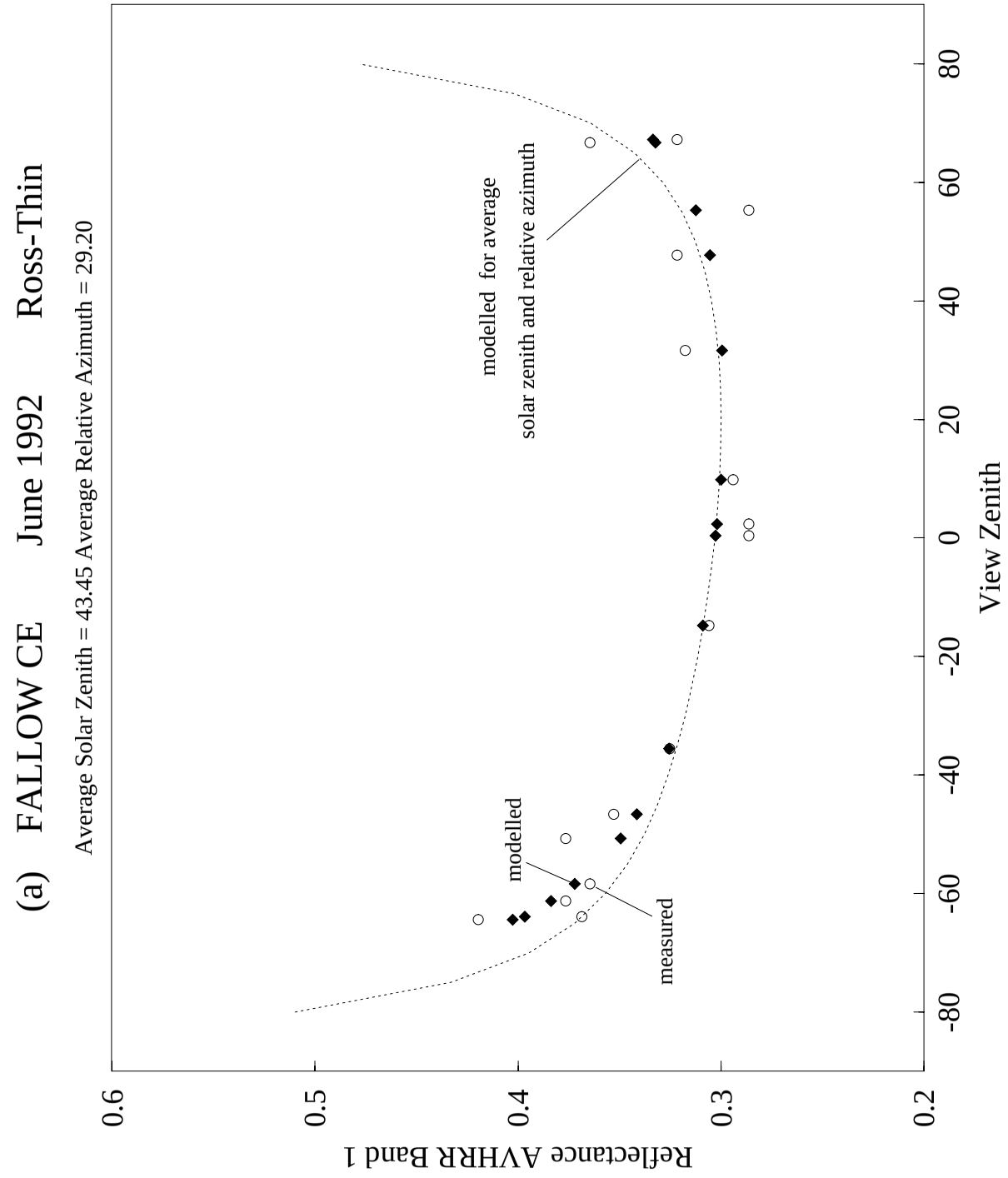

Figure 2: Part (a)

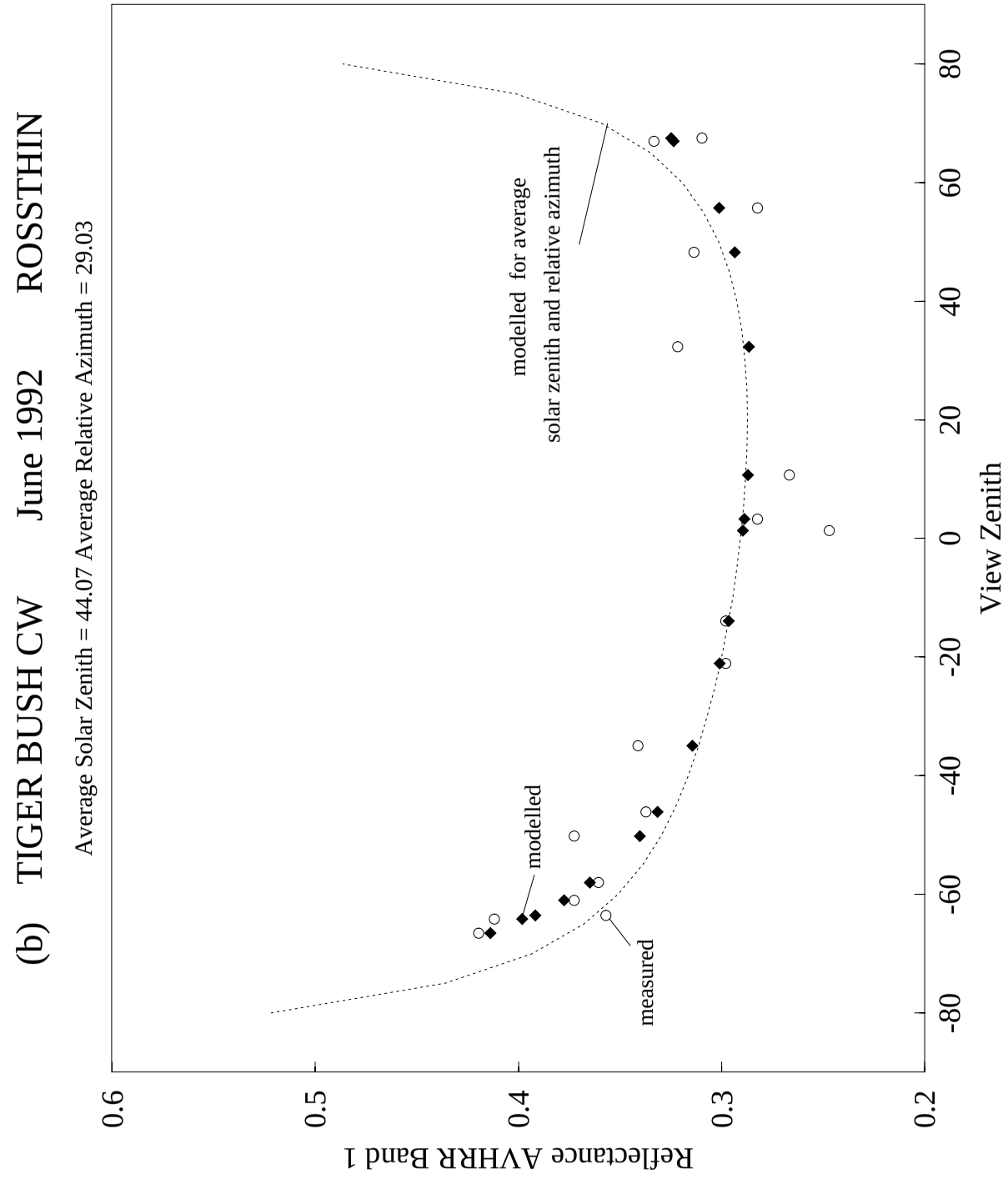

Figure 2: Part (b)

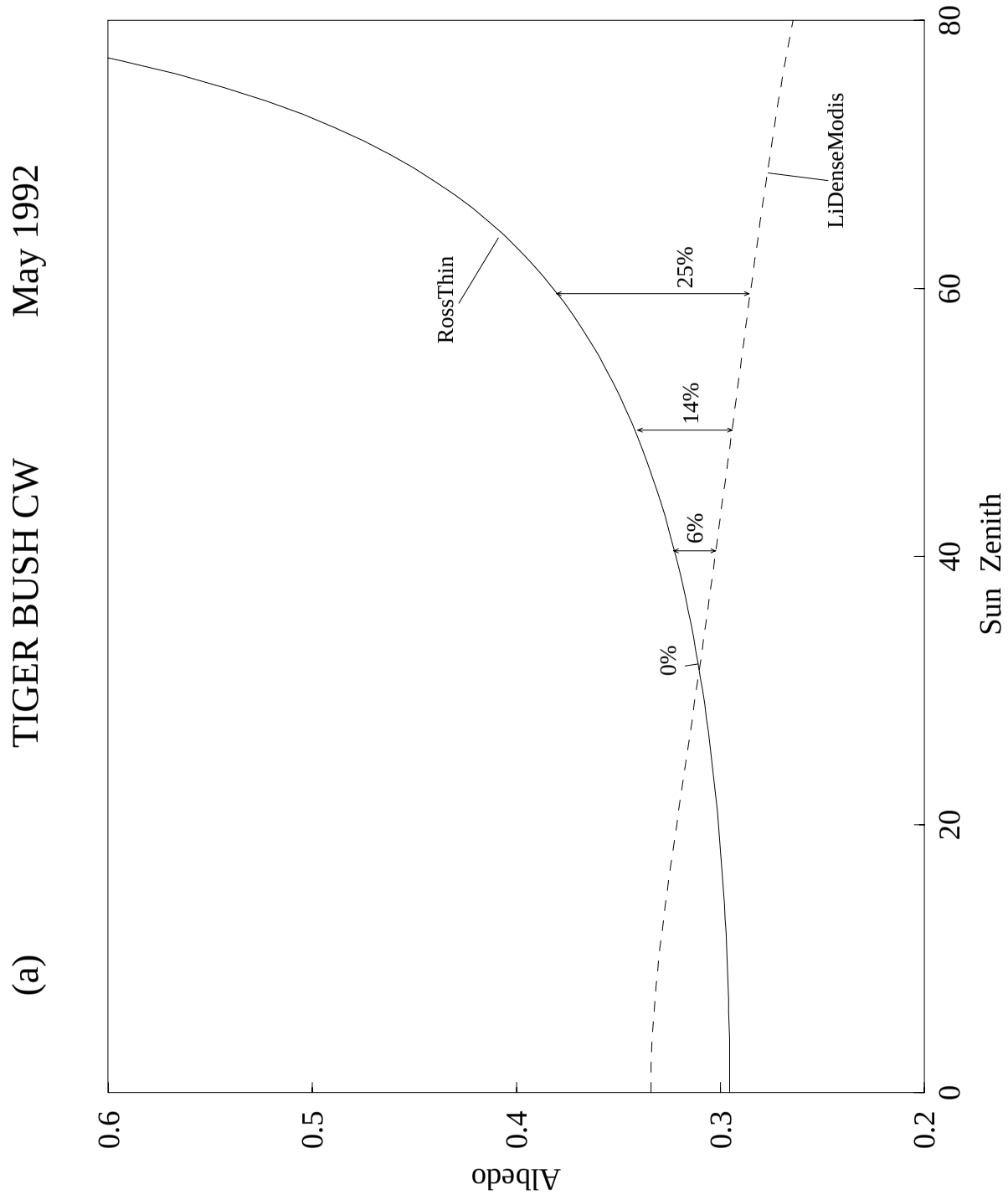

Figure 3: Part (a)

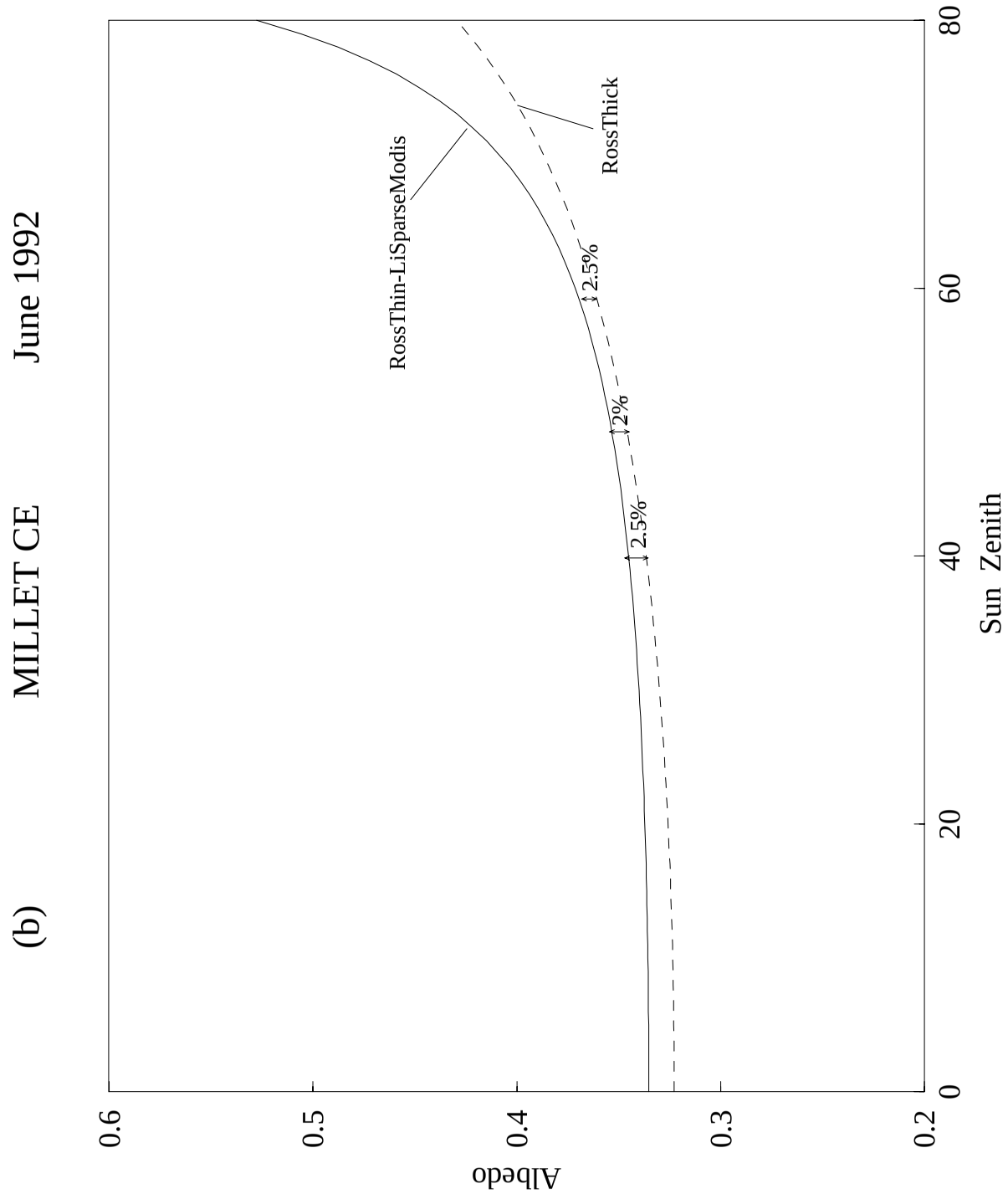

Figure 3: Part (b)

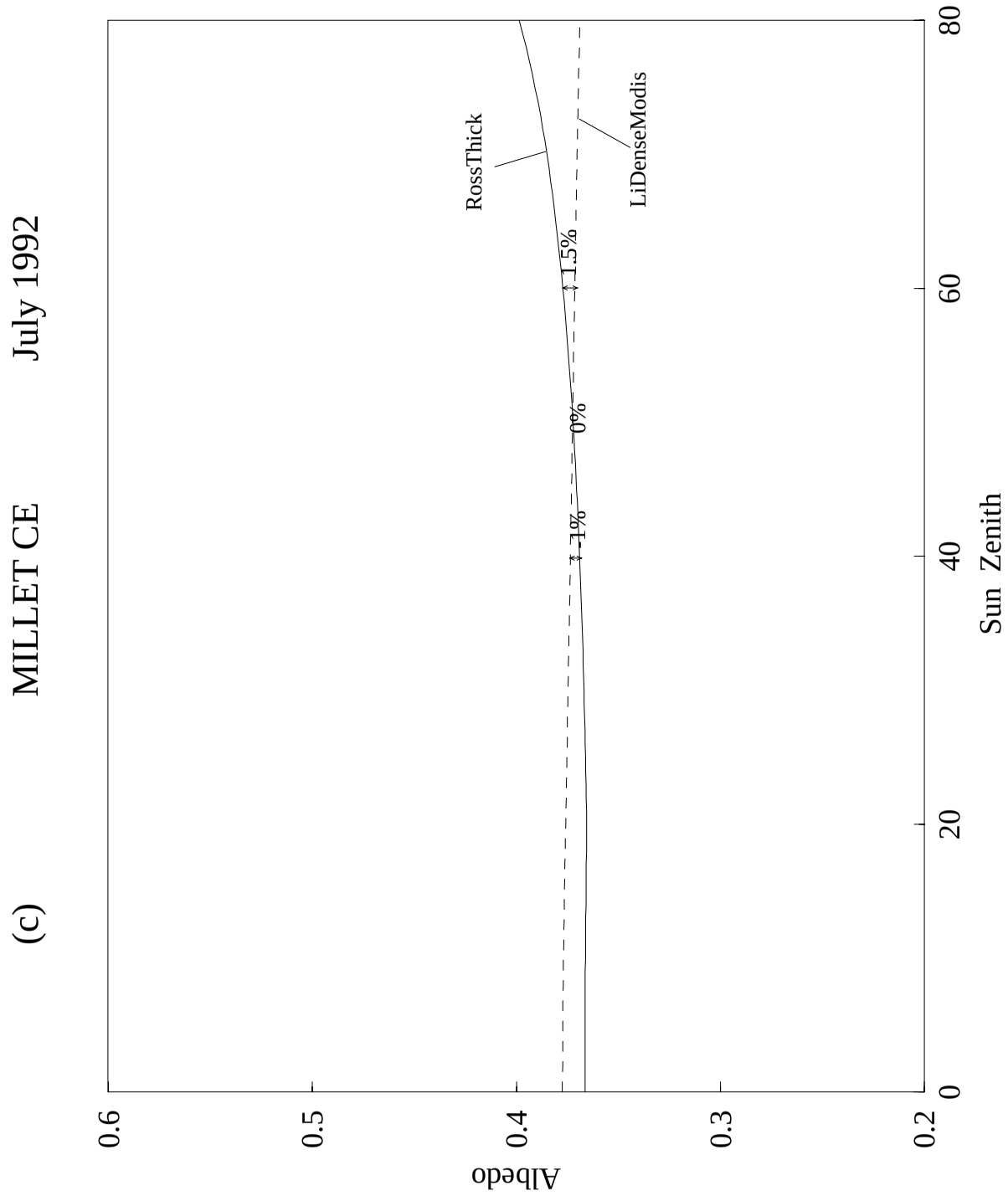

Figure 3: Part (c)

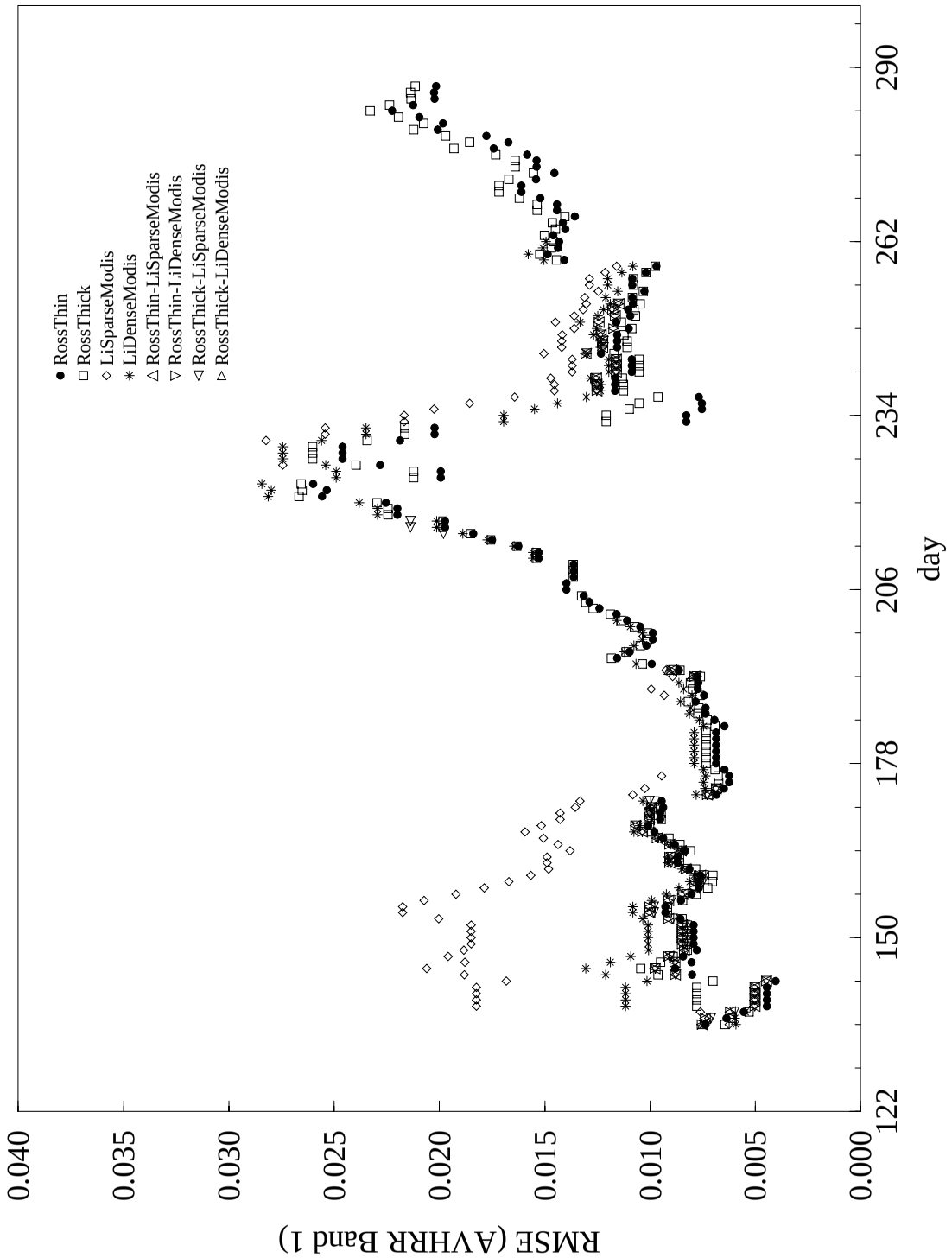
RossThin
RossThick
LiSparseModis
LiDenseModis
RossThin-LiSparseModis
RossThin-LiDenseModis
RossThick-LiSparseModis
RossThick-LiDenseModis
RMSE (AVHRR Band 1)
0.040
0.035
0.030
0.025
0.020
0.015
0.010
0.005
0.000
122
150
178
206
234
262
290
day

Figure 4:

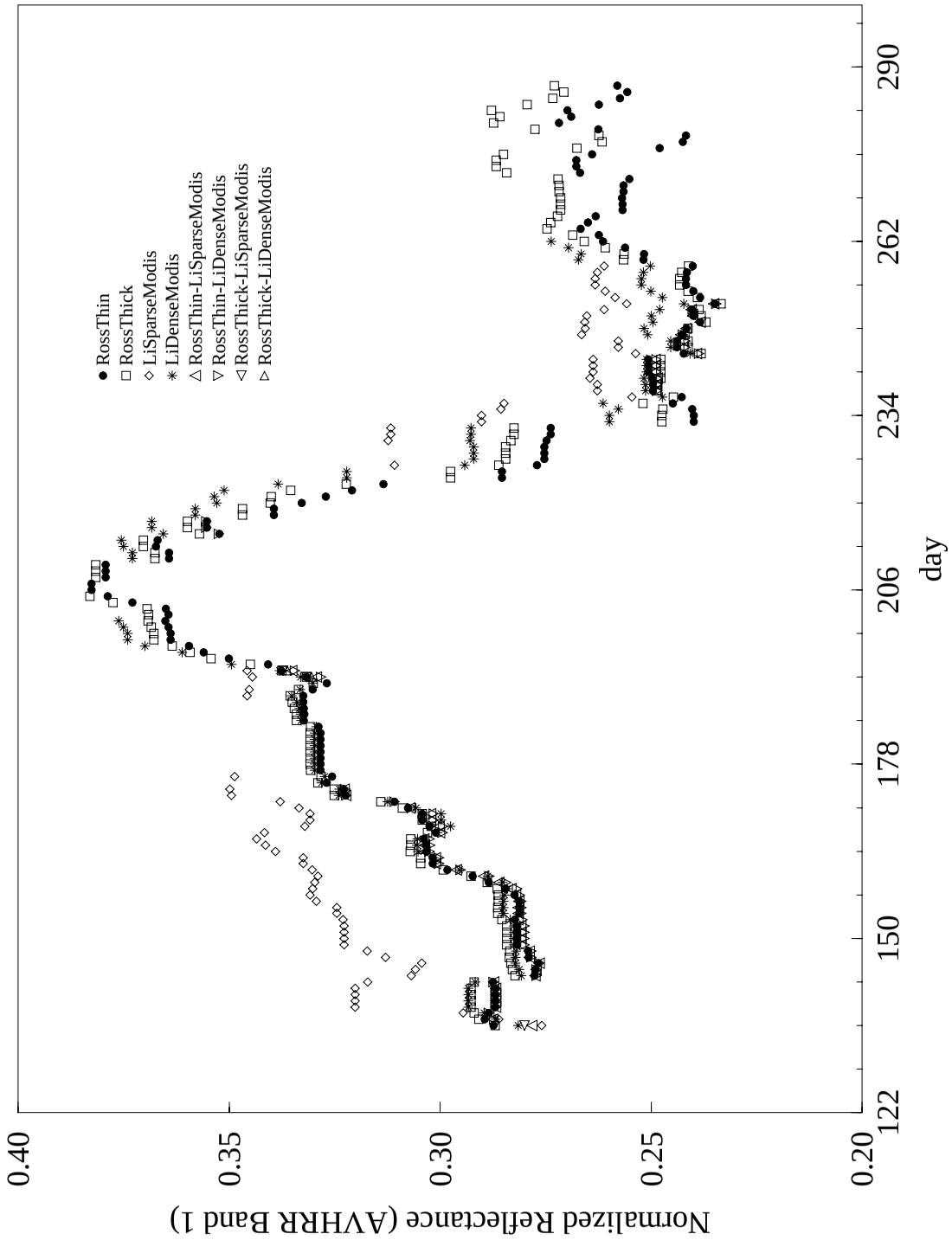

Figure 5: Part (a)

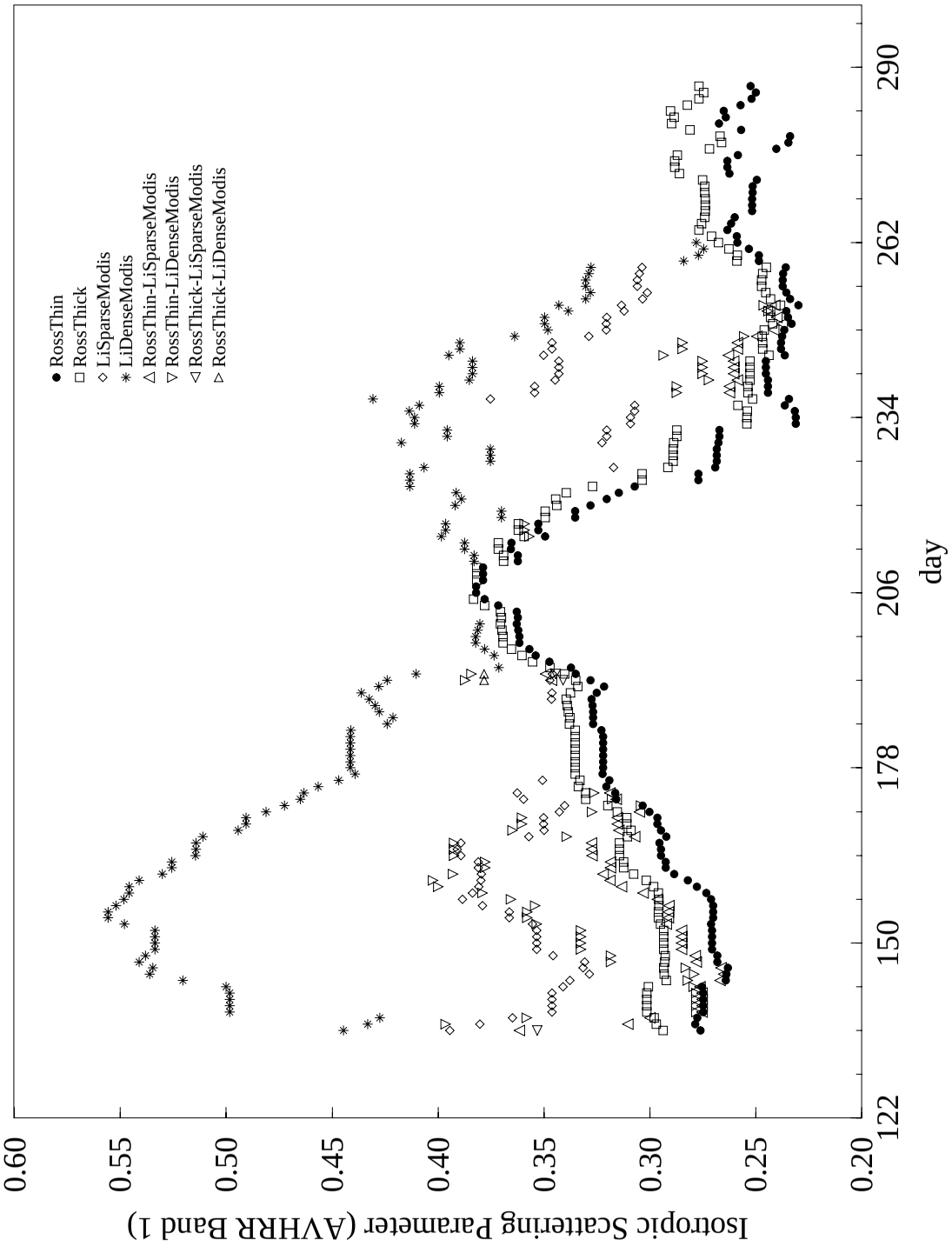

Figure 5: Part (b)

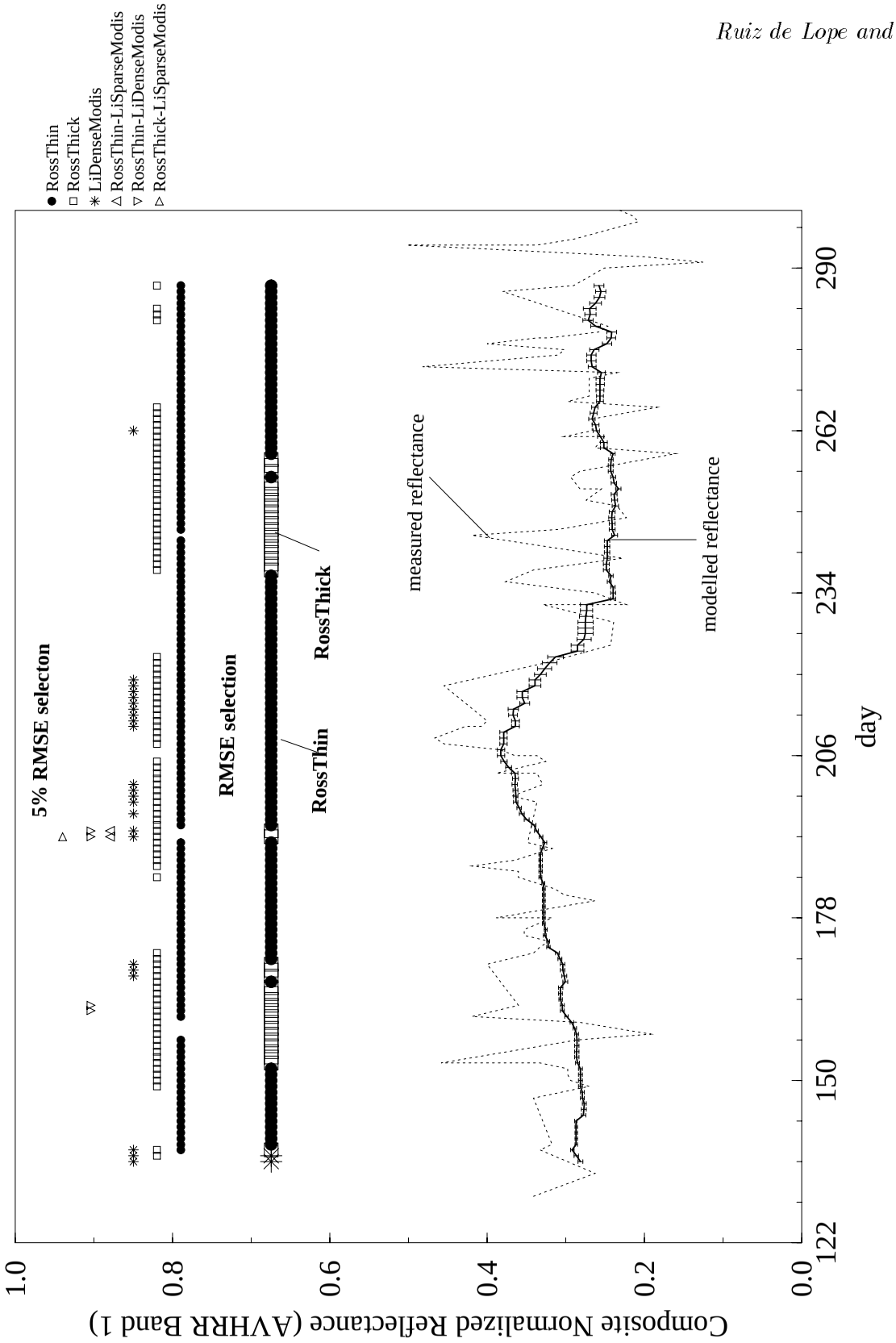

Figure 6: Part (a)

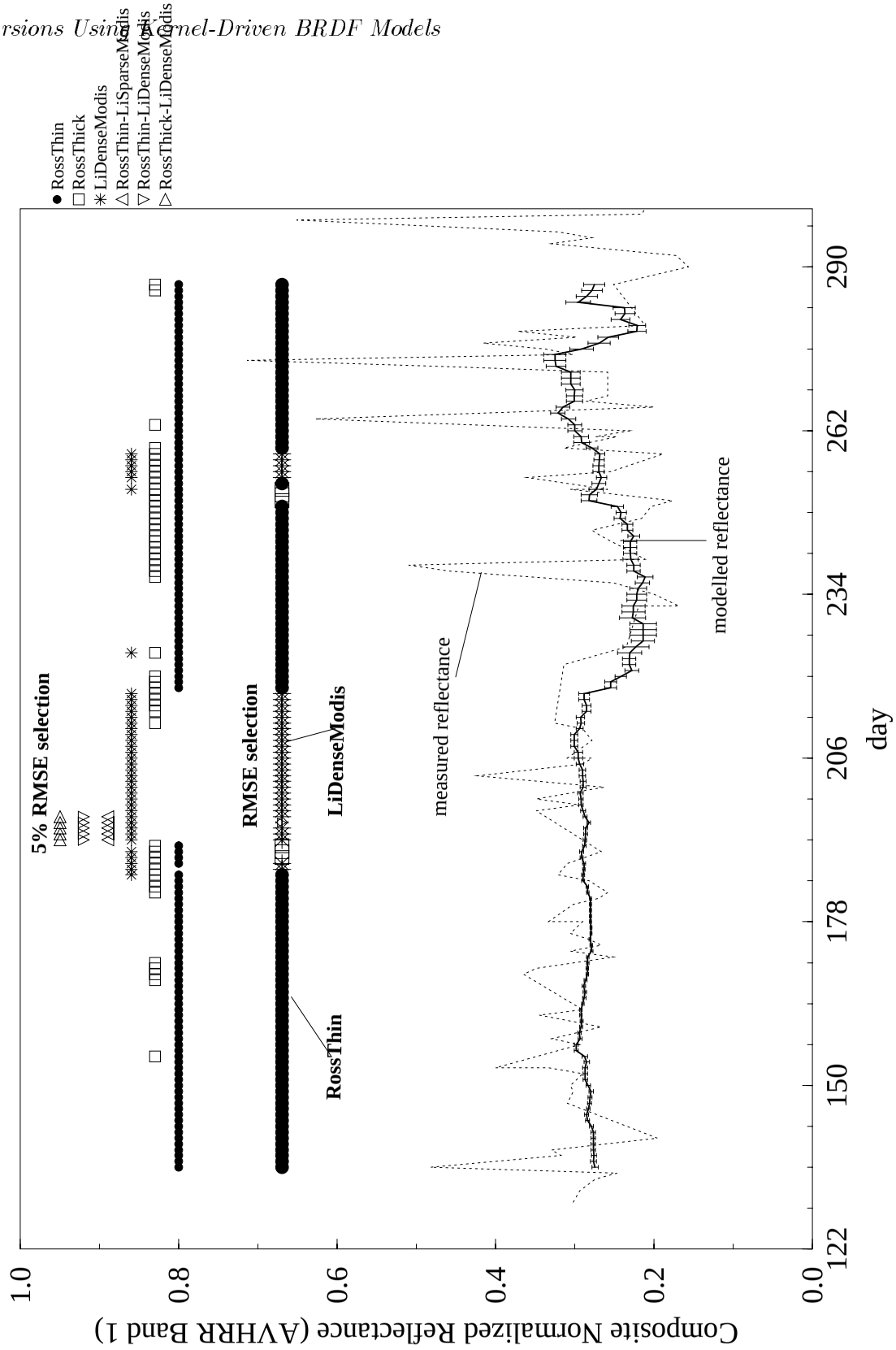

Figure 6: Part (b)

APPENDIX J: ESTIMATING LAND SURFACE ALBEDO IN THE HAPEX-SAHEL SOUTHERN SUPER-SITE: INVERSION OF TWO BRDF MODELS AGAINST MULTIPLE ANGLE ASAS IMAGES (SUMMARY OF A PAPER BY BARNSLEY ET AL.)

Estimating Land Surface Albedo in the HAPEX-Sahel Southern Super-Site: Inversion of Two BRDF Models Against Multiple Angle ASAS Images (Summary of a Paper by Barnsley et al.)

Researchers at University College London recently applied the Roujean-RossThin kernel-driven semiempirical BRDF model and the empirical modified Walthall BRDF model to directional image data obtained for a semiarid region of West Africa near Niamay, Niger (Barnsley *et al.*, 1996; Lewis *et al.*, 1995). In this study, NASA's Advanced Solid-state Array Spectrometer (ASAS) (Irons *et al.*, 1991) acquired image data from an aircraft platform over the HAPEX-Sahel west central, east central and southern super-sites on various dates during September 3–17, 1992. The ASAS acquires images at ten sensor view angles during a single overpass — one at nadir and nine others at 15° increments between 75° forward and 60° aft of the aircraft platform on which it is mounted. These images are recorded in 64 continuous narrow spectral wavebands in wavelengths ranging from the visible to the near-infrared. Spatial resolution is about 4 m. Data processing involved manipulating the multiple–view–angle and multiple flight–line ASAS image data in four steps: (i) geometric registration; (ii) radiometric correction; (iii) atmospheric correction; and (iv) estimation of the surface (spectral) BRDF and albedo through BRDF model inversion.

Geometric registration of the multiple-view-angle and multiple flight-line data was perhaps the most problematic task. Standard polynomial warping techniques are generally unable to cope with the very high frequency, localized geometric distortions present in most airborne scanner images. Consequently, Barnsley *et al.* (1996) used an automated image registration procedure based on "interest point" extraction and area-based matching of small patches of image around each interest point (Allison *et al.* 1991, Allison and Muller 1992) to define an initial polynomial mapping followed by pixel patch-by-pixel patch (typically 15 x 15 pixels) matching using adaptive least-squares image correlation (Otto and Chau, 1989). These techniques are capable of registering multiple view-angle ASAS images to subpixel accuracy (<0.4 pixels) globally throughout the scene (Allison *et al.* 1994). In this case, each of the off-nadir images was registered to the nadir view. Radiometric correction was effected using gain values provided by NASA to convert the instrument's raw DN values to spectral radiances. Atmospheric correction was applied by use of the 6S atmospheric correction code (Vermote *et al.* 1994) with atmospheric parameters drived from sun photometer data (Brown de Colstoun *et al.*, 1996).

With registered and corrected data at hand, the Walthall and Roujean models were inverted and fitted to the data on a pixel-by-pixel basis (Barnsley *et al.*, 1996). This allowed the construction of images of the weights associated with each term of each model. The nadir reflectance images in the blue and near-infrared bands have low contrast and appear noisy. In these bands, the models seem to be fitting noise rather than signal.

In contrast, the green and red bands show a coherent scene structure. The first parameters from both Walthall and Roujean models are strongly related to overall brightness and thus mimic the nadir reflectance. The second and third parameters of the Walthall model show little spatial structure, although some bright and dark spots seem to correlate well with particular patches in the nadir image. In contrast, the Roujean model shows strong spatial structure in both the first and second parameters. The second parameter is the weight of the geometric kernel, which seems to vary inversely with the first parameter. This indicates that the BRDF becomes more isotropic with increasing brightness, which is not unexpected if multiple scattering increases with brightness. The fine texture in the images of the third parameter may be related to fine errors in registration, rather than real changes in BRDF within the scene. Overall, the weight of the third parameter is quite low, indicating that volume scattering is not important for these surfaces. Since vegetation is quite sparse over most of the target area, this is not unreasonable. These results demonstrate that a pixel-by-pixel inversion of empirical/semiempirical models is possible, and that the model parameters vary systematically in a meaningful spatial pattern.

We present a selection of figures from this study. Figure 1 shows the multiple-view angle imagery used

registered to the nadir view and atmospherically corrected. Figure 2 shows spatial images of the retrieved BRDF model parameters, and of albedo, using the modified Walthall model, Figure 5 the same using the Roujean-RossThin model that is similar to the Ambrals BRDF model. Figure 3 shows a sample fit in several wave bands, Figures 4 and 6 the respective histograms os RMSEs found in the inversions carried out on a pixel by pixel basis.

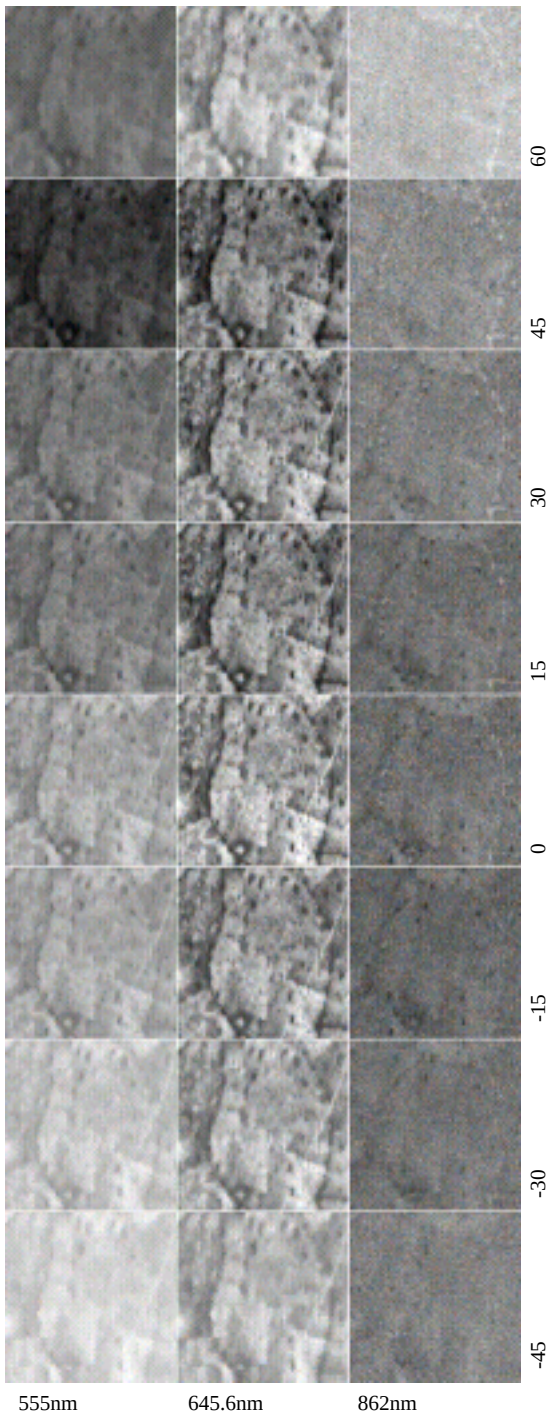

Figure 1: The multiple-view angle spectral bidirectional reflectance factor data sets used in the study. Each of the imahes is 128 by 128 pixels in size and has been extracted from co-registered and atmospherically corrected full-scene ASAS data. The figure shows the magnitude of the angular variations in detected reflectance. The angles reported in this figure are the nominal ASAS camera angles.

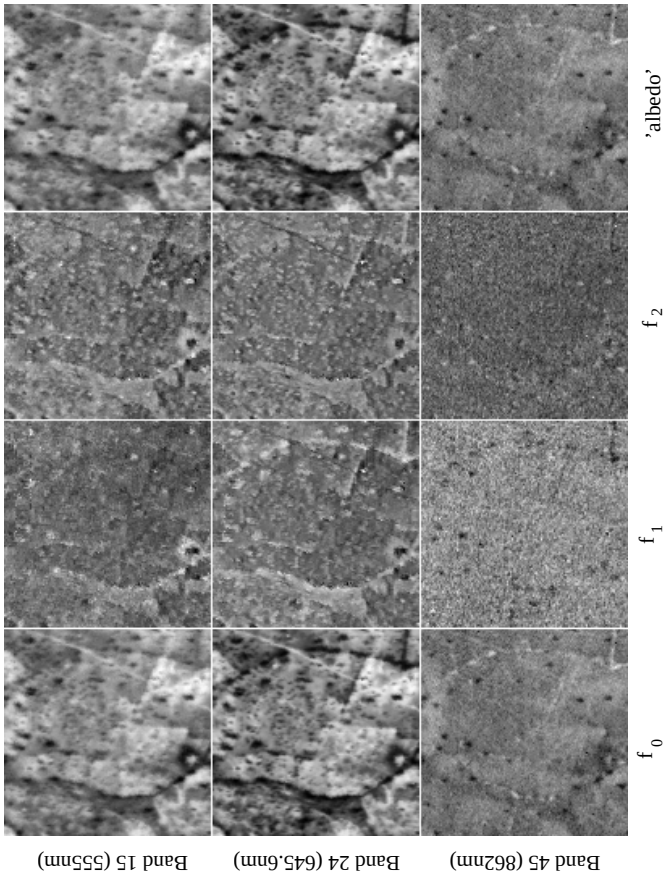

Figure 2: Spatially referenced data sets of the modified Walthall BRDF model parameters and the derived spectral albedo. These data have been produced by inverting the modified Walthall model against the spectral bidirectional reflectance factor data shown in the previous figure. Note, in particular, the spatial patterns that are evident in the values of the model parameters. These are closely related to spatial variations in the land cover and are boradly maintained in the spectral albedo data.

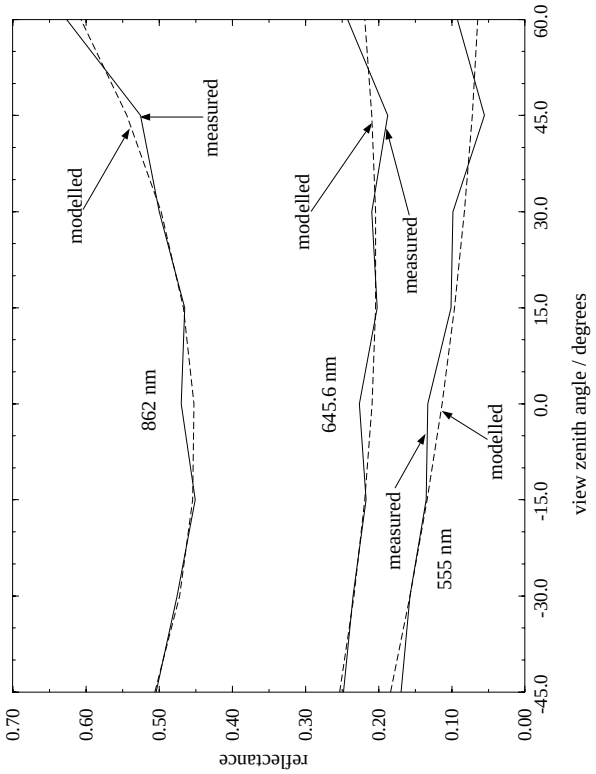

Figure 3: Plot showing the fits between the measured and the modelled spectral bidirectional reflectance factor data for the modified Walthall BRDF model.

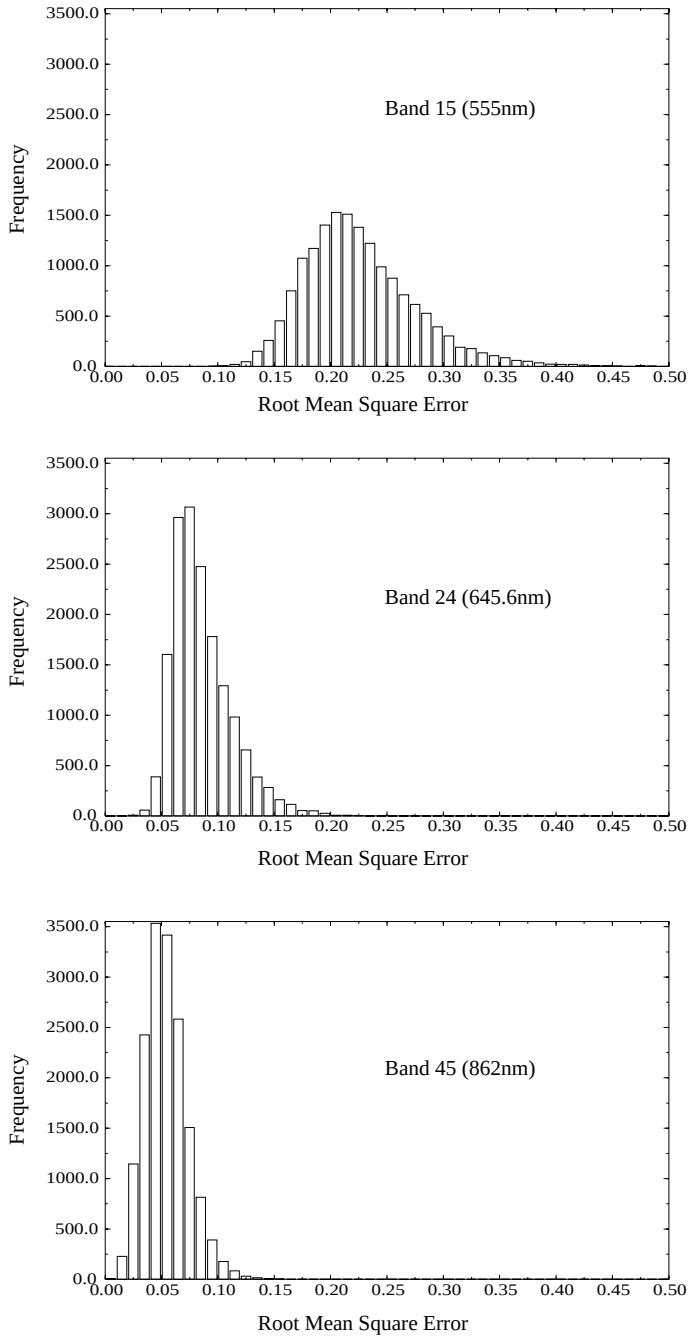

Figure 4: Histograms of the RMSE of the fit between the modified Walthall BRDF model and the multi-angle ASAS data in bands 15 (555nm), 24 (645.6nm) and 45 (892nm).

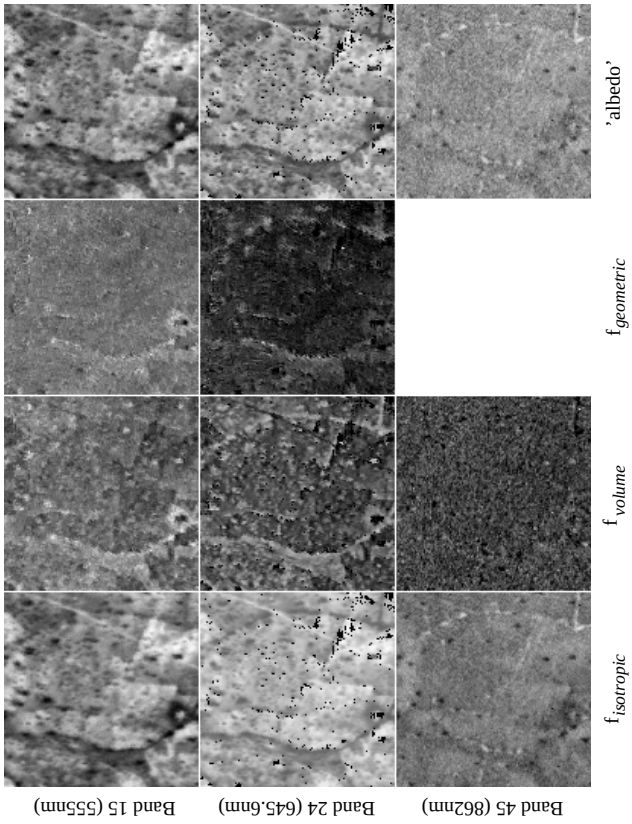

Figure 5: Spatially referenced data sets of the Roujean-RossThin semiempirical BRDF model parameters and the derived spectral albedo. These data have been produced by inverting the Roujean-RossThin model against the spectral bidirectional reflectance factor data shown in figure 1. Note that the spatial patterns evident in this figure are very similar to those obtained using the simpler empirical model (figure 2).

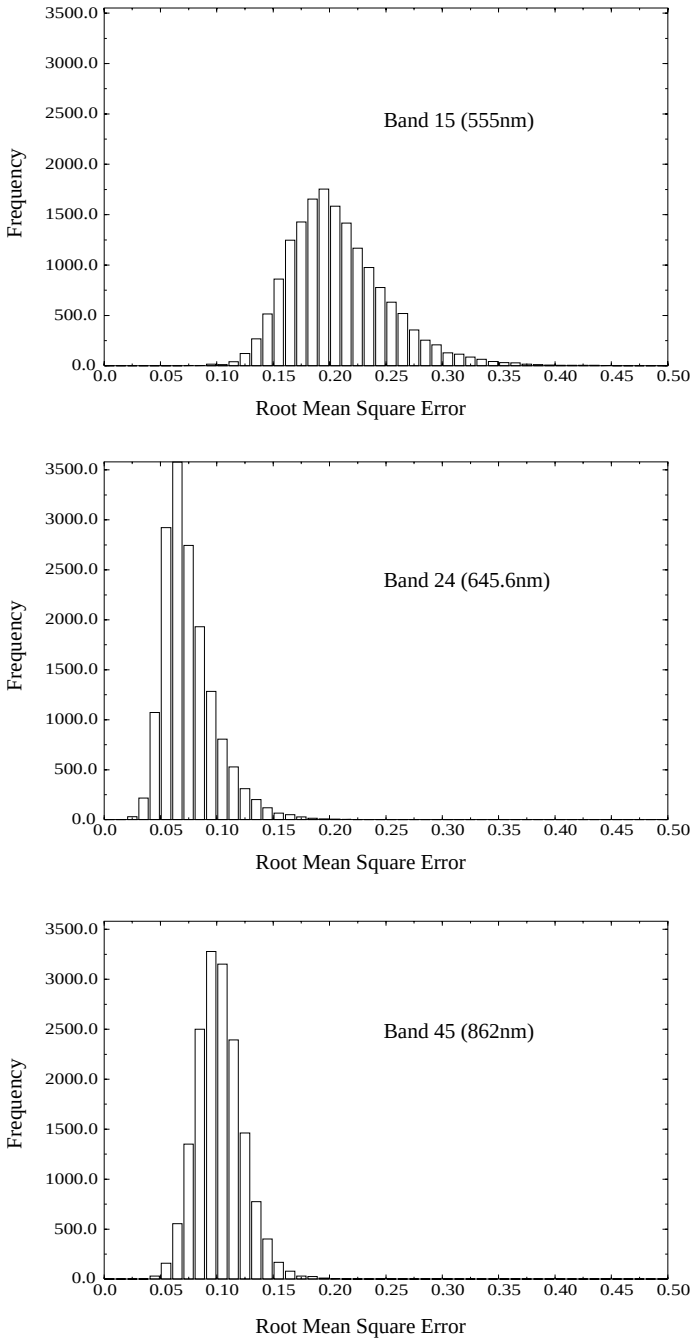

Figure 6: Histograms of the RMSE of the fit between the Roujean-RossThin BRDF model and the multi-angle ASAS data in bands 15 (555nm), 24 (645.6nm) and 45 (892nm).